Tropospheric Radiative Forcing from El Chichón and Mt. Pinatubo: Theory and Observations

by: Ellsworth G. Dutton
NOAA, Climate Monitoring and Diagnostics Laboratory
Boulder, CO 80303

Stephen K. Cox
Department of Atmospheric Science
Colorado State University
Fort Collins, CO 80523

Sponsoring Agencies:

National Oceanic and Atmospheric Administration, Climate Monitoring and Diagnostics Laboratory

National Aeronautics & Space Administration

Colorado State University

DEPARTMENT OF ATMOSPHERIC SCIENCE

PAPER NO. 586

TROPOSPHERIC RADIATIVE FORCING FROM EL CHICHÓN AND MT. PINATUBO: THEORY AND OBSERVATIONS

by

Ellsworth G. Dutton
NOAA, Climate Monitoring and Diagnostics Laboratory,
Boulder, CO 80303

and

Stephen K. Cox
Department of Atmospheric Science
Colorado State University, Fort Collins, CO 80523

September 1995

CSU Atmospheric Science Paper No. 586

Abstract

The possibility of volcanic effects on global and regional climate variables has had a long history of speculation, correlative study, and proposed physical mechanisms. The potential for widespread surface cooling following the extensive spreading of long-lived stratospheric aerosols following major volcanic eruptions is based on the partial blocking of solar radiation incident at the top of the troposphere. Relatively simple physical mechanisms oppose this potential for cooling: dominant forward solar scattering and absorption of outgoing infrared radiation by the aerosols. More complex considerations are the spatial and temporal variations of the distributed aerosol and its optical and physical properties; potential for water/ice cloud modification by the volcanic particles; surface albedo, water vapor, and cloud feedbacks to a temperature change; the role of the oceans in a large-scale radiatively forced temperature variation; possible circulation modifications; and other forced and random variations in climate. In the current work, rigorous radiative transfer calculations relative to a subset of the above considerations are carried out and compared to observational data to examine deterministic volcanic effects on climate. Specifically, zonally resolved volcanic radiative forcing at the tropopause, and other levels, is computed from the best available information on the spatial and temporal distribution of volcanic aerosols from two recent eruptions, El Chichón (Mexico, 1982) and Mt. Pinatubo (Philippines, 1991). Accuracy of the radiative calculations is partially verified with surface- and satellite-based irradiance observations. Maximum global seasonal-mean radiative forcings of -4.5 and -2.2 W m^{-2} are calculated following the Mt. Pinatubo and

El Chichón eruptions, respectively. Within hemisphere irradiance gradient anomalies of up to 16% at the tropopause are calculated for the second N. Hemisphere summer following the eruptions. The computed radiative forcing is applied to a simple hemispheric tropospheric temperature change model, assuming constant cloudiness and surface albedo, in an effort to explain observed global temperature records (NOAA Microwave Sounding Unit) following the two eruptions. Excellent agreement is seen between explained (modeled) and observed global and hemispheric temperature changes after the Mt. Pinatubo eruption, but not following that of El Chichón. Details of this work and some discussion of the results are given. A simple parameterization of the radiative forcing calculations is given that may prove useful in higher spatial and temporal resolution investigations.

Acknowledgments

We would like to thank Profs. Graeme Stephens, David Randall, Dave Krueger for their helpful comments on the first draft of this report, and Prof. Thomas McKee who also provided beneficial suggestions during the preliminary work. Dr. James Pollack provided much motivation for the this investigation. Appreciation is expressed to Nels Larsen, Dr. Bruce Forgan, Dr. John Barnes, Craig Long, Dr. Paul Stackhouse, and Dr. John Christy who supplied portions of the data used in this study. Thanks also to numerous NOAA/CMDL field observers who facilitated making the surface-based irradiance data available. A special thanks to Dr. Barry Bodhaine who provided technical assistance in preparation on the final manuscript. NOAA/ERL supplied many of the research resources that made this work possible. Drs. Michael King and Warren Wiscombe furnished some of the computer code used. This work was completed when one of the authors (Dutton) was a student at Colorado State University.

This research was sponsored by National Oceanic Atmospheric Administration, Climate Monitoring and Diagnostics Laboratory in Boulder, CO and National Aeronautics & Space Administration Contract Number NAG 1 1704.

Table of Contents

Abstract ii
Acknowledgments vi
Table of Contents v
List of Figures viii
List of Tables xiii

Chapter 1. Volcanic Radiative Forcing and Climate: An Introduction 1
1.1 Background on Volcanic Effects on Climate 1
1.2 Volcanic Radiative Forcing 5
1.3 Status 7
1.4 Purpose and Goals of Current Research 9
1.5 Research Approach 11
1.6 Principal Results 13

Chapter 2. Observations of Stratospheric Aerosols and Related Radiative Forcing 15
2.1 Spectral Aerosol Optical Depth 17
2.2 IR Optical Depth 30
2.3 Aerosol Height 31
2.4 Size Distributions 34
2.5 Solar Irradiance 37
2.6 IR Radiative Forcing 47
2.7 Net Allwave Irradiance 48
2.8 Underlying Albedo 48

Chapter 3. Radiative Transfer: Theory and Atmospheric Models 51
3.1 Model Development 51
3.2 Model Inputs and Execution 53

Chapter 4. Computation of Volcanic Radiative Forcing: Results and Comparisons 62
4.1 Brief Investigations with Basic RT Models 63
4.2 Comparison to ICRCCM 67
4.3 Altitude of Volcanic Radiative Forcing 70
4.4 Instantaneous vs. Equilibrium Radiative Forcing 70
4.5 Global Radiation Balance, Background Conditions 74
4.6 Global Gridded *V* Calculations 77
4.7 Radiative Forcing Comparisons 85
4.8 Atmospheric Heating Rates 98

Chapter 5. Verification, Discussion, Tropospheric Temperature Model, and Parameterizations 100
5.1 Discussion on the Confirmation of Computed *V* 100
5.2 Tropospheric Temperature Changes 110

5.3 Global Distribution of V 116
5.4 Parameterization 119
5.5 Comparison Between Volcanoes 126

Chapter 6. Summary and Conclusions 130
6.1 Summary 130
6.2 Conclusions 132
6.3 Concluding Remarks 137

Appendix A. Physical and Optical Properties of Stratospheric Aerosols 139

Appendix B. Observational Uncertainties 153

Appendix C. Radiative Transfer Equation and Models 158

Appendix D. Sensitivity Tests 179

References 196

List of Figures

Page	Figure
20	**Fig. 2.1** Aerosol optical depth for multiple wavelengths, as indicated, for Mauna Loa, Hawaii (top) and Rattlesnake Mt., Washington (bottom). Rattlesnake Mt. has had background subtracted.
21	**Fig. 2.2** Spectral aerosol optical depth from Alice Springs, Australia. (A) - 440 nm. (B) - 500 nm, (C) - 670 nm, (D) - 862 nm.
23	**Fig. 2.3** Wideband aerosol optical depth from NOAA/CMDL global baseline network. Latitude range of sites is 161 degrees.
25	**Fig. 2.4** 550 nm stratospheric aerosol optical depth compiled after El Chichón by Sato et al. [1993]
27	**Fig. 2.5** 550 nm stratospheric aerosol optical depth estimated after Pinatubo by Sato et al. [1993]
28	**Fig. 2.6** Midvisible aerosol optical depth anomalies derived from AVHRR after Pinatubo [Long and Stowe, 1994].
29	**Fig. 2.7** Midvisible anomalous aerosol optical depth above five sites from different data sources, as indicated.
32	**Fig. 2.8** Scattering plus absorption (solid) and scattering only (dashed) aerosol optical depth vs. wavelength computed from Mie theory using an inverted sized distribution from the zonal mean for the fourth season of 1991, in the northern subtropical zonal belt (910404). Upper and lower observed IR aerosol optical depths obtained from satellite and aircraft are indicated at three wavelengths by vertical lines. Note: scattering optical depth is almost zero so absorption optical depth nearly equals total optical depth for $\lambda > 4$ μm.
33	**Fig. 2.9** Ruby lidar aerosol backscatter as a function of height for four different time frames at Mauna Loa, Hawaii (Courtesy of John Barnes, NOAA/ CMDL).
36	**Fig. 2.10** Seasonal mean aerosol size distributions for both Laramie balloon in situ observations and as inverted from the Rattlesnake Mt. aerosol optical depth.

Page

40 **Fig. 2.11** Observed seasonal mean broadband solar irradiance from Mauna Loa, Hawaii - a) direct, b) diffuse, and c) total, for a solar zenith angle of 60°

42 **Fig. 2.12** Observed total solar irradiance from American Samoa: -*-) seasonal mean, - -) ± two standard error, solid lines) ± one standard deviation.

43 **Fig. 2.13** Observed total solar irradiance from South Pole, 19-23 December - middle line) average, outer lines) ± two standard deviations.

44 **Fig. 2.14** Seasonal statistical summary of observed total solar irradiance at a zenith angle of 60° near Boulder, Colorado. Box plots indicate mean, ±25%, maximum, minimum, and the relative number of data points indicated by the width of the box. Additional statistics are given in the text.

50 **Fig. 2.15** Annual variation of zonal mean TOA albedo as measured from ERBE, averaged over 1986 - 1988. (Note: values on the seasonal terminator are incorrect due to objective analysis plotting limitations)

54 **Fig. 3.1** Spectrally resolved real and imaginary index of sulfuric acid, as given by Palmer and Williams [1975]. The three different water solutions were used in sensitivity tests, with 75% used for most calculations.

57,58 **Fig. 3.2a,b** Linear function relationship between modeled solar reflectance at the tropopause and TOA as a function of surface albedo - dashed line) TOA, solid line) tropopause, a) for background conditions.

64 **Fig. 4.1** LOWTRAN7 and DISORTX modeled direct solar irradiance for sample case with solar zenith angle = 60°.

65 **Fig. 4.2** LOWTRAN7X and DISORTX modeled outgoing IR at TOA for sample case. Note significant differences at some wavelengths and overall bias.

66 **Fig. 4.3** LOWTRAN7X and DISORTX modeled downwelling IR for sample case.

68 Fig 4.4 Comparison between percentage variation in monthly mean clear-sky observed and test modeled total solar irradiance at Mauna Loa, Hawaii.

page

71 **Fig. 4.5** Modeled vertical profiles of solar and IR upward and downward irradiances for background tropical case, showing vertical resolution of atmospheric models - solid) upward SW, X dashed) IR down, dashed) IR upwards, and X solid) SW down.

72 **Fig. 4.6** Vertical profiles of volcanic radiative forcing, V, for grid-box 910406, downwards positive - (x dashed = ${}_{Ld}V$), (solid = ${}_{Su}V$), (dashed = ${}_{Lu}V$), and (x solid = ${}_{Sd}V$).

73 **Fig. 4.7** Vertical profiles of net V: (solid - ${}_{Sn}V$), (dashed - ${}_{Ln}V$), and (x solid - ${}_{An}V$).

75 **Fig. 4.8** Vertical profiles of difference between instantaneous and equilibrium IR V, for a 2 °C increase in lower stratospheric temperatures, (dashed - change in ${}_{Lu}V$), (solid - change in ${}_{Lu}V$), and (x solid - change in ${}_{Ln}V$).

76 **Fig. 4.9** Observed (solid) and computed (dashed) TOA zonal and annual mean radiation components: a) incoming solar, b) reflected solar, c) albedo, d) absorbed, e) outgoing IR, f) net allwave.

78-80 **Fig. 4.10**a-c Zonal and seasonal mean gridded and analyzed volcanic radiative forcing in W m^{-2} related to El Chichón: a) ${}_{Sn}V_{Tr}$, b) ${}_{Ln}V_{Tr}$, and c) ${}_{An}V_{Tr}$.

81-82 **Fig. 4.11**a-c Zonal and seasonal mean gridded and analyzed volcanic radiative forcing in W m^{-2} related to Pinatubo: a) ${}_{Sn}V_{Tr}$, b) ${}_{Ln}V_{Tr}$, and c) ${}_{An}V_{Tr}$.

84 **Fig. 4.12** Global and hemispheric mean ${}_{An}V_{Tr}$ computed from Figs. 4.10c and 4.11c.

89 **Fig. 4.13** Seasonal mean observed and modeled downward solar irradiance at Mauna Loa for a solar zenith angle of 60°. Xs are for model output using locally observed $\tau_A(\lambda)$, Os for $\tau_A(\lambda)$ from the zonal mean.

91 **Fig. 4.14** Observed (circles) and modeled ("x"s) ratios of change in diffuse to change in direct solar irradiance, ε, at Mauna Loa, Hawaii. Bold "+" in 1992 is for Pueschel et al. [1994] March 22 special case.

Page

93 **Fig. 4.15** Seasonal mean measured and observed clear-sky surface solar irradiance for American Samoa at a solar zenith angle of 45°. Solid lines a mean and ±1 standard deviation, the vertical bars on the observed mean is ±2 standard error, dashed lines are computed for zonal bands six and seven, nearest Samoa's latitude. The modeled values are normalized to pre-eruption conditions. The $\tau_A(\lambda)$ used was from the global grid.

94 **Fig. 4.16** Observed and modeled surface clear-sky solar irradiance from South Pole, 19-23 December for 1988-1993. Solid lines are observed means ±2 standard deviations, + with dashed lines are modeled for solar zenith angle equal 66.5° and locally observed midvisible τ_A.

96 **Fig. 4.17** Zonal mean computed V_{TOA} by season for El Chichón, solid line - ${}_{An}V_{TOA}$, short dashed line - ${}_{Sn}V_{TOA}$, and long dashed line - ${}_{Lu}V_{TOA}$. In the upper left of each frame is year and season (YR-S). The north (N) and south (S) hemispheric mean ${}_{An}V_{TOA}$ (W m^{-2}) are indicated in the lower left corner of each frame.

97 **Fig. 4.18** Same as **Fig. 4.21** except for Pinatubo.

99 **Fig. 4.19** Vertical profile of solar and thermal radiative atmospheric heating rates for volcanic stratospheric aerosol, Dashed line - IR, Solid line - SW.

104 **Fig. 5.1** Time Series comparison between V_{Tr} computed with balloon measured aerosol size distribution, -X-, and inverted from sunphotometer $\tau_A(\lambda)$ observations, -O-. Upper two curves are for ${}_{Ln}V_{Tr}$, and lower two for ${}_{Sn}V_{Tr}$.

109 Fig 5.2 $\tau_A(\lambda)$ computed from Mie calculations for inverted aerosol size distribution for Pueschel et al. [1994] 22 March 1992, 19 km size distribution.

113 **Fig. 5.3** Time series for hemispheric and global mean lower tropospheric air temperatures anomalies. Observations (solid line) are from the MSU satellite sensor with deseasonalized anomalies calculated from the mean of 1981-1990. Calculated values, Xs, are described in text and are normalized to the 1-yr mean observed anomalies for the 1 yr prior to each eruption, April 1982 and June 1991. Computed values are for a 1-yr time constant in the model.

115 **Fig. 5.4** Same as **Fig. 5.3** except for a 2.5-yr time constant following El Chichón.

Page

118 **Fig. 5.5** Time series of computed ${}_{An}V_{Tr}$, intrahemispheric gradients. Within each hemisphere the northern most zonal ${}_{An}V_{Tr}$ is subtracted from the southern most band. In both hemispheres, the two latitude bands nearest the equator were averaged together before the subtraction.

123 **Fig. 5.6** Dependent and independent, as defined in text, residuals from the difference between parametrically and RT computed ${}_{Sn}V_{Tr}$ (a & b) and ${}_{Ln}V_{Tr}$ (c & d) for Pinatubo (a & c) and El Chichón (b & d). Dashed line is the 1:1 ratio for comparison.

127 **Fig. 5.7** Global and hemispheric mean ${}_{An}V_{Tr}$ computed from parameterization Eq. 5.6 with coefficients taken from Table 5.3.

128 **Fig. 5.8** A comparison of the ${}_{Sn}V_{Tr}$ sensitivity to $\tau_A(550)$ for El Chichón and Pinatubo for a solar zenith angle of 60^o and surface albedo of 0.23. Straight lines are least squares fits, solid - El Chichón, dashed - Pinatubo.

162 **Fig. C.1** Schematic of vertical and angular structure of the DISORT (and DISORTX) RT models, with n = 33 and n' = 5. in DISORTX. "Theta0" is incident solar irradiance at TOA.

175 **Fig. C.2** Extraterrestrial solar irradiance, normally incident at the top of the earth's atmosphere at a distance of 1 A.U., spectrally resolved into 146 bands plotted at the bands' midpoint.

181 **Fig. D.1** Net irradiance in W m^{-2} (0.53 to 0.57 μm) at the tropopause as a function of 550 nm aerosol optical depth in the stratosphere.

182 **Fig. D.2** Modeled downward diffuse solar at 19 km ASL as a function of aerosol optical depth for single (dashed) and multiple (solid) scattering cases for different albedos and solar zenith angles as indicated.

183 **Fig. D.3** Net solar irradiance at tropopause as a function of varying stratospheric aerosol optical depth for different zenith angles and surface albedo cases.

185 **Fig. D.4** Various aerosol size distributions inverted from a single set of spectral aerosol optical depth observations, for grid-box 820304.

Page

187 **Fig. D.5** Sensitivity of ${}_{Sn}V_{Tr}$ (0.53 to 0.57 μm) to changes in surface albedo and solar zenith angle for grid-box 910404. The graphed lines are for different zenith angles, the top dashed line is for 5°, the next five lines, starting from the top are for 15°, 25°, 35°, 45°, 65°, and 75°, respectively. The dot/dash line is for 85° and represents an abrupt reversal that occurs between 75° and 85° with the line for 90° (not shown) being everywhere equal to zero.

188 **Fig. D.6** Sensitivity of the change in the TOA albedo, normalized to unit $\tau_A(500)$, as a function of surface albedo for various solar zenith angles. The solar zenith angles starting from the top of the graph are: 85°, 75°, 65°, 45°, 35°, 25°, 15°, and 5°. This figure was computed primarily for comparison to similar results presented by Harshvardhan [1979]

190 **Fig. D.7** Oceanic bidirectional reflectance function in the solar plane for a solar zenith angle of 45°. Dotted curve represents data provided by P. Minnis and the solid curve is as reproduced by a 10th degree Legendre polynomial. The reflectance function was normalized to one over the solar plane and multiplied by a mean surface albedo of 0.24.

List of Tables

Page

59 **Table 3.1** Atmospheric profiles used for various seasons and latitude bands.

69 **Table 4.1** Comparison of ICRCCM results to DISORTX and LOWTRAN7X calculations. "rms" is the rms differences among the ICRCCM cases.

86 **Table 4.2** Comparison between volcanic radiative forcing calculated in the current study and that published previously.

88 **Table 4.3** Differences between modeled and observed ${}_{Sd}V_S$ at Mauna Loa.

121 **Table 5.1** Regression coefficients and *t* values for individual fits to RT results for separate and combined volcanoes.

122 **Table 5.2** Summary of residual statistics for dependent and independent regression fits.

125 **Table 5.3** Coefficients and t values for various fits to ${}_{An}V_{Tr}$.

126 **Table 5.4** Range of variables used in regression fits.

150 **Table A.1** Aerosol population optical properties computed by MIEV0X compared to Diermendjian (1969)

184 **Table D.1** Statistics related to ${}_{Sn}V_{Tr}$ and ${}_{Ln}V_{Tr}$ computed for the different size distributions shown in **Fig. D.4.**

192 **Table D.2** Sensitivity of ${}_{Sn}V_{Tr}$ to variations in ω_O.

193 **Table D.3** Volcanic radiative forcing for fixed model inputs except for different model atmospheres as indicated.

194 **Table D.4** Irradiances calculated for different numbers of downward radiance streams at the tropopause for a volcanic aerosol case.

Chapter 1. Volcanic Radiative Forcing and Climate: An Introduction

1.1 Background on Volcanic Effects on Climate

Pollack et al. [1976] describe the early development of understanding the physical relationship between volcanic eruptions and climate, as summarized in the following. Climatic consequences due to volcanic eruptions were first suggested in 1784 by Benjamin Franklin who noted an association between a solar-blocking persistent haze, possibly from the eruption of an Icelandic volcano, and a cool period in 1783 - 84. W. Humphreys, in 1940, attempted a physical explanation for the cooling effect of volcanic aerosols but did not have sufficient information on the optical and physical properties of the volcanic aerosols. In 1969, M. Budyko refined Humphreys volcanic aerosol model and developed a model for global temperature change caused by decreased solar insolation due to volcanic eruptions with a surface albedo feedback. However, the Budyko model still had incomplete aerosol radiative properties. W. Sellers improved upon Budyko's work, in an 1973 paper, with a more physically realistic climate model, but he was interested in only tropospheric aerosols. Lamb [1970] examined climatic records and found a relationship between temperature records and some volcanic eruptions. Lamb went on to develop the volcanic Dust Veil Index (DVI) which showed correspondence between stratospheric dust loading and worldwide cooling, but in some cases DVI was deduced from the temperature record.

Most efforts to identify volcanically induced climate changes have consisted primarily of attempting to show that there was a detectable signal in global or zonal mean

tropospheric or surface temperatures [e.g., Mitchell, 1961; Lamb, 1970; Mass and Schneider, 1977; Oliver, 1976; Hansen et al., 1978; Angell and Korshover, 1985; Angell, 1988; Mass and Portman, 1989]. It is desirable to quantitatively identify the climatic response to any given volcano, past or future, to further understand other sources of variability in the earth's climate, e.g., sea surface temperatures, greenhouse warming, solar variations, and natural internal variability. Angell [1988] and Mass and Portman [1989] showed that if El Niño warming following the 1982 eruption of El Chichón was considered, there was identifiable volcanic global cooling of ~0.2 to 0.3 °C. Following the Mt. Pinatubo eruption in 1991, a distinct decrease in temperature of 0.5 °C globally, and near 0.8 °C in the N. hemisphere, was reported [Dutton and Christy, 1992; Hansen et al., 1993; Halpert et al., 1993] despite a moderate El Niño. Contrary to the above studies, Angell and Korshover [1985] used a statistical composite technique to examine the temperature effects of volcanic eruptions prior to 1980 and were only able to conclude that "in general, volcanic eruptions do not cause warming of tropospheric temperatures."

Budyko [1969] used a global energy budget model to show reasonable agreement between theoretical and observed responses in global air temperatures to a given change in incident solar irradiance, and suggested that volcanoes were the major contributors to such irradiance changes. Hansen et al. [1978] showed close agreement between a physical model and observed temperature change, both in magnitude and timing, for monthly averages three years following the Mt. Agung eruption (1963, 8° S) However, Hansen et al. analyzed only the tropics and subtropics and, like Budyko, used only a minimal description of the aerosol.

The currently proposed physical mechanisms by which long-lived (i.e., greater than one month) volcanic aerosols can perturb global and regional radiation budgets and thereby potentially affect climate, were suggested in several works [e.g., Pollack et al.,

1976; Coakley and Grams, 1976; Harshvardhan, 1979; Toon and Pollack, 1980; Chou et al., 1984; Lacis et al., 1992]. The scattering and absorption of solar and thermal infrared (IR) radiation by stratospheric aerosols were considered. It was suggested by these authors that, based on the anticipated optical properties of the aerosols, the loss of incoming solar irradiance due to the upwards scattering from the aerosol dominates related radiation budget perturbations, although absorption of solar and IR were also significant. Global and hemispheric mean radiation perturbations exceeding several W m^{-2} were predicted from radiative transfer (RT) theory and estimates of volcanic aerosol optical properties. Simple to sophisticated climate models were used to help ascertain the potential tropospheric temperature response to estimated radiative forcing. Hemispheric and global mean cooling potentials following major eruptions were estimated to be up to 2 ^{o}C.

All components of atmospheric radiation are potentially affected by an increase in stratospheric aerosols, with downwelling irradiances above the aerosol layer obviously being the least affected. The magnitudes of expected and observable irradiance changes are not well established. Volcanic influences were reported in total (direct + diffuse) solar irradiance measurements at the surface by Dyer and Hicks [1965], Viebrock and Flowers [1968], DeLuisi et al. [1983], Hay and Darby [1984], Wendler [1984], Dutton [1990a], Dutton and Christy [1992], Dutton et al. [1994], Hayasaka et al. [1994], and from space by Ardanuy and Kyle [1986] and Minnis et al. [1993]. Surface-based observations were for clear-sky cases only while satellite observations included water clouds. In the reported satellite data, it was difficult to separate irradiance variations due to stratospheric aerosols from changes that may have occurred in cloud properties or distribution.

Quantitative validation of the theoretical volcanic radiation perturbations by direct comparison to radiation observations would be an intermediate step to confirming related theories and to a further understanding of volcanic effects on climate. A direct comparison would utilize observed aerosol parameters in RT irradiance calculations and nearly simultaneous clear-sky irradiance observations. A few direct validation attempts have been made using surface observations [Coakley, 1981; DeLuisi et al., 1983; Hayasaka et al., 1994] and have not been successful. In these attempts, it was not clear if the lack of agreement was the fault of the radiation observations or the theoretical computations. Both are subject to large uncertainties. Minnis et al. [1993] claimed general global mean agreement in an indirect comparison between their volcanically perturbed satellite irradiance observations and the theoretical estimates reported by Lacis et al. [1992]. The Minnis et al. data were not distinguished from those with water cloud effects, and Lacis et al. used only hypothetical aerosol parameters and constant cloudiness. Mutual direct confirmation of theoretical and observational results was desirable to build confidence in both, so that one can be used in lieu of the other when necessary to identify potential climatic influence of a given eruption.

The potential climatic impacts of spatialotemporal variations in volcanic aerosols have not been extensively investigated, in part because accurate information on the distribution of aerosols and their optical properties were unavailable, and in part because many general circulation models (GCMs) were not developed to the extent where inclusion of volcanic aerosols was feasible. Barth et al. [1982], Dutton and DeLuisi [1983], McCormick and Veiga [1992], and Trepte et al. [1994] showed that significant latitudinal banding of stratospheric aerosols occurs following volcanic eruptions. Robock and Mao [1992] and Graf et al. [1993] have investigated some regional climate effects due to nonhomogeneous distribution of volcanic aerosols.

Herman et al. [1976], Harshvardhan [1979], Lenoble et al. [1982], and King et al. [1984] have investigated modeled volcanic radiation anomalies that include the effects of seasonal and latitudinal variations in solar zenith angle (θ_o) and albedo (α). None of the above studies used observed aerosol evolutions; however, King et al. [1984] did use an estimated aerosol dispersion based on initial El Chichón eruption characteristics. Also, these studies used spectrally, vertically, or otherwise abbreviated radiative transfer schemes, and none compared their theoretical results to observed radiation quantities.

Many previously mentioned efforts to detect volcanic signal in climate records relied on either the Volcanic Explosivity Index (VEI) [Newhall and Self, 1982] or the DVI to estimate the potential climatic effect of a particular eruption. Neither index was based on the magnitude of known or expected perturbations to the radiation field. Computation and verification of the actual radiative forcing from a given volcano, as done in the work, should permit a more rigorous assessment of potential for climate modification by providing perturbed radiation fields that can be directly or indirectly introduced into numerical climate models [Hansen et al., 1992 and Graf et al., 1993]

1.2 Volcanic Radiative Forcing

Volcanic radiative forcing can be defined as any change in atmospheric radiation caused by the addition of volcanic aerosols to the stratosphere, and will be denoted here as V in the most general case. Notation introduced later will define the wavelength, height, and direction of the affected radiation quantities. V is commonly called a "forcing" in that it represents a change in the energy budget, which may, in turn, cause a response in other atmospheric variables. Either observations or RT models can be used to estimate V as the difference between irradiances for otherwise identical conditions with

and without anomalous volcanic aerosols. Determining V in this manner cancels many RT model and instrumental biases that could otherwise mask the volcanic influence. In the remainder of this work, "computed," "calculated," "model," or "RT modeled" V refer to differential RT-model calculated irradiances and "observed" V refers to differential irradiance observations.

There are indirect volcanic effects which could either amplify or reduce V. For example, volcanic particles precipitating into the troposphere could modify cloud reflectance or otherwise alter cloudiness [Sassen et al, 1995]. Also, a significant tropospheric cooling could increase surface albedo due to extended snow cover. The radiative effects of any volcanically induced changes in cloudiness, water vapor, ozone, surface albedo, or tropospheric temperature were not considered in the current work.

As defined, V can be either instantaneous or equilibrium forcing according to Lacis et al. [1992] and IPCC [1995]. Instantaneous forcing does not account for any changes in the irradiance quantities that may occur because of the forcing. Equilibrium forcing accounts for those changes. To compute equilibrium V, the response of the atmosphere including feedbacks needs to be known. For example, equilibrium forcing would include enhanced downward IR at the tropopause as stratospheric temperatures increase due to absorption of solar and IR radiation by the volcanic aerosols and gases. The effects of a warming stratosphere on IR V will be investigated. Unless otherwise specified, all references to computed V in this work are to the instantaneous quantity, since these are the most readily calculated using only radiative transfer computations. Observations of V are inherently initially instantaneous, and then tend to become equilibrium, as new equilibrium is approached.

Spectral, directional, spatial, and temporal segregation of radiative quantities result in many different V components that can be identified. Only upward or downward

irradiances on horizontal surfaces were considered here, although RT models use multidirectional radiances to derive irradiance as discussed in Chapter 3 and Appendix C. Leading and trailing subscripts on V will be used to denote the many possibilities. The leading capital or numeric subscripts denote wavelength: "S" for solar, "L" for IR (longwave), "A" for allwave (S + L), or numeric values in nm. Leading lower case letters denote direction: "u" for upwards, "d" for downwards, and "n" for net (downward minus upward). Trailing subscripts are abbreviations or numeric values denoting height: "S" for surface (not necessarily sea-level), "Tr" for tropopause, "TOA" for the top of the atmosphere, or numeric values for km above sea level. For example, ${}_{Sn}V_{Tr}$ translates to "net solar volcanic radiative forcing at the level of the tropopause." Temporal and horizontal dependencies will be specified in the text as relevant.

1.3 Status

Recent eruptions have provided much observational data on the potential for their global climatic influence. This information has not been widely assimilated into current GCMs [Hansen et al., 1992]. El Chichón (17° N) in 1982 and Mt. Pinatubo (15° N) in 1991 propelled extensive amounts (>five megatonnes) of SO_2 into the stratosphere as observed by the Total Ozone Mapping Satellite (TOMS) [Krueger, 1983; Bluth et al., 1992]. These two volcanoes are the most likely of any to have produced identifiable radiative and climatic signals in the past 30 years. Some probable El Chichón and Pinatubo related climate perturbations have been reported by Angell [1988], Mass and Portman [1989], Dutton and Christy [1992], Robock and Mao [1992], Hansen et al. [1993], and Minnis et al. [1993]. However, extensive theoretical estimates of V using observed aerosol properties have not yet been published. Such calculations need to be

made and compared to irradiance observations to establish confidence in our ability to realistically confirm or validate related radiative theories.

Recent advances, along with currently available data, allow improved quantification of V, increasing the possibility of identifying the response of the atmosphere to this forcing. These advances include improved knowledge of the particular effluent from volcanoes that results in extended radiative forcing, improved observing systems that allow more complete temporal and spatial definition of the eruption clouds' physical extent, more complete climate observations that better represent global variations, expanded RT computing capability, and refined general circulation simulations that can elucidate the physical processes that transform V to climate variations [Hansen et al., 1988, 1992; Graf et al., 1993]. To compute V for a given volcanic eruption, certain information on the aerosol cloud must be acquired, as was done here for the eruptions of El Chichón and Pinatubo. To perform a complete study of the climatic impacts of these two eruptions, the preexisting global climate state, other independent climate forcings (sea surface temperatures, quasi-biennial oscillation (QBO), solar, random, CO_2, etc.), and feedback mechanisms would need to be considered; however, this is well beyond the scope of this work.

Abundant but incomplete and sometimes inaccurate direct observational information on the properties of the El Chichón and Pinatubo stratospheric aerosol clouds has been acquired from surface-based and airborne missions as well as from experimental and operational satellite platforms [e.g., *Geophys. Res. Lett.*, Nov. 1983 and Jan. 1992, special issues]. Such data include information on size, shape, composition, optical properties, spatial and temporal variation, as well as direct and indirect observations of radiation budget perturbations.

The aerosols remaining in the stratosphere for an extended period (greater than one month) have been deduced, and occasionally observed, to be almost entirely droplets of sulfuric acid (H_2SO_4) in solution with water [e.g., Turco et al., 1982]. These droplets grow from SO_2 vapor to small aerosols with peak concentrations in the 0.1 to 1.0 μm radius range where the Mie scattering of sunlight is particularly efficient. Volcanic SO_2 was lofted into the stratosphere at the time of the eruption and quickly (e-folding time of about one month) converted to H_2SO_4 droplets [Turco et al., 1982; Hofmann and Rosen, 1983; Pinto et al., 1989; Sheridan et al., 1992; Self et al., 1995]. The mass of SO_2 lofted into the stratosphere determines the quantity of long-lived aerosol loading and the height of the injection determines its lifetime. However, V is a poorly known nonlinear function of the initial stratospheric SO_2 injection [Pinto et al., 1989]. Also, only certain volcanic eruptions inject significant amounts of SO_2 into the stratosphere. The TOMS has provided an estimate of the amount of SO_2 added to the atmosphere by each volcanic eruption over the past 14 years [Amer. Geophys. Union, 1992]. To define the temporal and spatial variations of volcanic aerosol after the first month, during which most SO_2 has been converted to H_2SO_4, additional observations were required because TOMS cannot detect H_2SO_4 aerosols.

A variable horizontal distribution of aerosols develops from volcanic SO_2 [Barth et al., 1982; McCormick and Swissler, 1983; Dutton and DeLuisi, 1983; Stowe et al., 1992; Dutton and Christy, 1992; and others]. Instead of spreading uniformly over the globe or even a hemisphere as assumed in many earlier studies, most material has been observed to spend an important portion of its atmospheric life in a strongly latitude-dependent distribution [Halbert et al., 1993; Trepte et al, 1994]. This banding of the aerosol raises the possibility for modifying both hemispheric N/S temperature gradients and associated atmospheric circulation patterns [Pollack and Ackerman, 1983].

1.4 Purpose and Goals of Current Research

The purpose of this work is to investigate the zonal and global mean radiative forcing produced by the El Chichón and Mt. Pinatubo volcanic eruptions to aid in further determination of climatic effects potentially related to those eruptions. The specific goals of this work are:

1. Develop the capability to compute important components of V using observed optical, chemical, and physical properties of recent volcanic aerosols;
2. Quantitatively verify calculations and observations of selected components of V;
3. Examine spatial and temporal extents of V and estimate related hemispheric and global mean tropospheric temperature changes;
4. Examine sensitivity of calculated V to major variables and develop simple parameterizations.

Several related questions are to be answered:

1. Was sufficient information available to compute accurate, regionally or locally resolved V due to recent volcanic eruptions?
2. How well does computed V have to agree with an observation for confirmation?
3. What were the nature and significance of the regionally variable V patterns?
4. Can hemispheric mean temperature changes be estimated from computed V and confirmed with observations?

5. What information was there in the similarities and differences between the El Chichón and Pinatubo events?

These and other questions are relevant to the issues of whether and how V can or should be realistically introduced into GCMs.

1.5 Research Approach

The following outlines the research tasks that are to be carried out:

1. Accumulate and scrutinize relevant existing observations of irradiance and volcanic aerosol properties;
2. Develop realistic atmospheric RT computational capability founded on reliable and well tested existing computer codes;
3. Define RT model inputs that allow local and zonal resolution of V;
4. Independently and separately verify RT modeled and observed irradiance;
5. Compare observed to model-computed V for multiple cases;
6. Develop a physically based global temperature change model and compare results to observed temperature changes;
7. Investigate latitudinal gradients of V;
8. Develop simple parameterization for V for extended use in higher spatial and temporal resolution studies.

Because of the scope of this investigation, data from other investigators, as well as those of this author, were combined. Site specific and global data from surface- and satellite-based platforms were accumulated. The limitations of each data set acquired and utilized were examined. Observed data were assembled from just before each event to 2.5 years

after the eruptions of El Chichón and Mt. Pinatubo and for a 1-yr nonvolcanic background period. These data are extensive but only partially complete and include spatially and temporally variable spectral aerosol optical depth, particle size distributions, chemical composition, aerosol shape, vertical aerosol distribution, globally representative atmospheric constituent and temperature profiles, tropospheric albedo, and irradiance observations. Using these data, low resolution temporal and spatial evolutions of V were computed and sporadically compared with observations. The spatial resolution of this study was limited to zonal mean regions and specific points because there were insufficient available aerosol data to justify examination of longitudinal variations and because of computational limitations. Some longitudinal variations related to underlying albedo can be computed directly from the albedo sensitivity, if the underlying tropospheric albedo is known.

Published and well-tested computer codes for some computational aspects of this work already existed. However, in each case the code was adapted to the current application. The basic RT theory and relevant equations will be given, along with a rudimentary description of the additions and modifications to the existing computer code. Computed radiation quantities at the earth's surface, midtroposphere, tropopause, and top of the atmosphere will be examined using available observations to help evaluate the consistency and accuracy of the computations. Following Lacis et al. [1992], net allwave volcanic radiative forcing at the tropopause, ${}_{An}V_{Tr}$, will be used as an indicator of the total volcanic radiative effect on the tropospheric and surface temperatures.

Differences and similarities between the El Chichón and Pinatubo eruption clouds indicate what may be invariant in determining V. The spatial distribution of aerosol can be expected to vary between eruptions. Latitudinal banding could cause seasonal amplification or retardation of zonal temperature gradients depending on the timing and

location of the eruption. Contrasting El Chichón and Pinatubo presents an interesting example because the eruptions occurred at almost the same latitude and time of year. Observed differences in the micro- and macro-physical properties of the two volcanoes' aerosol populations can result in potentially different radiative forcing consequences.

Relative to previous work, the current work is most similar to the physical approach of Hansen et al. [1978], but with greatly expanded observations of aerosol optical properties, new RT models, major emphasis on direct verification of radiative forcing, investigation of zonal variations, a different temperature change model, and development of parameterizations. RT models will be sufficiently complete so that the computed V will be suitable for introduction into GCMs as anomalies to the radiative fields computed internally in the model, or as verification of anomalies produced by the GCM if it already accounts for aerosol properties. Parameterizations developed here will help facilitate such applications that may require considerably higher spatial and temporal resolution.

1.6 Principal Results

Zonally and seasonally resolved global volcanic radiative forcing was computed from similarly resolved observed aerosol optical properties for 2.5 years following the eruptions of both El Chichón and Pinatubo. These results differ from earlier related efforts in that newer and more complete RT models were used, and global aerosol optical properties were derived directly from observations of the volcanic aerosols. Previous studies relied primarily on abbreviated RT models and assumed or expected aerosol properties and spatial distributions. Observed changes in the surface and top of the atmosphere radiation components agree closely with computed values of volcanic radiative forcing. The zonal variations in V indicate significant perturbations to seasonal N-S gradients in global radiative input. A simple global and hemispheric temperature change model based on the

thermal mass of the atmosphere and oceans and the amount of energy lost to the two eruptions is developed and shows surprisingly excellent agreement with observed tropospheric temperature changes following Pinatubo, but there is little agreement between the model and observations after El Chichón. This suggests that the excellent agreement following Pinatubo was mostly fortuitous since the earth is not constrained to behave according to the assumptions of the simple temperature change model. Simple regression fits between the rigorously computed V and the major independent variables are determined and presented to supply an efficient way in which to use the current results in higher time and spatial scale investigations.

Chapter 2. Observations of Stratospheric Aerosols and Related Radiative Perturbations

Observations used for this study were irradiance measurements and those of the physical and optical properties of stratospheric aerosols as discussed in Appendix A, where some of the common notation and terminology used in this and subsequent Chapters are defined. Accurate information on the physical and optical aerosol properties allows computation of theoretical V that can be compared to appropriate irradiance observations; unfortunately, these parameters are not among those routinely observed. Available observations were limited in extent and completeness and frequently were experimental, which restricted their availability and raised questions about their accuracy and comparability. This was partly because it was impractical to set up an extensive observational program before a major eruption, considering their infrequent and unpredictable nature [Self et al., 1995]. Establishing observation programs after an eruption was also problematic because of the lack of time to prepare and the short life of the event (< two years). Also, observations beginning after the events provide no background information. Nonetheless, there is limited information available about volcanic stratospheric aerosols from three types of sources. First, a few long-term programs were established for various reasons. These include a few satellites with limited capabilities as discussed later, assorted surface-based sites with intermittent remote sensing of the stratosphere, and infrequent balloon-borne missions. Such long-term projects are designed to study all sources of stratospheric, and sometimes tropospheric,

aerosol variability and were not always well suited to observing the large magnitude of aerosol loading associated with recent major eruptions. A second category of available observations includes those that begin following an eruption. These were specifically designed to explore the extent of the evolving aerosol and its properties. Notable U.S. campaigns following El Chichón reported by Pollack et al. [1983], Dutton and DeLuisi [1983], McCormick and Swissler [1983], and Spinhirne [1983], and following Pinatubo by *Geophys. Res, Lett.*, Jan. [1992] special issue, Goodman et al. [1994], Russell et al. [1993] and Pueschel et al. [1994] consisted primarily of reconnaissance aircraft missions. Additionally, several existing surface-based programs increased observation schedules following major eruptions [Hofmann and Rosen, 1984; Dutton et al., 1987; DeFoor et al., 1992; Post et al., 1992]. The third information source was from measurements that were either in place before the eruption, or shortly after, in which the aerosol becomes a form of interference but provides an unexpected observational opportunity [e.g., Barth et al., 1982; Krueger, 1983; Grainger et al., 1993; Strong and Stowe, 1993; Lockwood and Thompson, 1986; Ackerman and Strabala, 1994]. Data from all three types of sources were included in this work.

Acquiring, evaluating, selecting, and processing observational data into a thorough and usable set of data describing the global evolution of two major volcanic eruption aerosol clouds and their effects was a formidable task. The data compilation used here, although extensive, is not complete since much essential data were either never collected or have yet to be made available, although more data were available following Pinatubo than from El Chichón. The data used here form a subset of what was available as of mid-1994.

2.1 Spectral Aerosol Optical Depth.

Spectral aerosol optical depth, $\tau_A(\lambda)$, (where λ is wavelength) of a volcanic cloud is the most useful observation for the computation of *V*. Monochromatic aerosol optical depths can be derived from measurements of the relative solar beam intensity as viewed through a defined path through the atmosphere. Basics of the measurement principle were taken from the simplest form of the radiative transfer equation, often called Beer's Law as given in Eq. 2.1.

$$I(\lambda) = I_O(\lambda) e^{-\tau(\lambda) m_r} \qquad \textbf{2.1}$$

In Eq. 2.1, m_r is the relative air mass, or the ratio of the slant to vertical path through the atmosphere. If the optical depths of other constituents at the same wavelength are known and m_r is the same for all constituents, $\tau_A(\lambda)$ is computed using:

$$\tau_A(\lambda) = \tau(\lambda) - \tau_{x_1}(\lambda) - \tau_{x_2}(\lambda) - .... - \tau_{x_N}(\lambda), \qquad \textbf{2.2}$$

where N is the number of constituents affecting attenuation at λ. Aerosol optical depth can be determined using directly transmitted solar radiation observations and Eqs. 2.1 and 2.2 as demonstrated by McCormick et al. [1978], Shaw [1983], Dutton et al. [1994], Russell et al. [1993], Stephens [1994], and others.

Although it is desirable to have as many wavelengths of $\tau_A(\lambda)$ information as possible covering the complete solar and thermal IR spectra, relatively few wavelengths are observed for both practical and operational reasons [Shaw, 1983]. Aerosol extinction is typically smoothly varying with wavelength, compared to the line structure of

characteristic gaseous absorption. Using the Junge relationships [Junge, 1963], as few as two wavelengths of aerosol extinction information have been used to describe complete aerosol size distributions. However, these expressions were developed for tropospheric aerosols and were not applicable to aerosols undergoing the life-cycle of stratospheric volcanic aerosols where mode radii are greater than 0.2 μm. Using as few as three wavelengths, observations following El Chichón showed a spectral signature that was incompatible with the Junge expressions [Dutton and DeLuisi, 1983]. The size distribution indicated by Dutton and DeLuisi data was monomodal with a radius peak in the submicrometer range [King et al., 1984]. Higher resolution, either in measured size distributions or in spectral extinction observations, has revealed additional bimodal structure. This suggests that more than three wavelengths would be useful for routine monitoring of volcanic clouds [Hofmann and Rosen, 1983; King et al., 1984; Asano et al., 1993; Stone et al., 1993; Goodman et al., 1994].

Typically, fewer than 10 wavelengths are used in a sunphotometer to observe $\tau_A(\lambda)$; additional wavelengths offer little additional aerosol size information. Limitations on the inference of size information from sunphotometer measurements arise from the maximum range of sensitivity of the most common silicon detectors ($\approx$ 0.35 to 1.1 μm), numerous spectral bands of absorbers whose effects are not known and cannot be separated from the aerosol effect, finite filter widths, and the fact that aerosols of a single size influence a wide range in wavelengths. Available $\tau_A(\lambda)$ data for this study were limited to five or fewer wavelengths.

Temporal and spatial information on $\tau_A(\lambda)$ for a particular volcano is required for climate diagnostics, although the required resolution is ill-defined. The data resolution

does not need be as high as that of prediction and diagnostic models because of spatial uniformity and slow change in the aerosol after the initial spreading of the cloud, as described by McCormick and Veiga [1992]. Satellite platforms provide $\tau_A(\lambda)$ data over extended time and space scales, but relatively few data were available. Two sets of long-term $\tau_A(\lambda)$ data for the northern hemisphere containing the volcanic signals of both El Chichón and Pinatubo were readily available. One was an updated version of that of Michalsky et al. [1990] from Rattlesnake Mountain, Washington (RSM, 46° N) and a second set from Mauna Loa, Hawaii (MLO, 19° N) described by Dutton et al. [1994]. A third data set from Alice Springs, Australia (ASA, 25° N) was also available for Pinatubo but does not include data from the El Chichón event. Other spectral data sets were known to exist but were not used in this study because of incompleteness, redundancy, or lack of availability and/or quality assurance.

The MLO $\tau_A(\lambda)$ data are shown in Fig. 2.1a for three wavelengths. Occasionally, a fourth wavelength was available at MLO but is not shown. Updated RSM data are shown in Fig. 2.1b, for five wavelengths. The ASA data [Personal communication: Bruce Forgan, Australian Bureau of Met.] are shown in Fig. 2.2.

2.1.1 Wideband and single wavelength solar optical depth

Midvisible total-column aerosol optical depth, $\tau_A(\text{vis})$, is the single most important property of the volcanic aerosol relative to computing V [e.g., Lacis et al., 1992]. Volcanic aerosols primarily scatter solar wavelengths and the greater $\tau_A(\text{vis})$ the more solar irradiance will be backscattered to space. Single wavelength and wideband optical depths were used to deduce the geographical extent and relative abundance of the aerosol.

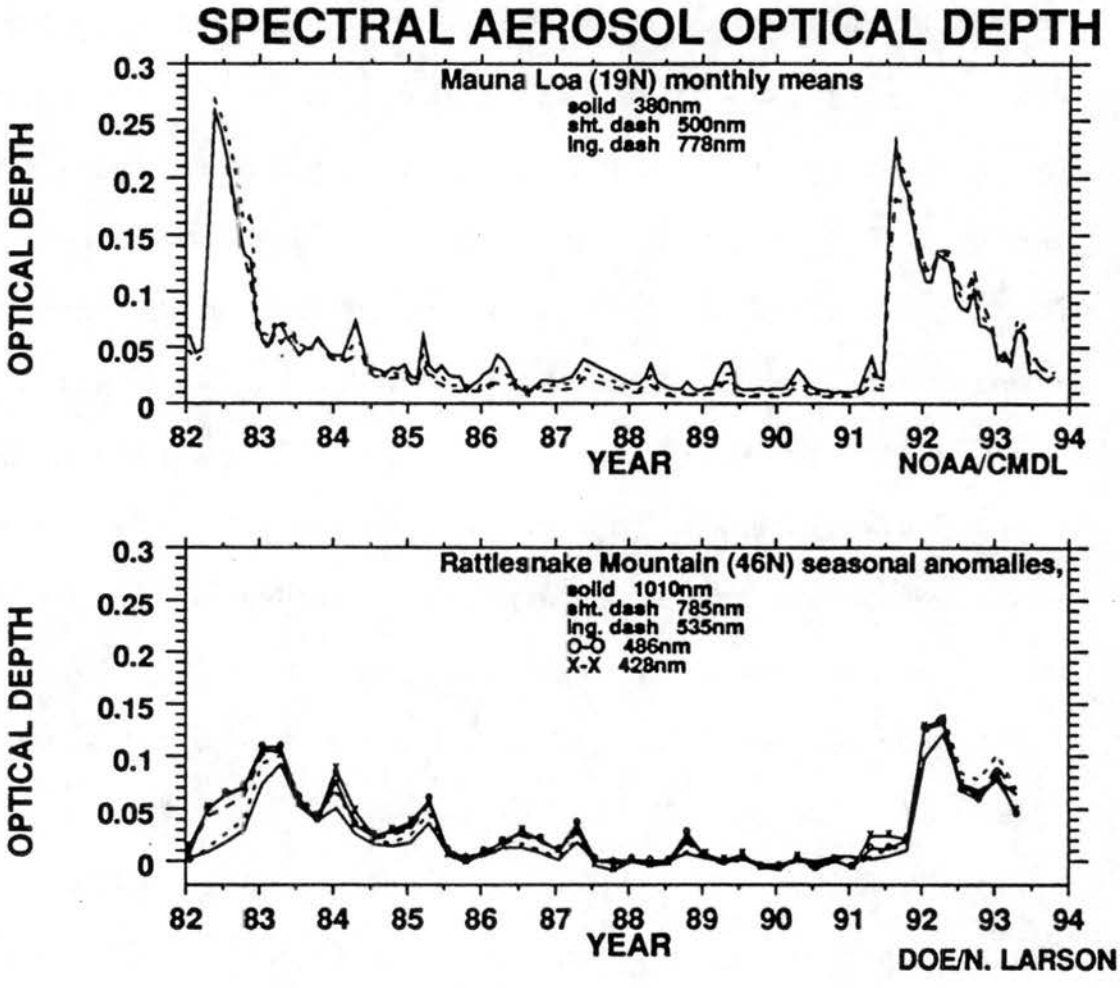

Fig. 2.1 Aerosol optical depth for multiple wavelengths, as indicated, for Mauna Loa, Hawaii (top) and Rattlesnake Mt., Washington (bottom). Rattlesnake Mt. has had background subtracted.

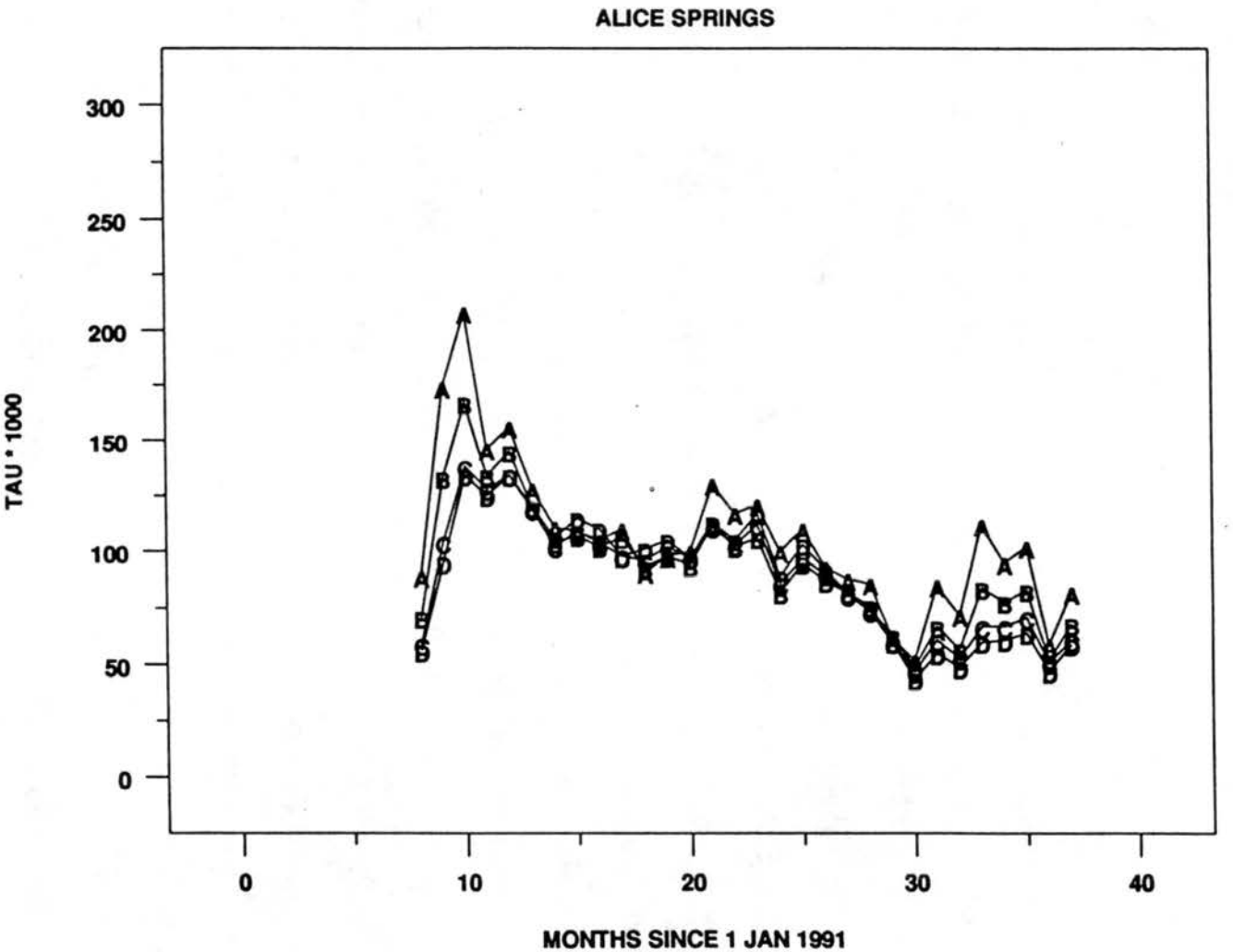

Fig. 2.2 Spectral aerosol optical depth from Alice Springs, Australia. (A) - 440 nm. (B) - 500 nm, (C) - 670 nm, (D) - 862 nm.

Measurements of scattered and direct solar radiation were used to determine τ_A(vis). These types of observations are often made because the instrumentation was simpler and more stable than that necessary for $\tau_A(\lambda)$. Wideband optical depths relating to El Chichón and Pinatubo derived from direct beam measurements were presented by Dutton and Christy [1992]. The Advanced Very High Resolution Radiometer (AVHRR) satellite aerosol optical depth data given by Stowe et al. [1992] and Long and Stowe [1994] were derived from scattered radiation. Bodhaine and Rosson [1988] and Rao et al. [1989] provided additional details on the derivation of the Dutton and Christy [1992] and AVHRR τ_A data sets, respectively.

The surface-observed aerosol τ_A(vis) optical depths given by Dutton and Christy [1992] comprise a time series starting before the El Chichón event continuing to the present and sparsely cover a spatial range from the Arctic to the Antarctic. These optical depth data have been updated and are shown in Fig. 2.3 through 1993. These data are for a spectral band of 0.3-0.7 μm. The optical depths in Fig. 2.3 were derived by repeatedly integrating Eq. 2.1 over λ for different spectral mean τ_A until a match was made with the observed 0.3-0.7 μm direct solar irradiance. The procedure was viable because little water vapor absorption was encountered in this band, but there are several inherent problems. Such problems include the dependence on absolute radiometric calibration, the need for knowledge of the absolute value of the extraterrestrial solar spectrum, and errors introduced when spectrally integrating Eq. 2.1. Nonetheless, these wideband data provide a reference for comparing the two eruptions at four fixed sites with common instruments, calibrations, intercomparisons, and data reduction procedures.

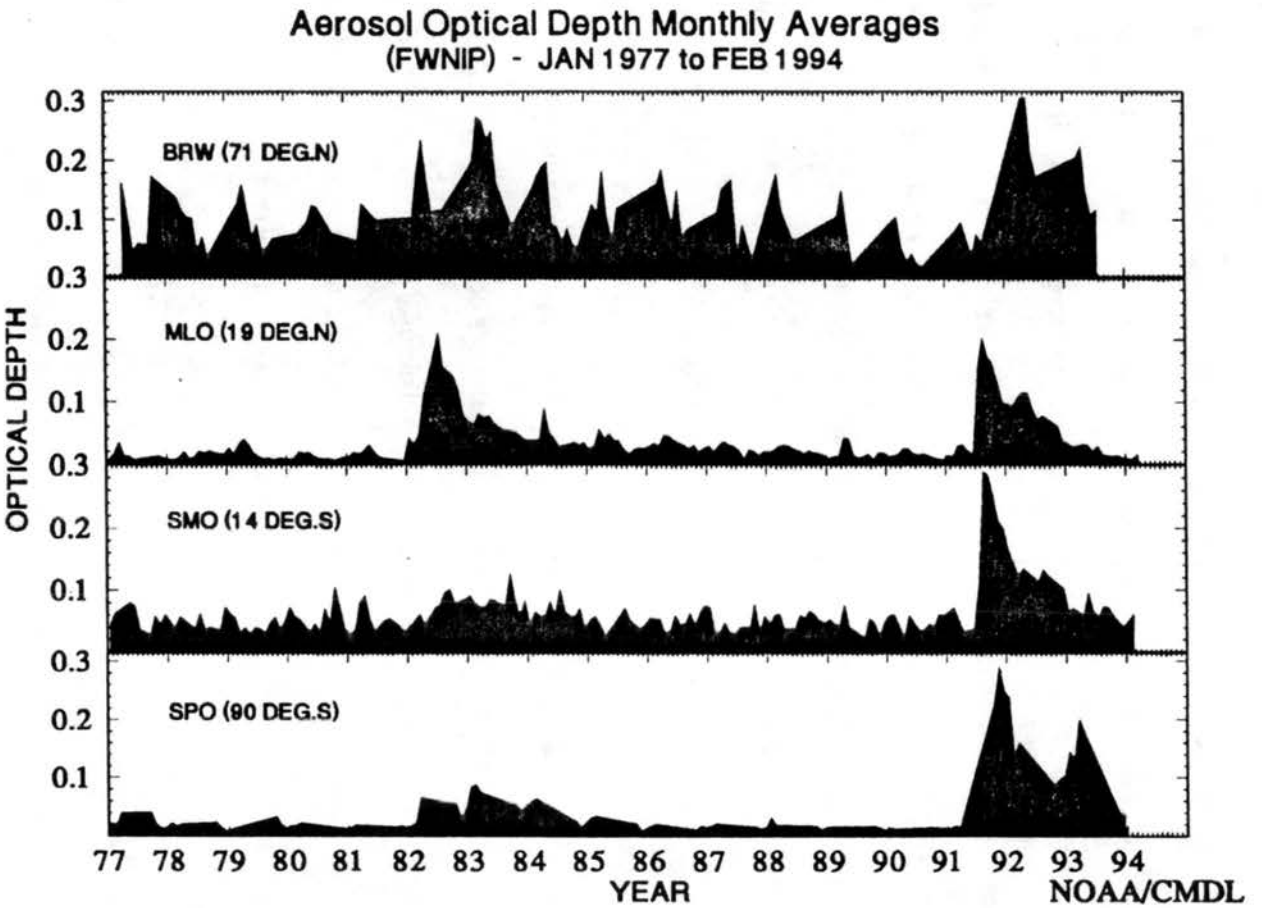

Fig. 2.3 Wideband aerosol optical depth from NOAA/CMDL global baseline network. Latitude range of sites is 161 degrees.

As seen in Fig. 2.3, El Chichón was primarily a northern hemisphere event, although small amounts were detected at 90° S, whereas the Pinatubo aerosol eventually spread more equally to both hemispheres. An integral with time over the data in Fig. 2.3 for all four sites shows an average Pinatubo $\tau_A(\lambda)$ 1.7 times greater than El Chichón, although large portions of the globe were not represented. These data were used primarily to assess the consistency of other available monochromatic data and wideband data.

Midvisible optical depths following El Chichón were given in *Geophys. Res. Lett.* [Nov. 1983 special issue], *Geophysica Internacional* [July 1984 special issue], and in individual papers previously cited. While satellite coverage of the El Chichón event was minimal, SAMII provided polar coverage and SME viewed the upper portion of the aerosol [Barth et al., 1982]. A recent and relatively complete global compilation of τ_A data for El Chichón has been given by Sato et al. [1993] who used previously published information. Sato et al. have produced $\tau_A(550)$ compilation for monthly averages in 24 zonal mean bands. Because of the relative completeness of this work, it will be used here as the main source for the geographic and temporal aerosol distributions after El Chichón. The Sato et al. data are shown in Fig. 2.4 for Jan 1982 through December 1985. The contrast between the Sato et al. compilation and other specific τ_A time series will be shown later.

Several additional sources of $\tau_A(\text{vis})$ were available for Pinatubo, primarily from satellites. The $\tau_A(\lambda)$ data at the boundaries of the initial spreading of aerosols were obtained from SAGE II. However, the main portion of the aerosol cloud became too dense, resulting in saturation of the SAGE II τ_A retrieval technique [Thomason, 1992]. Methods to approximately compensate for this saturation problem exist [McCormick and

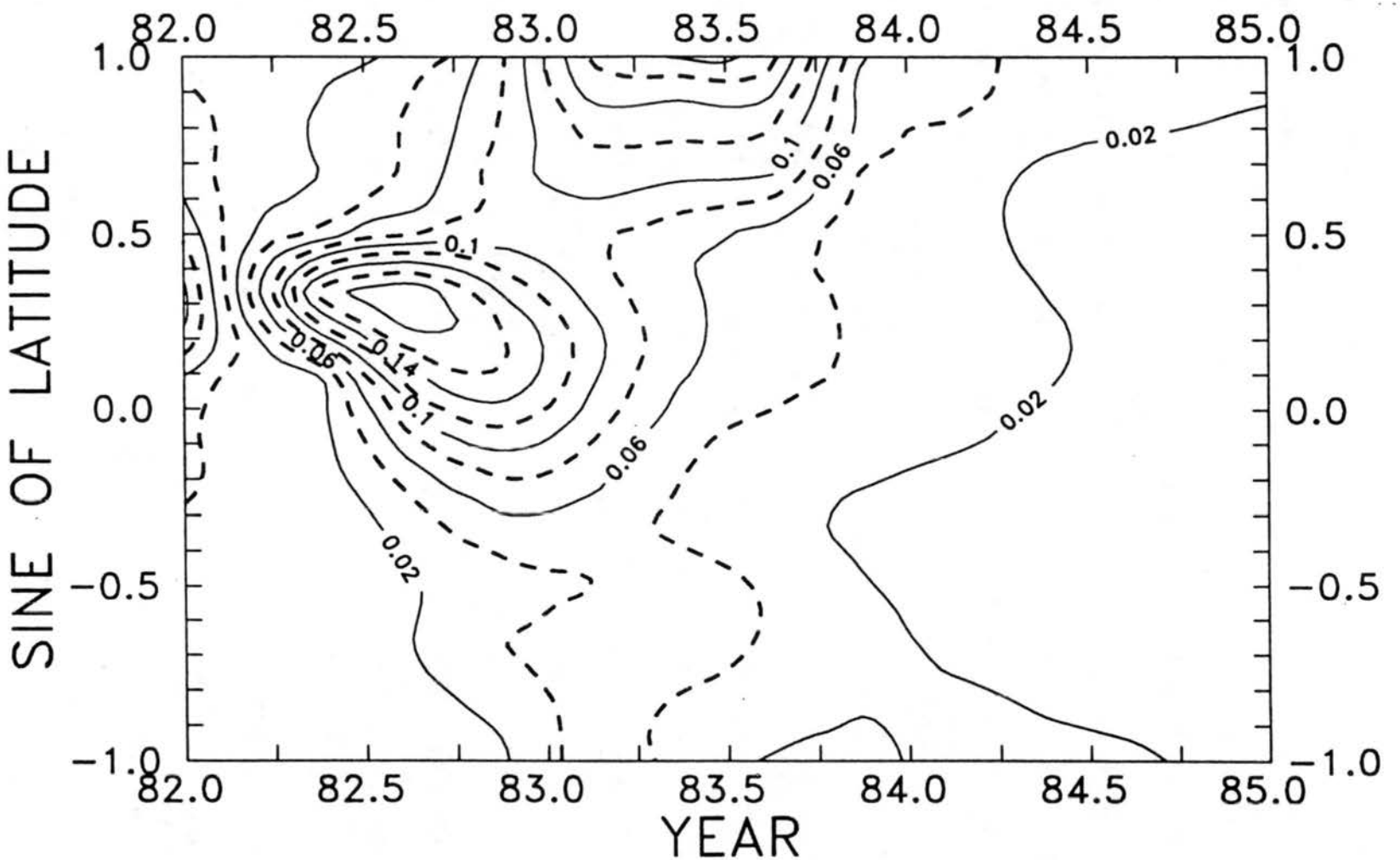

Fig. 2.4 550 nm stratospheric aerosol optical depth compiled after El Chichón by Sato et al. [1993]

Trepte, 1987; L. Thomason, NASA Langley, personal communication] and the revised data could soon become available. A compilation of the early Pinatubo global midvisible τ_A was presented for a single wavelength [Sato et al., 1993] based primarily on early SAGE II and SAM II and reconnaissance flights. Sato et al. data for 1991 through 1993 are shown in Fig. 2.5. Zonal mean AVHRR τ_A data for Pinatubo have been given by Long and Stowe [1994] and are shown in Fig. 2.6. Data are for a filter weighted average across the spectral range of 0.53 to 0.71 μm and were adjusted to 0.5 μm by the original authors. AVHRR data reduction uses the scattering properties of a model tropospheric aerosol with a different size distribution and refractive index than the stratospheric aerosol that dominated the signal for much of the record. Also, the AVHRR data can only be recovered over cloud free oceanic areas, and large background tropospheric optical depth contributions must be subtracted from the total signal. All these add to considerable uncertainty in the data [J. Pollack, NASA, Ames; C. Long, NOAA/CAC, personal comms.]. Despite these limitations, the AVHRR data correspond closely to similar data as shown in Fig. 2.7. This correspondence was primarily due to the volcanic signal being so great that AVHRR signal-to-error ratio becomes less important. The main differences between the AVHRR and Sato et al.'s compilations are in the peak values in the tropics during late 1991 and 1992. This was also an area of nearly nonexistent validation data from independent surface or aircraft sources and the area of maximum saturation in the SAGE II data [L. Thompson, NASA, Langley, personal comm.] that figured heavily into the Sato compilation. The global distribution of Pinatubo aerosol to be used for V computations in the current study comes from a combination of the Sato et al. and AVHRR data, based on comparisons to ancillary information, Fig. 2.7. Sato et al.'s data

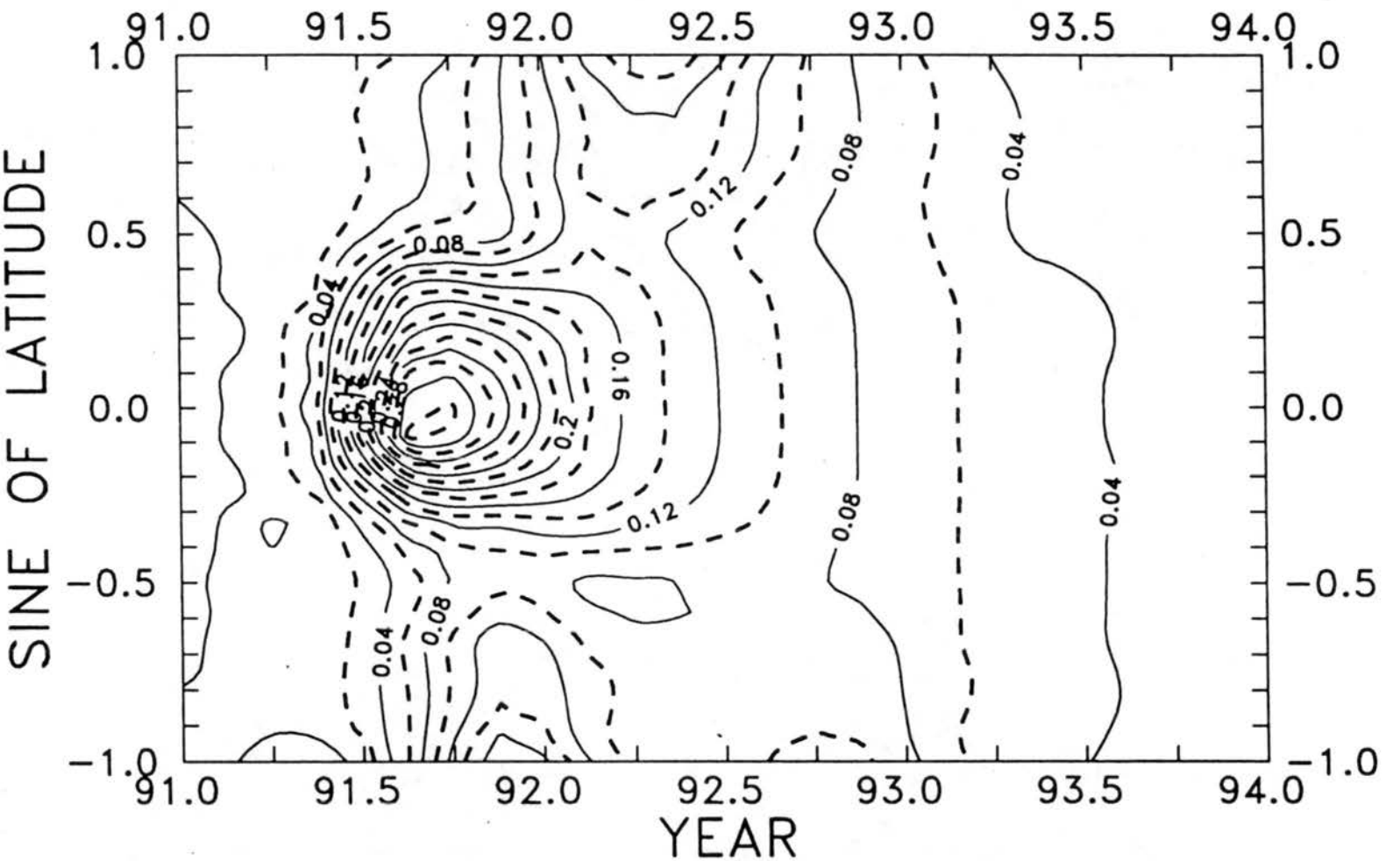

Fig. 2.5 550 nm stratospheric aerosol optical depth estimated after Pinatubo by Sato et al. [1993]

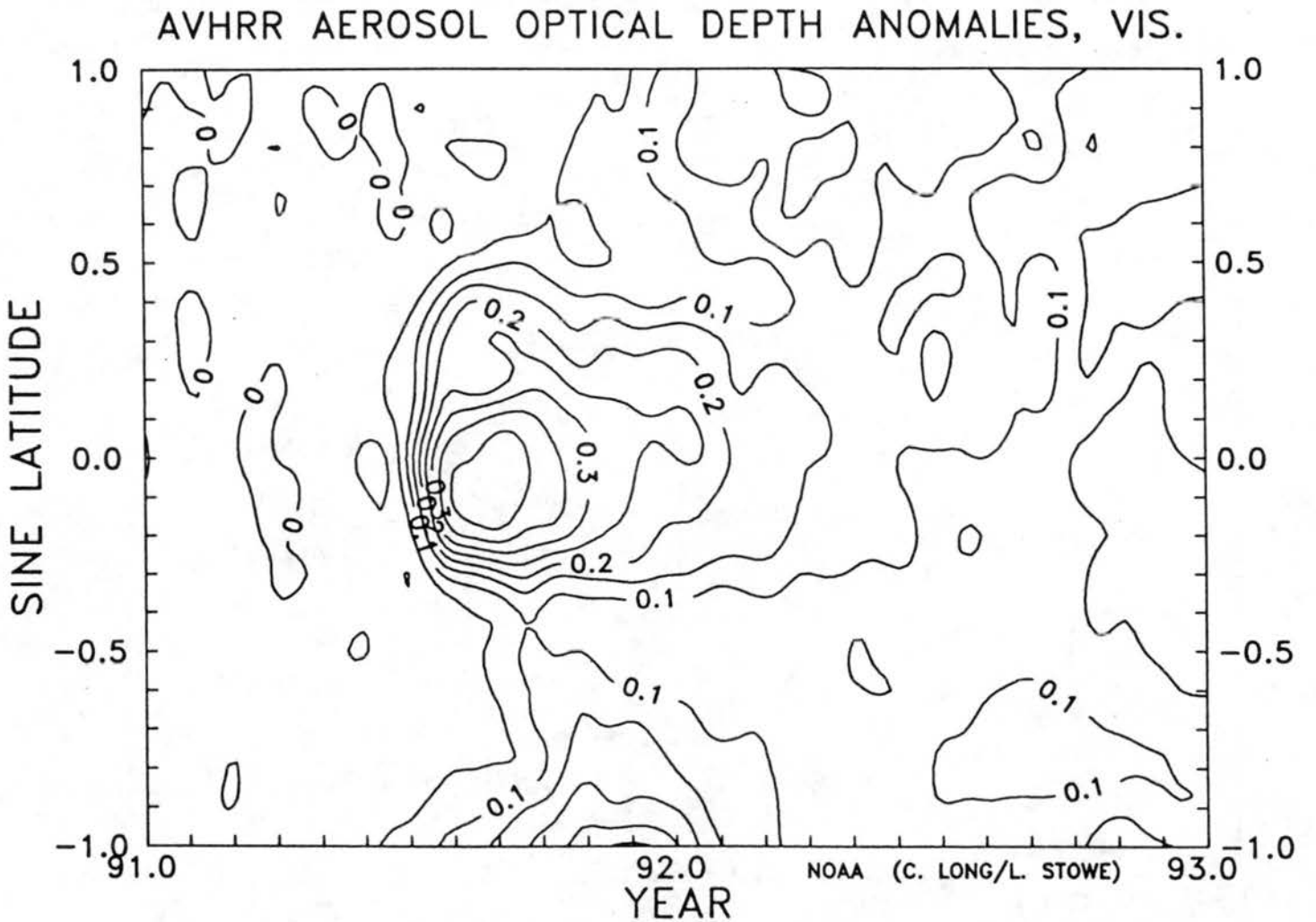

Fig. 2.6 Midvisible aerosol optical depth anomalies derived from AVHRR after Pinatubo [Long and Stowe, 1994].

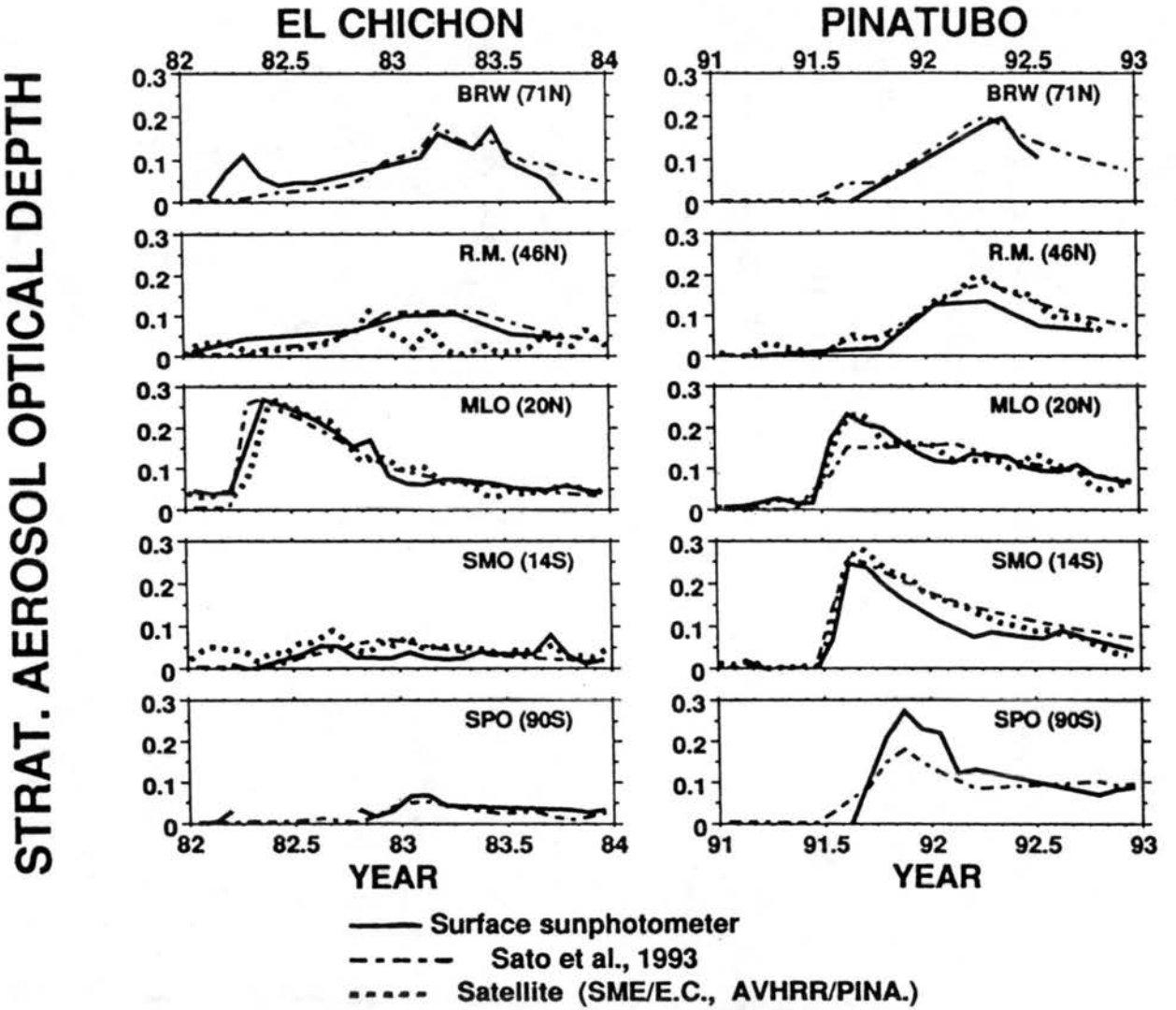

Fig. 2.7 Midvisible anomalous aerosol optical depth above five sites from different data sources, as indicated.

were used everywhere except in the tropics for the first year and half after the Pinatubo eruption where the AVHRR data were used. Further discussion of the accuracy of these data is given in Appendix B.

2.2 IR Optical Depth

Although IR aerosol optical depths, $\tau_A(\lambda>4.0)$, are necessary to compute ${}_{Ln}V$, they were not easily acquired. The approach used here was to compute the needed optical depths from observed inverted aerosol size distributions. A few satellite-observed $\tau_A(>4.0)$ have been reported and will be used here to constrain aerosol size inversions and to compare to Mie calculated values. At wavelengths longer than 5 μm it is possible to infer optical depth from aerosol emission observations. Such observations of stratospheric aerosol from the surface are not possible because of the absorbing atmosphere between the surface and aerosol. Useful $\tau_A(>4.0$ μm) observations of the Pinatubo aerosols from space have been obtained by Lambert et al. [1993] from ISAMS and by Ackerman and Strabala [1994] using the High Resolution Infrared Sounder 2 (HIRS2) on the NOAA series satellites. A global mean $\tau_A(12.1$ μm) value of 0.005 during Nov. 1991 to Apr. 1992 was reported by Lambert et al., and localized values of 0.03-0.06, 0.014-0.02, and .0012-.004 at 8.3, 11.1, and 12.5 μm respectively for the south Atlantic during August 1991 were given by Ackerman and Strabala. These aerosol properties were found from the observed excess emission, relative to that computed using climatological concentrations of various trace gases, assuming negligible aerosol scattering. Observations of $\tau_A(>4.0$ μm) El Chichón were obtained by Barth et al. [1982] using the SME satellite but optical depths were not reported. Witteborn et al. [1983] deduced a

τ_A(8.5 μm) of 0.012 at 20° N in December 1982. The observed τ_A(>4.0 μm) were compared to those computed from Mie theory using the inverted size distributions in Fig. 2.8, where the Mie computed values fall within the range of observations. The maximum difference between computed and observed $\tau_A(\lambda)$ at three wavelengths was 0.02.

2.3 Aerosol Height

Information on the heights of the El Chichón and Pinatubo clouds used in this study were taken from lidar information of McCormick et al. [1984], DeLuisi et al [1984], Post [1984], DeFoor et al. [1992], and Post et al. [1992] and from dust sonde data of Hofmann and Rossen [1983], Deshler et al. [1992], and from satellite data by Barth et al. [1982], McCormick et al. [1992], Pitts and Thomason [1993], and Grainger et al. [1993]. While much detail on the vertical structure of the evolving cloud was contained in these data, only low vertical resolution information was needed and used in the current work.

Although some differences were seen in the vertical distributions of the two eruption clouds, both can be described as initially being detected as high as 35 km. In the tropics aerosols were distributed between ~19 km and 30 km with a peak near 25 km. As the aerosol layer moved poleward it was observed to lower along with the tropopause height. The aerosol peak height, or centroid, has sometimes been observed to settle relative to the tropopause [e.g., Lambert et al., 1993]. However, the maximum backscattered signal generally just diminishes with time as the largest droplets settle leaving the altitude of maximum scattering the same, as seen for the MLO lidar record in Fig. 2.9.

The main aerosol cloud from both eruptions was initially confined to the lower stratosphere in various layers between 5 and 10 km above the tropopause and lowered

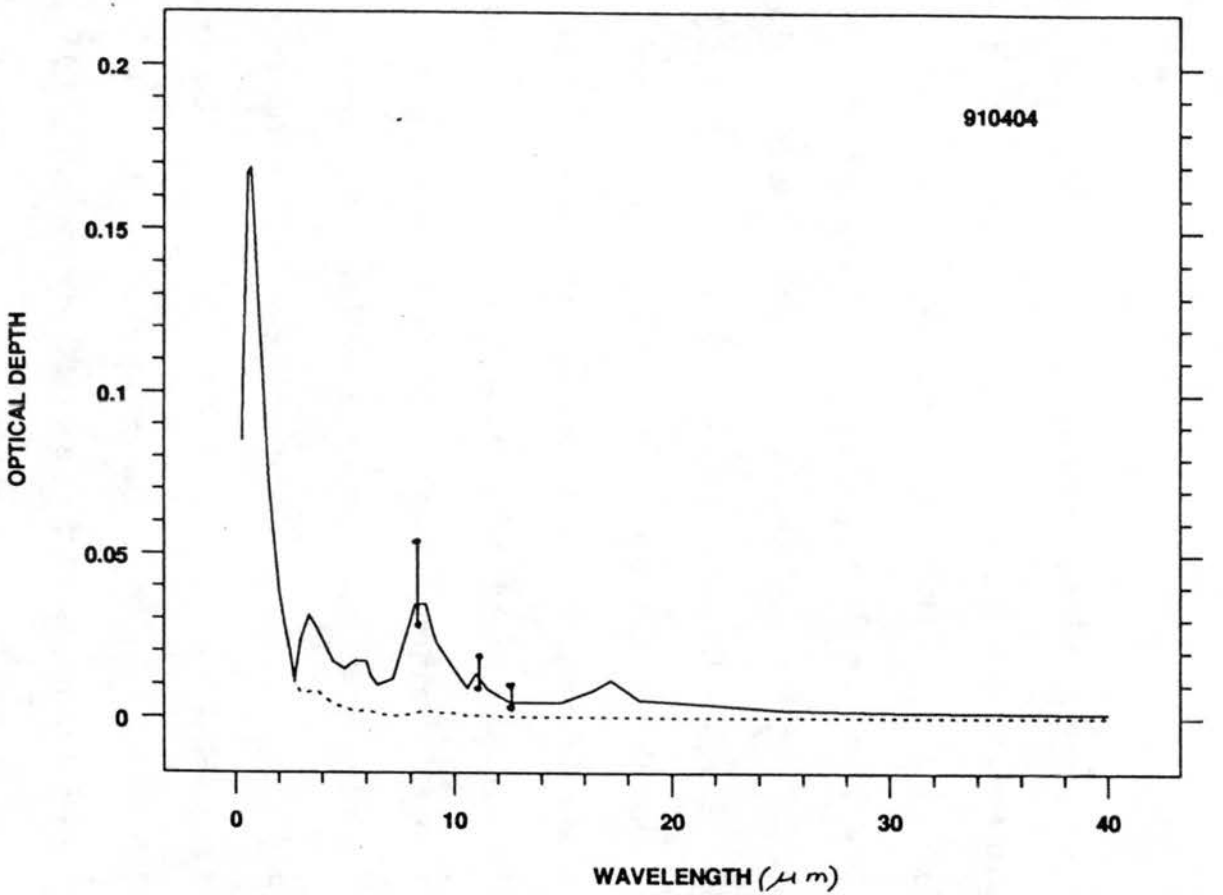

Fig. 2.8 Scattering plus absorption (solid) and scattering only (dashed) aerosol optical depth vs. wavelength computed from Mie theory using an inverted sized distribution from the zonal mean for the fourth season of 1991, in the northern subtropical zonal belt (910404). Upper and lower observed IR aerosol optical depths obtained from satellite and aircraft are indicated at three wavelengths by vertical lines. Note: scattering optical depth is almost zero so absorption optical depth nearly equals total optical depth for $\lambda > 4$ μm.

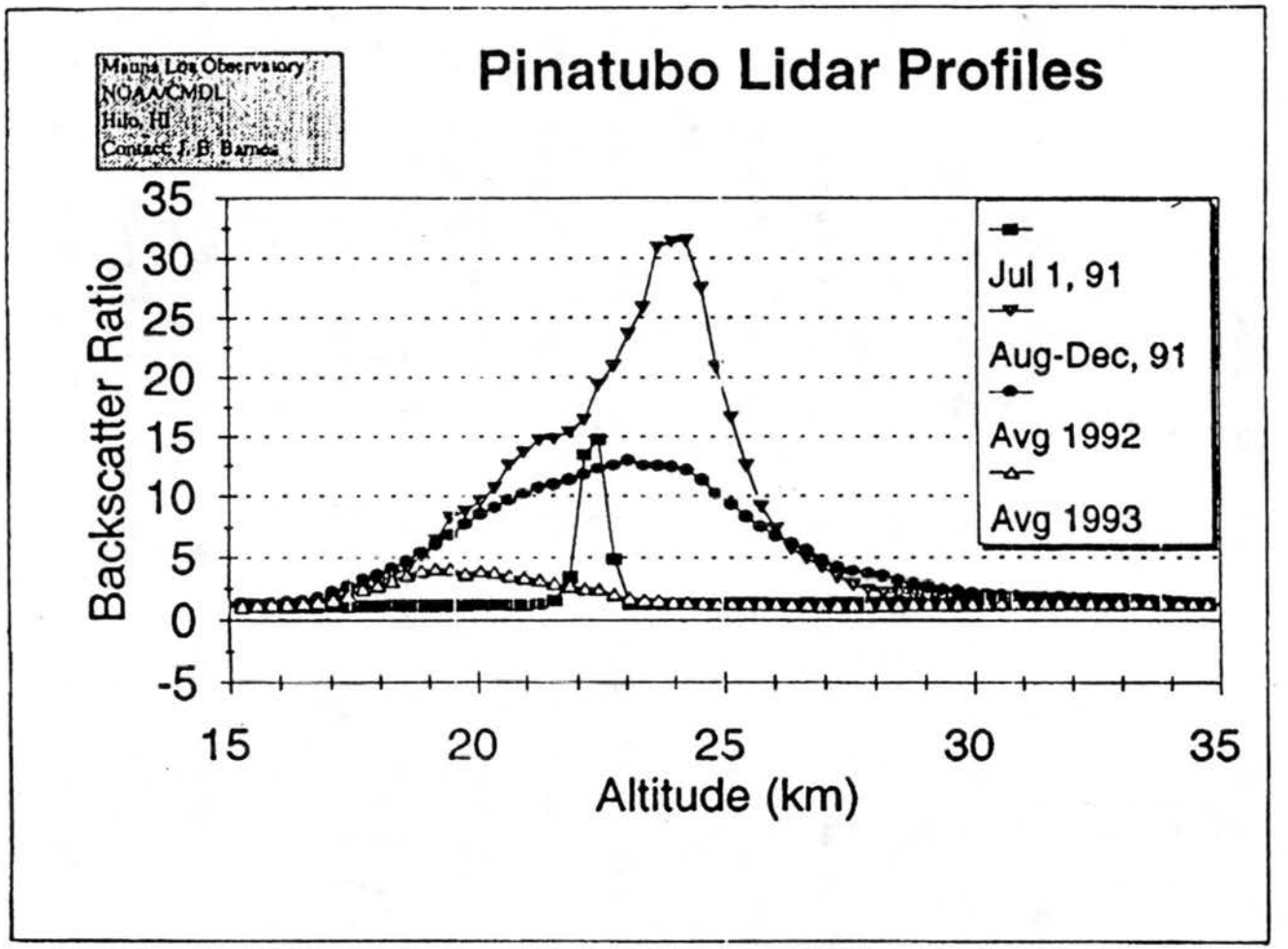

Fig. 2.9 Ruby lidar aerosol backscatter as a function of height for four different time frames at Mauna Loa, Hawaii (Courtesy of John Barnes, NOAA/ CMDL).

slowly with time. An e-folding time of 10-16 months was observed for recent volcanic clouds, depending on latitude [Hofmann, 1988; Yue et al., 1991; Stone et al., 1993; Moorthy et al., 1994], with the shorter e-folding times observed in the lower latitudes where horizontal dispersion contributes to the decrease.

2.4 Size Distributions

Both remote sensing and in situ techniques can be used to obtain an aerosol size distribution, $n(r)$. Remote sensing techniques typically use the Mie inversion of spectral optical depth as discussed in Appendix A, which combines the uncertainties of observations and the inversion technique. In situ techniques use optical counters [e.g., Goodman et al., 1994; Ackerman and Cox, 1982] or filter collections [e.g., Sheridan et al., 1992]. Remote sensing techniques can be applied at ground-based sites or from satellite and airborne platforms. The ground and satellite systems provide quasi-continuous measurements during daytime cloud-free periods. Satellites provide extensive areal and temporal coverage. Satellites have typically observed too few wavelengths successfully to be used for the size inversion estimates in this study. SAGEII observes a sufficient number of wavelengths [Thomason, 1992] but has not supplied total column values due to saturation problems mentioned earlier. Several in situ observations of aerosol size distributions were reported following the El Chichón and Pinatubo eruptions. The Wyoming balloon program [Hofmann and Rosen, 1983; Deshler et al., 1992] consists of routine observations for both El Chichón and Pinatubo, but was limited in temporal resolution, one per month on the average. Wyoming data also apply primarily to a single location, although a few flights were made at other locations. Oberbeck et al. [1983] and

Knollenburg and Huffman [1983] report in situ volcanic aerosol size data following El Chichón. Several series of aircraft observations following Pinatubo were presented by Goodman et al. [1994] and Pueschel et al. [1994], but again were usually limited to sampling once every few months. These aircraft flights were normally limited to the lowest altitudes of the aerosol, between 18 and 19 km, over western North America. Such quasi-continuous records were useful to provide a partial view of the evolution of the aerosol and to enable comparison to indirect size estimates.

The $\tau_A(\lambda)$ data that were used for the size distribution inversions were discussed in Sec. 2.1. An advantage of having used those data sets to obtain size information was the high time resolution, up to several times weekly at a fixed location; this was sufficient for computing seasonal averages over the complete vertical column. The aerosol size distributions used in this study are from Mie inversion of those data sets as described in Appendix A. Size distributions inverted from the RSM and directly measured distributions over Laramie, Wyoming are shown in Fig. 2.10. The balloon-sonde data in Fig. 2.10 have been integrated with height. Both similarities and differences are seen between the results from the two techniques. Comparison between in situ and remotely sensed size distributions was complicated by spatial variability. In general, there was agreement to within an order of magnitude and overall shape through most of the size range. The El Chichón balloon data show a distinct tendency toward a bimodal distribution not seen in the other data sets. The second most important feature of the size distribution, after the overall magnitude is the effective radius (defined in Sec. 5.4) [Lacis et al., 1992], and shows little variation between the two techniques as also shown in

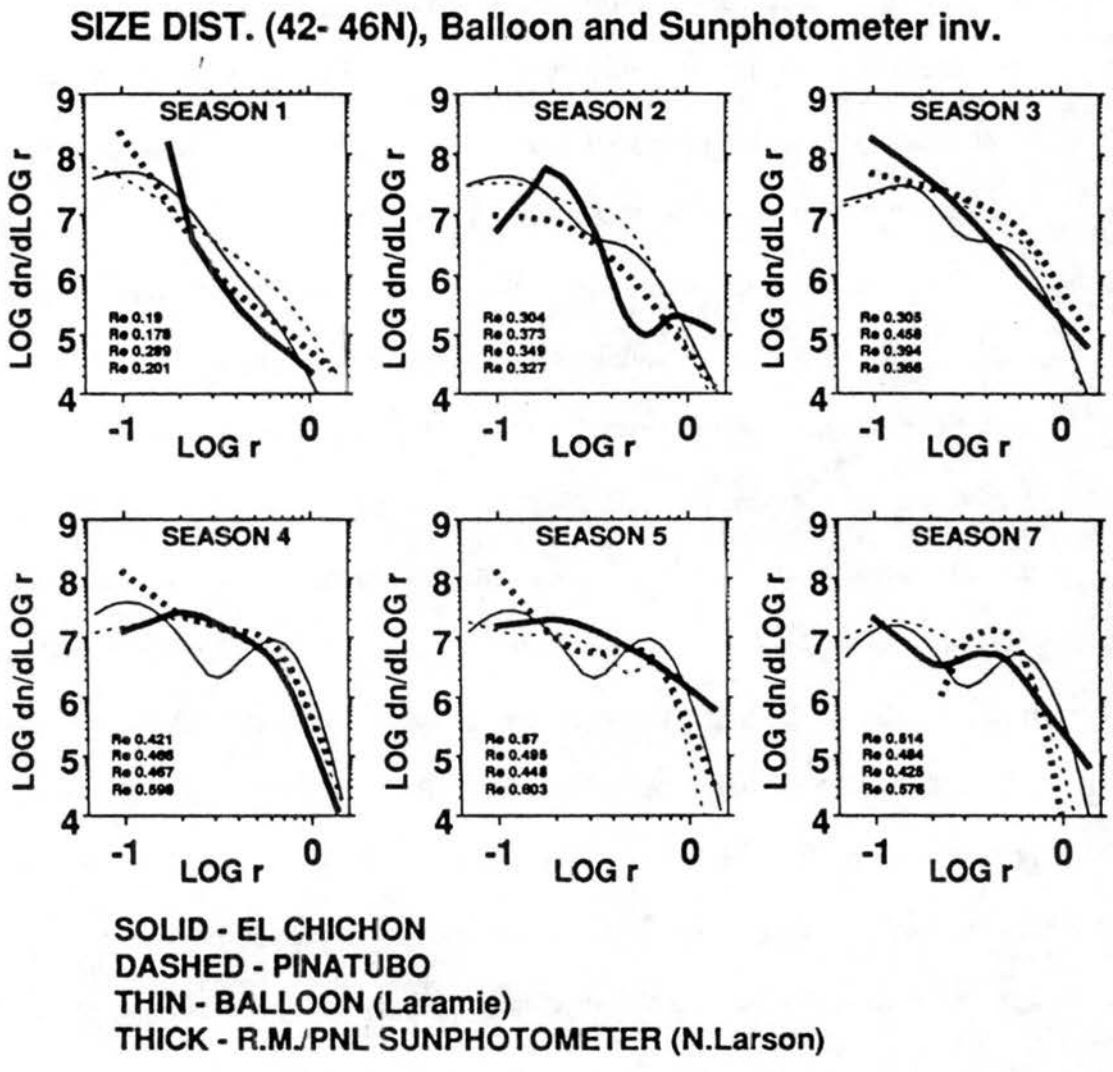

Fig. 2.10 Seasonal mean aerosol size distributions for both Laramie balloon in situ observations and as inverted from the Rattlesnake Mt. aerosol optical depth.

Fig. 2.10. A comparison between RT calculations using size distributions derived from the two techniques will be given in Sec. 5.1.1.

It was expected that there would be different size distributions at different heights in the cloud because of faster settling of the larger particles. Observations of such differences are limited to the Wyoming balloon, some aircraft data, and the upper portion of SAGEII data [Thomason, 1992]. Vertical variations in aerosol size were not accounted for in the models used in this study.

2.5 Solar Irradiance

Observations of broadband solar irradiance adequate to confirm theoretical V estimates are uncommon [Coakley, 1981; Ardanuy and Kyle, 1986; Mass and Portman, 1989; Dutton, 1990a; Mass and Portman, 1990]. This was because of instrumental and sampling resolution problems as well as the general lack of climatic time-scale observational efforts. Nonetheless, there are several reports on the influence of volcanic aerosols on solar irradiance [Dyer and Hicks, 1965; DeLuisi and Herman, 1977; DeLuisi et al., 1983; Hay and Darby, 1984; Wendler, 1984; Dutton, 1990a; Ardanuy and Kyle, 1986; Dutton and Christy, 1992; Minnis et al., 1993; Saunders, 1993; Hayasaka et al., 1994]. These reports reveal considerable uncertainty in the absolute magnitudes of irradiance perturbations. Often clouds and tropospheric aerosols masked the volcanic signal in surface-based total solar (direct plus diffuse) irradiance observations because the signal from the largest recent eruptions was no more than 5%. High altitude surface sites provide the best opportunity for accurately detecting a volcanic signal in total solar

irradiance because of frequent clear-sky conditions, and a minimum of water vapor and tropospheric aerosols overhead.

Satellites have observed global irradiance variations following major eruptions. Ardanuy and Kyle [1986] reported regional (northern polar) planetary albedo increase of around 20%. Minnis et al. [1993] reported a 3 W m^{-2} reduction in the global mean net radiation budget at the top-of-the-atmosphere (TOA) following the eruption of Mt. Pinatubo. The Minnis et al. result included water and ice cloud effects and possible cloud feedback effects.

2.5.1 Surface-based solar irradiance observations

Surface-based solar irradiance measurements are commonly made with pyranometers. With proper operation and careful attention to calibration history, pyranometers have an accuracy of about 2% over a wide range of solar zenith angles, and have even better precision [Nelson and Dutton, 1994]. However, with the ${}_{sd}V_S$ being only a few percent and the natural variability being two orders of magnitude greater, detection of the volcanic signal can be difficult.

Surface irradiance data sets from various locations, mountain tops, high plains, and sea-level sites have been accumulated and analyzed for potential detection and verification of ${}_{sd}V_S$ following the recent two eruptions. Of the four components of the surface radiation budget, upward and downward solar and IR, the downward solar is most directly affected by the stratospheric aerosol. The ${}_{sd}V_S$ signal may be tentatively identified as a correlative decrease in the irradiance [e.g., Dyer and Hicks, 1965]. However, in such cases there was often enough variability to prevent statistical verification of the

perturbation much less confirm specific RT computations [Coakley, 1981]. A few notable data sets have shown volcanic signals and were used here to substantiate RT models.

Much of the surface downward solar data used in this study were collected at the NOAA Climate Monitoring and Diagnostics Laboratory (CMDL) remote sites using Eppley pyranometers and pyrheliometers. These instruments have been regularly calibrated and/or intercompared with reference standard instruments traceable to the WMO World Reference Radiation (WRR) scale. Details of the observational procedures and some previous products of CMDL projects were given by Dutton [1990b], Dutton and Christy [1992], and Dutton et al. [1985a, 1987, 1989, 1991, 1994]. Specific data sets examined for El Chichón and Pinatubo radiative forcing are discussed below.

The CMDL site at Hawaii (MLO, 19.5^{o} N, 3.4 km ASL) has frequent morning clear-sky conditions. Solar data from MLO have been previously used to detect volcanic signals [e.g., Mendonca et al., 1978; DeLuisi et al., 1983]. Monthly mean total solar irradiance for clear skies since 1979 are shown in Fig. 2.11c. The data have been normalized to the mean sun-earth distance. Influences of the two recent major eruptions are evident in Fig. 2.11. The MLO total irradiance record is the sum of two independently observed components, the vertical component of the direct beam and the diffuse sky radiation which are shown in the Fig. 2.11a,b. The total irradiance from the summation is more accurate because a cosine response error in the pyranometer is minimized. Having the direct and diffuse components measured separately at specific zenith angles also allows further analysis of the volcanic signal, as discussed by Coakley [1981] and as investigated here in Sec. 5.1.4.

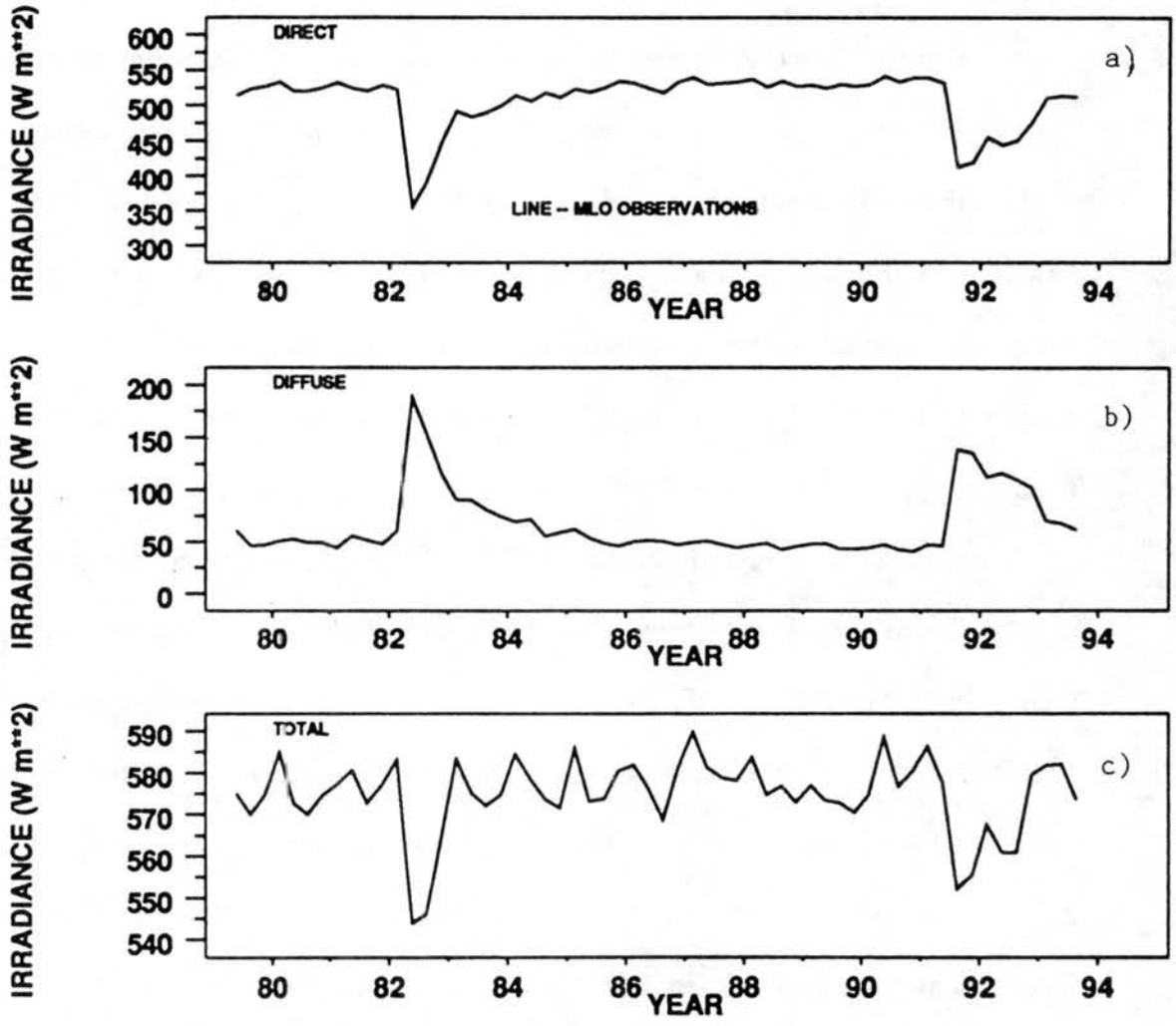

Fig. 2.11 Observed seasonal mean broadband solar irradiance from Mauna Loa, Hawaii - a) direct, b) diffuse, and c) total, for a solar zenith angle of 60°

Total solar irradiance data from, American Samoa (SMO, 14° S, 10 m ASL), have been screened to identify infrequent clear-sky cases. Clear-sky irradiances, mean and standard deviations, are shown in Fig. 2.12 as function of time for a 45° solar zenith angle for before and after the Pinatubo eruption. Presence of the Pinatubo aerosol was suggested, although the variability in the data was greater than at MLO. Data following El Chichón where not examined because the optical depth over Samoa was much less than for the Pinatubo case.

The CMDL South Pole site (SPO, 90° S, 3600 m ASL) is another dry high altitude location at which the volcanic influence on the downward solar irradiance should be more readily seen, except that it is distant from the eruption sources. Viebrock and Flowers [1968] showed a 4-5% decrease in SPO total solar irradiance during the 1963/64 and 1964/65 mid-austral summers due to the eruption of Agung (March 1963, 8° S). Figure 2.13 shows SPO clear sky downwards solar irradiance for solstice zenith angles for several years around the Pinatubo eruption. The possible influence of Pinatubo was apparent with a 4% decrease in total downward irradiance in the first summer season after Pinatubo. Again, the much lower aerosol optical depth at this site (Fig. 2.3) following El Chichón does not warrant investigation.

Solar irradiance data collected by CMDL at Boulder, CO (BLD, 40° N, 1.6 km ASL) [Dutton, 1990b] provides both an opportunity and a challenge to detect the volcanic signal in total solar irradiance data. The site is higher and drier than most continental sites, but less so than the sites examined previously. Also, as seen in Fig. 2.5, the optical depth over BLD was not as high as at the MLO and SMO sites. Data collected between 1990 and 1993 were filtered for clear skies and are shown in Fig. 2.14 for a zenith angle of

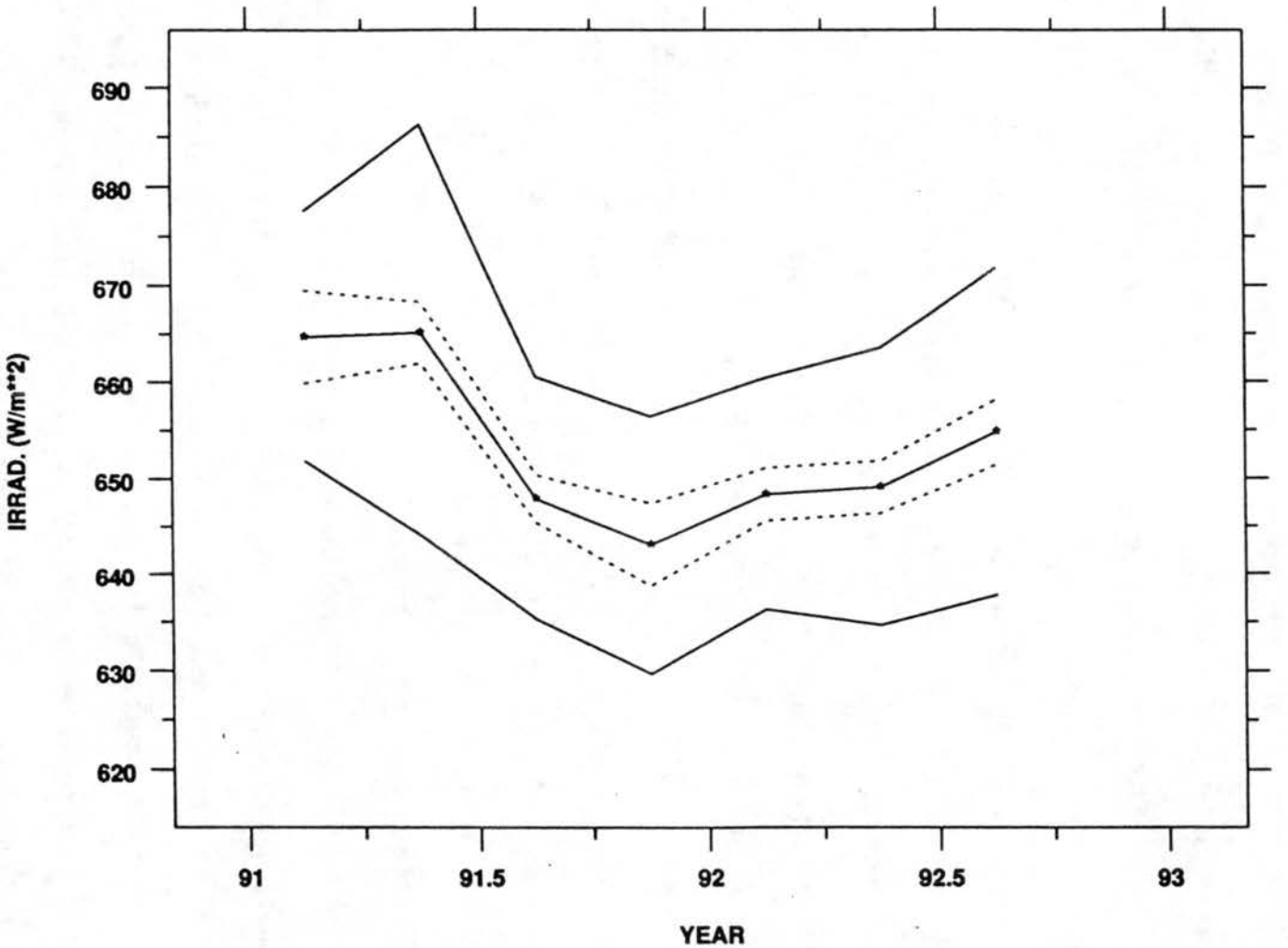

Fig. 2.12 Observed total solar irradiance from American Samoa: -*-) seasonal mean, - -) ± two standard error, solid lines) ± one standard deviation.

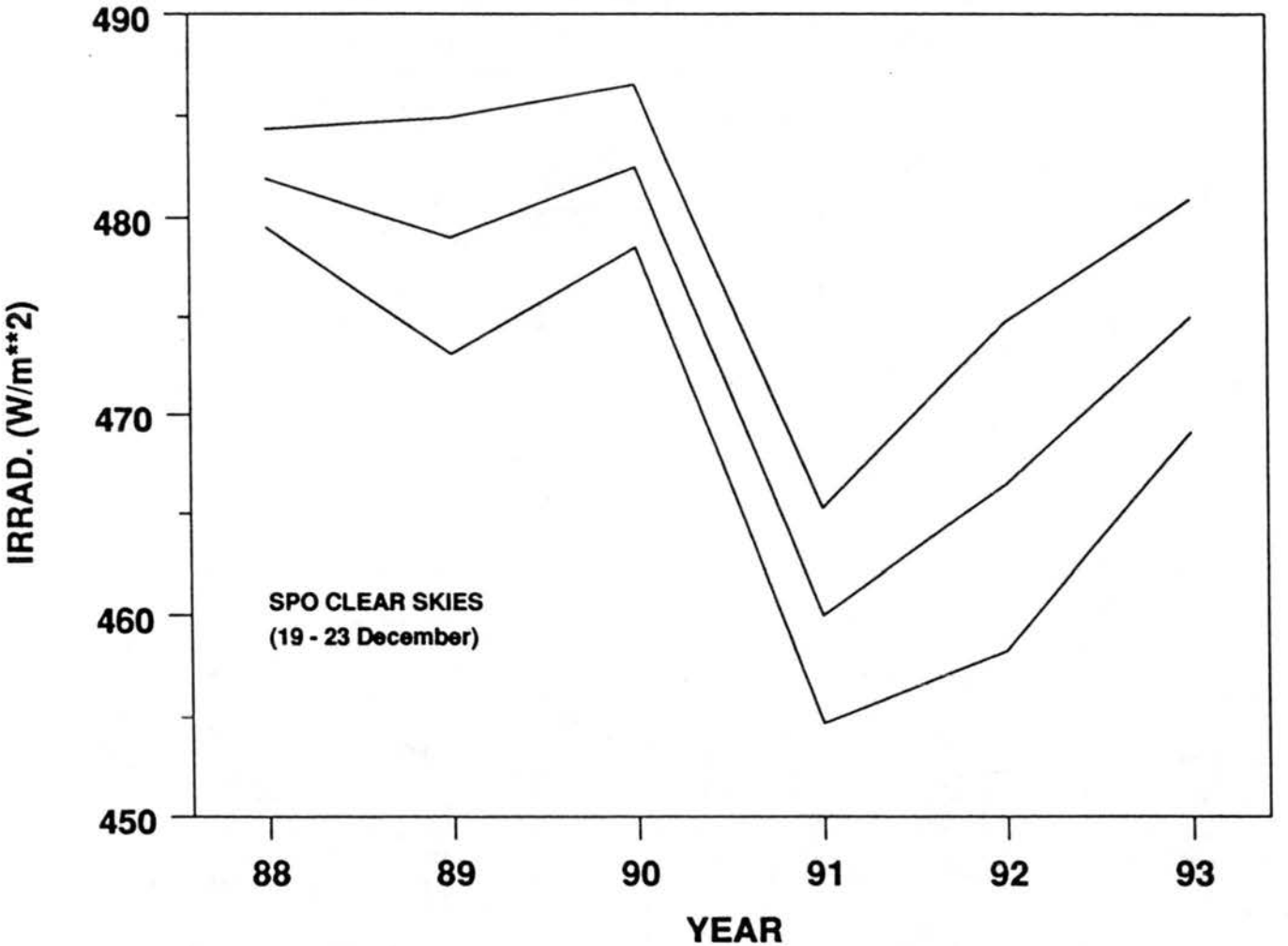

Fig. 2.13 Observed total solar irradiance from South Pole, 19-23 December - middle line) average, outer lines) ± two standard deviations.

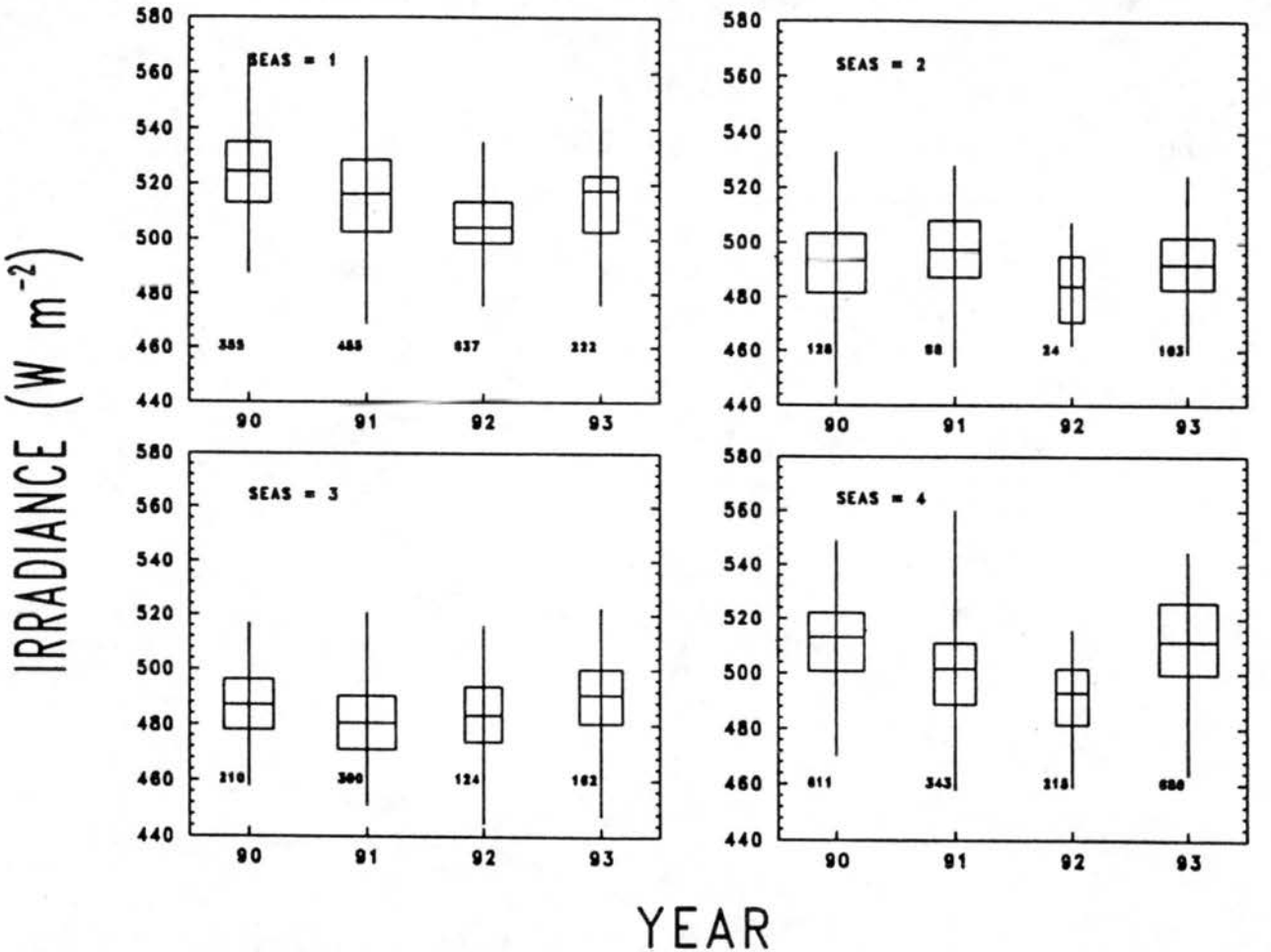

Fig. 2.14 Seasonal statistical summary of observed total solar irradiance at a zenith angle of 60° near Boulder, Colorado. Box plots indicate mean, ±25%, maximum, minimum, and the relative number of data points indicated by the width of the box. Additional statistics are given in the text.

60°. Seasonal means for late 1991 and 1992 show decreases of up to 20 W m^{-2}, statistically significant at the 99% level compared with the 1990. There could be several reasons for this decrease. Further evidence that the diminished irradiance at BLD and the other sites was due to volcanic aerosols will come from close agreement between these observed decreases and RT model results using observed optical properties for, or near, each location.

Solar irradiance observations at Kwajalein (KWAJ, 8° N, 2 m ASL) were examined for volcanic influence following Pinatubo. The optical depths over this site were higher than at any of the other investigated sites. Although a strong signal (25% decrease) was found in the direct solar beam data, the total solar irradiance data showed no evident signal. Rare clear skies, high water vapor concentrations, and an instrument exchange the month before the eruption all contributed to the lack of a detectable signal.

Total solar irradiance data from other surface sites [Dyer and Hicks, 1965; Rao and Bradley, 1983; Hay and Darby, 1984; Wendler, 1984] have indicated the presence of volcanic signals but have not been further investigated in this study because of the lack of sufficient information required to compute associated perturbed irradiances.

2.5.2 Satellite observed solar irradiance

Extensive effort has gone into observing reflected solar radiation from space. Ardanuy and Kyle [1986] and Minnis et al. [1993] have reported ${}_{Su}V_{TOA}$ following the eruptions of El Chichón and Pinatubo, respectively. Both reports included the radiative effects of any changes that may have occurred in tropospheric cloudiness from before to after the eruption, making a comparison between surface-based clear-sky data and RT

model results difficult. Ardanuy and Kyle observed a ${}_{Sn}V_{TOA}$ value up to -10 W m^{-2} attributable to El Chichón only in the polar regions starting seven months after the eruption. Minnis et al. report maximum monthly ${}_{Sn}V_{TOA}$ values of -15 W m^{-2} near the equator in the first five months after Pinatubo. Both studies also provided information on the zonal distribution of ${}_{Sn}V_{TOA}$, but again Ardanuy and Kyle's results were limited to latitudes north of 50° N and south of 50° S while the Minnis et al. period of record ends six months after the eruption and covers the latitude belt between 40° N and 40° S. Minnis et al. and Ardanuy and Kyle note general agreement with global calculations of Hansen et al. [1992] and Harshvardhan [1979], respectively, but did not give any modeled values of V specific to their observations.

2.5.3 Aircraft and ships

Solar irradiance has been observed following the Pinatubo eruption from aircraft flying below the stratosphere [Valero and Pilewskie, 1992; Saunders, 1993], and from ships in the western Pacific [Hayasaka et al., 1994]. Neither Valero and Pilewskie nor Saunders report a decrease in downward solar irradiance although both did report large stratospheric aerosol optical depths and computed decreases in total irradiance. Hayasaka et al. did detect an apparent Pinatubo signal of between -15 and -43 W m^{-2} for observations normalized to a zenith angle of 0°. However, their measurements were inconsistent with their modeled -8 W m^{-2} effect. This discrepancy could be explained by the lack of valid aerosol optical properties at the time and location of the irradiance observations.

2.6 IR Radiative Forcing

Positive ${}_{Ld}V_{Tr}$ can be expected for three reasons. First, the refractive index of H_2SO_4 is highly absorptive for many IR wavelengths. Secondly, there is a small amount of H_2SO_4 absorption for the solar wavelengths causing a slight increase in the aerosol temperatures. Similarly, the third source of increased downward IR is increased temperature of the aerosol layer due to the absorption of upwelling IR. Enhanced upward IR at the TOA, ${}_{Ln}V_{TOA} < 0$, would be caused by the same three reasons that ${}_{Ld}V_{Tr}$ is positive. (The initial warming of the lower stratosphere within the volcanic plume is caused by absorption of solar UV wavelengths by SO_2 [Lary et al., 1994], which is not further considered here) However, upwelling IR above the volcanic cloud decreases because the usual upwelling IR below the volcanic cloud is partially absorbed by the cloud and reradiated upwards at a much lower temperature. This was apparently a more dominant effect than the three sources of enhancement since ${}_{Ln}V_{TOA} > 0$, as will be shown in Chapter 4. Also the upwelling IR from the troposphere would be diminished if the troposphere cools. A positive ${}_{Ln}V_{TOA}$ is consistent with maintaining a radiative balance for the planet since ${}_{Sn}V_{TOA}$ is negative (to be shown.)

Observations of IR irradiance showing ${}_{Ld}V_S$ are not known to exist. The basic measurements are less common than for solar and the expected signal much smaller. Even at higher altitude sites, the natural clear-sky variability in this signal is dominated by H_2O and temperature making detection of ${}_{Ld}V_S$ unlikely. Observations at MLO or SPO, good locations to observe any signal, were not available for analysis. Also, no IR irradiance data were reported from aircraft flying below either eruption's aerosol cloud.

Minnis et al. [1993] observed ${}_{Ln}V_{TOA}$ with the maximum, 5 to 7 W m^{-2} at 5° N in the first two months after the eruption. The global mean, 40° S to 40° N, for the first four months after the eruption was indistinguishable from zero, according to Minnis et al. Tropospheric clouds make the Minnis et al. results difficult to interpret strictly in terms of the stratospheric aerosol effects. Ardanuy and Kyle [1986] were also unable to discern if positive ${}_{Lu}V_{TOA}$ in their data was due to El Chichón or clouds.

2.7 Net Allwave Irradiance

Net radiative cooling, or heating, of the troposphere and surface may be specified by the net allwave irradiance at the tropopause [Hansen et al., 1992; Lacis et al., 1992]. Observations of this quantity have not been made, but are readily modeled given basic RT model input parameters. Net irradiance can be obtained by combining the net solar and net IR data discussed previously. A maximum zonal ${}_{An}V_{TOA}$ of -3.5 W m^{-2} after El Chichón, using Nimbus 6 and 7 ERB budget data, and of -11 W m^{-2} following Pinatubo were reported by Minnis et al.; they also reported a global mean ${}_{An}V_{TOA}$ of -2.7 W m^{-2}.

2.8 Underlying Albedo.

The reflectivity underlying an aerosol layer is important in finding the net radiative effect of the aerosol layer [e.g., Harshvardhan, 1979; Herman et al., 1976; King et al., 1984]. The underlying albedo determines the amount of energy that would have been reflected without the aerosol and establishes the extent of the anomaly created by the aerosol. Furthermore, the reflected radiation interacts with the aerosol layer, again modifying the net solar radiation emerging from the top of the layer. Generally, aerosols

over a bright surface would have less of an effect on the net solar irradiance at any level than the same aerosol over a darker surface. This effect is shown quantitatively in Appendix D, Sec. D.3. For stratospheric aerosols the underlying reflection results from the troposphere and surface.

The broadband solar planetary albedo with spatial and temporal resolution has recently become available from the Earth Radiation Budget Experiment (ERBE) data set [Whitlock et al., 1993]. These data cover the period of 1986 through 1988 when few volcanic aerosols existed. ERBE data are available as monthly means on a 280-km by 280-km grid for the entire globe. Zonal seasonal means of TOA albedo for these data are shown in Fig. 2.15. The difference between the reflectivity at the tropopause and that at the TOA is small and due primarily to Rayleigh scattering in the absence of volcanic aerosols. A linear relationship between albedo at the TOA and lower altitudes exists, dependent on conservative scattering and atmospheric absorption [Cess et al., 1991]. Using an RT model version of this linear relationship, the ERBE data were used to find representative surface albedos required in subsequent clear-sky RT V calculations. This will result in approximating tropospheric reflectivity with clouds, with the assumption that the average cloudiness, ground cover, tropospheric aerosols, and sea state for 1986-1988 were not significantly different than during the two eruption events.

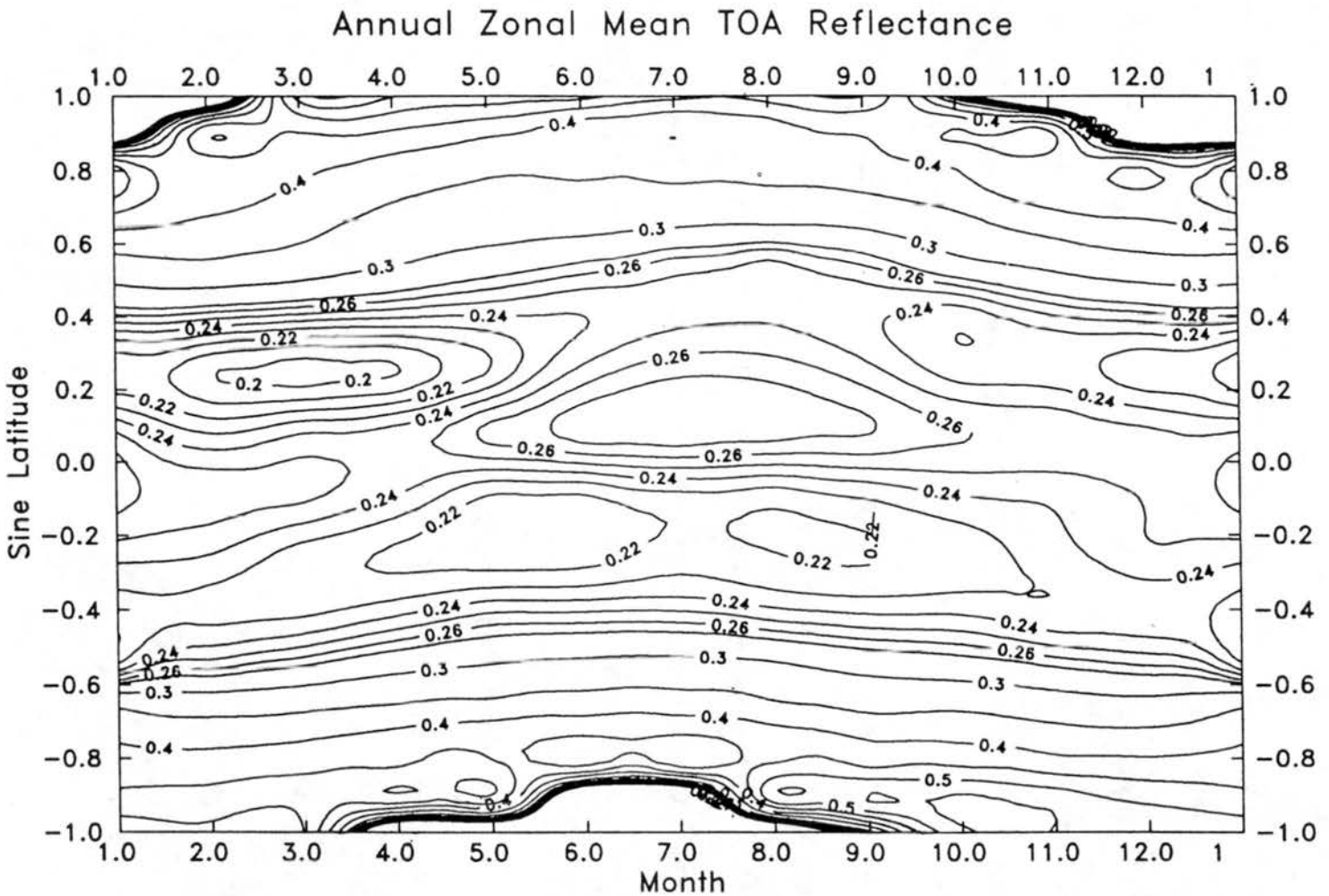

Fig. 2.15 Annual variation of zonal mean TOA albedo as measured from ERBE, averaged over 1986 - 1988. (Note: values on the seasonal terminator are incorrect due to objective analysis plotting limitations)

Chapter 3. Radiative Transfer: Theory and Atmospheric Models

Radiative transfer theory provides the mathematical tools to compute electromagnetic radiative energy at different locations and from different directions within and on the boundaries of a semi-transparent medium such as the earth's atmosphere. Radiation at any point within this domain varies as a function of the strength and position of radiant sources and the composition of the medium. The mathematical equations that describe the transfer of electromagnetic radiation through the atmosphere have been extensively developed [e.g., Chandrasekhar, 1960; Goody, 1964; Liou 1980, 1992].

3.1 Model Development

Adaptations of existing solutions to the RT equation were carried out for the calculations required here as described in Appendix C. It was necessary to compute time and spatially dependent radiant fields for various atmospheric conditions, including and excluding stratospheric aerosols of volcanic origin. A realistic RT model was required that includes observationally consistent variations in solar geometry, vertical structure, aerosol optical properties, additional atmospheric constituents, temperature, and underlying reflection. Many different approaches have been used to estimate V utilizing varying RT schemes, aerosol properties, spatial and temporal resolution, and treatment of albedo [e.g., Pollack et al., 1976; Harshvardhan and Cess, 1976; Coakley and Grams, 1976; Herman

et al., 1976; Lenoble et al., 1982; King et al., 1984; Lacis et al., 1992]. Herman et al. [1976], Lenoble et al. [1982], Harshvardhan [1979] and King et al. [1984] examined zonal variations of volcanic aerosol forcing, but without observed aerosol evolution or the vertical resolution necessary for comparing with available observations.

Two widely disseminated and tested radiative transfer computer codes were used as cores around which were built the necessary RT models for the current investigation. One core code was the discrete ordinates (DO) solution to the complete two-dimensional, plane-parallel, multiple-scattering, equations as originally formulated by Chandrasekhar [1960] and usefully implemented by Stamnes et al. [1988] and references therein. LOWTRAN7 [Kneizys et al., 1988] was the other code used. DO code was used for modeling in the solar wavelengths, 0.18-4.0 μm, where multiple scattering was significant. LOWTRAN7 was used in the IR, 4.0-100 μm, primarily because extensive constituent radiative property data bases were incorporated in the original code. A summary of each code follows a brief discussion of the formulation of the radiative transfer equation (RTE) in Appendix C. The solar model is called DISORTX; the IR model is referred to as LOWTRAN7X.

The RT models developed for this study are unique in the sense that they were specifically intended to produce results directly comparable to a variety of observations and that they are also sufficiently realistic to simulate volcanic forcing over the globe and over the lifetime of actual eruption clouds. Few attempts have been made to confirm modeled V with observations. Coakley [1981] had to make several assumptions to convert previously computed theoretical V to quantities that could be observed and verified. The radiation fields computed here were compared to limited observations for

mutual verification, used for diagnostic purposes, used to develop and test simple parameterizations, and could be introduced as perturbed radiative forcing into global dynamic models, although this last step was beyond the scope of this work.

3.2 Model Inputs and Execution

The RT models developed in Appendix C were used here for stand-alone investigations of model sensitivities and for site-specific comparison to observations. Also, the model inputs were compiled to form global coverage so that global time-dependent V can be computed. The results are presented in Chapter 4. Aerosols were added 5 to 15 km above the tropopause according to volcanic aerosol height distributions given in Sec. 2.3. Aerosol optical depth, single scatter albedo, and phase functions with the spectral resolution of the models were determined from Mie theory using 75% H_2SO_4 droplets with a size distribution determined by inversion from low resolution spectral optical observations. More spectral structure was introduced in the Mie computed optical depths due to the variation of the imaginary part of the index of refraction at wavelengths >2 μm (Fig. 3.1).

Sensitivity studies were conducted to investigate the effects of variations in optical depth, absorption, particle size distribution, surface albedo, spatial and temporal averaging, and model internal variables such as number of quadrature angles. Site-specific model runs were accomplished by specifying as closely as practical local conditions, $\tau_A(\lambda)$, albedo, and θ_O, at the time of irradiance observations to which the RT model will be compared. For the global cases, representative surface reflectances, atmospheric

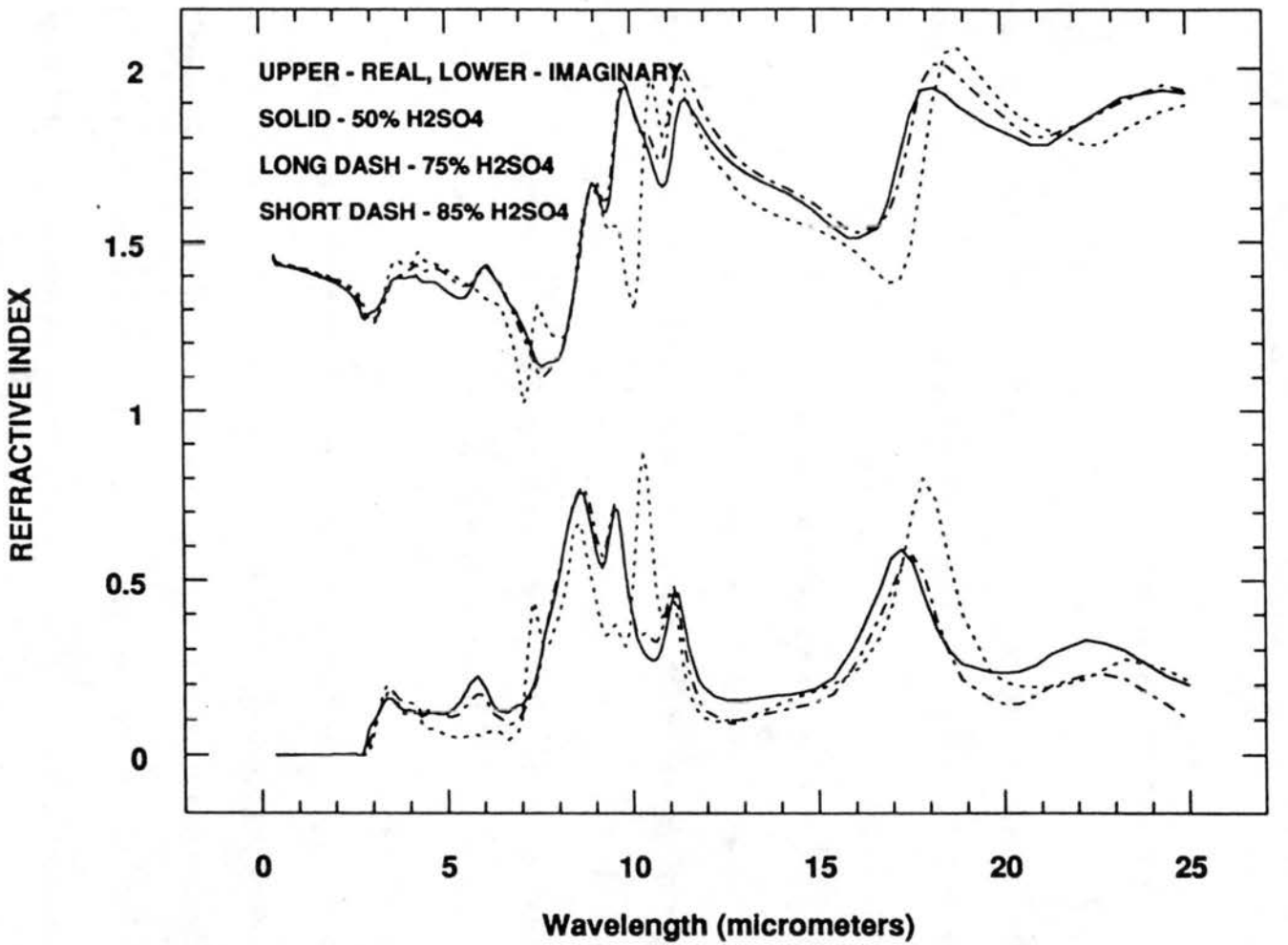

Fig. 3.1 Spectrally resolved real and imaginary index of sulfuric acid, as given by Palmer and Williams [1975]. The three different water solutions were used in sensitivity tests, with 75% used for most calculations.

constituents, aerosol loadings, and solar geometry were specified. The following describes the specification of the global RT model inputs.

3.2.1 Global Calculations

Seasonal mean $\tau_A(550)$ values for 10 equal area zonal mean bands were determined from the global data compiled by Sato et al. [1993] and that obtained from AVHRR measurements immediately following Pinatubo (Figs. 2.4, 2.5, and 2.6). The zonal bands, with latitude bounds of $\sin^{-1}(1.0)$ to $\sin^{-1}(0.8)$ and so on, were numbered 1 to 10 from north to south. Seasonal mean optical depth data for the two volcanic events covering the periods of Jan. 1982 through Dec. 1984 and Jan. 1991 through Dec. 1993 were used. Aerosol observations for 1990, when near background stratospheric aerosols were observed [e.g., Dutton et al., 1994], were used to determine background irradiance levels for each season. Seasons were defined as solar lagged seasons, i.e., means of Jan.-Mar., Apr.-Jun., etc., and were numbered one to four from the first of the calendar year for reference. Each zonal/seasonal grid-box is identified by year, season, and latitude band, i.e., 920307 is for 1992, third season (July - Sept.), and 12-24° S.

Spectral aerosol optical depth for each grid-box was determined by linearly scaling $\tau_A(\lambda)$ obtained at the nearest of three surface-based sites to agree with $\tau_A(550)$ observed for that grid-box. The three surface-based sites for which $\tau_A(\lambda)$ data were available were located at 46° N, 19° N, and 25° S. Data from the 25° S site were unavailable following El Chichón but that omission has little effect since El Chichón aerosols were restricted primarily to equatorial and northern latitudes (Fig. 2.3). Aerosol size distributions were obtained by Mie inversions of the scaled $\tau_A(\lambda)$ using a program call RADINV supplied

by Mike King as described in appendix A. These size distributions were taken as representative of the zonal band and seasonal average grid-box. Size distributions for the grid-boxes correspond to the widest aerosol size range for which a Mie inversion was successful. The wavelengths of the $\tau_A(\lambda)$ observations vary within the range 0.380 to 1.06 μm and the radius range of the inversions was from 0.1-1.1 μm. The inverted size distributions for each grid-box were then used to calculate higher spectral resolution scattering and absorption optical depths as well as phase functions using Mie calculations. The Mie calculations were performed with MIEV0X as described in Appendix A. The Mie results for the phase functions are in the form of Legendre weights for the number of streams specified for DISORTX, and in the form of an asymmetry factor for LOWTRAN7X. Although only three to five wavelengths of optical depth information were input to RADINV, optical properties were returned from MIEV0X for up to 146 wavelengths. he model atmospheres used in the global RT models consisted of vertical profiles of temperature, pressure, and gaseous constituents compiled by McClatchey et al. [1972]. The specific model atmosphere used at each grid point on a seasonal and zonal basis are indicated in Table 3.1

The tropospheric and surface reflectance representative of global and seasonal varying conditions was determined for the TOA ERBE data base. These TOA measurements were averaged over three non-volcanic years to give seasonal means in 120 zonal bands. TOA albedo as a function of surface albedo for clear-skies is shown in Figs. 3.2a,b. Although, the exact relationship between TOA and surface albedo for varies somewhat with zenith angle and aerosols, a single adjustment curve was used here because only a narrow range of zenith angles was used, 55° to 80°, and the albedo sensitivity of V in

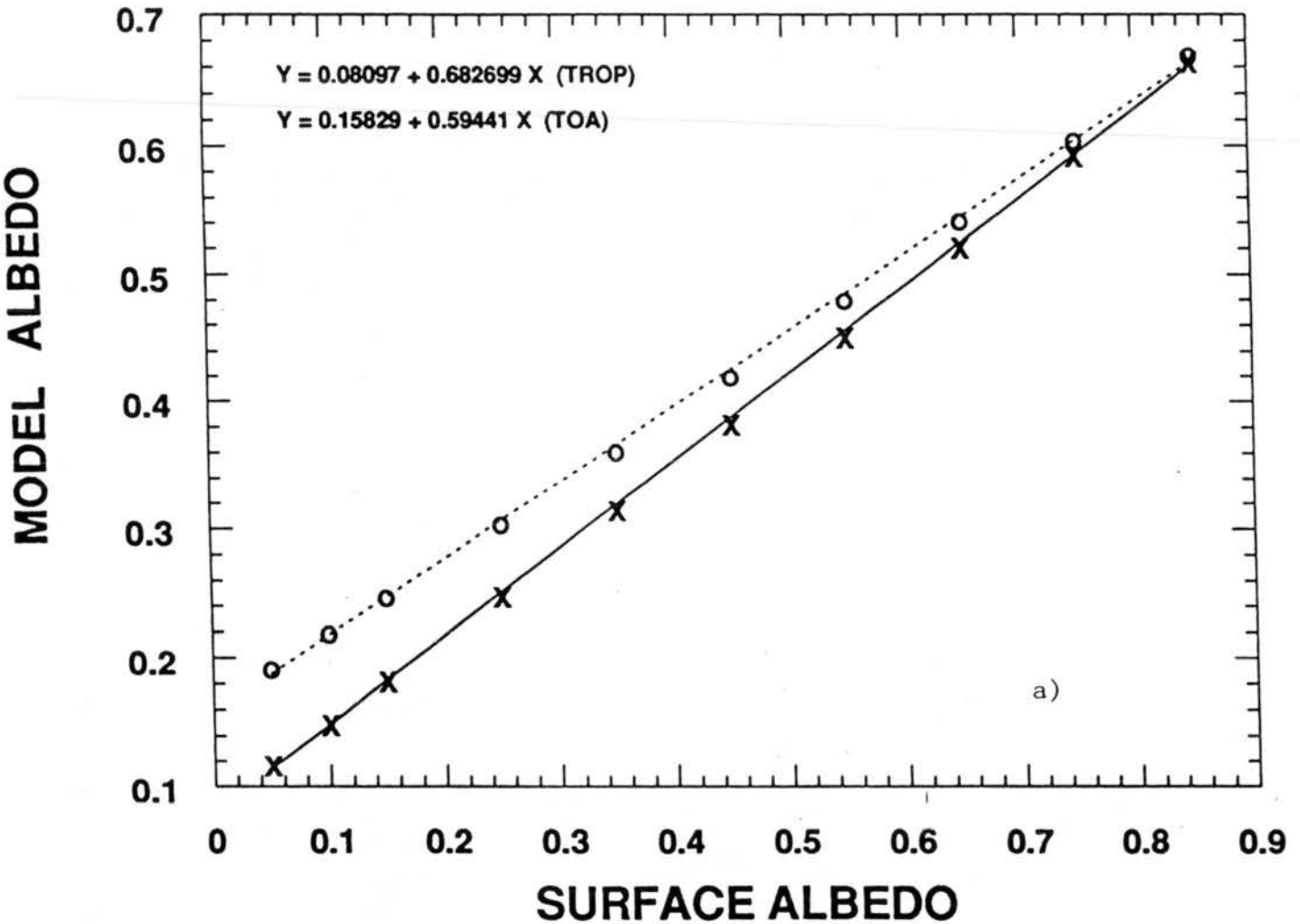

Fig. 3.2 Linear function relationship between modeled solar reflectance at the tropopause and TOA as a function of surface albedo - dashed line) TOA, solid line) tropopause, a) for background conditions, b) for maximum El Chichon aerosol loading.

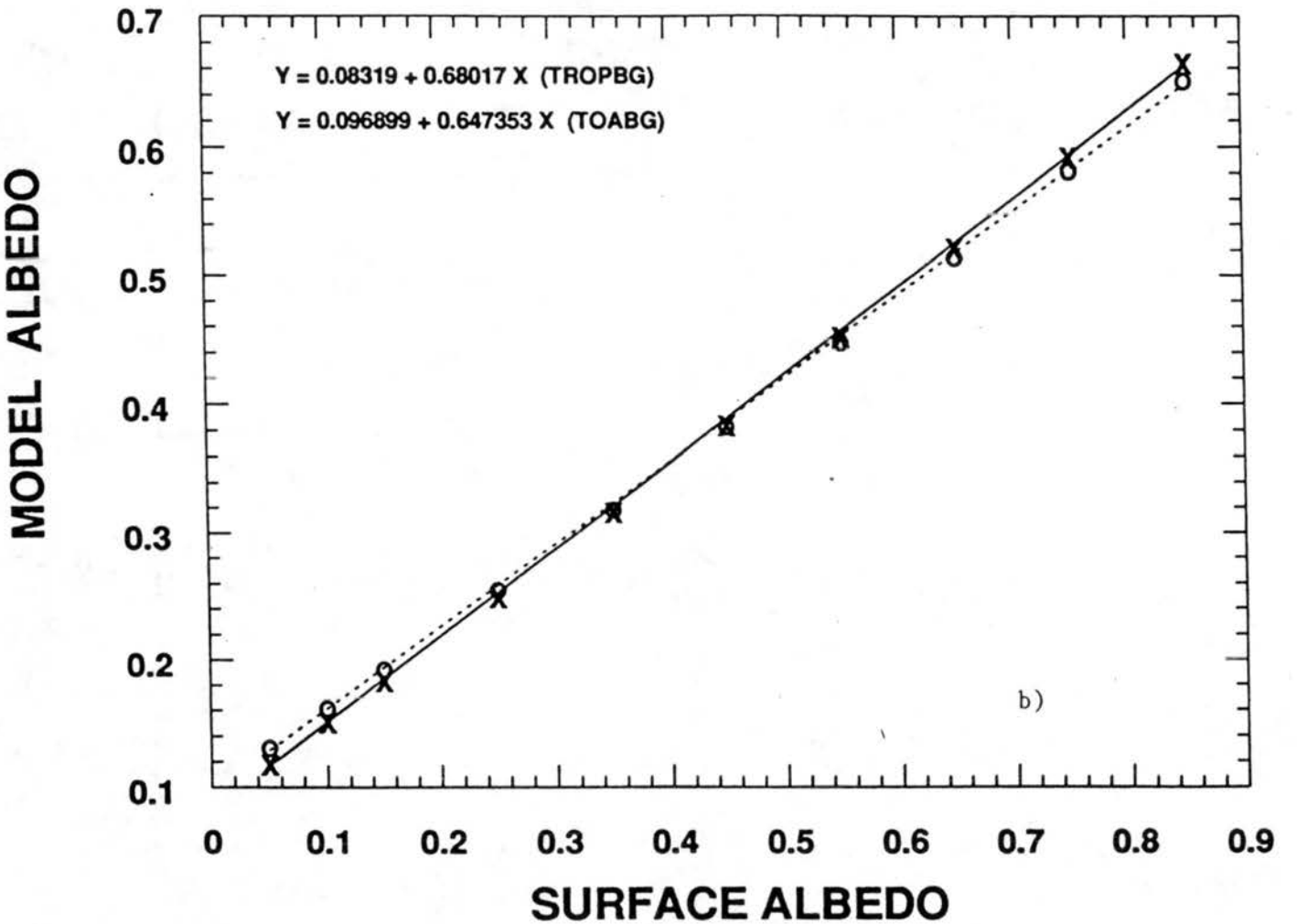

Fig 3.2b (see caption on previous page, Fig 3.2a)

Table 3.1 Atmospheric profiles used for various seasons and latitude bands.

	SEASON			
Lat. Band	1	2	3	4
90 - 53 N	SAW	SAS	SAS	SAW
53 - 37 N	MLW	MLS	MLS	MLW
37 - 24 N	MLW	MLS	MLS	MLW
24 - 12 N	TRP	TRP	TRP	TRP
12 N - 0	TRP	TRP	TRP	TRP
0 - 12 S	TRP	TRP	TRP	TRP
12 - 24 S	TRP	TRP	TRP	TRP
24 - 37 S	MLS	MLW	MLW	MLS
37 - 53 S	MLS	MLW	MLW	MLS
53 - 90 S	SAS	SAW	SAW	SAS

SAW - Subarctic winter
SAS - Subarctic summer
MLS - Midlatitude summer
MLW - Midlatitude winter
TRP - Tropical

this range was small, as will be shown in Chapter 4. This procedure, while giving a realistic tropospheric reflectance, will give incorrect radiative profiles in the troposphere because of the incorrect vertical reflection distribution, which was not of concern here. he albedos applied at the surface are Lambertian and spectrally constant across the solar spectrum. Model albedos simulate a zonal combination of land surface, cloud top, tropospheric aerosol, and ocean surface reflection for broadband flux only; therefore, bidirectional and wavelength dependent reflectance functions were not utilized. Effects of non-Lambertian surface reflectivity on V are discussed in Appendix D, Sec. D.3.

The effects of diurnally and seasonally varying solar geometry must be considered in a globally representative model. Each DISORTX model run was for a fixed solar geometry and could be repeated as often as necessary to produce a 24-h integral. An estimate to a 24-h integral can be found by determining the mean solar zenith angle for the sunlit portion of the day. Then, perform one model run for that mean angle and multiply the result by the fractional length of solar day for the specified location. The mean solar zenith angle and length of day are given by Eqs. 3.1 and 3.2. This procedure only gives exact results when the horizontal incident irradiance varies linearly with $\cos(\theta_o)$ and is an approximation within the atmosphere for clear skies because of the dominant effect of $\cos(\theta_o)$ on total irradiance. The representative solar zenith angle and fractional day length for each global grid point were determined by integrating Eqs. 3.1 and 3.2 over the time and latitude span of each. Kiehl and Solomon [1986] have analyzed these two approaches and have concluded that the mean angle approach yields irradiances to within 2% of 30-min resolution daily integrals. In a comparison conducted for this study, a single DISORTX irradiance calculated using the mean daily solar angle agreed to within 1% of a daily integral based on multiple DISORTX runs with 10-min resolution.

$$\cos(\theta) = \frac{h*\sin(L)*\sin(\delta) + \cos(L)*\cos(\delta)*\sin(h)}{h} \qquad \textbf{3.1}$$

Where: L = latitude; δ = solar declination.

$$\cos(h) = -\tan(L)*\tan(\delta) \qquad \textbf{3.2}$$

note: $h = 0$ for $\cos(h) > 1$, $h = \pi$ for $\cos(h) < -1$, and fractional day = h / π

For the global model runs, the complete vertical/spectral model was run once for each of the ten zonal means for each 3-month average of atmospheric constituents and solar geometry for six volcanic years (1982-1984, 1991-1993) and one background year (1990). This resolution was chosen as a compromise among available data, scale of expected V variations, and available computer resources. Improvement of the global model would be expected if weekly, or even monthly, resolution was used, especially during the first three months following the eruption when the distribution of aerosol was rapidly changing; however, the unavailability of global optical depth data precludes higher time resolution.

3.2.2 Local RT model calculations

DISORTX and LOWTRAN7X were also run with inputs intended to simulate specific local conditions or simulate the effects of varying a single model variable. In each case, two runs were necessary, one with and one without volcanic aerosol so V could be computed. These model runs were carried out to allow comparison to specific observations, compare to earlier models, investigate vertical structure, or to identify particular features of the model sensitivities for enlightenment and development of parameterization schemes.

Chapter 4. Computation of Volcanic Radiative forcing: Results and Comparisons

The radiative transfer models described in both the previous chapter and Appendix C (DISORTX and LOWTRAN7X) were run for site-specific conditions or with temporal and spatial global variability of the atmospheric constituents and their optical properties, as assembled in Sec. 3.2. Calculations at the surface, tropopause, and TOA permit comparison with observed and previously published results. In addition to aerosol anomalies, the models' performance was tested in several ways. Modeled absolute irradiances were compared to those from the Intercomparison of Radiation Codes Used in Climate Models (ICRCCM) given by Fouquart and Bonnel [1991] for solar and Ellingson et al. [1991] for IR. Sensitivity tests were conducted to determine the models' response to several variables and those sensitivities were compared to those previously published. The sensitivity tests provide insight for developing parameterizations useful in incorporating volcanic aerosol forcing into higher resolution studies. Global zonal-mean background irradiances computed from DISORTX and LOWTRAN7X were compared to global radiation budget observations from satellite given by Campbell and Vonder Haar [1980]. In addition, the rigorous RT calculations reported here could provide a comparison for GCMs that already contain parameterized RT schemes and produce their own V.

Computed V was contrasted with other earlier theoretical work and a minimal set of satellite and surface-based observations presented in Chapter 2. The current model results generally fall within the range of earlier theoretical estimates and may help to narrow

some uncertainties of those earlier values because many used hypothetical aerosol models. Several sets of observations substantiate model computations.

4.1 Brief Investigations With Basic RT Models

4.1.1 Spectral model output

The spectral output of DISORTX for both solar and a test IR case was compared to LOWTRAN7 to evaluate the performance of DISORTX. Figure 4.1 shows the sea-level direct solar beam from ≈ 0.3 μm to 2.5 μm at a zenith angle of 60° for both DISORTX and LOWTRAN7 for the same model atmosphere. LOWTRAN7 was run with 20 cm^{-1} spectral resolution. Differences in spectral resolution are evident but the integral difference between the two was less than 0.5%. Figures 4.2 and 4.3 show a similar comparison except for upwards IR at the TOA and downward IR at the surface, respectively. Offset differences of up to 35% are seen in Fig. 4.2 at some wavelengths, with a near constant bias of several percent. Lack of complete correlated-k distribution data and the water vapor continuum probably account for the departures of DISORTX from LOWTRAN7. Because of these comparisons, the IR version of DISORTX was replaced with LOWTRAN7X which contains much more complete constituent information and does not need to simulate multiple scattering.

4.1.2 Single-layer, aerosol-only test DISORT model

A simple investigation of the solar effects of volcanic aerosols was performed by running a single layer version of DISORT in which only the optical properties of aerosols were introduced along with the extraterrestrial solar irradiance and representative clear-sky underlying albedo. The modeled volcanic aerosol effect here, ${}_{Sd}V_{Tr}$, is expressed as a percentage decrease in downward irradiance from the top to the bottom of the layer.

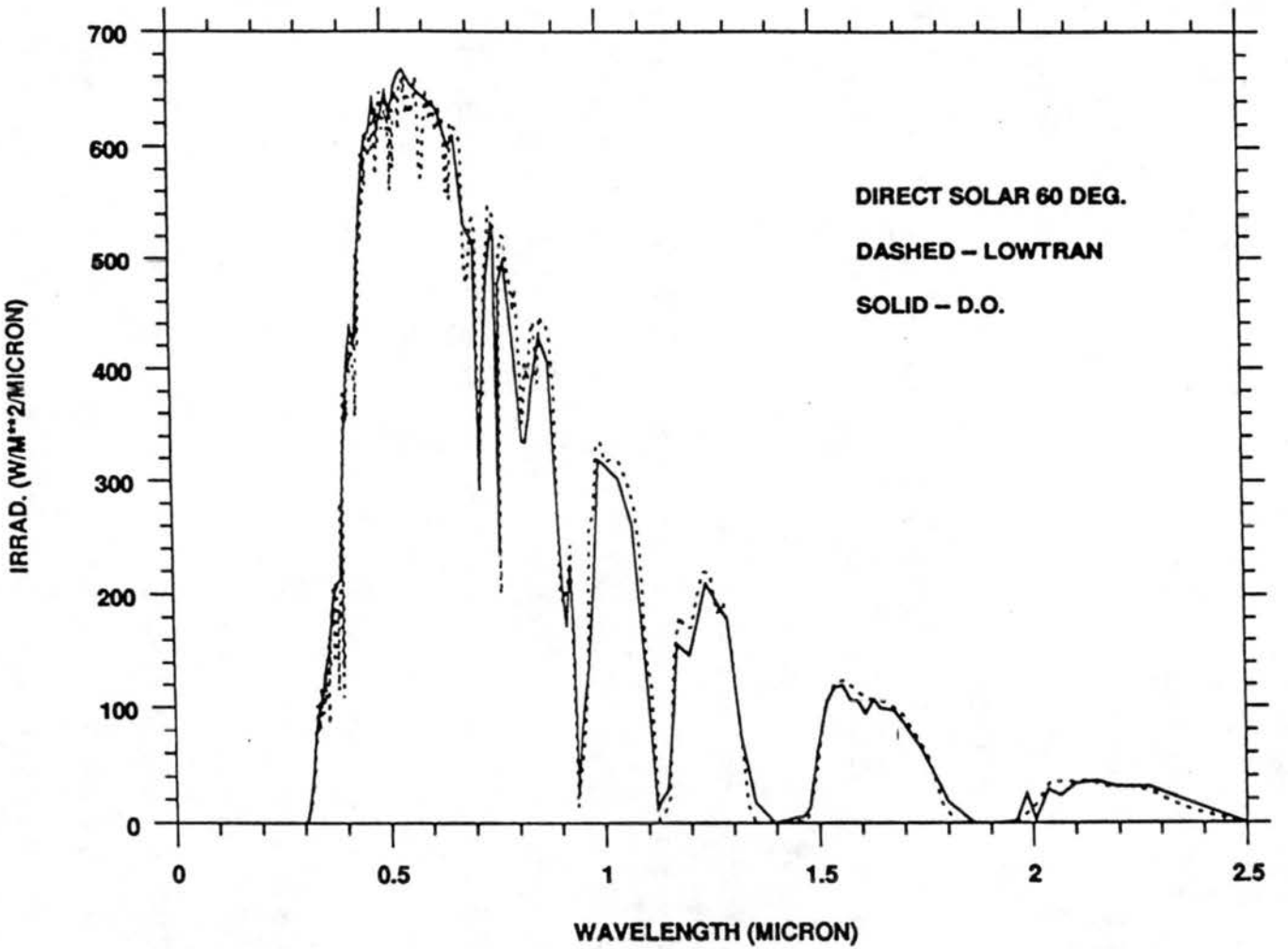

Fig. 4.1 LOWTRAN7 and DISORTX modeled direct solar irradiance for sample case with solar zenith angle = 60°.

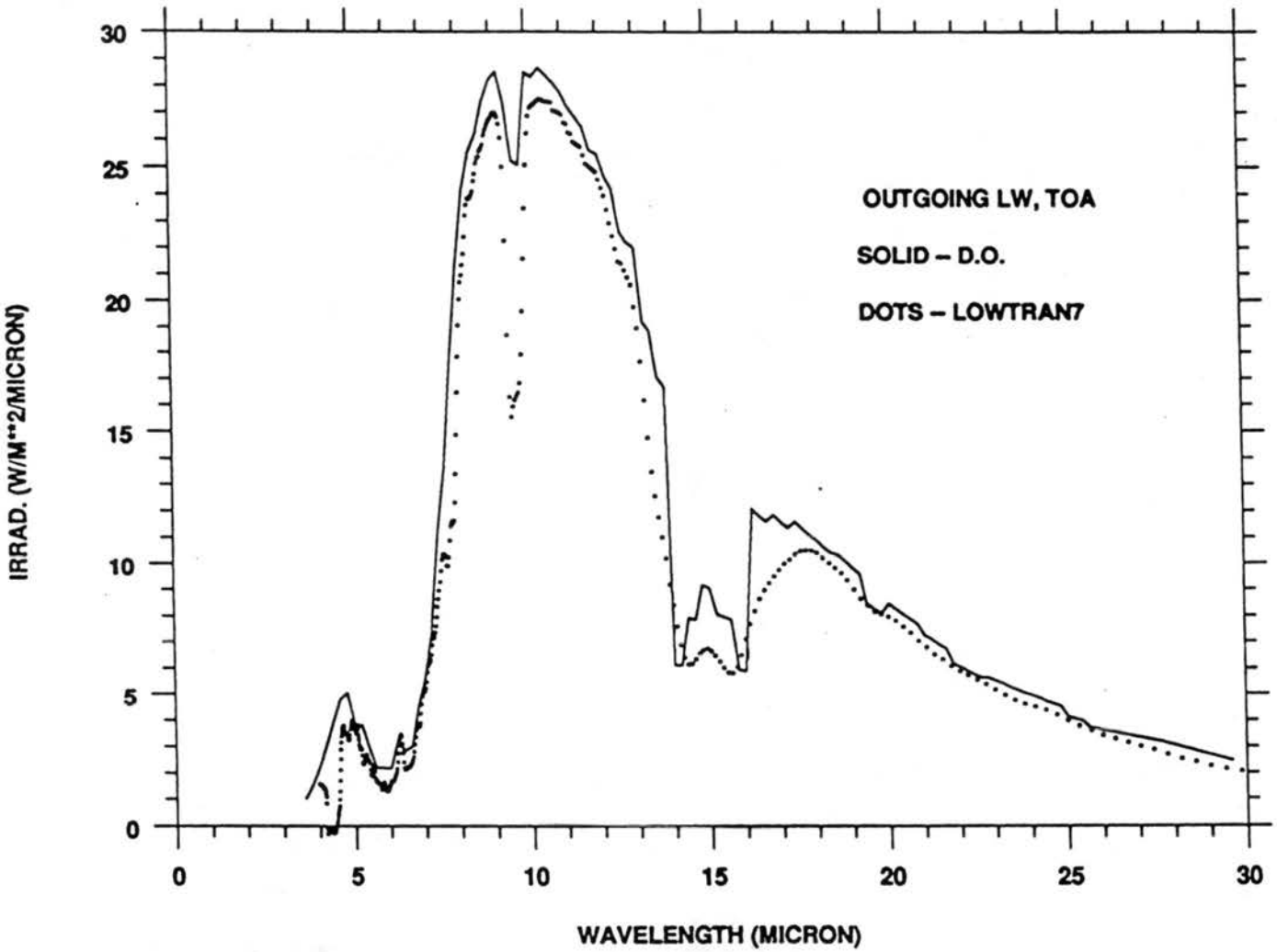

Fig. 4.2 LOWTRAN7X and DISORTX modeled outgoing IR at TOA for sample case. Note significant differences at some wavelengths and overall bias.

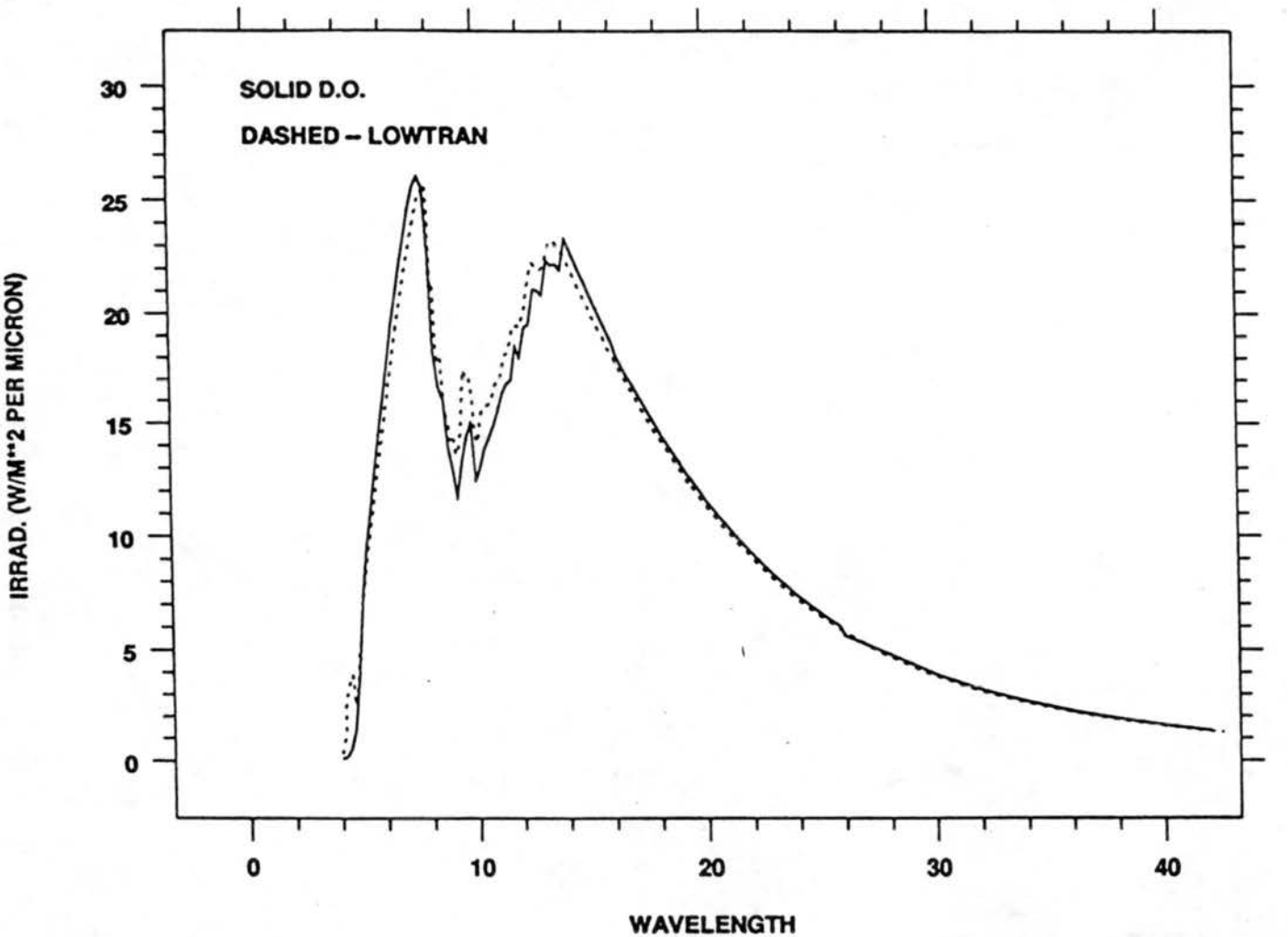

Fig. 4.3 LOWTRAN7X and DISORTX modeled downwelling IR for sample case.

These calculations were carried out using the aerosol optical properties observed over Mauna Loa, Hawaii from 1981 to 1993, with the results shown in Fig. 4.4. Also shown in Fig. 4.4 are corresponding Mauna Loa irradiance observations. The much higher variability in the observations in Fig. 4.4 is due to other atmospheric constituents not included in this simple model, such as water vapor. Figure 4.4 suggests that aerosols were a major factor in the drop in irradiance seen in 1982 and 1991/1992. A more accurate and thorough investigation of aerosol effects requires incorporation of realistic atmospheric conditions so that the incident spectral irradiance from above and below the aerosol layer can be better defined, as was done with DISORTX and LOWTRAN7X.

4.2 Comparison to ICRCCM

The ICRCCM provides a set of standard atmospheric conditions for which radiative transfer computations can be made and compared to numerous RT models used by various organizations from around the world. ICRCCM summaries presented by Fouquart and Bonnel [1991] and Ellingson et al. [1991] include models ranging from line-by-line to wideband. In their summaries, Fouquart and Bonnel, and Ellingson et al. have eliminated some outliers and have presented means and standard deviations of the remaining group of models. Results of the two participating line-by-line models were specifically identified. The line-by-line models, which can be considered most accurate, are close to the ICRCCM consensus. This adds credibility to the interpretation that the consensus was a quality standard against which other models can be referenced. As a test of DISORTX and LOWTRAN7X, several ICRCCM cases were run and the models' outputs compared to the ICRCCM summaries (Table 4.1). All test cases were for clear skies with defined Lambertian surface albedo, atmospheric constituent and temperature profiles, and

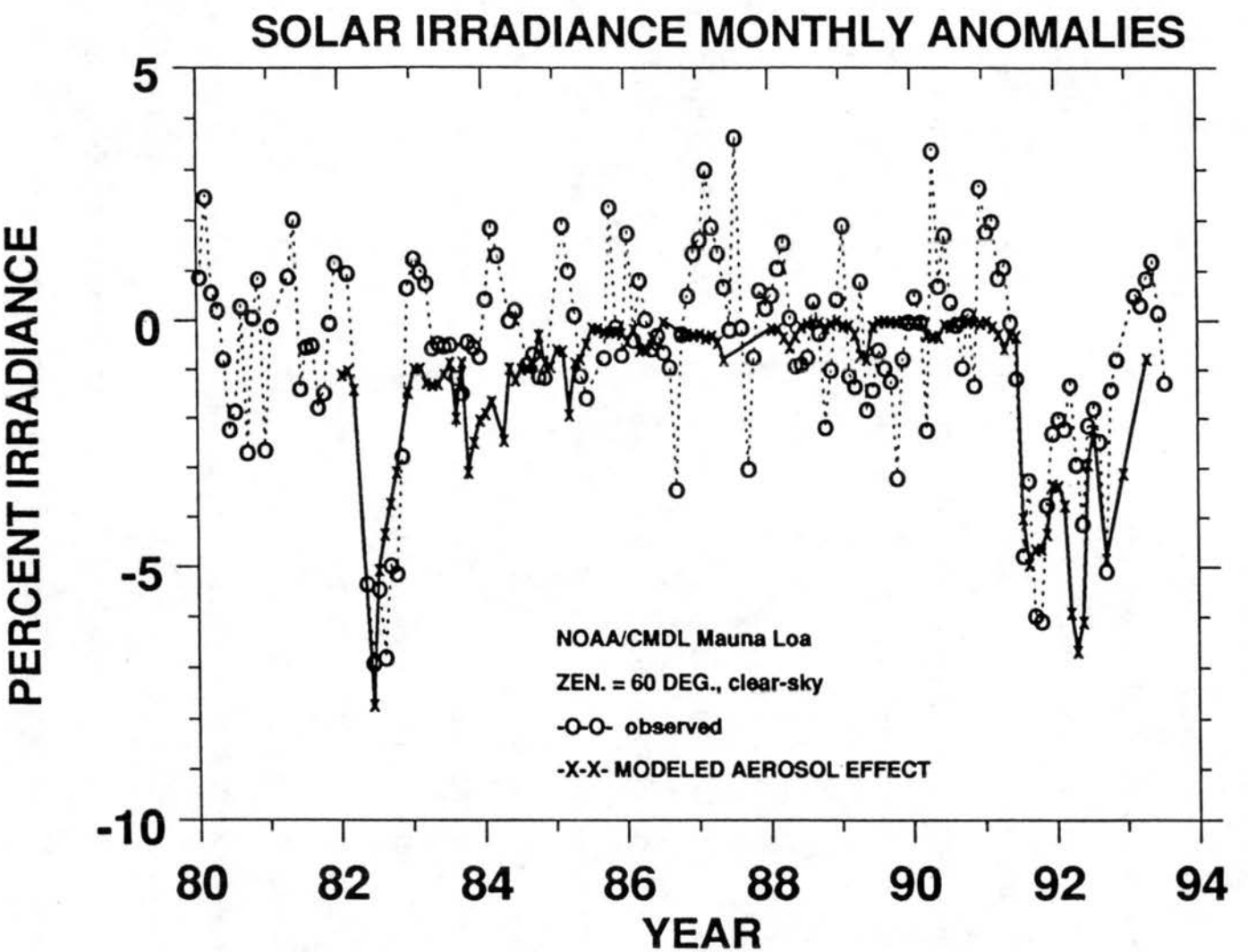

Fig 4.4 Comparison between percentage variation in monthly mean clear-sky observed and test modeled total solar irradiance at Mauna Loa, Hawaii.

Table 4.1 Comparison of ICRCCM results to DISORTX and LOWTRAN7X calculations. "rms" is the rms differences among the ICRCCM cases.

ICRCCM Case #		θ_o	alb	RT Model	ICRCCM ($W\ m^{-2}$) mean	rms diff.	Current work
SW							
31	MLS	30	0.2	DISORTX	943.7	2%	940.6
32	MLS	30	0.8	DISORTX	985.0	2	987.0
33	MLS	75	0.2	"	235.8	2	236.1
34	MLS	75	0.8	"	246.2	4	246.8
35	TRP	30	0.2	"	932.6	2	926.6
36	TRP	30	0.8	"	975.0	2	974.1
37	TRP	75	0.2	"	234.9	3	232.0
38	TRP	75	0.8	"	246.5	4	242.9
39	SAW	30	0.2	"	999.6	1	1020.5
40	SAW	30	0.8	"	1043.7	2	1068.1
41	SAW	75	0.2	"	255.3	3	263.5
42	SAW	75	0.8	"	265.1	3	274.9
LW							
25	TRP			LOWTRAN7X	391.0	3	381.4
27	MLS			"	343.4	2	338.5
28	SAW			"	167.7	5	173.4

solar geometry. None of the aerosol cases were used because too few ICRCCM models included aerosols and the ICRCCM results were inconclusive, especially for large optical depths. It is seen in Table 4.1 that DISORTX and LOWTRAN7X results were within the rms difference of the ICRCCM participants, except case 39. This suggests that the model features implemented specifically for this work (mostly in DISORTX) were executing correctly, including spectral integration, correlated *k*-distribution attenuation, radiance integration to irradiance, Rayleigh scattering, and vertically complete structure. However, several important model features remain unconfirmed from this analysis, e.g., aerosol effects and global temporal/spatial sampling.

4.3 Altitude of Volcanic Radiative Forcing

Development of a vertically complete RT model allows examination of V at all levels. The vertical distribution of V affects atmospheric thermal stability and is critical in large scale models that account for the vertical redistribution of heat. Also, vertically resolving the modeled V allows comparison to observations made at different heights. Various investigators have calculated V at the surface, tropopause, bottom of the aerosol layer, top of the aerosol layer, and TOA. The vertical resolution used in DISORTX and LOWTRAN7X has been chosen to be 2 km in the lower stratosphere and 1-3 km in the troposphere. Figure 4.5 highlights the vertical resolution of the two RT models and shows the computed downward and upward irradiances for background stratospheric aerosols.

Figure 4.6 shows vertical profiles for all four components of V modeled near peak Pinatubo aerosol loading between 21 and 30 km. These profiles vary little with height except near and within the aerosol layer. The ${}_{Sn}V$, ${}_{Ln}V$, and ${}_{An}V$ for this case are shown in Fig. 4.7 and display similar vertical variation. ${}_{An}V_{Tr}$ represents the net radiative impact on the troposphere and surface, and was used for demonstration, comparison to previous results, and additional applications.

4.4 Instantaneous vs. Equilibrium Radiative Forcing

Radiative forcing presented thus far has been instantaneous. For ${}_{Lu}V_{Tr}$ and ${}_{Lu}V_{TOA}$ it could be important to compute an equilibrium forcing as being more realistic because of the dramatic change in stratospheric temperature resulting from increased IR absorption. Labitzke and McCormick [1992] and Christy and McNider [1994] have noted observed changes in stratospheric temperature after Pinatubo and El Chichón. Previous theoretical estimates [Lacis et al., 1992; Pollack et al., 1976; Coakley and Grams, 1976; and others]

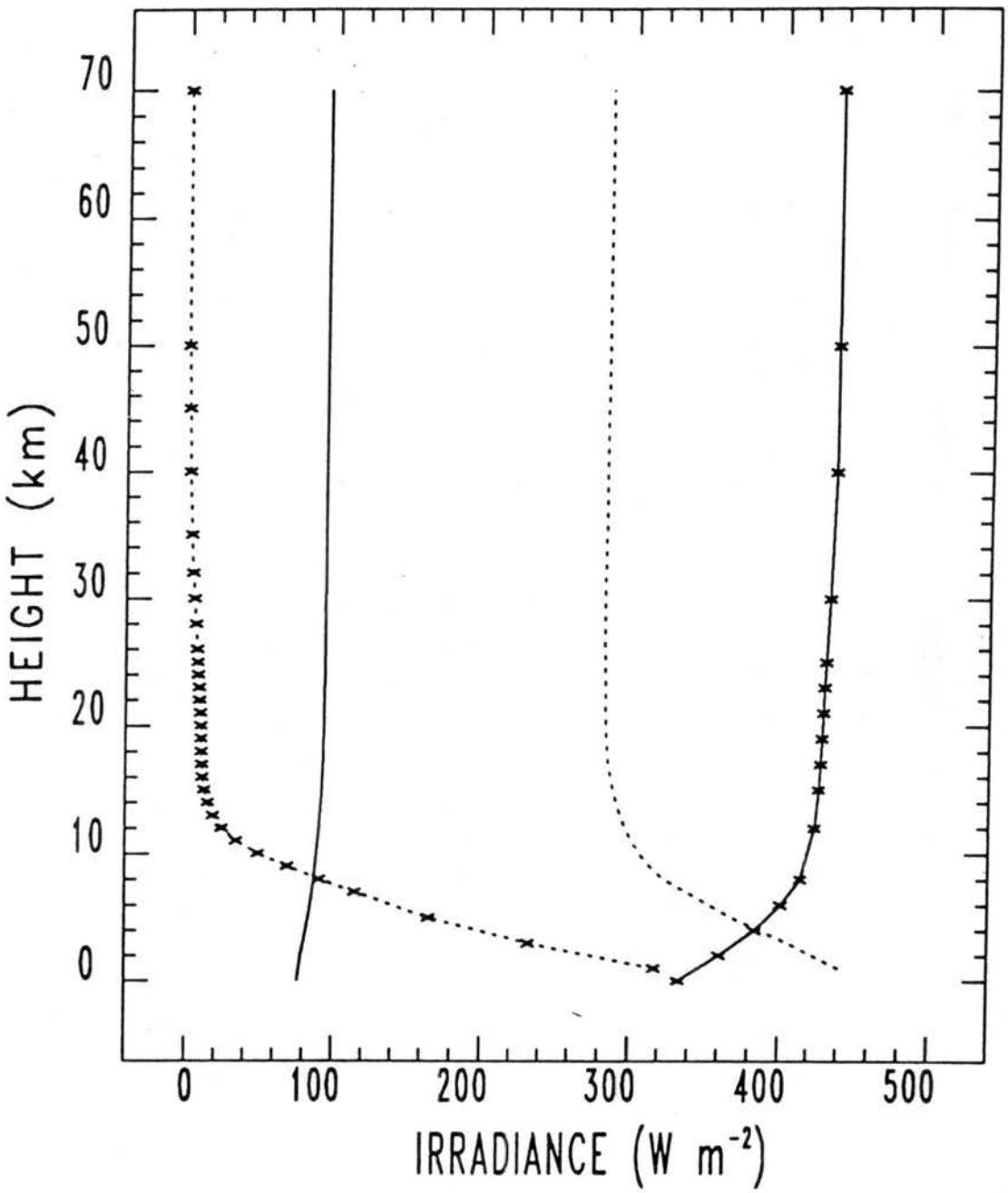

Fig. 4.5 Modeled vertical profiles of solar and IR upward and downward irradiances for background tropical case, showing vertical resolution of atmospheric models - solid) upward SW, X dashed) IR down, dashed) IR upwards, and X solid) SW down.

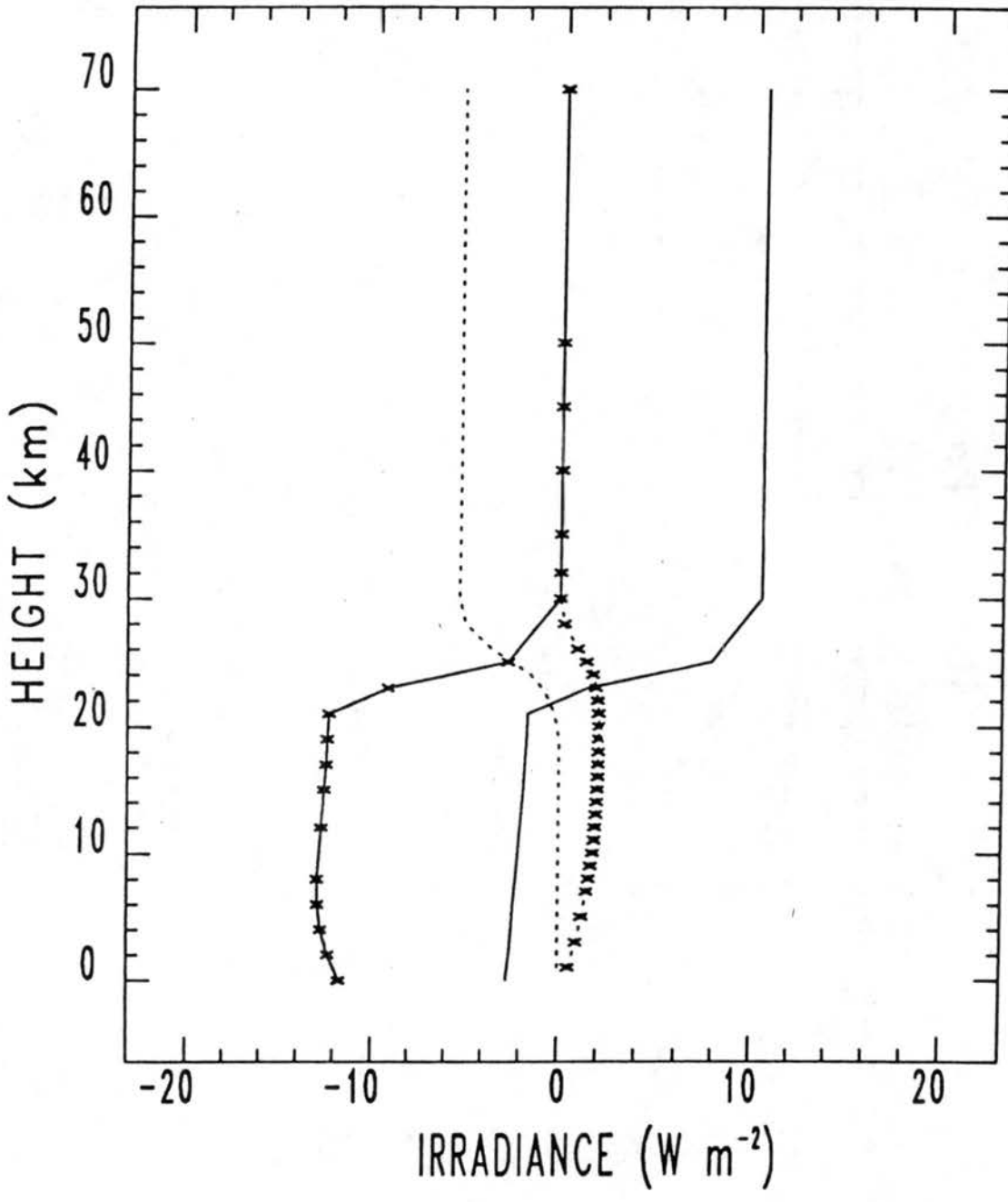

Fig. 4.6 Vertical profiles of volcanic radiative forcing, V, for grid-box 910406, downwards positive - (x dashed = ${}_{Ld}V$), (solid = ${}_{Su}V$), (dashed = ${}_{Lu}V$), and (x solid = ${}_{Sd}V$).

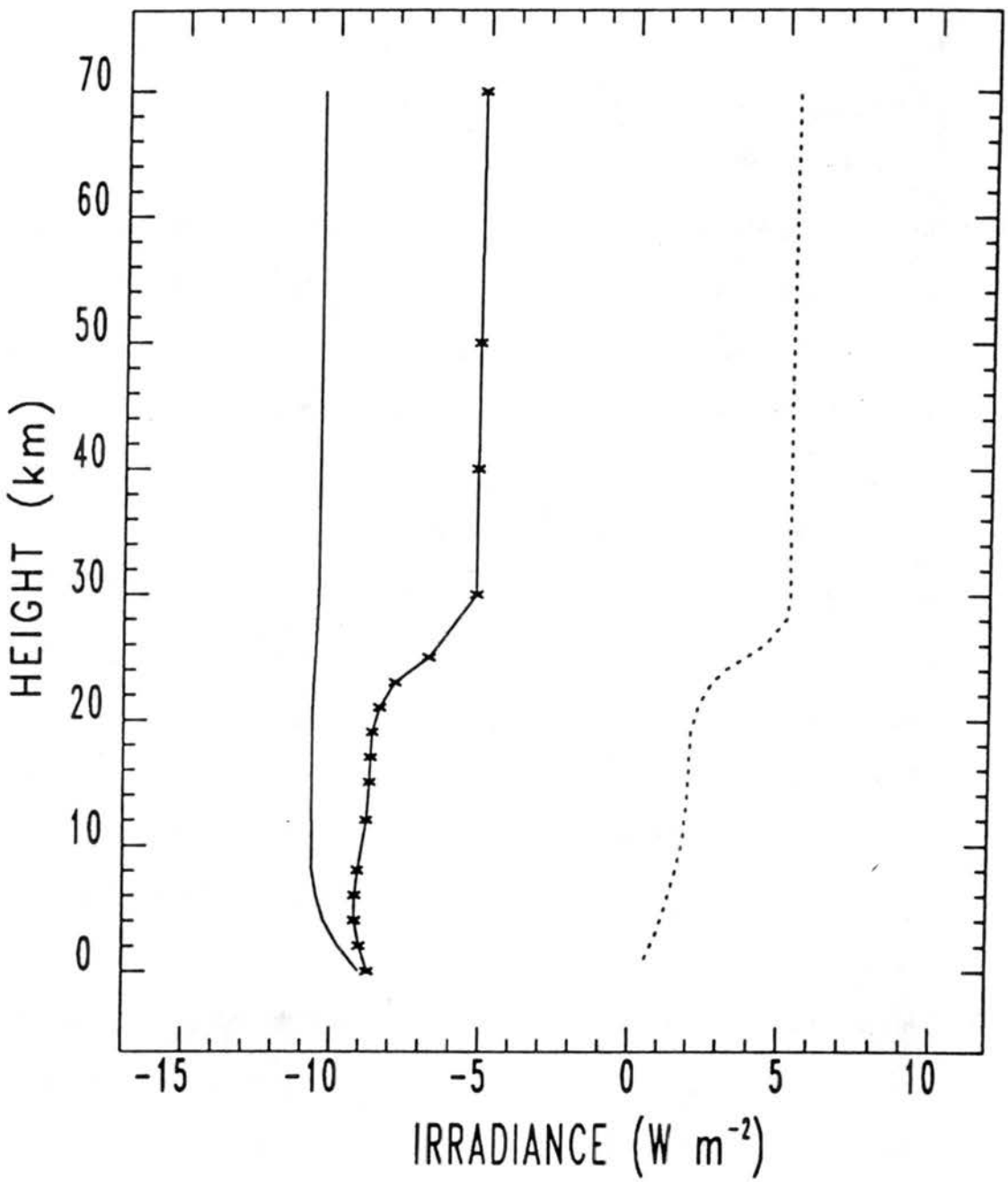

Fig. 4.7 Vertical profiles of net V: (solid - ${}_{Sn}V$), (dashed - ${}_{Ln}V$), and (x solid - ${}_{An}V$).

had suggested stratospheric warming several degrees greater than that observed, 1-3 °C. To examine the effect of observed increased stratospheric temperatures on V computed from LOWTRAN7X, the atmospheric model temperatures were increased by 2 °C within the level of the volcanic aerosol. This test case is shown in Fig. 4.8 where vertical profiles of delta V (equilibrium - instantaneous) are given. The increased downwelling IR below the aerosol cloud due to the higher equilibrium temperature in the stratosphere was 0.3 W m^{-2}, which is an order of magnitude less than the associated ${}_{La}V$.

4.5 Global Radiation Balance, Background Conditions

The global radiative model developed here, while intended to study the anomalous effects of volcanic aerosols, is a relatively complete but low resolution model of the total zonal mean radiation budget at the TOA, except clouds, which would increase outgoing LW at the TOA, were not included in the IR. Model irradiances computed for the background (volcanically undisturbed) year, 1990, were compared with observations of the zonal mean budgets for annual means as presented by Campbell and Vonder Haar [1980]. Figure 4.9 shows observed and modeled (DISORTX and LOWTRAN7X) annual zonal radiative quantities. The correspondence between the models and these observations suggests that the models did a reasonable job of simulating the global radiation budget, although the differences are important. Cloud IR effects were estimated by the difference between computed clear-sky outgoing IR and that that was necessary to obtain model radiation balance, net equal to 0.0 W m^{-2}, at the TOA. Global radiation balance was obtained (forced) by subtracting 17 W m^{-2} from the computed outgoing longwave for each latitude band in Fig. 4.9e. This implied IR cloud forcing is not necessarily accurate because all the cumulative model and observational errors were incorporated into the deduced IR cloud effects. Differences in albedo and reflected irradiance (Fig. 4.9c,b,

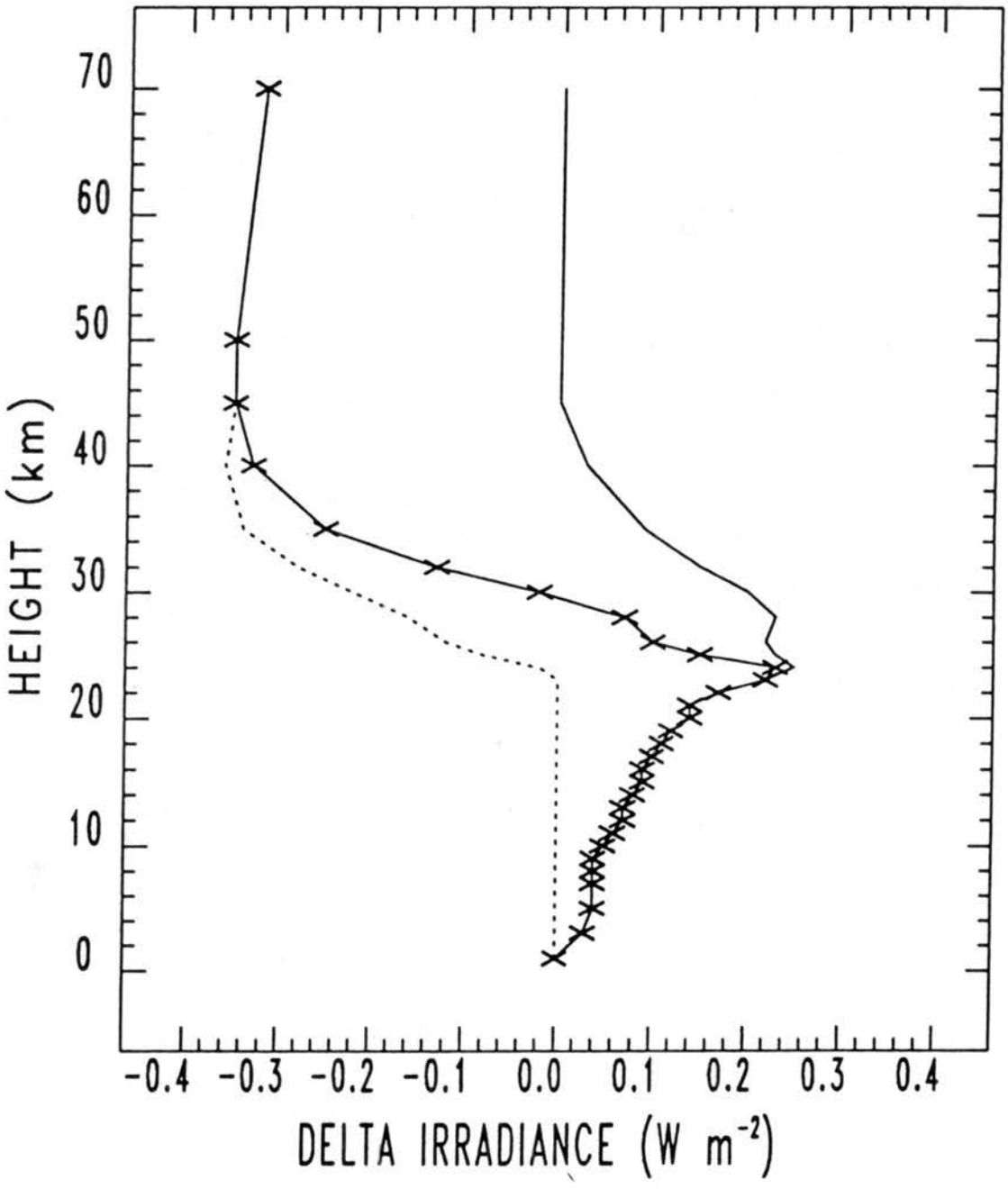

Fig. 4.8 Vertical profiles of difference between instantaneous and equilibrium IR *V*, for a 2 °C increase in lower stratospheric temperatures, (dashed - change in $_{Lu}V$), (solid - change in $_{Lu}V$), and (x solid - change in $_{Ln}V$).

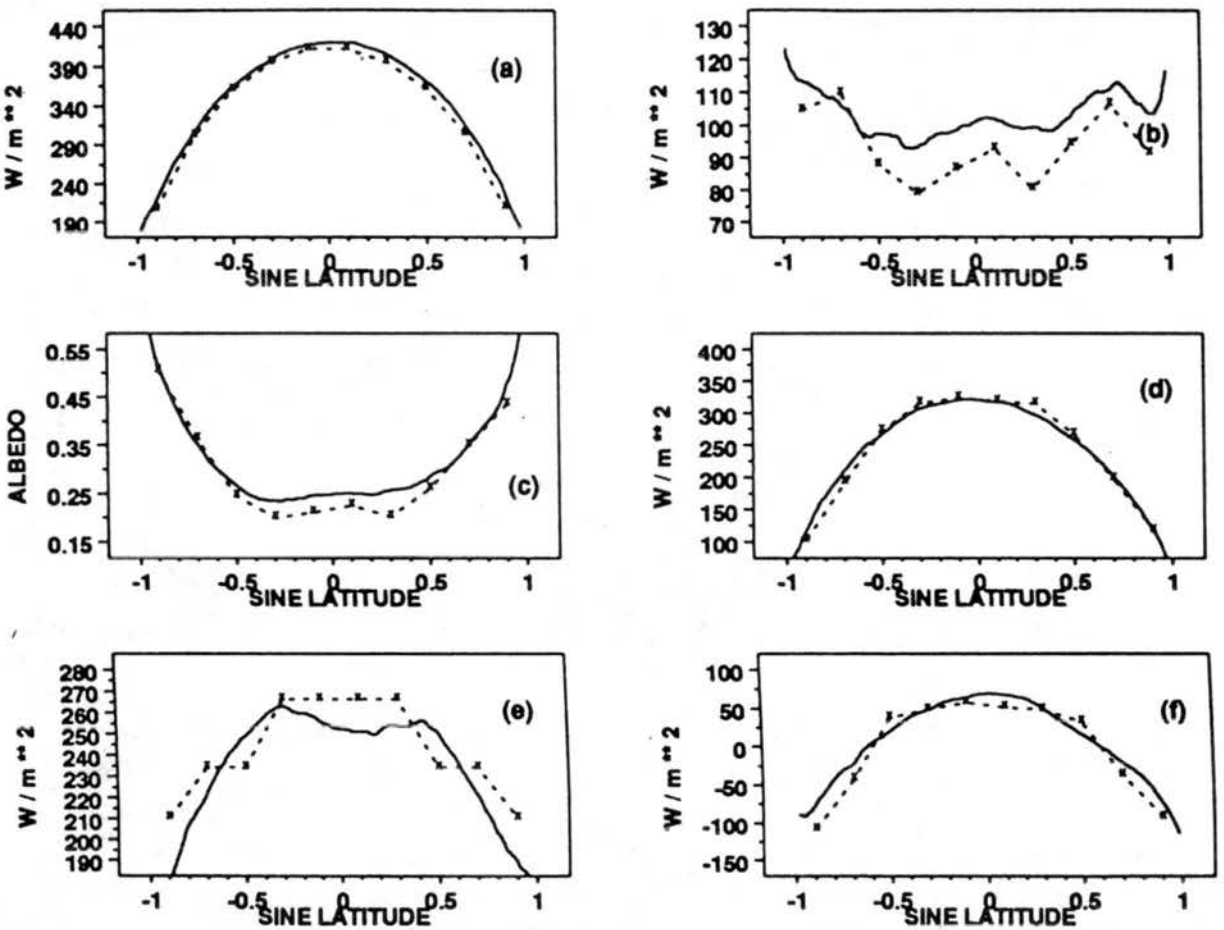

Fig. 4.9 Observed (solid) and computed (dashed) TOA zonal and annual mean radiation components: a) incoming solar, b) reflected solar, c) albedo, d) absorbed, e) outgoing IR, f) net allwave.

respectively), and as propagated into absorbed and net (Fig. 4.9d,f) are due to small inaccuracies in the parametric manner in which tropospheric reflection was introduced into DISORTX.

Differences are also seen in the latitudinal distribution of outgoing IR (Fig. 4.9d). This is due in part to model resolution, but also to an inadequate temperature profile for the polar regions. For the latitude bands of 90° to 53°, N and S, the winter and summer subarctic model atmospheres were used. The curves in Fig. 4.9d would correspond better if the winter profile had been used for all seasons. Although many minor discrepancies between the modeled and observed irradiances exist, it appears that the models have correctly incorporated some additional features not tested by ICRCCM results, such as choice of spatial and temporal variation of realistic model atmospheres and planetary albedo, and inclusion of solar geometry variations, and correct spatial and temporal averaging and integration.

4.6 Global Gridded *V* Calculations

DISORTX and LOWTRAN7X were run for the zonal/seasonal grid inputs, described in Sec. 3.2, over both 3-yr volcanic periods. Upward and downward total irradiances were computed for 33 levels in the IR and 17 levels in the solar. A background aerosol model was determined and used for each season for one year. These background values were then subtracted from the computed irradiances for the two 3-yr volcanic events. The 1990 seasonal mean stratospheric aerosol over Mauna Loa was used to represent background stratospheric aerosol conditions for all latitude bands. Computed ${}_{Sn}V_{Tr}$, ${}_{Ln}V_{Tr}$, and ${}_{An}V_{Tr}$ for the entire grid domain for both eruptions are shown in Figs. 4.10a-c and 4.11a-c. The hemispheric and global means of ${}_{An}V_{Tr}$ are shown in Fig. 4.12a,b. These results will be discussed and utilized later.

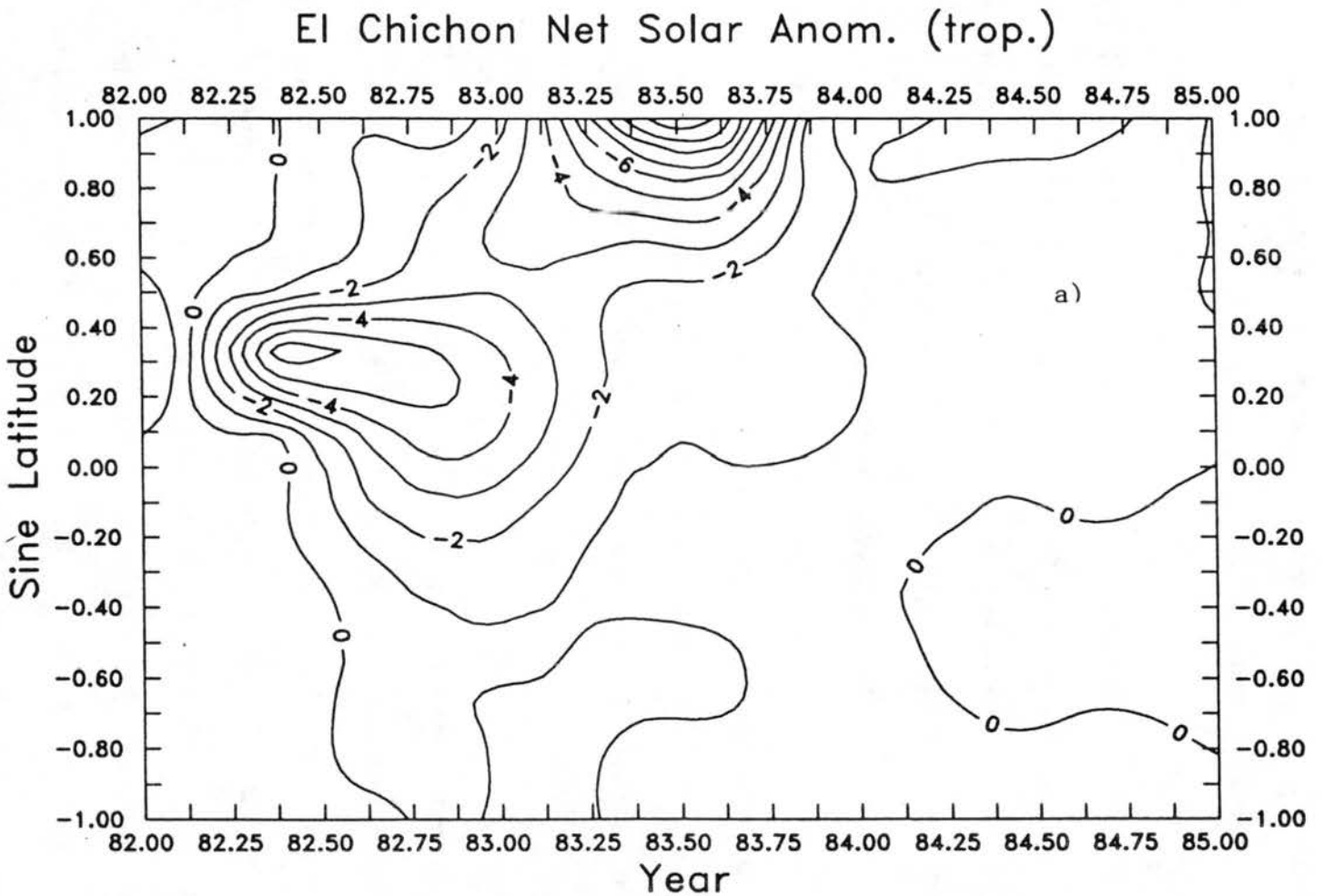

Fig. 4.10 Zonal and seasonal mean gridded and analyzed volcanic radiative forcing, in W m^{-2}, related to El Chichón: a) ${}_{Sn}V_{Tr}$, b) ${}_{Ln}V_{Tr}$, and c) ${}_{An}V_{Tr}$.

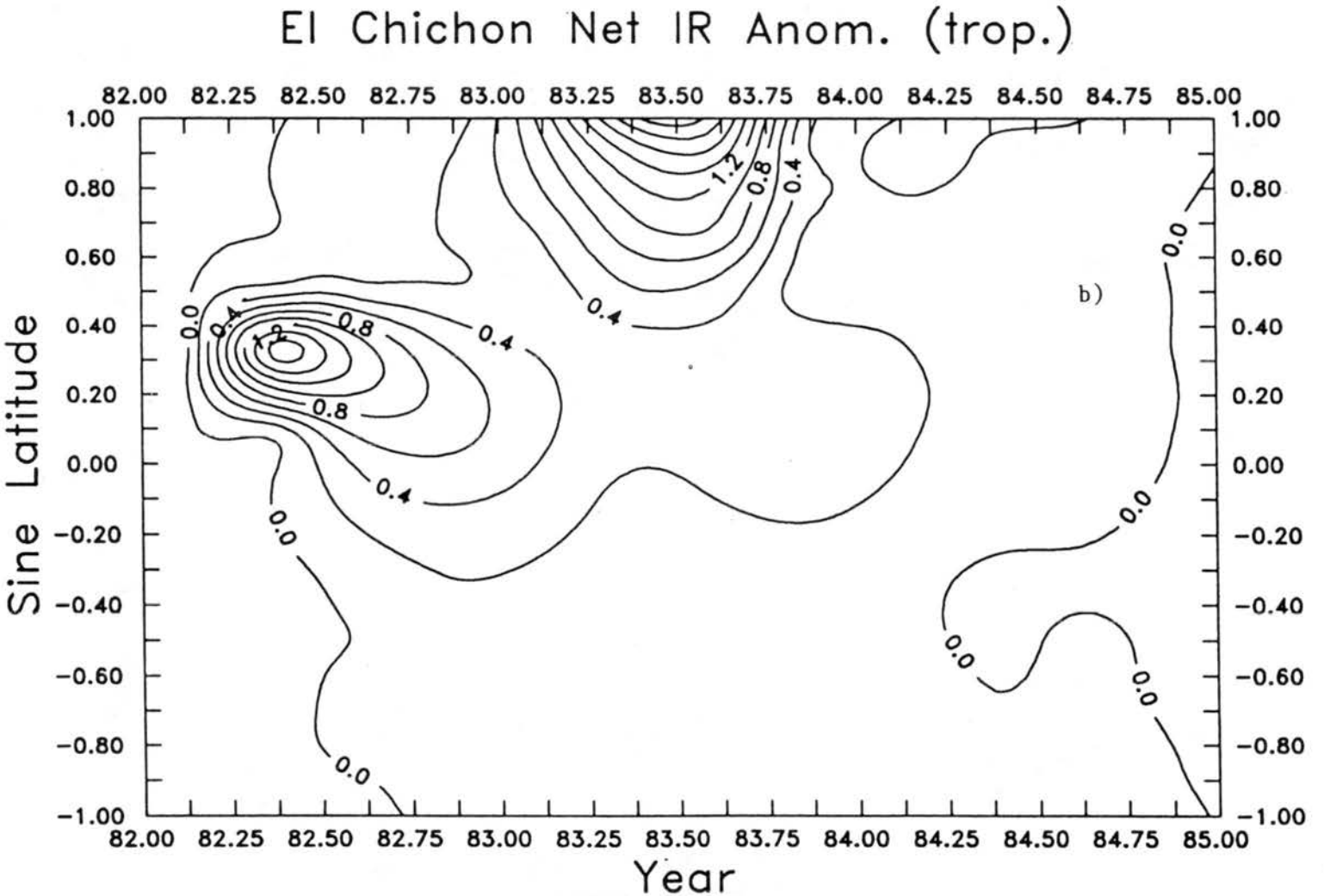

Fig 4.10b (see caption on Fig 4.10a)

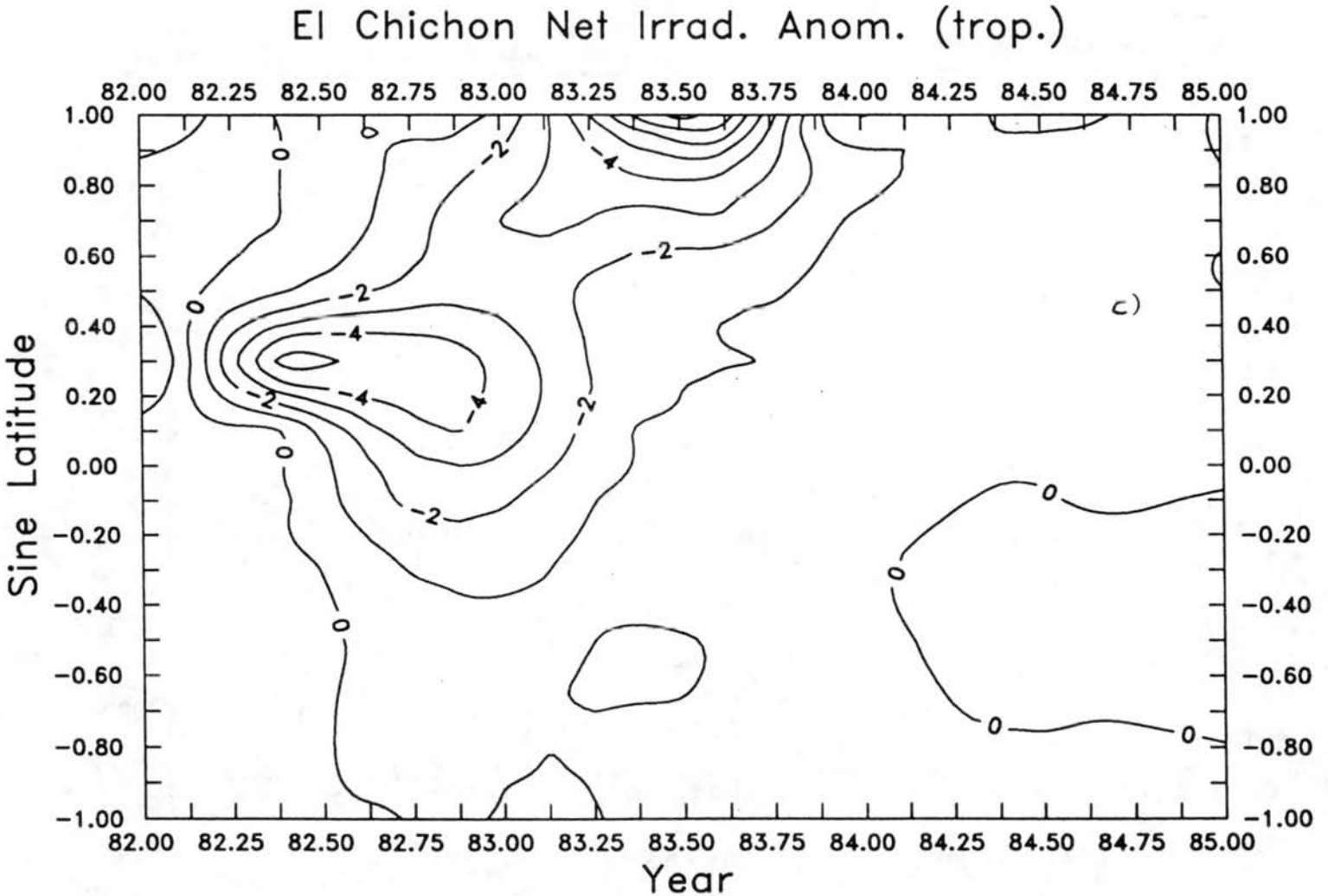

Fig 4.10c (see caption on Fig 4.10a)

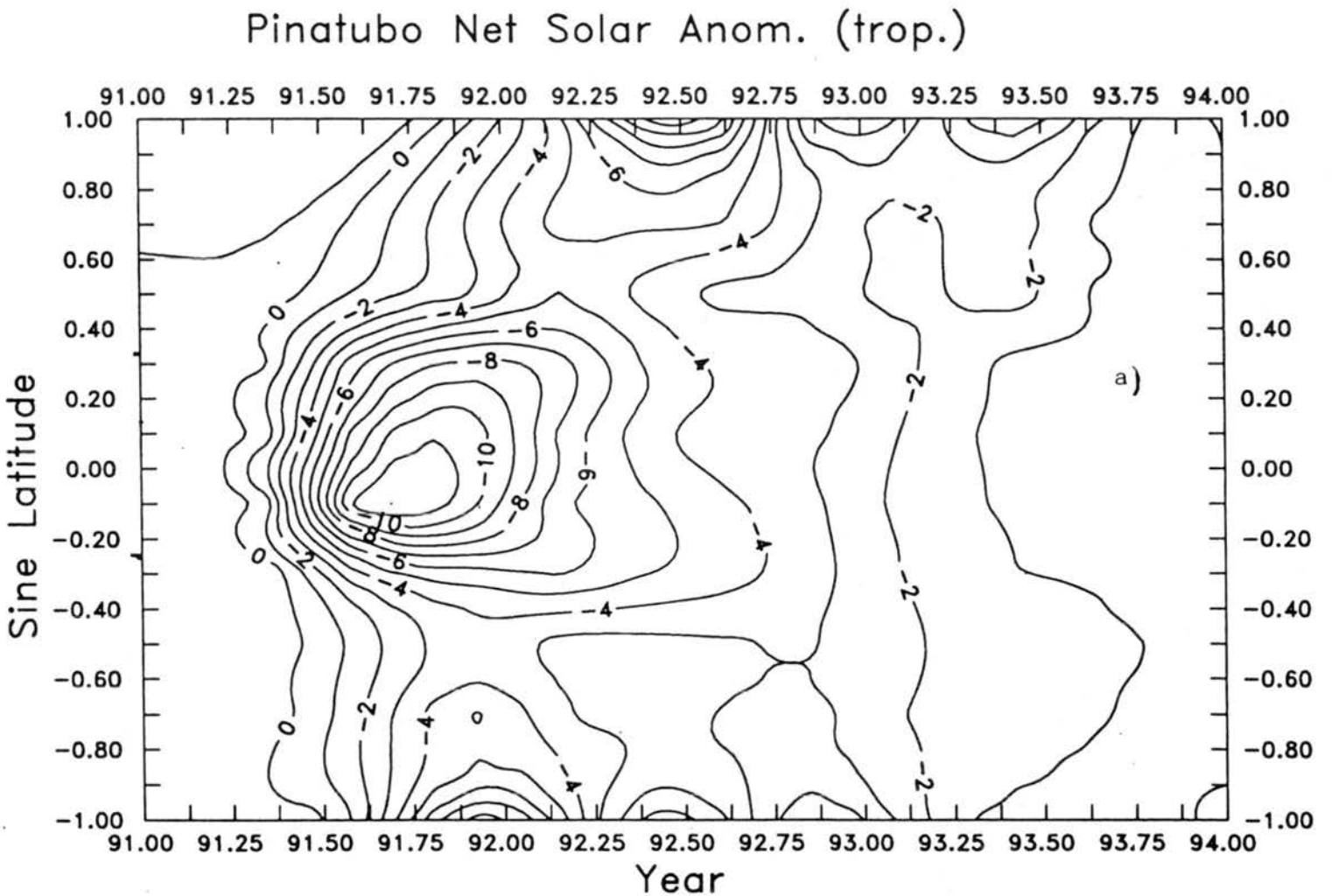

Fig. 4.11 Zonal and seasonal mean gridded and analyzed volcanic radiative forcing in W m^{-2} related to Pinatubo: a) ${}_{Sn}V_{Tr}$, b) ${}_{Ln}V_{Tr}$, and c) ${}_{An}V_{Tr}$

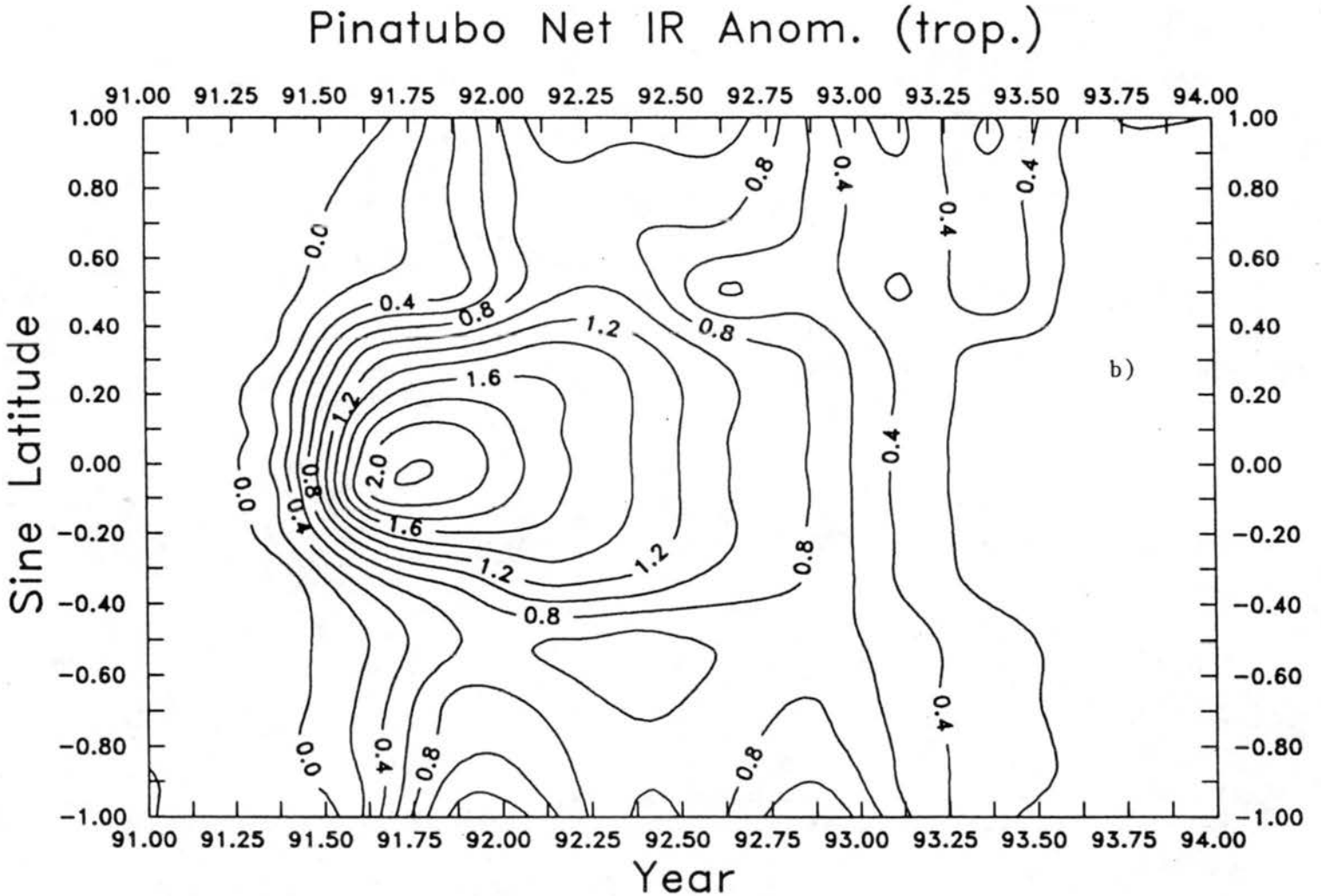

Fig 4.11b (see caption on Fig 4.11a)

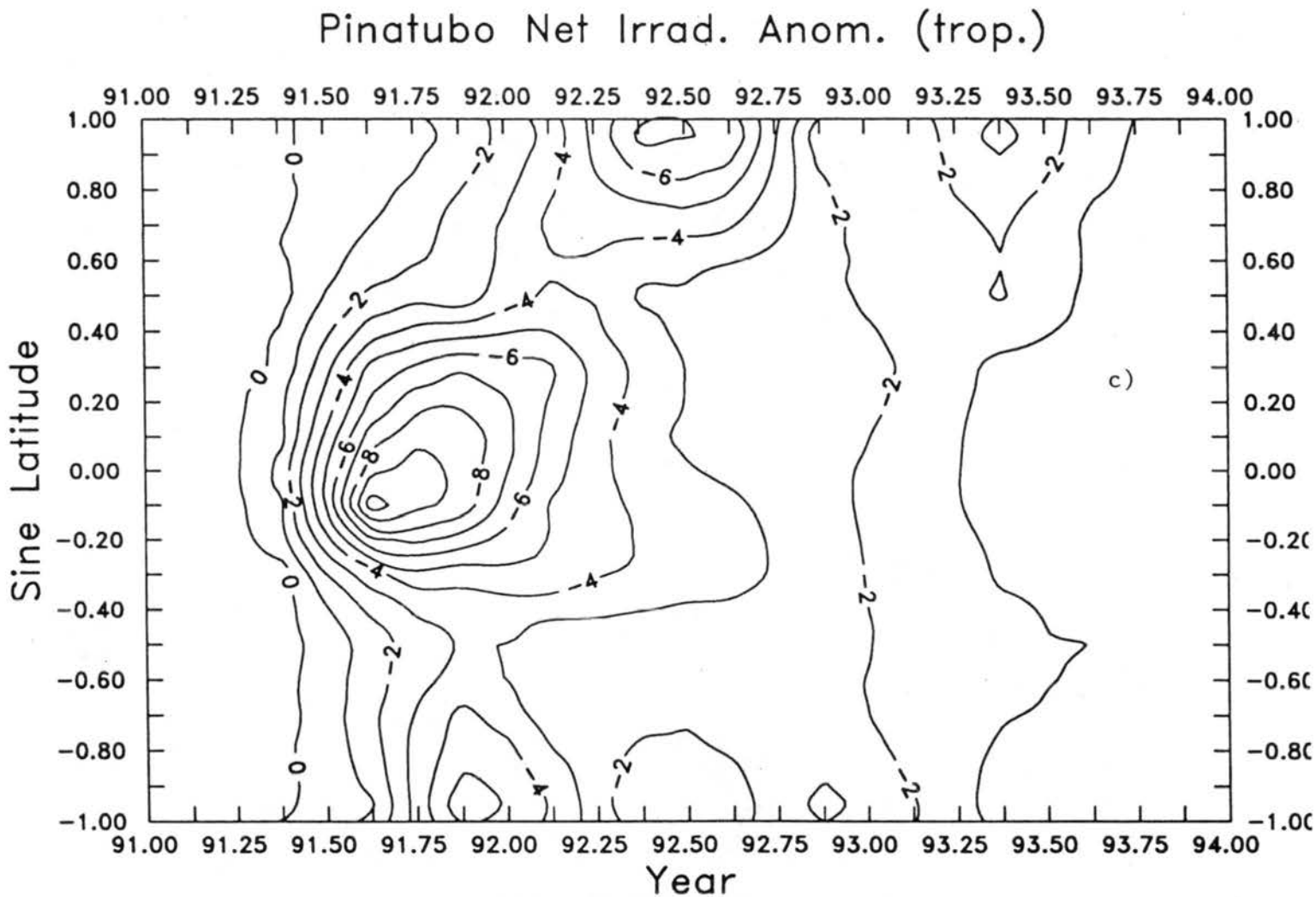

Fig 4.11c (see caption of Fig 4.11a)

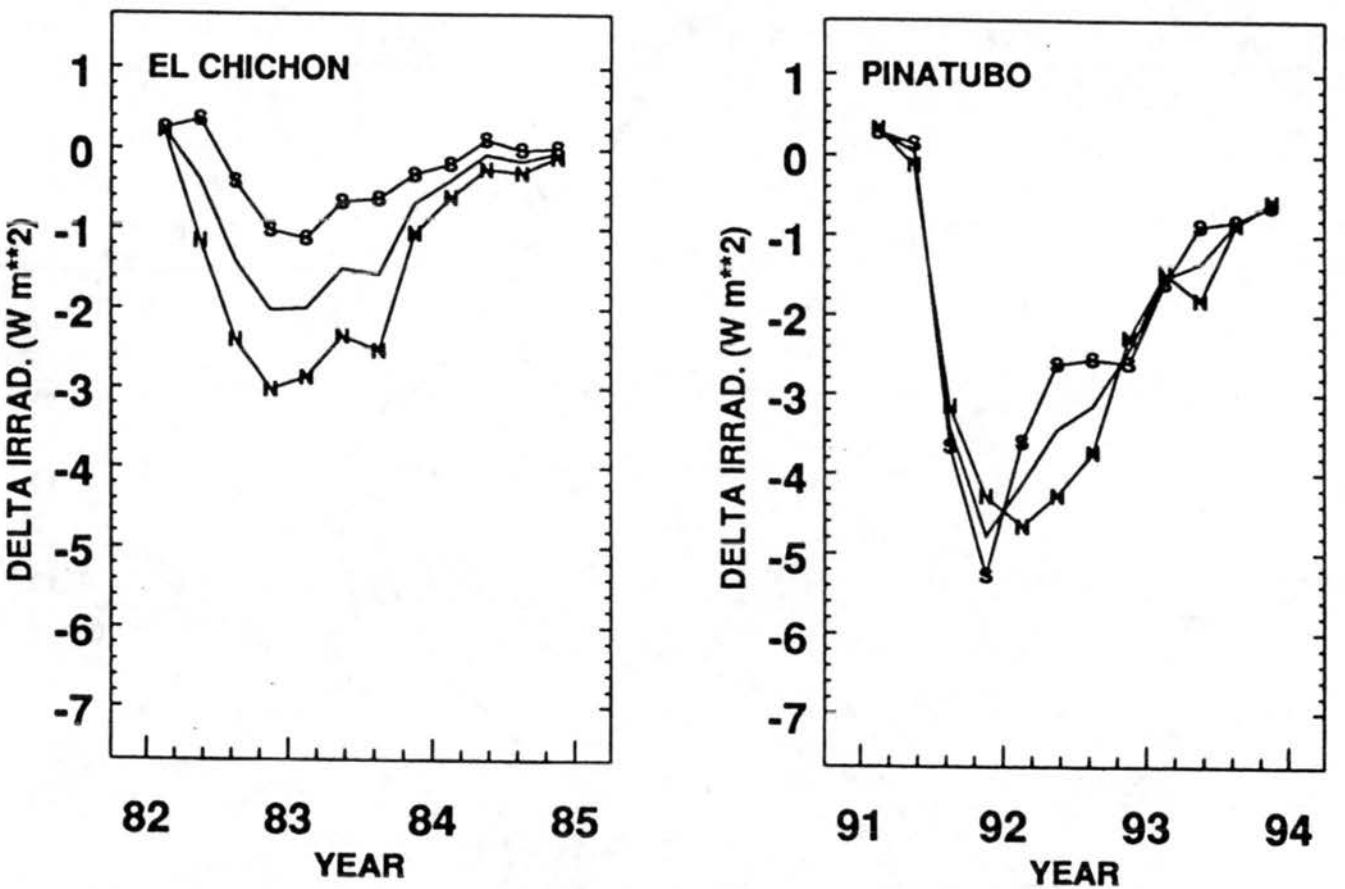

Fig. 4.12 Global and hemispheric mean ${}_{An}V_{Tr}$ computed from Figs. 4.10c and 4.11c.

4.7 Radiative Forcing Comparisons

Numerous approximations, assumptions, simplifications, interpolations, and observational input uncertainties were incorporated in the radiative transfer models. The effects of some of these were considered with the various sensitivity tests presented in Appendix D. However, typically the total uncertainty of the model cannot be easily ascertained. Implementation of the DO method, introduction of the correlated-k distributions, errors in the input information, incompleteness, and spatial representativeness, spectral integration, radiance to irradiance conversion, and possible execution flaws all contribute to potential errors in V. Previously demonstrated absolute accuracy in RT results builds confidence in the relative, or differential, accuracy. However, any errors in the introduction of volcanic aerosols to the models do not cancel. Comparison between independent observations and computations scrutinizes the complete RT model. To further investigate the possible impact of these uncertainties, RT modeled Vs were compared with previous theoretical calculations and relevant observations. These comparisons can only be made for the limited locations where measurements exist, almost exclusively at the earth's surface, or above the atmosphere. Good agreement from the few possible comparisons will be used as proxy verification of model results at other levels within the atmosphere. The quality of agreement is referenced to a percentage of V, with mean agreement to within 20% classified as good, within 10% as very good.

4.7.1 Earlier theoretical results

Previous published quantitative results that are directly related to those here are shown in Table 4.2. The following comments refer to Table 4.2. Hansen et al. [1992] presented only global mean V and used an estimated aerosol evolution. Harshvardhan [1979] considered monthly and latitudinal variations in albedo and solar geometry, similar

to the present study, but only considered a uniformly distributed aerosol and primary scattering. Lenoble et al. [1982] also considered seasonal and latitudinal variations, but obtained unreasonable solar flux anomalies using a realistic distribution of aerosol; although their technique appears correct the error was in the final step of converting

Table 4.2 Comparison between volcanic radiative forcing calculated in the current study and that published previously.

	Current	Previous
Global mean ${}_{An}V_{Tr}$	-4.8 W m^{-2}	-4.5 W m^{-2}
τ_A(500 nm)= 0.15		[Hansen et al., 1992]
${}_{An}V_{Tr}$ τ = 0.10		
Lat. = 0°, Feb.	-3.0 W m^{-2}	-2.5 W m^{-2}
60° N, Aug.	-7.0 W m^{-2}	-5.0 W m^{-2}
		[Harshvardhan, 1979]
Reflectance of El Chichon		
20° N Nov. 1982 (from above		
the aerosol) τ = 0.13		(different aerosol models)
λ < 0.83 μm	0.015	0.032 0.025 0.028
λ > 0.83 μm	0.011	0.011 0.013 0.017
		[King et al., 1984]
Δ global albedo		
τ = 0.10	0.011	0.008
		[Pollack et al., 1976]
Global mean ${}_{An}V_{TOA}$		
τ_A(500 nm) = 0.15	-4.8 W m^{-2}	-7.25* W m^{-2}
		[Lenoble et al., 1982]

* published as -23.2 W m^{-2} for τ = 0.03, but with an obvious error of factor of 16, the corrected value was then multiplied by 5 to estimate a result for τ = 0.15.

reflectance and transmission functions to flux anomalies. King et al. [1984] presented annual mean reflectance, transmittance, and absorption functions for observed and inverted size distributions following El Chichón and as a function of latitude. Of these different approaches, King et al. comes the closest to the current work, but their analysis was only for El Chichón and did not incorporate observed evolutions of the size distributions or the observed spatial distribution of optical depth. Also, King et al. did not compute fluxes but presented reflectance, transmittance, and absorption functions, which were not verified with observations. The factor of two difference between the current work and King et al. for the El Chichón cloud reflection at $\lambda < 0.83$ μm, in Table 4.2, has not been resolved.

4.7.2 Comparisons with observations

The accuracies of the computed irradiance anomalies were further evaluated by comparing them with observations. Suitable observations against which the model results can be compared were limited for several reasons discussed in Sec. 2.Observations contain errors, random and biased, but are independent of those in the RT model. Comparison conditions were often less than ideal in that different spatial and temporal scales exist. Therefore, it was important to make as many comparisons as possible between the model results and observations.

4.7.2.1 Surface-based observations

Surface-based irradiance observations have an advantage of being relatively easy to maintain over a long time-period that provides background information against which episodic events can be compared. Their major disadvantages are having a large portion of the atmosphere between them and volcanic clouds and representing only a small

portion of the global, or even regional, phenomena. Surface solar irradiance records from four globally diverse locations are next examined for clear-sky ${}_{sd}V_S$ and compared to DISORTX results.

4.7.2.1.1 Mauna Loa

The downward solar irradiance time series from MLO, was described in Sec. 2.5.1. MLO data were compared to site-specific RT model output. Specific local conditions used for this analysis were the observed $\tau_A(\lambda)$, solar zenith angles corresponding to the instantaneously observed irradiances, albedo, and actual altitude. Monthly means of $\tau_A(\lambda)$ were used along with estimated surface reflectance.

Observed and computed downwelling clear-sky solar irradiance are shown in Fig. 4.13 for a solar zenith angle of 60° at MLO. The absolute magnitude of the irradiance was normalized to the 1990 background period with the mean ratio for the obs/model = 0.956 for that period. Two modeled results are shown, one using the zonal mean $\tau_A(\lambda)$ of the global grid and the other for the locally observed $\tau_A(\lambda)$. There was a small improvement in the agreement when using local observations. Mean differences between the observations and models (obs. - model, after background normalization) for both El Chichón and Pinatubo, excluding the 1990 normalization period, is given in Table 4.3. There is a total mean difference of 0.4 W m^{-2} with a standard deviation of 7 W m^{-2}. The large standard deviation was due, in part to variability in the observations due to unmodeled water vapor

Table 4.3 Differences between modeled and observed ${}_{sd}V_S$ at Mauna Loa.

Tau conf.	Period	Mean Diff. W m^{-2}	S.D. W m^{-2}	N	95%
Zonal	EC	-2.5	7.91	3	4.8
Zonal	Pina	0.9	6.3	12	4.0
Local	EC	0.0	6.7	13	4.1
Local	Pina	0.2	6.0	12	3.8

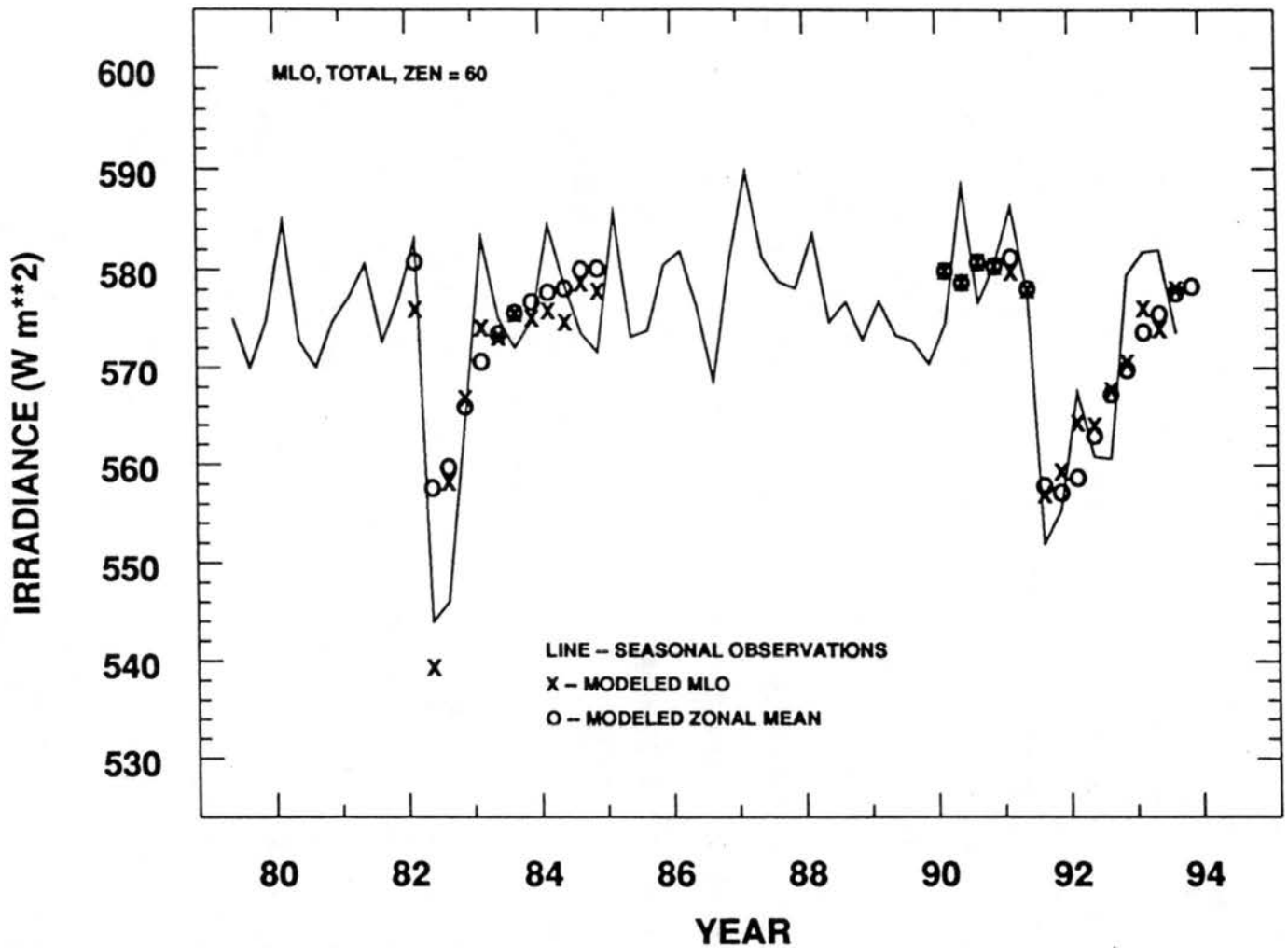

Fig. 4.13 Seasonal mean observed and modeled downward solar irradiance at Mauna Loa for a solar zenith angle of 60°. Xs are for model output using locally observed $\tau_A(\lambda)$, Os for $\tau_A(\lambda)$ from the zonal mean.

variability. Better agreement is seen after Pinatubo, although very good agreement is seen for both.

Further investigation of the volcanic aerosol influence in the MLO observational data was possible because direct beam and diffuse solar irradiance were measured and modeled separately. These two quantities were used by Coakley [1981] to investigate the ratio of the change in diffuse to the change in direct solar irradiance for a volcanic episode relative to background conditions. This ratio (ε) is an extinction efficiency in that it shows the loss of total downward irradiance relative to that removed from the direct beam. Therefore, ε is primarily dependent on the scattering phase function ($P(\theta)$) and single scattering albedo (ω_o), and provides a rare opportunity to verify their combined effect. Figures 2.11b,c show the separate monthly mean direct and diffuse components that were seasonally averaged and summed to give total irradiance shown in Figs. 2.11a and 4.13. Modeled and observed monthly mean ε following El Chichón and Pinatubo are given in Fig. 4.14 using 1990 as the background or reference period from which the changes in diffuse and direct were computed. The value of ε is negative because as diffuse increases due to aerosols, the direct decreases. Observations in Fig. 4.14 have been fitted with a running smoother to remove month-to-month variability arising from short term variations in water vapor and tropospheric aerosol. The modeled and observed ε are nearly identical, -0.82 ± 0.01, for both volcanoes in the months immediately following both eruption. Then, about 6 months after El Chichón and 10 months after Pinatubo there was a departure toward -0.9 with El Chichón showing a larger swing. The verification immediately following the eruptions suggests that the combination of $P(\theta)$ and ω_o was adequately determined and introduced into DISORTX, at least initially following

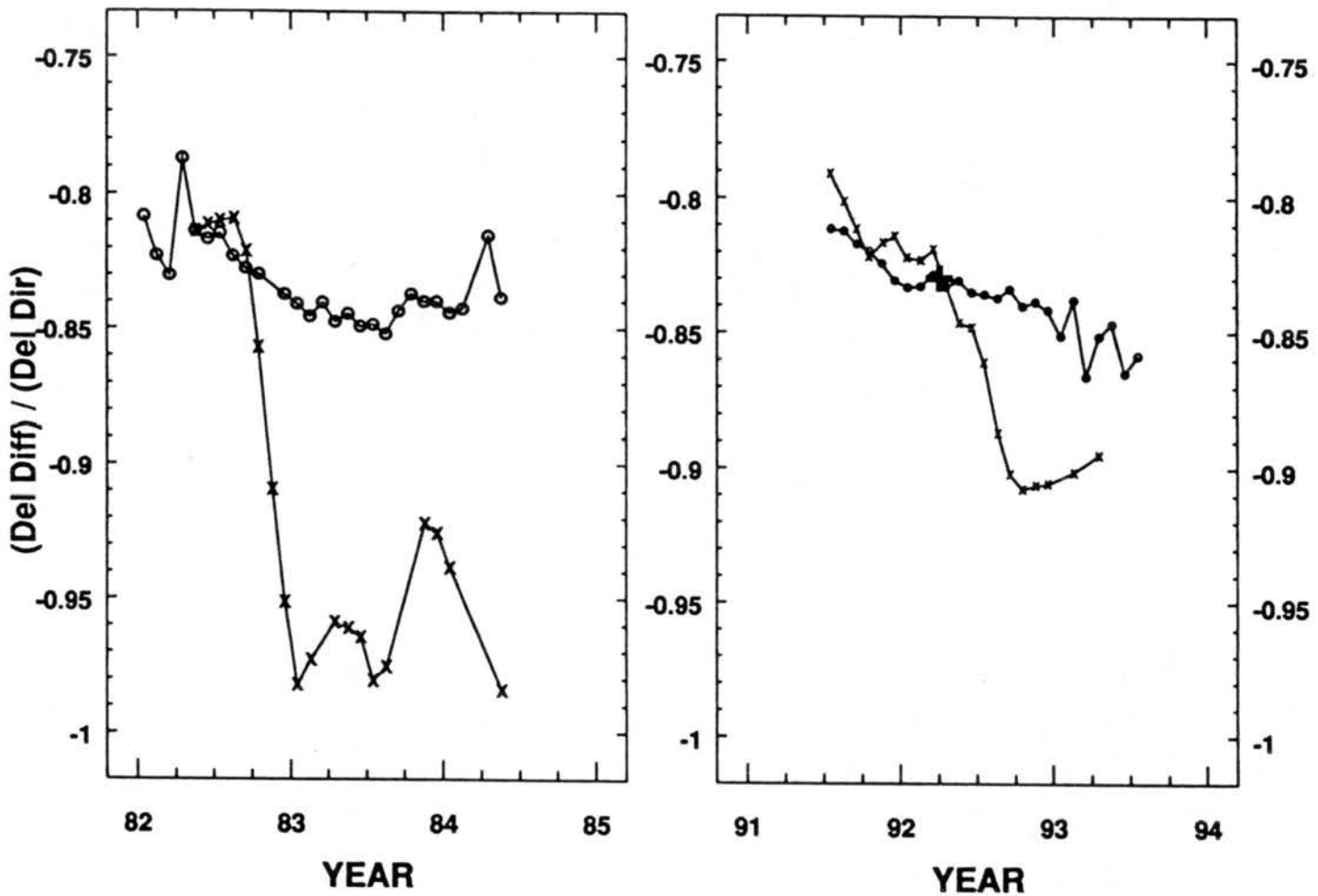

Fig. 4.14 Observed (circles) and modeled ("x"s) ratios of change in diffuse to change in direct solar irradiance, ε, at Mauna Loa, Hawaii. Bold "+" in 1992 is for Pueschel et al. [1994] March 22 special case.

these eruptions when τ_A and V were maximum. Possible explanations for the divergence of observations and models in Fig 4.14 are discussed in Sec. 5.1.4.

4.7.2.1.2 American Samoa

Following Pinatubo, SMO was just south of the maximum in optical depth and a notable signal in the pyranometer record exists (Fig. 2.12). Unlike MLO, $\tau_A(\lambda)$ data were not acquired so comparisons between observed and calculated ${}_{Sd}V_S$ were made using the global grid optical depth. Both observed and DISORTX results are shown in Fig. 4.15. Two sets of DISORTX outputs are given, one for the zonal band containing SMO (7) and the next nearest (6). These two results bracket the observations and an average of the two would be in good agreement with the observations. This is an example of where a higher spatial resolution model would be more appropriate.

4.7.2.1.3 South Pole

Two site-specific model results were used for comparison at SPO, one for the $\tau_A(\lambda)$ from the global gridded data and one where grid optical depths were scaled up to equal the locally observed wideband τ_A. Observed and modeled solar irradiances near summer solstice are given in Fig. 4.16, after model results were normalized to the observed pre-eruption levels. The apparent Pinatubo ${}_{Sd}V_S$ is -22 W m^{-2} in both the model and observations. For the results given in Fig. 4.16, locally observed τ_A were used and very good agreement is seen. South Pole gridded aerosol optical depths were approximately one-half those locally observed. It was not expected that SPO would necessarily represent the entire southern most latitude band.

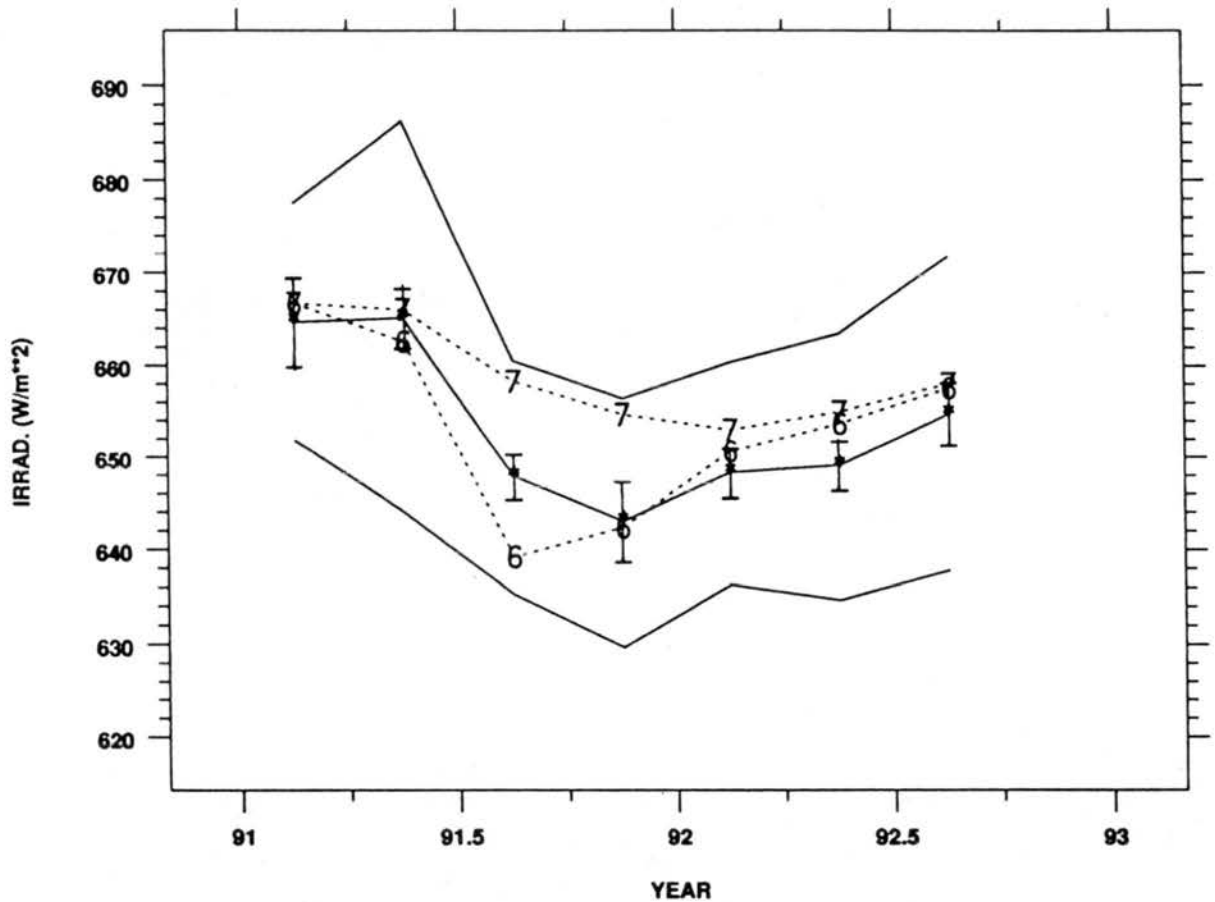

Fig. 4.15 Seasonal mean measured and observed clear-sky surface solar irradiance for American Samoa at a solar zenith angle of 45°. Solid lines a mean and ±1 standard deviation, the vertical bars on the observed mean is ±2 standard error, dashed lines are computed for zonal bands six and seven, nearest Samoa's latitude. The modeled values are normalized to pre-eruption conditions. The $\tau_A(\lambda)$ used was from the global grid.

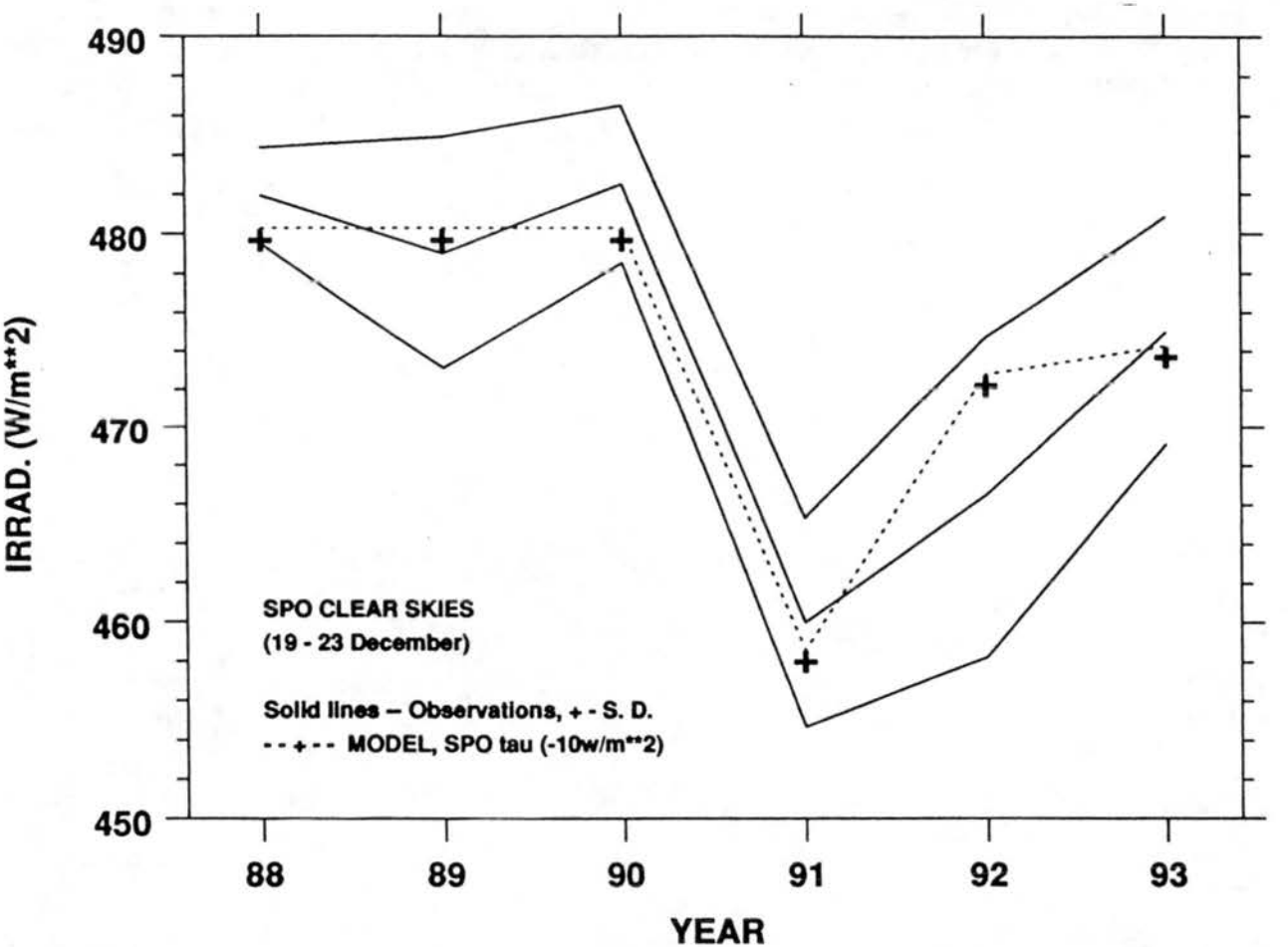

Fig. 4.16 Observed and modeled surface clear-sky solar irradiance from South Pole, 19-23 December for 1988-1993. Solid lines are observed means ±2 standard deviations, + with dashed lines are modeled for solar zenith angle equal 66.5° and locally observed midvisible τ_A.

4.7.2.1.4 Boulder

Further corroboration between modeled and observed ${}_{Sd}V_S$ following Pinatubo is noted in a clear-sky record from Boulder (Fig. 2.17). The net difference between the mean of the observations and models for the nine seasons following the eruption of Pinatubo was 0.8 (s.d. = 7) W m^{-2}. The large standard deviation, similar to MLO, was likely due to water vapor and tropospheric aerosol variations not included in the model. Global zonal $\tau_A(\lambda)$ were used and again the agreement was very good.

4.7.2.2 Satellite observations

Comparisons with satellite observations of V_{TOA} were accomplished by using the TOA irradiance computed by the models. Because of several limitations of the satellite data mentioned previously, comparisons with the model were not conclusive, but were included in the following for lack of other TOA observations. Figure 4.17 shows the DISORTX and LOWTRAN7X zonal mean TOA anomalies by season after El Chichón. Ardanuy and Kyle [1986] report an observed ${}_{Sn}V_{TOA}$ of -8 to -10 W m^{-2} about one year after the El Chichón eruption in the high northern latitudes. This corresponds to Fig. 4.17 panels 83 2 and 83 3 where a value of -8 W m^{-2} is seen for high northern latitudes, which also was the maximum for the El Chichón event. Lower latitude signals of comparable magnitude were seen in the model results but were not detected by Ardanuy and Kyle because of clouds, particularly with the enhanced cloudiness related to the 1982/83 El Niño. This suggests that while Ardanuy and Kyle were only able to clearly distinguish the maximum high-latitude volcanic forcing in their analysis, it was in good agreement with the presently modeled forcing.

Figure 4.18 shows the DISORTX and LOWTRAN7X zonal TOA anomalies for 1991 through 1993. The 91 3 and 91 4 panels in Fig. 4.18 correspond to satellite observations

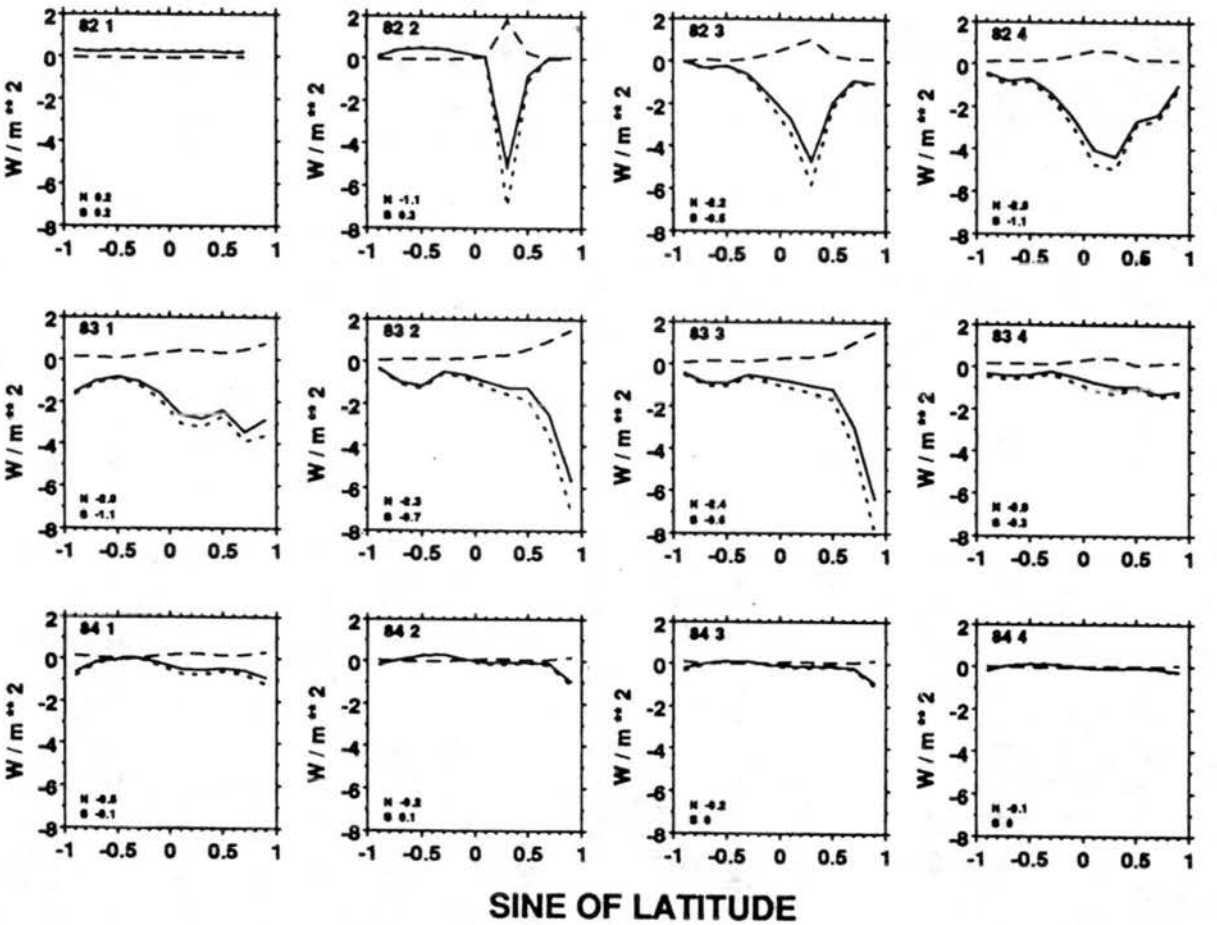

Fig. 4.17 Zonal mean computed V_{TOA} by season for El Chichón, solid line - ${}_{An}V_{TOA}$, short dashed line - ${}_{Sn}V_{TOA}$, and long dashed line - ${}_{Lu}V_{TOA}$. In the upper left of each frame is year and season (YR-S). The north (N) and south (S) hemispheric mean ${}_{An}V_{TOA}$ (W m^{-2}) are indicated in the lower left corner of each frame.

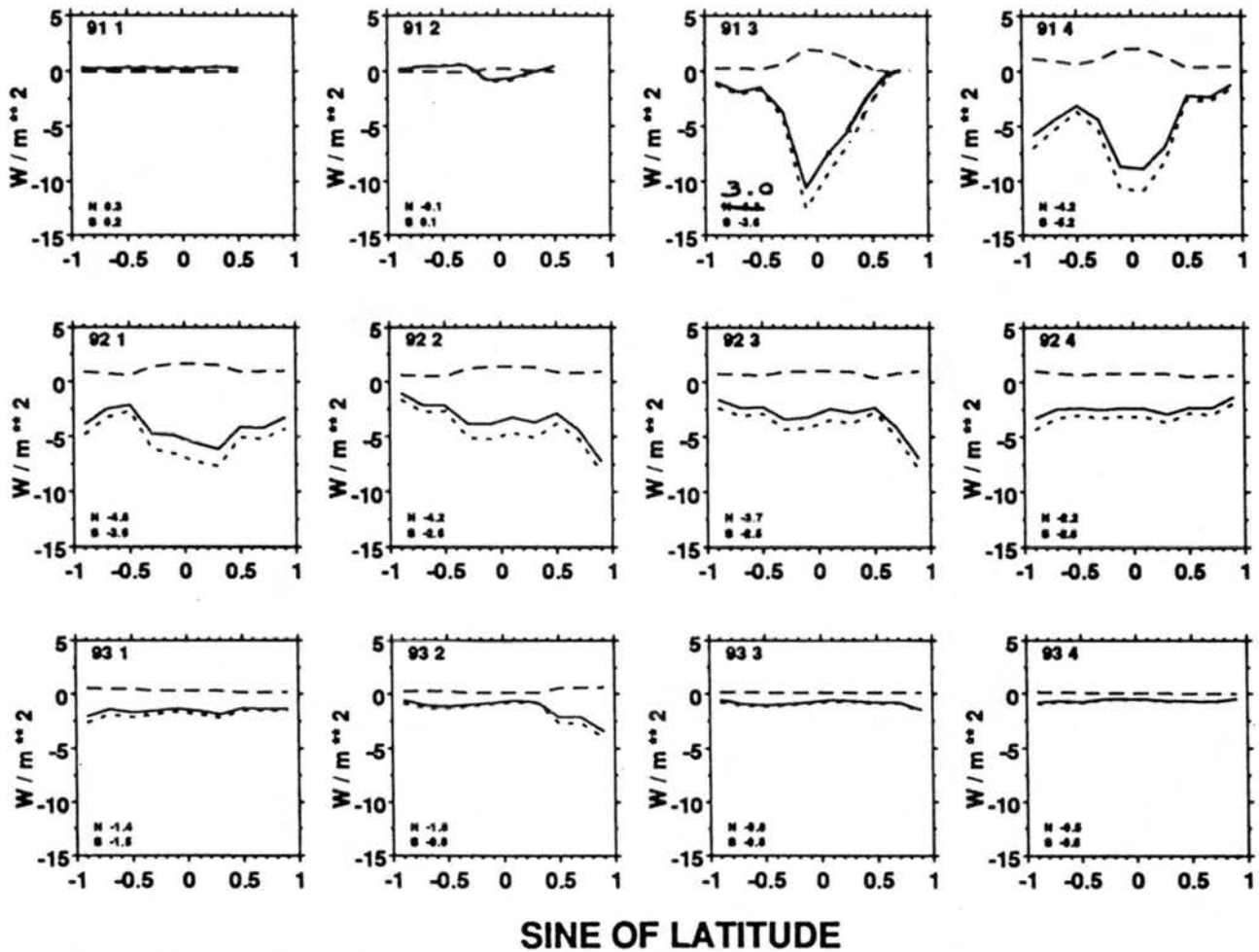

Fig. 4.18 Same as Fig. 4.21 except for Pinatubo.

between 40° N and 40° S in Fig. 4 of Minnis et al [1993]. The maximum ${}_{Sn}V_{TOA}$ is just over -10 W m^{-2} just south of the equator in Fig. 4.18 and Minnis et al.'s Fig. 4. (Note a sign convention difference exists between the two Figures.) There is good to very good agreement between the two figures for ${}_{Sn}V_{TOA}$. ${}_{Lu}V_{TOA}$ shows general agreement in magnitude and distribution, with the satellite ${}_{Lu}V_{TOA}$ being 2-3 W m^{-2} (>50%) larger than model values in the tropics. This is consistent with Minnis et al.'s observation that some tropical clouds appeared enhanced, in extent and brightness, after the eruption. The overall comparison between the modeled and detected satellite signals is within about ±2 W m^{-2}, which can be considered good agreement considering ${}_{An}V_{TOA}$ in the first year after the eruptions.

4.8 Atmospheric Heating Rates

Vertical profiles of computed IR and Solar flux divergence anomalies caused by the volcanic aerosol, converted to radiative heating rates using usual procedures [e.g., Liou, 1992], are shown in Fig. 4.19. Striking IR heating was seen in the aerosol layer, qualitatively consistent with observations [Labitsky and McCormick, 1992; Christy and McNider, 1994]. Atmospheric heating rates do not reveal the major tropospheric climatic effect because the greatest magnitude change in radiative heating is at the earth's surface. The loss of net downward radiation to the troposphere and surface represents the climatic forcing on tropospheric temperature.

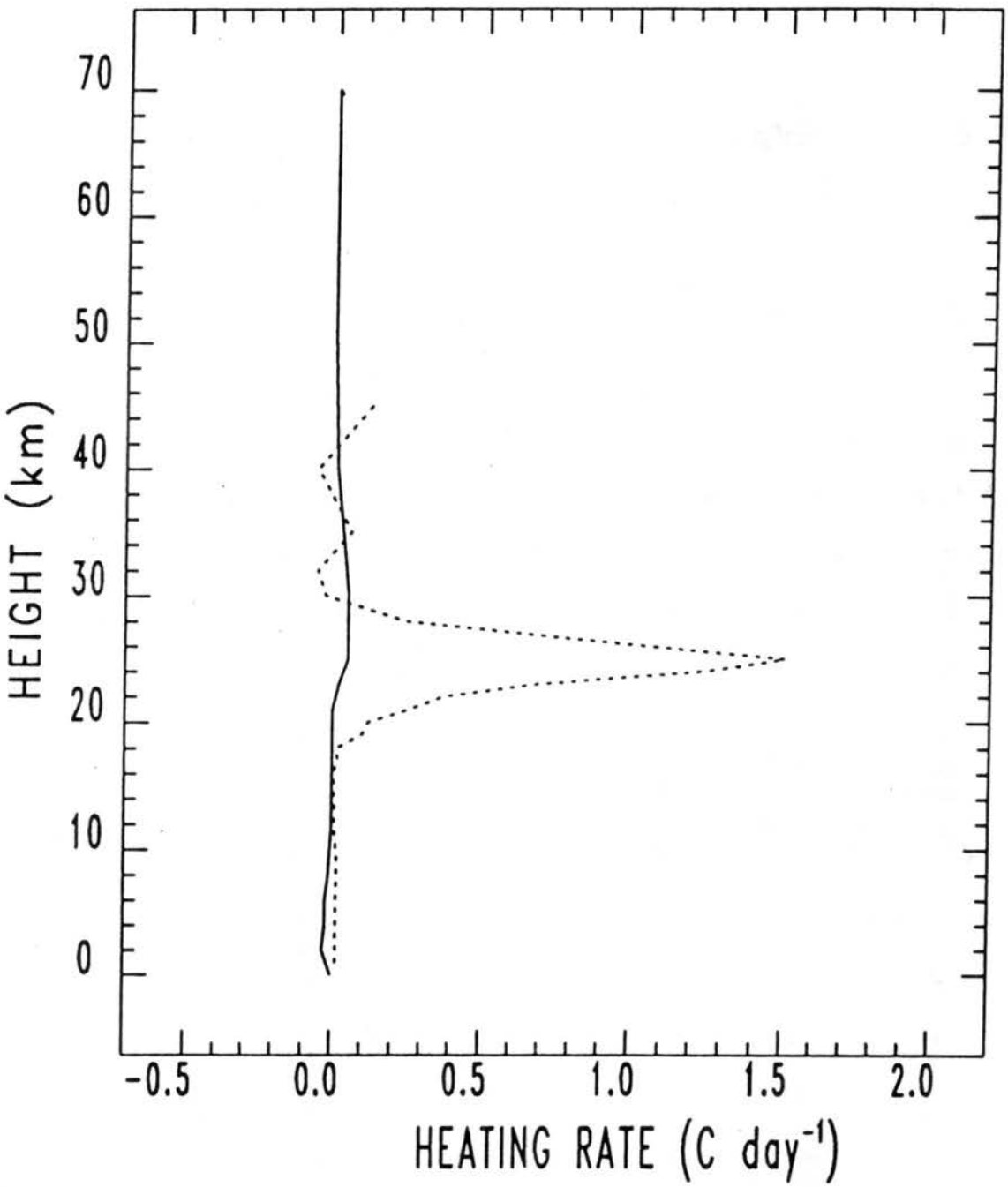

Fig. 4.19 Vertical profile of solar and thermal radiative atmospheric heating rates for volcanic stratospheric aerosol, Dashed line - IR, Solid line - SW.

Chapter 5. Verification, Discussion, Tropospheric Temperature Model, and Parameterizations

5.1 Discussion on the Confirmation of Computed *V*

Irradiance anomalies computed here substantiate the major conclusions of two decades ago [Pollack et al., 1976; and others]. That is, for volcanic aerosols above the troposphere, the upward reflectance of incident solar radiation by the aerosol layer dominates all other radiative processes, solar and IR, relating to the cloud and causes a net loss of radiant energy by the troposphere. Sensitivity studies in Appendix D suggest this to be true beyond the range of uncertainty introduced by possible errors in the models or their inputs. This is because realistic ranges of model input parameters did not produce results contrary to the basic finding of dominating reflected-solar effects, nor did the tested range of model configurations. Since the nearly complete rigorous RT model calculations were made with extended spectral, vertical, and directional resolution as well as being globally representative, only substantially different aerosol optical properties could produce a contrary result. Substantially different aerosol properties would be inconsistent with the aerosol observations from many different sources reported and used here. Primary remaining questions are how accurately can *V* be computed using available input information, and how well do these models agree with observations?

The calculation of V and limited successful comparisons to observations not only help to verify RT theories and assumptions but also encourages further investigation of expected atmospheric responses to the forcing. Independent validation of both RT

modeled and observed irradiances is first desirable to insure meaningful comparisons between the two. It is not considered necessary to verify basic elements of RT theory. However, the difficulty in obtaining adequate model input information and numerous assumptions as well as approximations leads to much uncertainty in computed V. Likewise, observational errors in the confirmation data sets may be significant. With potentially large errors in both models and observations, the merit of comparing the two must be established. The current work strives to do this by independent verification of models and observations to the extent possible, and then by comparing to each other for further mutual validation.

5.1.1 Independent verification of model calculations

DISORTX and LOWTRAN7X agreement with selected ICRCCM cases was within the range of ± the rms error of the mean ICRCCM results over a wide range of cases (Table 4.1 and discussion in Sec. 4.1) The use of RT models for computing global zonal means requires additional implementation involving daily mean solar zenith angles, areal and temporal averaging, and tropospheric and surface albedo considerations, features not included in the ICRCCM cases. These additional features were tested, in part, by favorable comparisons (Sec. 4.5) to previously published global zonal mean TOA observations.

Multiple scattering was identified as an important process and was specifically included in the analytical solutions to the RTE inherent in DISORTX. Comparisons to ICRCCM aerosol cases were not accomplished since ICRCCM was inconclusive with respect to aerosols. Aerosols are routinely included in LOWTRAN7, but the aerosol used here was a "user defined" case that cannot be readily validated against standard LOWTRAN7 results. Therefore, the accuracy of the complete introduction of aerosols

into the RT models was not independently confirmed. However, individual aspects of including aerosols in the RT models were substantiated as follows.

Mie scattering theory and associated assumptions, were used extensively to incorporate aerosols into the RT models. The assumption of sphericity was made throughout. Limited direct observational evidence has shown that nonspherical particles make up a very small portion of the cloud after a few months. Remaining nonspherical particles were coated with H_2SO_4 [e.g., Sheridan, 1992; Pueschel et al., 1994] and tend toward spherical shape. Similarly, there was the assumption used throughout the work that the refractive index of the volcanic cloud was that of H_2SO_4 in 75% solution with water. Several in situ samples of volcanic aerosol indicate that the material was predominantly H_2SO_4. It was shown in Appendix D that small variations in the % solution did not have significant impact on V.

Mie theory for single particles had to be applied to aerosol populations. MIEV0X was implemented to accomplish this and was tested by comparing various computed aerosol populations' (cm^{-3}) optical properties with those computed by Deirmendjian [1969], as shown in Table A.1. The assumption of noninteraction between individual particles can become invalid for long paths and high aerosol concentrations. While a modeled vertical column could be divided into enough segments so that this assumption would always be true, there was no vertical resolution in the observed $\tau_A(\lambda)$ data used here. The noninteraction assumption was made for size inversions over the entire stratospheric column. Submicron particles in the stratospheric column may approach a limiting condition where the noninteraction assumption may not be completely valid, but was not specifically further investigated here.

Uncertainty and limitations of Mie size inversions used in this study are discussed in Appendix A (Sec. A.2.3) and Appendix D (Sec. D.2). Some resulting size distributions

were compared to other in situ observations. This analysis was not ideal because of the lack of spatial and temporal coincidence, which is not possible under even the most ideal real conditions. Figure 2.10 shows some correspondence in size distributions obtained from different techniques, but not in detail. The effect of the difference between in situ and nearby inverted size distributions was investigated by running otherwise identical model inputs with each type of distribution. There is virtually no difference in the resulting *V* (Fig. 5.1). Another concern was the range of size inversion results possible from a single set of $\tau_A(\lambda)$ inversion inputs. Again, RT model calculations were carried out using many different size distributions with insignificant effects in either the solar or IR *V*, Table 4.2. The large particle mode (r >1.0 μm) investigated by King et al. [1984] was not indicated in data assembled here. The smaller radius second mode at 0.6-0.7 μm reported by Pueschel et al. [1994] dominates but only seems to exist at the bottom of the stratospheric layer. This larger mode does not appear to substantially alter the total column effective size range. A second and larger mode was seen by Pueschel et al. in the size distributions used in this study but not with the dominance of that seen in the lower portion of cloud. The size distributions used here were forced to dn(r)/dlog(r) = 1 at r ≥1.7 μm, consistent with in situ observations of no particles larger than 1.5 μm. This was to insure Mie inversions did not produce erroneous large particles.

The modeled IR irradiances used aerosol optical properties obtained from Mie calculations weighted heavily by the large particle end of the aerosol size distribution, which was not well determined. This was because few observations of $\tau_A(\lambda)$ at wavelengths greater the 1 μm were obtained and utilized in the size inversion process. Observed and computed τ_A(>4.0 μm) are shown in Fig. 2.8 and suggests that the values computed and utilized in this study are correct to within the range of those observations. Using that range of τ_A(>4.0 μm) in the RT models causes a < 1 W m^{-2} difference in the

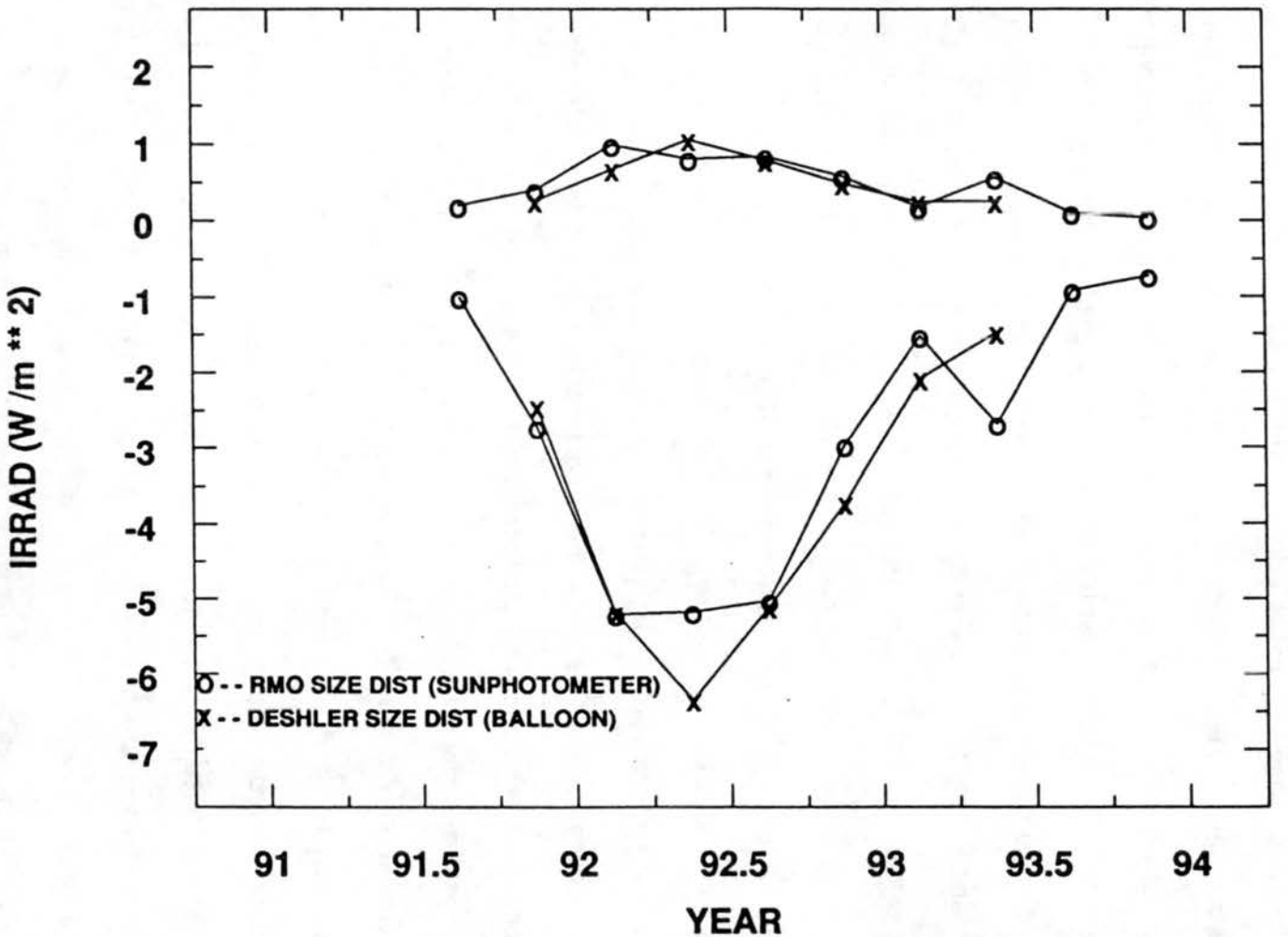

Fig. 5.1 Time Series comparison between V_{Tr} computed with balloon measured aerosol size distribution, -X-, and inverted from sunphotometer $\tau_A(\lambda)$ observations, -O-. Upper two curves are for ${}_{Ln}V_{Tr}$ and lower two for ${}_{Sn}V_{Tr}$.

${}_{Ln}V$, assuming a linear response in ${}_{Ln}V$ to observed $\tau_A(\lambda)$. Table 4.2, which shows the effects of widely differing numbers of particles in the 1-1.5 μm range. The IR irradiances obtained from LOWTRAN7X were close (±0.5 W m^{-2}) to theoretical values given by Lacis et al. [1992], as seen in comparing Lacis et al.'s Fig. 2a to the parameterized expression for ${}_{Ln}V_{Tr}$ developed in Sec. 5.5. Confidence is placed in the computed IR irradiances because direct aerosol size observations find minimal contribution from larger particles, which would be expected to quickly settle out of the stratosphere. Since ${}_{Ln}V$ remains small relative to ${}_{Sn}V$ over the entire range of uncertainty, the lack of additional confirmation information in the IR region was not detrimental.

5.1.2 Independent verification of observations

The uncertainty and accuracy of the observations utilized in this study are discussed in detail in Appendix B and will not be repeated here. All surface-based observations used here were obtained from measurement programs where attention to operational detail, particularly calibration and data evaluation, was well documented. The differentially-computed observed V signal eliminates the largest known sources of instrumental error. Still, the possibility of some error exists because of unknown temporal drifts, possible gross errors, and slight nonlinearity in the instruments, as discussed in Appendix B. Individual observational irradiance data sets may contain sources of uncertainty and natural variability that can mask a volcanic signal. Of the five locations that were examined, only Kwajalein failed to display a probable volcanic signal in the global irradiance measurements, although model results and experience from the other sites suggested that it should have had a signal (not previously shown). Extensive cloudy conditions and an instrument exchange in the month before the eruption probably contributed to the failure to detect a volcanic signal at Kwajalein.

Surface total solar irradiance data were acquired at sites where direct solar beam observations were also made. Exact timing of the volcanic influence can often be readily seen in a continuous time series of direct beam observations. This permits close correlation with the indicated signals in total irradiance. Also, the irradiance data used here have been carefully screened for clear-sky conditions to assure that the indicated volcanic signal was not due to a water cloud effect; however, changes in tropospheric aerosols on the same time scale could be confused with a volcanic signal. In summary, the observations of V cannot be totally independently verified but were the best available from routine observations, including the satellite observations.

5.1.3 Mutual validation of computed and observed V

Multiple comparisons were needed to validate models and observations. It was most important to validate V in the solar region because that was where the largest forcing occurred. Both surface-based and satellite observations were examined. Of the four surface sites used in this study, one following El Chichón and all four following Pinatubo, three showed agreement between model results and observations at the ±2 W m^{-2} level for ${}_{Sd}V_S$ (Sec 4.7.2). The other case (SMO) was located in a region of a strong gradient in the V field but showed the potential for agreement if higher resolution observations were used. Computed ${}_{Su}V_{TOA}$ values are also consistent with available satellite data.

There is insufficient information to claim that the ${}_{Ln}V$ computed for this study agrees or disagrees with observations. However, there are no significant inconsistencies between known observations and modeled ${}_{Ln}V$. The expected and observed signals were small and therefore percentage differences were large. However, the differences were almost the same as in the solar region. Modeled values of ${}_{Lu}V_{TOA}$ were smaller (0.5-2.0 W m^{-2} for τ = 0.15-0.3) than those reported by Minnis et al. [1993]. The Ardanuy and Kyle [1986]

IR observations agree with those computed here for El Chichón. Small differences between the satellite observed $\tau_A(\lambda > 4.)$ and those obtained from Mie theory using inverted size distributions (Fig 2.8) lends further confidence to the computed ${}_{Ln}V$ values. No observations of ${}_{Ld}V$ were known to exist within the troposphere.

5.1.4 Discussion of comparison between observed and modeled ε

The overlap between the observed and modeled change in diffuse to change in direct irradiance ratio (ε) immediately following both El Chichón and Pinatubo (Fig. 4.14) supports the combined solar absorption and backscattering of the modeled aerosol. The best agreement in ε exists when greater optical depths and larger V exist. Therefore, even if the ε analysis does reveal an improperly modeled aerosol feature late in the life of the aerosol, the result on climate forcing is relatively small. Values of $\varepsilon \approx 0.9$ observed over one year after the eruptions are still within the range of those computed by Pollack et al. [1976], as presented by Coakley [1981].

There are several explanations for the eventual divergence of the observed and modeled ε (Fig. 4.17). These possibilities include an incorrectly determined $P(\theta)$ and/or ω_o in the model, a change in another atmospheric attenuator, or irradiance measurement errors. Reexamination of site records for the irradiance observations reveals no cause to suspect the observations. However, the shift in ε does occur after the maximum τ_A, and the signals in both the solar direct and diffuse are small and closer to the inherent error in the observations. Dehydration of the atmosphere over MLO did apparently occur in late 1982 and all of 1983 [Dutton et al., 1985b]. The decrease in monthly mean precipitable water above MLO of greater than 50% was seen starting in November of 1982 continuing through March 1983. Also, the entire year of 1983 was 25% below the

average of the previous five years. Less water vapor after a volcanic event causes a relative increase in the observed direct beam but not a corresponding decrease in the diffuse; this would also cause ε to decrease (become more negative). A similar analysis of water vapor over MLO following Pinatubo has not been carried out.

Another explanation for the eventual ε shift to an indication of less efficient total extinction could be a shift in aerosol size distribution not detected by the three to four wavelengths of $\tau_A(\lambda)$ information obtained at MLO. Several authors [e.g., Oberbeck et al., 1983; Hofmann and Rosen, 1983; Stone et al., 1993; Pueschel et al., 1994] have reported the appearance of a secondary peak in the aerosol sizes near 0.7 μm radius several months to one year after the eruption.

A short modeling experiment was preformed to evaluate the potential effect on ε from an enhanced secondary peak in *n(r)* several months after the eruption. The mean of several strong bimodal Pinatubo size distributions, reported by Pueschel et al. [1994] for 22 March 1992 at 20 km at latitude of 28° N, were used to compute aerosol optical properties. The resulting $\tau_A(\lambda)$ distribution is shown in Fig. 5.2. Figure 5.2 is inconsistent with any other observed $\tau_A(\lambda)$ assembled for this research (Figs. 2.1 and 2.20). Pueschel et al.'s sample was from the bottom of the cloud and would be expected to contain disproportionate numbers of larger particles, relative to the vertical column. The 22 March 1992 Pueschel et al. (1994) derived aerosol optical properties were used in a separate run of DISORTX from which ε was then computed. The resulting modeled ε is also shown on Fig. 4.21 and equals the others, although it represents an extreme *n(r)* case. These results suggest that the differences between the observed and modeled ε several months after each eruption are not due to a large particle mode missed by the $\tau_A(\lambda)$ observations and subsequent Mie inversions.

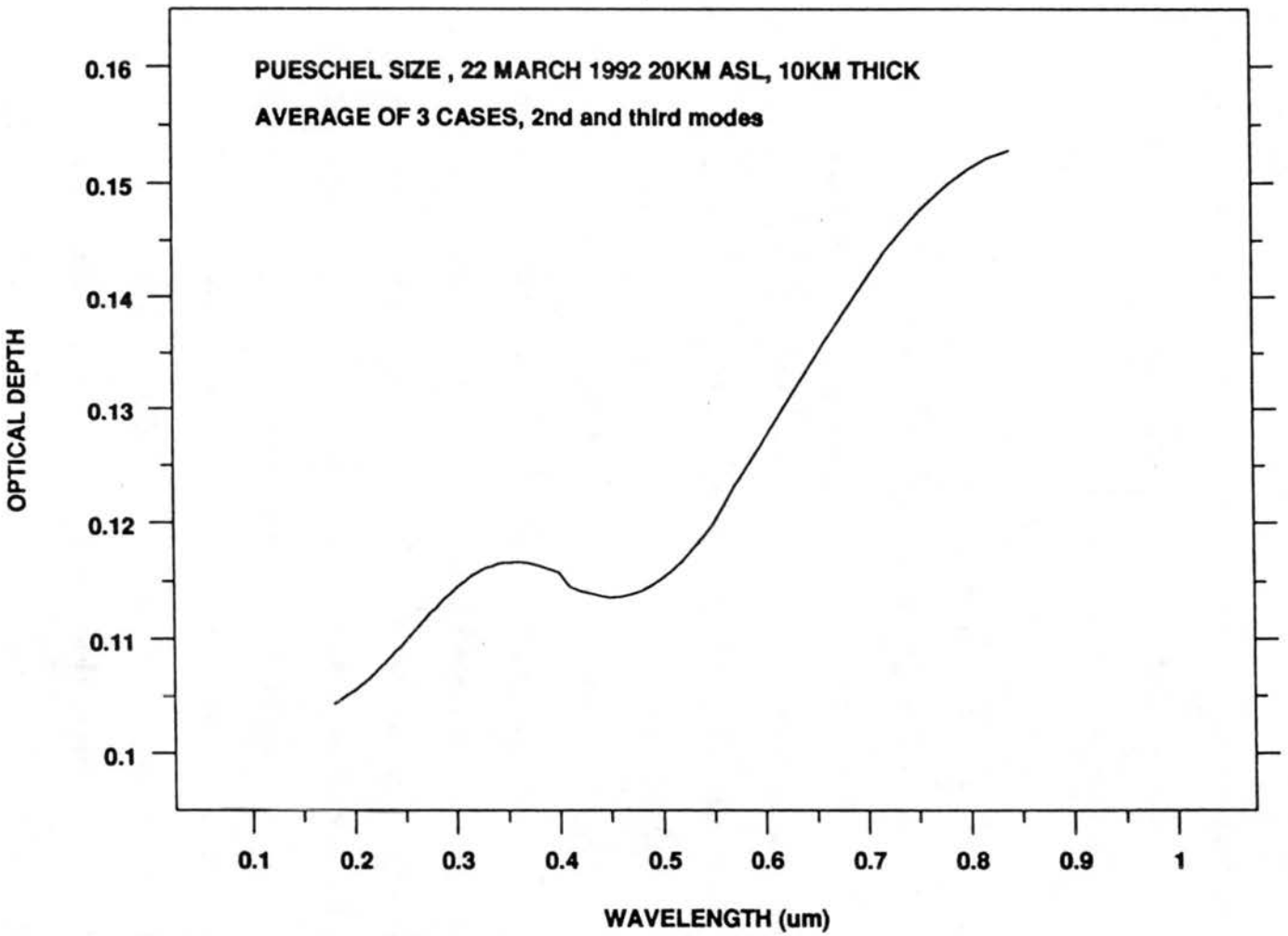

Fig 5.2 $\tau_A(\lambda)$ computed from Mie calculations for inverted aerosol size distribution for Pueschel et al. [1994] 22 March 1992, 19 km size distribution.

5.1.5 Indirect validation of V: the expected troposphere temperature response

Indirect confirmation of the magnitude of ${}_{An}V_{Tr}$ may be sought in observations of tropospheric temperatures [Hansen et al., 1978]. A decrease of net radiation at the tropopause may lead directly to tropospheric cooling. A model based on this suggestion is developed in the next section.

5.2 Tropospheric Temperature Changes

The translation of ${}_{An}V_{Tr}$ into changes in surface and tropospheric temperature and subsequent changes in atmospheric circulation is often left as a task for a complex GCM. However, on a hemispheric and seasonal mean basis there was a possibility of observing volcanically induced temperature changes directly [e.g., Mitchell, 1961; Angell and Korshover, 1985; Mass and Portman, 1989]. Dutton and Christy [1992] suggested that observed lower-tropospheric hemispheric temperature changes observed by the TIROS microwave sounding unit (MSU) showed a volcanic signal following both El Chichón and Pinatubo. The present study enables us to address the question: "Are the observed MSU temperature perturbations consistent with the mean radiative forcing computed here?"

The time series of hemispheric mean ${}_{An}V_{Tr}$ computed here is shown in Fig. 4.19. There was a net loss of energy entering the troposphere in each hemisphere. Assuming each hemisphere to be in radiative equilibrium with space before the eruptions, it may be possible to estimate the temperature change that occurs in the mass that loses that energy using the First Law of Thermodynamics. If no work is done, the time rate of change of temperature is given by Eq. 5.1. The thermal mass of each hemisphere was taken to be that of the atmosphere and annually mixed depth of the ocean. It was assumed that other

energy reservoirs did not release or accumulate heat. It is further assumed that there is

$$\frac{dT}{dt} = \frac{dE}{(M_a c_p + M_o c_w)} \qquad \textbf{5.1}$$

Where: dT/dt = temperature change per unit time

dE = change in energy per unit time;

M = mass of the system (a – atmos., o – ocean);

c = specific heat of M.

complete vertical and horizontal mixing such that the temperature change in the ocean mixed layer and troposphere are the same. The utility of this simple model depends on whether atmospheric temperature will respond significantly to a 1- to 3-yr radiative forcing perturbation and if such a response can be detected. The use of the 1-yr ocean mixing depth corresponds to a global thermal mass that will respond to ~1-yr time scale heating perturbations. An atmospheric response to year-long perturbations in radiative forcing is expected since it is observed that the seasonal temperatures lag normal seasonal radiative forcing by only six weeks. In this temperature change model, the troposphere and upper ocean temperatures follow each other and respond by the end of the season in which an energy anomaly, ΔE, occurs. ΔE is computed as the departure from ${}_{An}V_{Tr}$ averaged over the previous year, consistent with the use of the annually mixed ocean. Temperature changes computed by such a model do not, of course, include temperature variations from other causes.

The global oceanic mass used was 7.5×10^4 kg m^{-2} corresponding to the annual mean mixing thickness of 75 m [Li et al., 1984]. Tropospheric mass (1013 mb to 300 mb) is

7.1×10^3 kg m^{-2}. The specific heat of water is 4.19 J g^{-1} deg^{-1} and for dry air is 1.004 J g^{-1} deg^{-1}. The heat capacity of the earth's solid surface was neglected. For these calculations, the northern hemisphere surface was taken to be 53% ocean, and that of the southern hemisphere, 90% ocean. Multiplying the mass per unit area by the relative amount of area (1.0 for the atmosphere and 0.53, 0.90, and 0.715 for the oceans) yields ΣMc in Eq. 5.1. ΣMc_p is equal to 1.66×10^8, 2.84×10^8, and 2.32×10^8 J deg^{-1} for the N. and S. hemispheres and the globe, respectively. Using these values and the temporal variations in ${}_{An}V_{Tr}$ to calculate ΔE, temperature changes were computed using Eq. 5.2.

$$T = T_o + \frac{dT}{dt}\Delta t \qquad \textbf{5.2}$$

Starting with the equilibrium temperature and combining Eqs. 5.1 and 5.2, the temperature changes following El Chichón and Pinatubo were computed and are shown in Fig. 5.3. In the calculation of the hemispheric-mean temperature anomalies, it was assumed that there was no exchange of heat between the hemispheres. Also shown in Fig. 5.3 are the hemispheric-mean lower-tropospheric temperatures observed from the MSU described by Spencer and Christy [1990, 1992] who claim precision to within 0.02 °C averaged over each hemisphere. The MSU lower troposphere temperature data for a weighted vertical column gridded for the entire globe and used here to compare to the model results since the model assumes complete mixing. The modeled temperatures were normalized to the observed data for one year before each eruption.

Following Pinatubo, the largest difference between the modeled and observed temperature anomalies occurs near the maximum in observed cooling and is coincident with a maximum in an El Niño event that existed during most of the 3-yr period [Kousky,

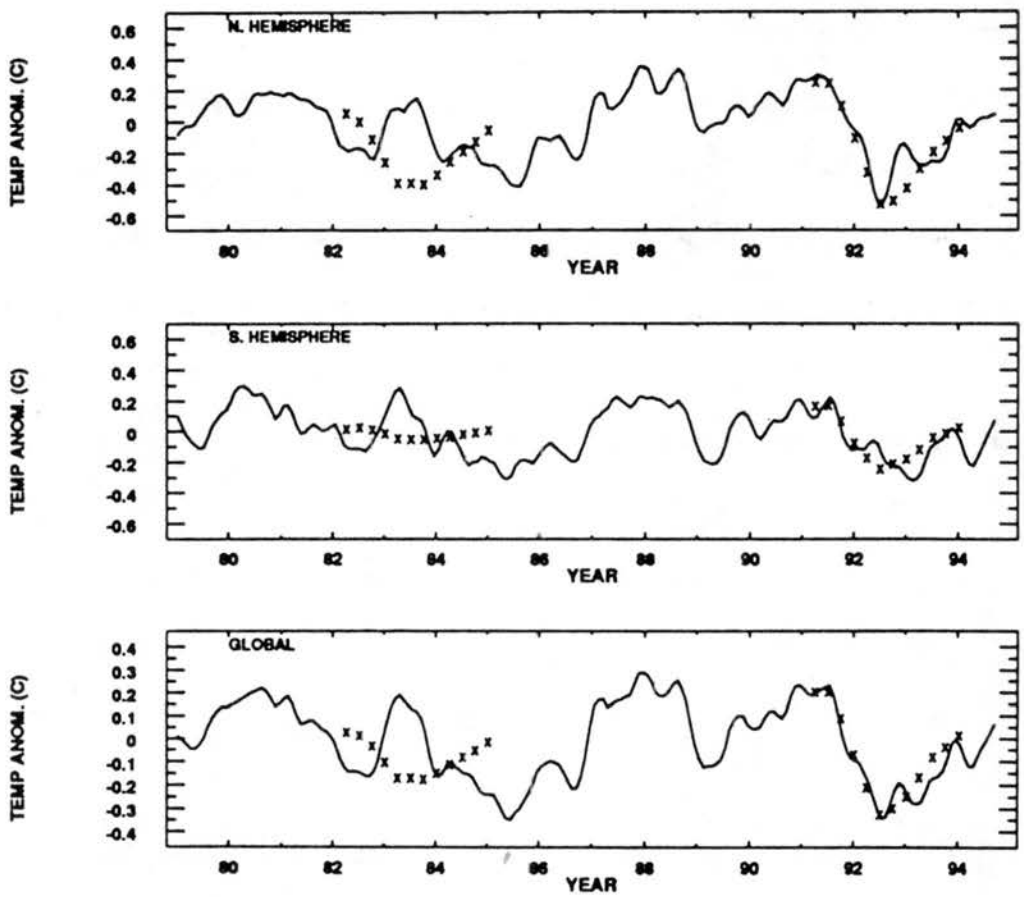

Fig. 5.3 Time series for hemispheric and global mean lower tropospheric air temperatures anomalies. Observations (solid line) are from the MSU satellite sensor with deseasonalized anomalies calculated from the mean of 1981- 1990. Calculated values, Xs, are described in text and are normalized to the 1-yr mean observed anomalies for the 1 yr prior to each eruption, April 1982 and June 1991. Computed values are for a 1-yr time constant in the model.

1994]. There is close correspondence between the two data sets in the rate and timing of temperature decrease, the total temperature change, the timing of minimum temperature, and the rate and timing of rewarming. Fluctuations similar in magnitude are seen elsewhere in the observed temperature record, but none are particularly close to fitting the particular form of the modeled temporal temperature changes.

A major El Niño occurred just after El Chichón and is known to have altered normal heat exchange between the ocean and troposphere [Mass and Portman, 1989; Dias and Kiladis, 1993]. This fact invalidates a principal assumption of the proposed temperature change model. There is, therefore, little similarity between the modeled and observed temperature change following El Chichón seen in Fig. 5.3. Nonetheless, there was less radiation heating of the surface and troposphere during 1982 and 1983. A notable decrease in temperature does follow the El Chichón volcanic event by 2-3 years. This later decrease in temperature was consistent with a simulated temperature change model that allows for a longer time to respond to the initial radiative forcing, given the same ΣMc.

The length of time over which ${}_{An}V_{Tr}$ was averaged to determine ΔE was based on the use of the annual ocean mixing depth, but it could be a tuneable model variable if the ocean responds differently, i.e., it takes more or less than a year for the upper 75 m to respond to a given event. Allowing ΔE following El Chichón to be based on a ${}_{An}V_{Tr}$ averaging time of 2.5 years instead of 1 year, the resulting modeled temperature changes are given in Fig. 5.4. The modeled temperature change now better tracks the global mean, considering the El Niño warming, but does not track the hemispheric means. This dichotomy might be explained on this time scale because the hemispheres would lose their thermal identity assigned in the model and only the global mean would be properly modeled. With this revised model the magnitude of the global cooling agrees with the

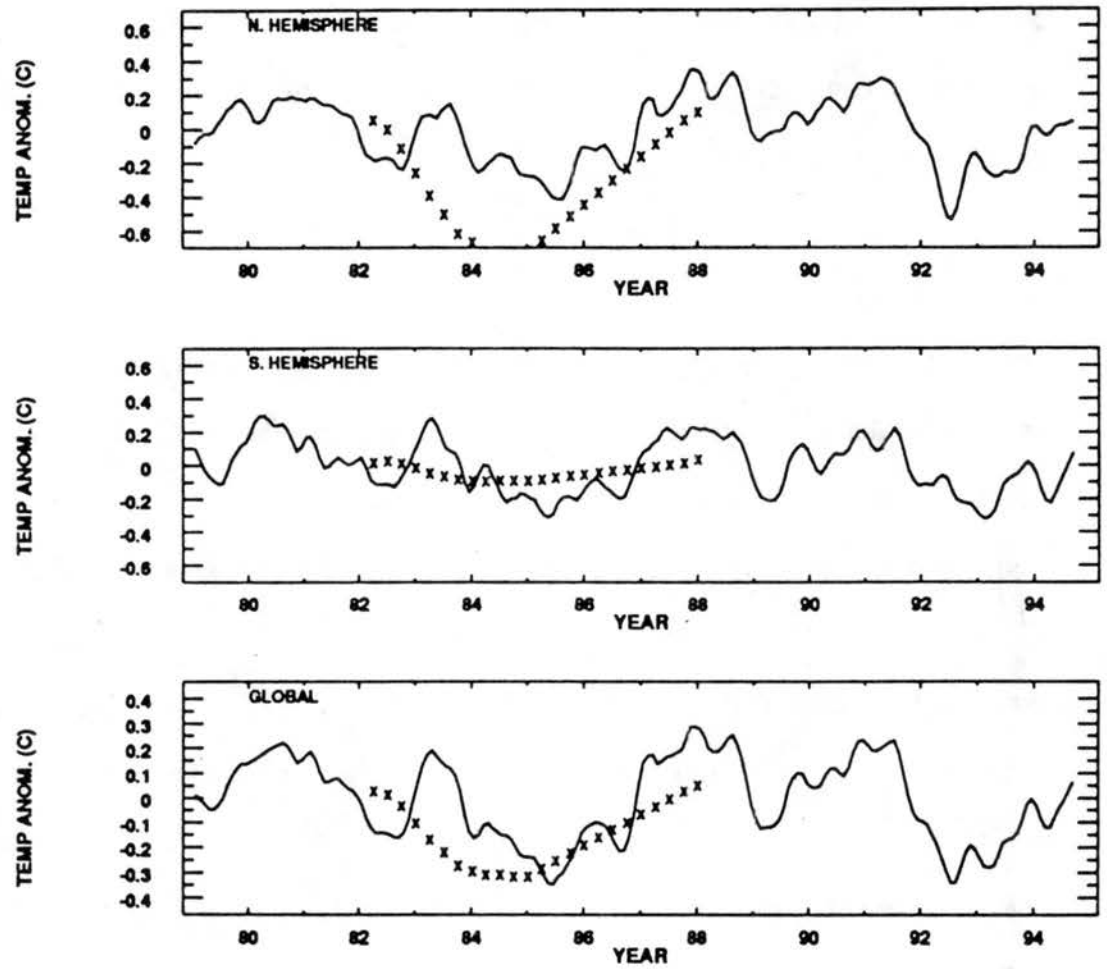

Fig. 5.4 Same as Fig. 5.3 except for a 2.5-yr time constant following El Chichón.

observations but the timing still does not agree well. This suggests that 2.5 years was not the optimum time variable (a value just less than 2.5 years would give better agreement with the rewarming), or that other sources of global temperature variations were dominating. It is, therefore, fortuitous that the ΔT model and observations show such close agreement following Pinatubo. This suggests that the global ocean/atmosphere system may have behaved according to the assumptions of the ΔT model following Pinatubo but is not constrained to do so.

5.3 Global Distribution of V

The computed ${}_{An}V$ appears to be sufficiently accurate to examine the potential effects on climatic features of the planet. Besides determining the mean temperature of the planet, the radiation input to the earth atmosphere system also establishes and helps maintain atmospheric circulation patterns due to a spatial distribution inherent in earth-sun geometry. Modifications to the normal distribution of energy deposition could be expected to modify those circulation patterns, if such modifications are of sufficient magnitude. Robock and Liu [1994] have begun such investigations relative to volcanic forcing.

The spatial and temporal variations of V from El Chichón and Pinatubo (Figs. 4.17 and 4.18) reveal substantial differences in ${}_{An}V_{Tr}$ within a given hemisphere and between eruptions. To properly evaluate the effects of any particular volcanic event on atmospheric circulation, this distribution and its evolution should be accounted for. V was most dominant in the low latitudes in the first few seasons following each eruption, which by nature of the timing of the El Chichón and Pinatubo eruptions was in the northern hemisphere summer and fall, respectively. Following both eruptions the maximum V moved to the northern polar region. The zonal distribution of V was affected by factors

other than the distribution of the aerosol. These include underlying albedo and solar zenith angle/length of day. The global model developed for this study accounts for these variables within the limitations of the mean zonal and cloudiness formulations. North/south gradients in V and their relationship to the undisturbed radiative gradient are discussed below.

Figure 5.5 shows the ${}_{An}V_{Tr}$ differences between the Tropical (0^{o} - 23^{o}, N and S), and high latitudes (53^{o} - 90^{o}, N and S), tropical minus polar, for both the northern and southern hemispheres following both El Chichón and Pinatubo. Negative values indicate greater loss in net radiative energy in the tropics. Similar intrahemispheric gradients were seen in the N. hemisphere after El Chichón and Pinatubo. Several aspects of the anomalous gradients are worth discussion. First, the normal gradient over the latitude range and season used in Fig 5.5 is only ~45 W m^{-2} [Campbell and Vonder Haar, 1980], and the volcanic perturbation was 7 W m^{-2} or 16% of the normal gradient. There also was a reversal in sign of the gradient anomaly in the northern hemisphere from the first to second summer after the eruptions. This reversal phenomenon was not as dominant in the S. hemisphere. The reversal follows, of course, the migration of the aerosol maximum to the northern polar region and the seasonal change in solar geometry. The change in the volcanically induced N. hemisphere gradient from one summer to the next was equal to 30% of the normal summer gradient. This results in a tendency to weaken the N. hemispheric N/S temperature gradient the first summer after the eruption and to strengthen it in the second summer. These results can be compared to the solar irradiance gradient that could repeat each year to within 2 W m^{-2} in the absence of a volcanic anomaly, based on an analysis of ERBE TOA data during 1985-1988. There was little effect on the first or second winter's gradient. The noted induced gradient anomalies

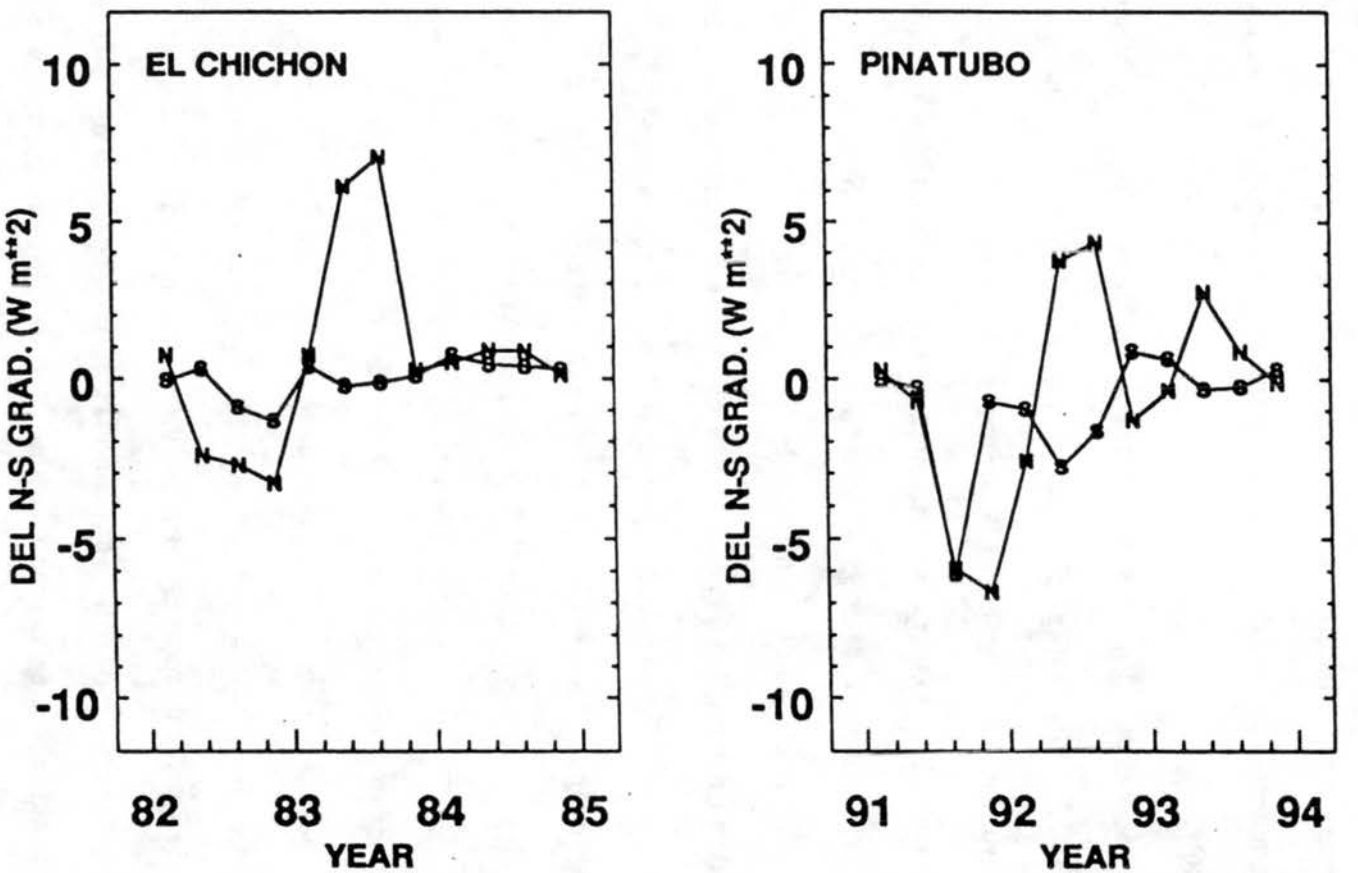

Fig. 5.5 Time series of computed ${}_{An}V_{Tr}$, intrahemispheric gradients. Within each hemisphere the northern most zonal ${}_{An}V_{Tr}$ is subtracted from the southern most band. In both hemispheres, the two latitude bands nearest the equator were averaged together before the subtraction.

essentially disappeared after two years when the aerosol was more uniformly spread and considerably decreased.

5.4 Parameterization

Extensive, complex, and rigorous RT calculations were performed here to obtain values of V. Inspections of the results and input variables suggest the possibility of simpler parameterization of V. Such a parameterization process should strive to yield values within the uncertainty established for rigorous computations. Global gridded RT results presented so far provide 232 vertically resolved cases that cover a large realistic range of global conditions following two major volcanic eruptions. From these, highly simplified expressions for ${}_{Sn}V_{Tr}$, ${}_{Ln}V_{Tr}$, and ${}_{An}V_{Tr}$ are developed in the following.

The relationship between major variables and V has been explored through theoretical analysis and model sensitivity studies here and elsewhere. Simple linear functions in τ_A for various components of V have been given by Lacis et al. [1992] and Minnis et al. [1993]. Linear, or slowly varying, relationships between V and both θ_0 and albedo (α) over ranges of θ_0 and α have been noted in the current work. Considering these relationships, several multivariate fits to the RT-computed gridded ${}_{An}V_{Tr}$ for El Chichón and Pinatubo were devised. Additional variables accounting for the length of solar day (Λ) and the particle size distribution effective radius (r_e) and their squares to account for noted nonlinearities, were also included as variables in the regression fits. Equation 5.3 defines r_e as used by Hansen and Travis [1974]. Lacis et al. [1992] showed a nonlinear relationship between V and r_e. The Λ variable was included as a linear and squared

$$r_e = \frac{\int_{r_1}^{r_2} r\pi r^2 n(r)dr}{\int_{r_1}^{r_2} \pi r^2 n(r)dr} \qquad \textbf{5.3}$$

variable in the IR fit to account for seasonal variations in atmospheric composition, mostly water vapor and temperature. General expressions for multivariate expressions fit to ${}_{Sn}V_{Tr}$ and ${}_{Ln}V_{Tr}$ are given by Eqs. 5.4 and 5.5. Some colinearity, or correlation, between the selected variables exists, e.g. between Λ and Λ^2. This colinearity does not affect the multi-linear regression procedure [Crow et al., 1960] other than to complicate sorting out the most important variables. The coefficients A through F_2 were determined by least squares fit to the RT-computed ${}_{n}V_{Tr}$. (Note: The θ subscript "o" is dropped in following.)

$${}_{Sn}V_{Tr} = A + B\tau + C\theta + D\alpha + E\Lambda + Fr_e + F_2 r_e^2 \qquad \textbf{5.4}$$

$${}_{Ln}V_{Tr} = A + B\tau + E\Lambda + E_2\Lambda^2 + Fr_e + F_2 r_e^2 \qquad \textbf{5.5}$$

Equations 5.4 and 5.5 were fit for the two eruptions individually and combined. Various forms of the equations were tested to improve the fit before selection of the forms given. Both τ_A(550 nm) and broadband τ_A were used, with the final coefficients given for τ_A(550 nm) because it is more widely available, although fits using τ_A(vis) give

Table 5.1 Regression coefficients and *t* values for individual fits to RT results for separate and combined volcanoes.

	A	*B*	*C*	*D*	*E*	E_2	*F*	F_2	rsd ($W\ m^{-2}$)
El Chichon									
${}_{Sn}V_{Tr}$	-1.2	-35.5	4.12	4.65	-4.07	0.0	3.27	-7.05	0.503
t	1.6	27.	3.9	2.9	5.3		1.5	2.2	
${}_{Ln}V_{Tr}$	0.95	6.13	0.0	0.0	0.34	-2.20	4.20	0.0	0.144
t	0.8	16.0			2.9	3.5	4.5		
Pinatubo									
${}_{Sn}V_{Tr}$	-2.00	-39.5	6.59	8.55	-7.44	0.0	3.74	-7.67	0.51
t	2.4	46.0	5.8	5.0	9.2		1.6	2.2	
${}_{Ln}V_{Tr}$	0.10	7.35	0.0	0.0	0.37	-2.61	4.96	0.0	0.15
t	0.9	31.0			3.0	3.9	5.1		
Combined									
${}_{Sn}V_{Tr}$	-1.55	-38.8	5.22	6.45	-5.63	0.0	3.36	-6.95	0.53
t	2.6	57.0	6.5	5.3	9.8	0.0	2.1	2.9	
${}_{Ln}V_{Tr}$	0.12	7.13	0.0	0.0	0.34	-2.55	4.75	0.0	0.15
t	1.6	38.0			4.0	5.6	7.2		

small improvement. Coefficients for each respective volcano are given in Table 5.1. The regression analysis was done with the DATAPLOT package of interactive graphical and statistical analysis software [provided by J. Filleben, National Institute for Standards and Technology, Gaithersburg, Maryland]. The *t* value given in Table 5.1 is the ratio between the fitted coefficient and the standard error of determination of that coefficient.

Considering the number of independent points used in the fits (>100) and normal probability distribution function, coefficients with $t \geq 2.0$ are significant at the ≥95% level. The computed coefficients and statistics show that there are no significant differences in any of the coefficients from one eruption to the other. Assuming no differences, a single fit resulting from input from both volcanoes should give the best general results since the fit is to the most points and over a larger range of conditions. Coefficients of such a combined fit are also given in Table 5.1. Residuals from the fits and the application of those fits are further examined. Coefficients of Eqs. 5.3 and 5.4 were derived from fits to one volcano and tested by using those coefficients to calculate ${}_{Sn}V_{Tr}$ and ${}_{Ln}V_{Tr}$ for the other volcano and differencing the results with respect to the RT models. Fit residuals (dependent) and application residuals (independent) were used to evaluate the quality of each fit and each independent application. Dependent residuals refer to the difference between V computed by RT models and Eqs. 5.3 and 5.4 using coefficients derived from the same volcano. Independent residuals are the difference between RT model results and application of Eqs. 5.3 and 5.4 with coefficients determined from the other volcano. Figure 5.6 shows the dependent and independent residuals for the solar and IR components separately for both volcanoes. Table 5.2 summarizes the statistics for those residuals shown in Fig.

Table 5.2 Summary of residual statistics for dependent and independent regression fits.

	Mean	S.D.	Max	Min
	W m^{-2}			
EC Dependent				
${}_{Sn}V_{Tr}$	0.0	0.49	1.1	-3.4
${}_{Ln}V_{Tr}$	0.0	0.14	0.69	-0.44
EC Independent				
${}_{Sn}V_{Tr}$	0.8	0.57	1.9	-2.4
${}_{Ln}V_{Tr}$	0.2	0.15	0.54	-0.58
Pina. Dependent				
${}_{Sn}V_{Tr}$	0.0	0.50	1.7	-1.9
${}_{Ln}V_{Tr}$	0.0	0.14	0.33	-0.40
Pina. Independent				
${}_{Sn}V_{Tr}$	-0.23	0.61	1.0	-2.9
${}_{Ln}V_{Tr}$	-0.70	0.16	0.50	-0.33

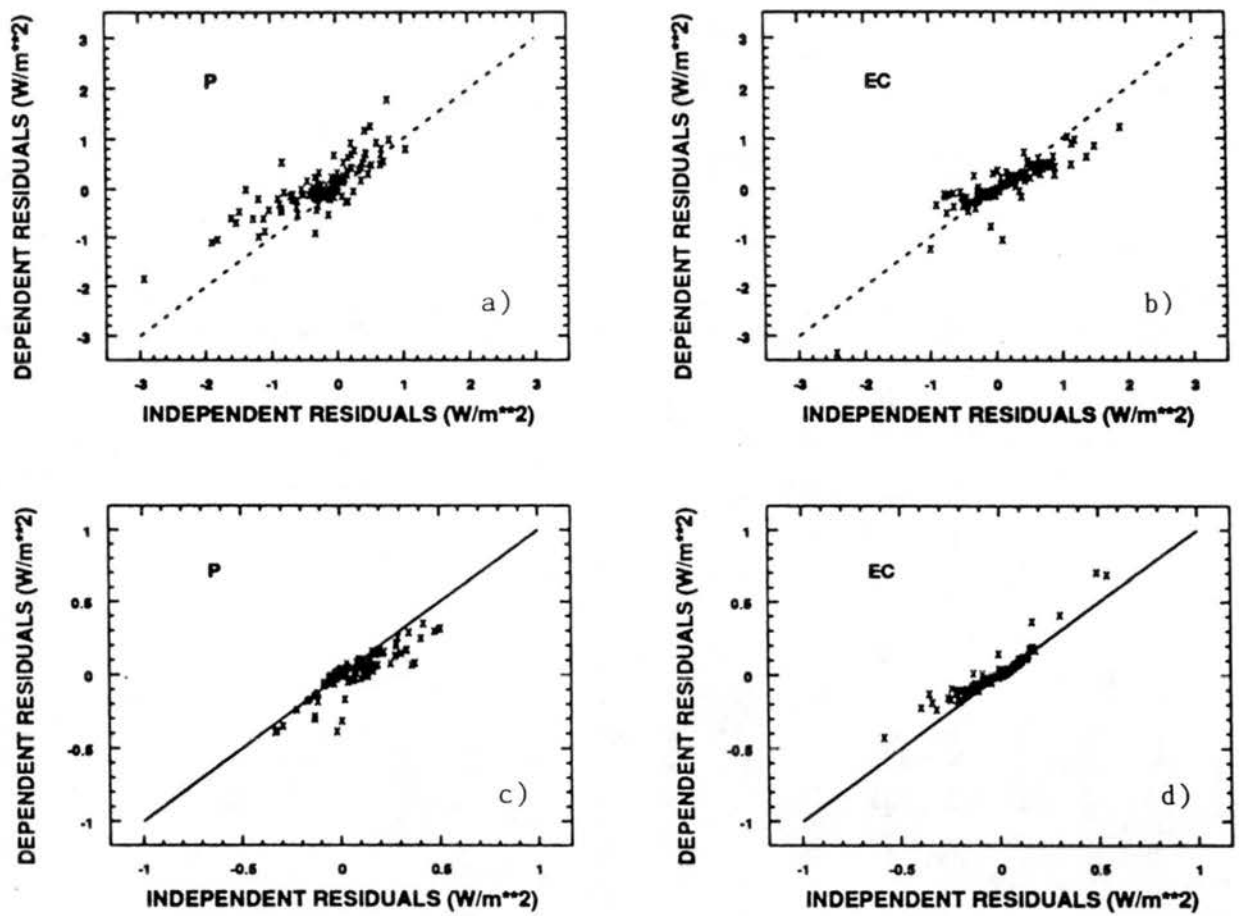

Fig. 5.6 Dependent and independent, as defined in text, residuals from the difference between parametrically and RT computed ${}_{Sn}V_{Tr}$ (a & b) and ${}_{Ln}V_{Tr}$ (c & d) for Pinatubo (a & c) and El Chichón (b & d). Dashed line is the 1:1 ratio for comparison.

5.6. It is seen that there is little difference between the independent and dependent residuals for a given eruption or between the residuals of either eruption, except that due to the overall larger magnitude of Pinatubo V. Dependent and independent residual standard deviations are near 0.5 W m^{-2} for the solar and 0.2 W m^{-2} in the IR. Given the maximum of just over -10 W m^{-2} for ${}_{Sn}V_{Tr}$ and 1.5 W m^{-2} for ${}_{Ln}V_{Tr}$, the parameterized functions are within 25% (range) and generally to within 10% (±2 S.D.). The maximum size of any independent residual was 2.9 W m^{-2}, which occurs in the northern most latitude zone in the third season of 1992 (920301). This and the second most outlying point, 2.4 W m^{-2} at grid 830301, correspond to unusual observed spectral optical depths such that the parameterized fits, weighted heavily on $\tau_A(550)$, do not reproduce the rigorously modeled values. he difference between the forms of Eqs. 5.3 and 5.4 suggest that the best parameterized estimate of ${}_{An}V_{Tr}$ might be the sum of parameterized ${}_{Sn}V_{Tr}$ and ${}_{Ln}V_{Tr}$. Nonetheless, several simpler parameterizations of this quantity were investigated. The initial equation fit to ${}_{An}V_{Tr}$ (combined from both volcanoes) was a combination of all five variables used for ${}_{Sn}V_{Tr}$ and ${}_{Ln}V_{Tr}$ in Eq. 5.6.

$$ {}_{An}V_{Tr} = A + B\tau + C\theta + D\alpha + E\Lambda + E_2\Lambda^2 + Fr_e + F_2 r_e^2 \qquad \textbf{5.6} $$

$$ {}_{An}V_{Tr} = A + B\tau + C\theta + D\alpha + E\Lambda + E_2\Lambda^2 \qquad \textbf{5.7} $$

$$ {}_{An}V_{Tr} = A + B\tau + C\theta + D\alpha + E\Lambda \qquad \textbf{5.8} $$

$$ {}_{An}V_{Tr} = A + B\tau + C\theta + E\Lambda \qquad \textbf{5.9} $$

$$ {}_{An}V_{Tr} = A + B\tau \qquad \textbf{5.10} $$

Fitted coefficients and statistics for Eq. 5.6 and several other simplifications given by Eqs. 5.7 through 5.10 are given in Table 5.3. In fitting Eq. 5.6 to the RT results for ${}_{An}V_{Tr}$ it was found that the dependent residuals are statistically equivalent to those from the ${}_{Sn}V_{Tr}$

Table 5.3 Coefficients and t values for various fits to ${}_{An}V_{Tr}$.

Eq.	A	B	C	D	E	E_2	F	F_2	rsd ($W\ m^{-2}$)
5.6	-0.56	-31.7	5.71	6.39	-9.92	4.31	0.898	-2.33	0.45
t	0.8	55.0	7.5	6.2	3.7	1.8	0.65	1.2	
5.7	-0.66	-32.2	5.73	6.62	-9.68	4.06	0.0	0.0	0.46
t	0.9	60.0	7.5	6.3	3.5	1.6			
5.8	-1.56	-32.1	5.18	6.68	-5.27	0.0	0.0	0.0	0.47
t	3.1	60.0	7.5	6.4	11.0				
5.9	-1.29	-31.9	0.99	0.0	-2.79	0.0	0.0	0.0	0.49
t	8.5	55.0	4.1	0.0	8.6				
5.10	0.37	-31.9							0.56
t	7.0	49.0							

+ ${}_{Ln}V_{Tr}$ case. Simpler parameterized models were formed by successively dropping the less important, or less common terms. Not all possible combinations of variables were used for the fits because of the expected dominance of a few.

Equation 5.8 has the maximum number of terms with all the coefficients statistically significant at the ≥ 95% level. These regression expressions should not be used outside

the range of input variables (Table 5.4) for an accuracy of ≤ 2 W m^{-2}. These regression fits could be derived for other levels in the atmosphere, but height could not be used as a linear regression variable, as suggested by Fig. 4.6. Table 5.3 shows that aerosol optical depth is by far the most dominant variable. The inclusion of other variables makes small improvements, as indicated by the residual standard deviation (rsd). The parameterizations used for any particular application will depend on input data available, acceptable error ranges, and any particular requirements of that application. To further evaluate the parameterization, summaries of global radiative forcing using the RT and the parameterization results were analyzed. Figure 5.7 shows the global and hemispheric means ${}_{An}V_{Tr}$ where the ${}_{An}V_{Tr}$ was computed from the regression equation and can be compared to Fig. 4.19 where the full RT code was used.The maximum difference between Figs. 5.7 and 4.19 is 0.65 W m^{-2} with 90% of the points within 0.4 W m^{-2}.

Table 5.4 Range of variables used in regression fits.

Variable	Maximum	Minimum
τ	0.4	0.0
θ	50°	81°
Λ	3hrs	21hrs
r_e	0.15μm	0.55μm
α	0.23	0.6

5.5 Comparison Between Volcanoes

Computed and observed V for El Chichón and Pinatubo generally substantiate the findings of previous work. The main differences between eruptions are in the magnitude and distribution of the τ_A. There are also observed differences in $\tau_A(\lambda)$ and resulting size distributions. The effect of this was seen when comparing computed ${}_{Sn}V_{Tr}$ over MLO where the ${}_{Sn}V_{Tr}$ sensitivity to τ_A(500 nm) was higher for Pinatubo, Fig. 5.8. This difference between the two volcanoes, ≈ 2 W m^{-2} at τ_A(500 nm) = 0.2, was small compared to differences in spatial distribution of τ. Any effects of these differences were

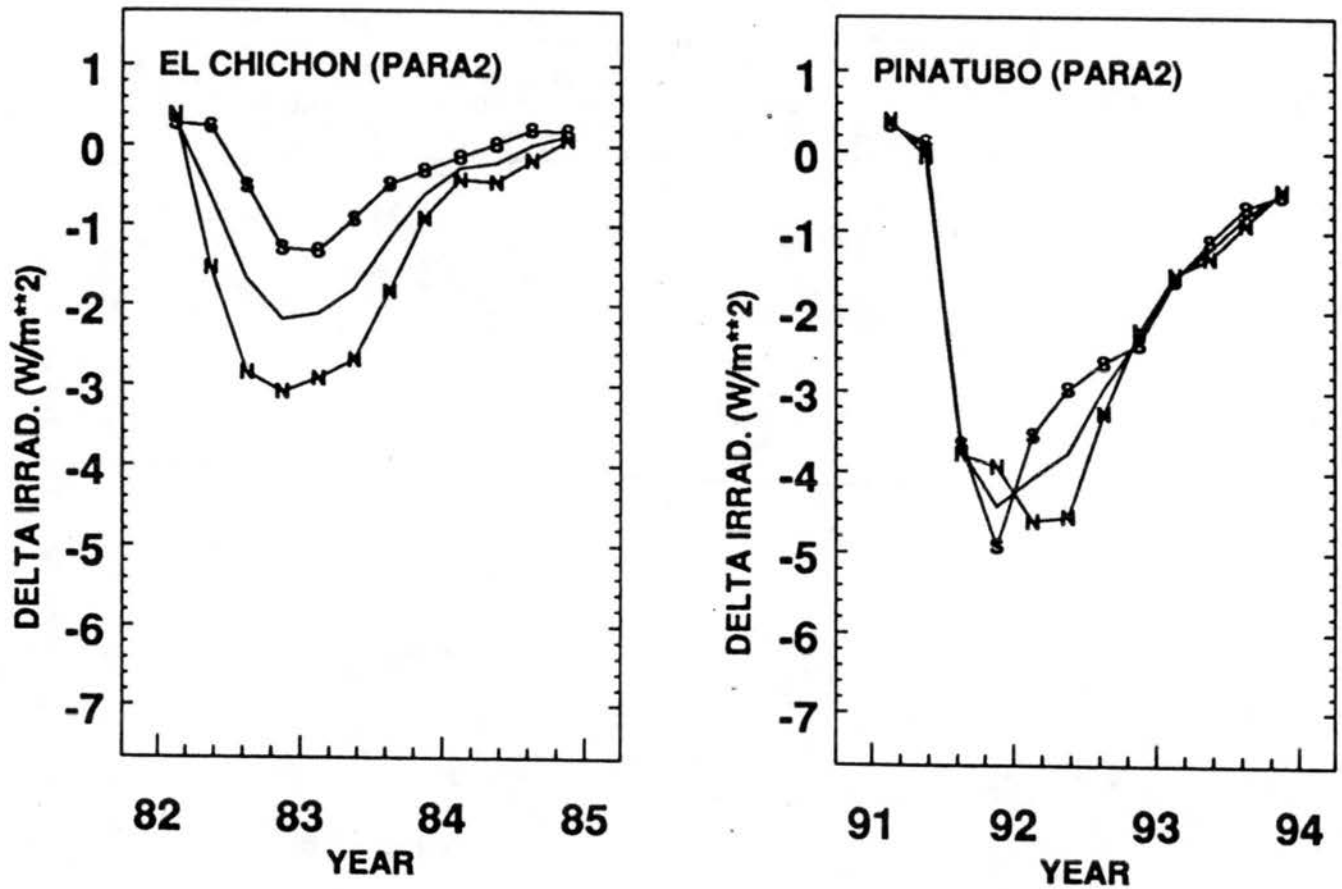

Fig. 5.7 Global and hemispheric mean ${}_{An}V_{Tr}$ computed from parameterization Eq. 5.6 with coefficients taken from Table 5.3.

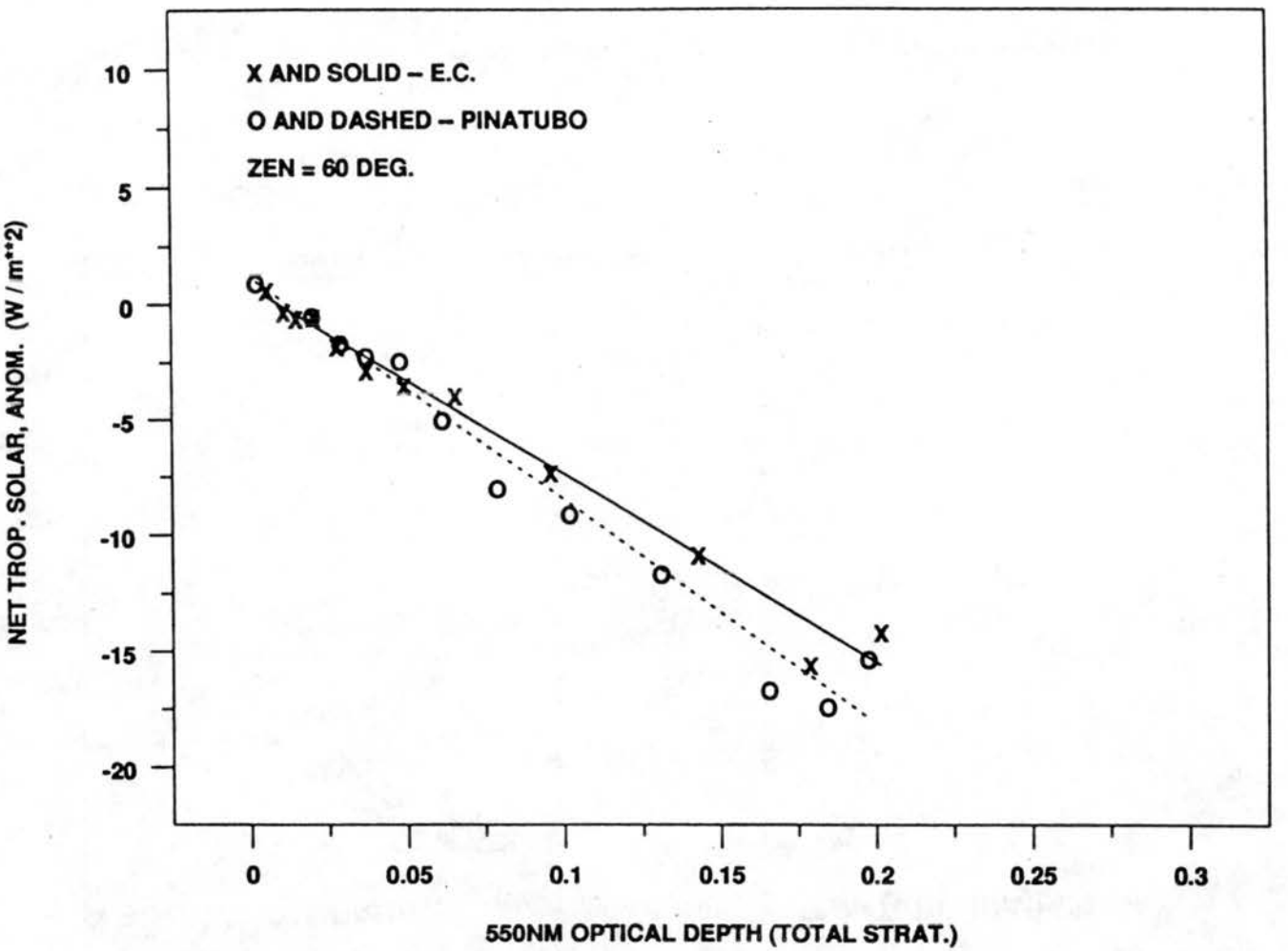

Fig. 5.8 A comparison of the ${}_{Sn}V_{Tr}$ sensitivity to $\tau_A(550)$ for El Chichón and Pinatubo for a solar zenith angle of 60° and surface albedo of 0.23. Straight lines are least squares fits, solid - El Chichón, dashed - Pinatubo.

undetected globally, when considering parameterizations of V for each volcano individually. Observational information sources differed for the two eruptions so that disparate observational biases can exist and contribute to the observed differences in $\tau_A(\lambda)$. Any such biases do not appear to significantly affect global V characteristics as suggested in the comparison of regression equation statistics (Table 5.1 and 5.2) for the separate fits to El Chichón and Pinatubo.

The maximum global mean ${}_{An}V_{Tr}$ following El Chichón was -2.2 W m^{-2} and was -4.5 W m^{-2} following Pinatubo. Maximum forcing existed for < 6 months in both cases and recovered to < 0.5 W m^{-2} by the end of each 3-yr study period, which was 2.75 years after El Chichón and 2.5 years after Pinatubo. Integrating over the entire 3-year period, the ratio between the two eruptions was 2.5. El Chichón had three times the ${}_{An}V_{Tr}$ in the N. hemisphere as in the S. hemisphere, while the ratio was 1:1 after Pinatubo.

Chapter 6. Summary and Conclusions

6.1 Summary

Model-computed and observed irradiance fields for background and enhanced stratospheric aerosols cases were used to determine volcanic radiative forcing, V. Existing RT models were adapted to the requirements of this study to compute irradiance. Various independent observations of aerosol properties following recent eruptions were evaluated and combined to provide realistic physical and optical aerosol models that could be incorporated into both global zonal and local RT models. Computed and observed values of V were opportunely compared, with close agreement between the two demonstrated. The present work varies from similar earlier published work primarily in that in the current work actual observed spatial and temporal evolutions of the aerosol were used, new RT models were used, emphasis was placed on comparisons to observations, a simple thermal mass temperature change model was used, and parameterizations were developed. Radiative transfer models were also used to examine their sensitivity to various input variables.

Globally varying volcanic radiative forcing was computed for the first 2.5 years following the El Chichón and Mt. Pinatubo eruptions, a period when the aerosol would have its maximum influence on the earth's energy budget. The effect of the presence of the stratospheric aerosol was a reduction in radiant energy input to the troposphere, highly dependent on the τ_A(vis.) and to a lesser extent on other variables (θ, α, Λ, T, r_e, or $\tau_A(\lambda)$). Maximum global mean net V at the tropopause ($_{An}V_{Tr}$) following El Chichón was

-2.2 W m^{-2} and was -4.5 W m^{-2} following Pinatubo. Maximum forcing occurred 6-9 months after both the eruptions, persisted for about three months, and recovered to < 0.5 W m^{-2} by the end of each three-year study period, which was 2.75 years after El Chichón and 2.5 years after Pinatubo. Integrating V over the entire 3-yr period of study, the ratio between the two eruptions was 2.5. El Chichón had three times the ${}_{An}V_{Tr}$ in the northern as the southern hemisphere while the ratio was 1:1 after Pinatubo because of the more even spreading of the Pinatubo aerosol.

The computed ${}_{An}V_{Tr}$ was used to estimate global and hemispheric mean temperature change (ΔT) variations using a simple thermal model based on the First Law. Modeled ΔT are remarkably similar, correlation coefficient = 0.86, to MSU observations after Pinatubo. After incorporating an adjustment to the time response of the thermal model, there was moderate similarity between modeled and observed global mean temperature anomalies after El Chichón. Volcanic impacts on hemispheric temperatures were greater in the N. hemisphere because of its lower heat capacity, given equal V in the two hemispheres. El Chichón also had a larger impact in the N. hemisphere because of larger aerosol loading there.

The magnitude of the intrahemispheric N-S irradiance gradient produced by the two volcanic events anomalies were as large as 16% of normal. This suggests the possibility for a significant effect on hemispheric temperature gradients. Similar intrahemispheric gradients were seen in the N. hemisphere after El Chichón and Pinatubo. The impact on hemispheric gradients becomes much less after the first 1-1.5 years following the eruption as the aerosol becomes uniformly distributed in the horizontal and stratospheric loading diminishes.

Lastly, the RT-computed *V*s were used to obtain highly parameterized models that can simulate the rigorous results and provide economical higher time and spatial resolution for additional applications, if higher time resolution aerosol data become available.

A major emphasis has been placed on comparison and verification of each step of this research. The purpose of this has been to support assumptions, approximations, and uncertainty analysis of both the RT model and observations. Absolute confirmation of all aspects of this work cannot be claimed because too few cases were available for comparison. Instead, there is a good indication that the assumptions were reasonable and that no major aspects of the problem have been overlooked or incorrectly developed. Previous research by this author and many others, has allowed this work to focus on the data assimilation, computation, verification, and application. Many conclusions that can be drawn from the current work support and refine the earlier works referenced throughout this study. Foremost of those is that using H_2SO_4 spherical droplets as the principal long-lived volcanic aerosol results in reflected solar energy dominating perturbations to the tropospheric radiation budget. A more specific problem addressed here is quantifying the irradiance anomalies with sufficient accuracy to be useful in further evaluation of the volcanic impact. Original results from the current work are: quantitative agreement with original independent observations, demonstration of the utility of available volcanic $\tau_A(\lambda)$ data, a higher time and spatial resolution of realistic V than typically presented, development of a tropospheric temperature change model, and new parameterizations of V.

6.2 Conclusions

Considerable confidence was gained in the ability to compute V because of the favorable comparison with observations. Because of the confidence in the modeled V,

it was possible to draw further conclusions based solely on the models that cannot be readily confirmed with observations, or with caution, from additional observations not readily modeled. Many conclusions come out of this work, some incidental and others relating directly to the goals of this research. Those conclusions are listed in the following under three groups: those based on the comparison between models and observations, those based solely on observations, and those based solely on RT models.

6.2.1. Following is a list of conclusions based on the comparison between RT models and observations.

1. Long-lived volcanic aerosol chemical properties were adequately specified as predominantly H_2SO_4/H_2O spherical droplets in 75% solution, as proposed previously.

2. Selected surface observations of clear-sky solar irradiance accurately show the effects of volcanic aerosols.

3. Aerosol size distributions obtained from inversions of spectral optical depth observations in the $\lambda < 1.0$ μm region were sufficiently accurate to use in both solar and IR RT calculations of V, as long as negligible numbers of particles with $r > 1.7$ μm are included.

4. Global aerosol distribution compilations used in this work did not always provide sufficient resolution to compute V at individual sites.

5. The combined upward scatter and absorption by volcanic aerosols were accurately determined by both RT models, solar and IR, using observed aerosol optical properties and by certain observations of the direct and diffuse solar irradiance.

6. A simple thermal mass model of the globe and each hemisphere can reproduce mean global and hemispheric troposphere temperature anomalies following an eruption, depending on the time response of the ocean. The ocean response time may have varied after Pinatubo as compared to El Chichón.

7. RT models and observations were sufficiently determined so that they can, with caution, be used individually to further investigate aspects of volcanic radiative forcing. However, the thermal mass model should not be used predictively.

6.2.2 Conclusions based solely on observational information accumulated for this study are listed next.

1. El Chichón aerosol remained primarily in the northern hemisphere while Pinatubo eventually spread more evenly to the N. and S. hemispheres. The aerosols from both eruptions displayed banded latitudinal structure.

2. The maximum τ_A immediately following both eruptions was in the tropical regions, with the maximum occurring in the N. hemisphere after El Chichón and in the S. Hemisphere after Pinatubo.

3. There was an accumulation of volcanic aerosol in the northern polar region during the second summer after both eruptions.

4. The globally averaged aerosol optical depth after Pinatubo was greater by a factor of ~2 than after El Chichón.

5. Volcanic $\tau_A(\lambda)$ measured at three globally separated sites displays a maximum in the mid- to long-wavelength portion of the visible spectrum (not shown in detail), which results in an $n(r)$ peak in the 0.3-0.5 μm range.

6.2.3 Conclusions based on the RT models using both observed and hypothetical input information are given in the following.

1. ${}_{Sn}V$ is approximately linearly decreased as underlying albedo is increased, within limited ranges of other variables.

2. The range of aerosol size inversion results obtained from a single set of $\tau_A(\lambda)$ observations does not significantly affect either ${}_{Sn}V$ or ${}_{Ln}V$.

3. Small decreases in solar ω_O, down to 0.98 simulating impurities in the H_2SO_4 droplets, do not significantly affect ${}_{An}V$.

4. ${}_{Sn}V$ was up to an order of magnitude greater and opposite in sign to ${}_{Ln}V$ globally. The effects of this are most readily seen at the surface and transmitted to the rest of the system by mixing. Direct anomalous radiative heating of the atmosphere was dominated by IR warming within the volcanic cloud.

5. Solar radiative anomalies at specified solar zenith angles as large as 35 W m^{-2} were computed and verified with observations to within 10–20%. Seasonal solar mean anomalies were as large as -10 to -15 W m^{-2}. The maximum mean global ${}_{An}V_{Tr}$ was -2.2 and -4.5 W m^{-2} following El Chichón and Pinatubo, respectively, and decreased to < 0.5 W m^{-2} by 2.5 years after the eruption.

6. N. hemisphere summer N-S gradients in ${}_{An}V_{TOA}$ were 16% of the normal and reversed in sign from the first to second year following both eruptions.

7. Simple multiple linear regression fits to model results provides a tool for broader application of this work to higher time and spatial resolution investigations. Aerosol optical depth was by far the most dominant variable, but with others including, albedo, mean daily solar geometry, effective aerosol radius, making statistically significant contributions.

6.3 Concluding Remarks

The spatialotemporal variations of radiative forcing from El Chichón and Pinatubo vary considerably from previously published estimates of volcanic forcing, primarily because actual observed aerosol optical property evolutions were not anticipated or incorporated in those earlier works. Most previous work had concentrated on global or hemispheric mean quantities with uniform spatial distribution and uniform exponential decay with time. Present work agrees with those mean quantities, but permits further use of the radiative perturbation computations because of the spatial resolution. Within-hemisphere zonal variations of the radiative perturbations affect the global temperature gradients and may have a profound influence on atmospheric circulation patterns. Figs. 4.17 and 4.18 show an order of magnitude variation in the net tropopause radiative forcing within a hemisphere. The same magnitude of variation is seen between the two eruptions, for the same latitude and lapse time after each eruption. Observed spatial distributions lead to regionalized forcing, the effects of which are not obvious.

Any conclusions concerning regionalized forcing due to volcanic eruptions are only possible given knowledge of the global evolution of the aerosol using surface-based and satellite observations. The ability to assess climate impact of any future eruptions will require at least comparable global coverage. Availability of these data is not assured, although pending future satellite programs (EOS, SeaWiFS, SAGE III, and AVHRR) will contribute to this need. Ground-based data were extremely useful in this work because of the longevity of some records and the ability to continually obtain accurate $\tau_A(\lambda)$ data during maximum volcanic aerosol concentration. Additional well-located ground sites would be useful to assure better spatial resolution of $\tau_A(\lambda)$ after the next eruption, with or without satellite coverage. Surface measurements complement the satellites by providing economical long-term data that can validate satellite estimates and cover periods

when satellite data are unavailable. Aerosol optical depth data acquired during nonvolcanic periods provides information on background, natural variability, any long-term trends or cycles, and are useful in radiation budget studies in which the level of accuracy is significantly affected by aerosols. The temperature anomalies following future eruptions will be difficult to predict with precision, especially with respect to timing of maximum cooling because of interactions with ocean heat exchange. However, it may be possible, depending on the availability of aerosol optical depth data, to compute the amount of energy removed from the system by the volcanically induced anomaly.

Appendix A. Physical and Optical Properties of Stratospheric Aerosols.

Background stratospheric aerosols have been described in many papers [e.g., Junge et al., 1961; Toon and Pollack, 1973; Hofmann et al., 1975; Russell et al., 1976; Pollack et al., 1981; Turco et al., 1982]. These aerosols are concentrated in a lower layer of unknown origin called the Junge layer; this layer is comprised primarily of sulfates in the submicrometer size range. Optical depth for the background aerosol is about 0.005 in the midvisible range [Russell et al., 1976] and has only a negligible impact on the earth's radiation budget [Turco et al., 1982]. The global distribution of stratospheric aerosols appears to show a tendency for banding with maximums in the tropics and polar regions, a pattern also seen when excess volcanic aerosols are present [Trepte et al., 1994].

Certain types of volcanic eruptions, explosive with high sulfur content, can propel large amounts of SO_2 into the lower stratosphere where it forms small water solution droplets of H_2SO_4 [Turco et al., 1982; Rampino and Self, 1984]. These H_2SO_4 droplets increase the background aerosol optical depth by up to two orders of magnitude [Dutton et al., 1994; and others]. Stratospheric volcanic aerosols are sporadic but long-lived, globally but unevenly distributed, and widely observed but incompletely quantified.

Knowledge of the composition, size, shape, and concentration of these aerosols is required to allow determination of their optical properties as a detailed function of wavelength by using Mie theory if the aerosols are spherical. With the aerosol optical property information, it was possible to proceed with the RT computations necessary to determine V, as discussed in Chapter 3.

A.1 General Physical and Chemical Description

The specific physical/chemical description of the initial volcanic effluent varies among volcanoes, among different eruptions of the same volcano, and during a given eruption depending on the geological setting of the volcano and force of the eruption [Self et al., 1995, and references therein]. The magnitude of V depends strongly on the total quantity of the ejected SO_2 lofted into the stratosphere and subsequently converted to sulfuric acid, H_2SO_4, droplets [Rampino and Self, 1984; Turco et al., 1982; and others]. Pinto et al. [1989] suggested that droplet concentration and mass steadily increases with increasing SO_2 mass up to a point where additional mass begins to sufficiently increase the particle radius (r) and causes increasingly rapid precipitation of H_2SO_4 out of the stratosphere. Pinto et al. also point out that certain chemical feedback processes will limit the conversion of SO_2. Both El Chichón and Pinatubo injected less than 30 Mt SO_2 [Amer. Geophys. Union, 1992], which according to Pinto et al. [1989] was well within the range of linear increase in aerosol optical depth with mass of injected SO_2. SO_2 that reaches the stratosphere forms liquid drops of H_2SO_4/H_2O with an e-folding time of about 30 days [Hofmann and Rosen, 1983; Read et al., 1993; Winkler and Osborn, 1992]. These droplets remain suspended in the stratosphere for up to several years [Cadle et al., 1976; Turco et al., 1982; Yue et al., 1991; Stone et al., 1993].

The properties of material other than H_2SO_4 in the long-lived volcanic cloud are not well known. Other components of the volcanic effluent are either gases (CO_2, H_2O, CO, and HCl) that do not contribute to particle formation in the stratosphere (some water goes into the formation of H_2SO_4 solution), or solid crustal particles that mostly fall out within a few days to one month [Self et al., 1995]. Samples collected by balloon over Wyoming 1.5 to 2 months after the eruption of Mt. Pinatubo showed that 95-98% of all volcanic particles in the stratosphere were aqueous H_2SO_4 with no indication of a solid particle

nucleus [Sheridan et al., 1992]. Small amounts of crustal material have been observed attached to H_2SO_4 droplets, up to one year after the eruption [Shapiro et al., 1984]. Lacis et al. [1992] simulated small additions of crustal material by increasing the aerosol solar absorption to reasonable limits, with only a minor effect on *V*. It is common to consider the long-lived stratospheric aerosols to be solely liquid drops of H_2SO_4 in 75% solution with water [e.g., Pollack et al., 1976; Coakley and Grams, 1976; Harshvardhan, 1979; King et al., 1984; Lacis et al., 1992]. The extent of agreement between RT models that use H_2SO_4 droplets as the sole aerosol material and irradiance observations (as demonstrated in Chapters 4 and 5) indicates that the actual presence of other materials is unimportant.

SO_2 injected into the stratosphere by El Chichón and Pinatubo was estimated to be 8-10 Mt and 16-20 Mt, respectively [Krueger, 1983; Bluth et al., 1992]. These estimates are subject to minor modification [A. Krueger, NASA, Goddard, personal comm.]. Many other eruptions have occurred in the past 20 years [Amer. Geophys. Union, 1992], but have either failed to produce large amounts of SO_2 (e.g., St. Helens in 1980) or have failed to loft a large enough portion of SO_2 into the stratosphere (e.g., Nyamuragira in 1981.) The material making up the aerosols becomes particularly important when considering the material's complex refractive index *(m)* which is necessary to compute scattering and absorption from Mie theory.

Volcanic H_2SO_4 droplets are assumed to be spherical because of the theoretical shape of micrometer and submicrometer size liquid drops and based on direct observations. These drops are spherical because surface tension forces dominate other forces on the liquid molecules, depending on size. Larger drops are subjected to additional forces that can distort their shape; however, for the size range of particles considered in volcanic clouds (< 1.5 μm) such distortions are minor. With concentrations of the droplets in this

size range being < 300 cm^{-3} collisions between droplets that could cause other distortions are virtually nonexistent [Goodman et al., 1994; Deshler et al., 1993]. This concentration and size of particles also relate to the validity of application of Mie scattering theory to multiple spheres as discussed later. Given that the volcanic aerosols of interest are spherical droplets of H_2SO_4 in solution with H_2O, the main additional physical features of interest are size distributions, lifetime in the stratosphere, and their spatial distribution during that lifetime.

A.1.2 Size Distribution

An aerosol size distribution is a size-resolved number concentration *(n(r))* for the aerosol population. The distribution is often expressed as the number of particles within a specified range of sizes, *dn(r)/dr* (or sometimes *dn/dlogr*.) A general description of the evolution of the volcanic aerosol size distribution based on observations and theory was given by Hofmann and Rosen [1983], and Pinto et al. [1989]. The aerosol grows quickly during gas-to-particle conversion, initially from sub 0.1 μm particles to distributions with a peak *r* between 0.15 μm and 0.3 μm, sometimes with a secondary mode at 0.6-1.1 μm, and finally to a distribution with a peak *r* up to 0.4-0.5 μm. This secondary peak is not well understood and was observed to vary with time, altitude, and the size resolution of the measurements. It may result initially due, in part, to the crustal component and later due to growth of droplets from the smaller radius peak. Hofmann and Rosen [1983], Stone et al. [1993], Deshler et al. [1993], and Goodman et al. [1994] all show a second mode near r = 0.7 μm about one year, or more, after the eruptions. Michalsky et al. [1990], Deshler et al. [1993], Goodman et al. [1994], and Dutton et al. [1994] show the evolution of volcanic aerosol size distributions during the first two years following major

eruptions. Various sample volcanic aerosol size distributions used for the current work are given in Chapter 2.

The largest particles in the size distribution have the most significant impact on the IR absorption and may not be well determined because most observational records did not provide reliable data at r ≥1 μm. Balloon sounding data from Wyoming data show no aerosols >1.5 μm [T. Deshler, personal communication.] The Improved Stratospheric and Mesospheric Sounder (ISAMS) on board the Upper Atmosphere Research Satellite (UARS) have provided infrared aerosol optical depths [Lambert et al., 1993] consistent with no significant contribution from particles larger than 1.5 μm. Sensitivity studies presented later show that there was only a small change in ${}_{Ln}V$ as a function of the large particle tail variations. A very strong peak at greater than 1 μm can have important influence on ${}_{An}V$ as investigated by King et al. [1984]. A peak at such a large radius was only rarely reported following El Chichón and was nonexistent in the size distributions deduced for this study.

Stratospheric lifetime of an aerosol is also related to its size by determining its fall velocity [Kasten, 1968]. Other processes such as induced vertical motion due to heating, droplet growth and evaporation, and horizontal and vertical advection also affect stratospheric aerosol lifetimes.

Because of the remoteness of volcanic layers from the ground, greater than 22 km in the tropics for both El Chichón and Pinatubo, opportunities to measure aerosol sizes in situ are limited to occasional aircraft missions [e.g., Shapiro et al., 1984; Goodman et al., 1994] which can only reach the lower portion of the cloud, or are limited to isolated balloon flights [e.g., Hofmann and Rosen, 1983; Deshler et al., 1992]. Remote sensing of the cloud from the surface or moving platform permits estimates of the aerosol size

distributions [e.g., King et al., 1978, 1984; Asano et al., 1993; Dutton et al., 1994] as discussed in Sec. A.2.4.

A.1.3 Geographical Extent

Information on the geographical extent and magnitude of a particular volcanic cloud is crucial to a climatic assessment of *V*, particularly the extent to which heating perturbations will be spatially distributed. There is little ability to predict when or where a volcanic eruption will occur and there is even less ability to estimate its potential climatic impact, i.e., stratospheric injection of SO_2 [Self et al., 1995]. Location and season of a major stratospheric SO_2 injection partially determine the initial global aerosol distribution. The predictable and random components of the stratospheric circulation, coupled with radiatively induced dynamics within the cloud, are responsible for the remaining features of the stratospheric distribution [Young et al., 1994].

Initial estimates of the mass of SO_2, its approximate height, and horizontal dispersal immediately following an eruption can be detected with TOMS sensors. TOMS can only follow the cloud for the first few weeks because of the rate of SO_2 conversion to H_2SO_4. Visible satellite imagery can also detect and track the water vapor and ash in the initial eruption plume, in some cases for two to three weeks during which time the material can complete one circuit around the world [Robock and Matson, 1983]. Ground stations directly in the path of the original plume [e.g., DeLuisi et al., 1983] and reconnaissance aircraft directed to the plume [e.g., Valero and Pilewskie, 1992] also obtain early information on the dispersion of the cloud.

As the long-lived stratospheric aerosol layer forms and spreads it can be detected and quantified by existing surface-based stations where radiometer, sunphotometer, and/or lidar observations exist. Satellites and aircraft play a key role in monitoring the dispersal

of the volcanic aerosols via remote sensing techniques using either atmospheric path attenuation or emission [e.g., Barth et al., 1982; McCormick and Veiga, 1992; Stowe et al., 1992; Sato et al., 1993]. Single or broadband wavelength observations are sufficient to detect and quantify the relative magnitude of the cloud while multiple wavelength observations can also monitor the evolution of the aerosol size distribution. Specific data used for the spatial distributions of El Chichón and Pinatubo are given in Chapter 2.

A.1.4 Height of Aerosol

The height of the aerosol cloud helps establish how long it will take the cloud to settle out of the stratosphere since gravitational settling is a notable removal mechanism [Pinto et al., 1989]. A 0.07-μm radius particle would take five years to fall out of the tropical stratosphere, starting at 25 km, while a 0.3-μm droplet would take just over a year [Lambert et al., 1993]. This second value is roughly consistent with observed e-folding time of stratospheric volcanic optical depth [Stone et al., 1993]. Aerosol height data are also needed for correct placement of the volcanic material in a vertically resolved RT model, however, the modeled V in the troposphere and at the surface has little dependence on the exact height of the lower stratospheric cloud [Lacis et al., 1992].

The cloud height can be measured with lidar [e.g., McCormick et al., 1978; DeFoor et al., 1992; Post et al., 1992] at those sparse locations where such capabilities exist. Height data may also be obtained by certain limb scanning satellites (e.g., Stratospheric Aerosol and Gas Experiment [SAGE] I and II, Stratospheric Aerosol Monitor [SAM] I and II, Solar Mesosphere Explorer [SME], and Upper Atmosphere Research Satellite [UARS]). Balloon and aircraft sensors also provide occasional information.

A.2 Aerosol Optical Properties

Optical properties required to solve the RT equation (discussed in detail in Chapter 3 and Appendix C) are the spectral scattering and absorption optical depths, $\tau_{AS}(\lambda)$ and $\tau_{AA}(\lambda)$, respectively, and the directional scattering pattern described by what is commonly known as the scattering phase function, $P(\theta)$, where θ is the angle between incident and scattered radiation in 3-d space. The relevant spectral range is 0.2-4 μm for solar (SW) and 4-100 μm for the IR. Total aerosol optical depth, $\tau_{AS}(\lambda) + \tau_{AA}(\lambda)$ or $\tau_A(\lambda)$, can be defined in several ways, but it may be most illustrative to refer to Eq. A.1, which describes the total attenuation of a beam of direct radiation.

$$\tau_A(\lambda) = \ln\left(\frac{I_2(\lambda)}{I_1(\lambda)}\right) \qquad \textbf{A.1}$$

In Eq A.1, I_1 is the incident monochromatic intensity and I_2 is the exiting monochromatic intensity from a vertical path through aerosols only. It was assumed that the addition of other atmospheric constituents to the path did not affect $\tau_A(\lambda)$ and each additional contribution was additive to the total optical depth, τ. It is possible to find clear-sky $\tau_A(\lambda)$ directly from observations of the direct solar beam using photometric techniques [e.g., Shaw, 1983; Dutton et al., 1994; and discussion in Sec. 2.1.1]; however, it is not possible to use only $\tau_A(\lambda)$ to separate the scattering and absorbing components, or to deduce any information about the phase function. Numerous and extensive, but incomplete, observations of $\tau_A(\lambda)$ after Pinatubo and El Chichón will be extremely useful in computing the related *V*.

Techniques have been developed to measure or estimate aerosol absorption from observations, either in situ or remotely [e.g., Rosen et al., 1978; Ogren et al., 1981; Clark

and Charlson, 1985]. Most require specialized equipment that was not widely deployed for making extensive atmospheric observations. One approach was to obtain an estimate of aerosol refractive index, $m = n_r - in_i$, and compute $\tau_{AS}(\lambda)$ from Mie calculations. The refractive index for H_2SO_4 in various percentages solution with water has been given by Palmer and Williams [1975]. The absorption of solar radiation by volcanic aerosols is expected to be small because $n_i < 10^{-4}$ for H_2SO_4, which is below the limits of detectability of observation techniques. Aerosol absorption is often expressed in terms of the single scatter albedo, $\omega_o = \tau_{AS}(\lambda) / \tau_A(\lambda)$. Ogren et al. [1981] and Clark et al. [1983] report stratospheric $\omega_o > 0.98$ following the eruptions of Mt. St. Helens and El Chichón, respectively; this value was consistent with an H_2SO_4 aerosol with a small amount of contaminant. At the longer solar wavelengths and in the thermal IR n_i becomes large and the absorption by a sufficient concentration of droplets is significant.

Few techniques for directly measuring $P(\theta)$ have been developed [Tanaka et al. 1989] and no results following El Chichón or Pinatubo are known to have been reported. Directional scattering of solar wavelengths by $0.2 < r < 1.0$ μm spherical particles is largely in the forward direction [van de Hulst, 1957]. Since the amount of energy lost to the troposphere is mostly in the backscattered portion, small changes in the scattering pattern could make large percentage changes in lost energy. For RT computations, reliance is generally placed on $P(\theta)$ found from Mie theory after having determined a size distribution [e.g. King et al., 1984 and Hansen et al., 1992]

A.2.1 Mie theory

The mathematical solution describing the absorption and directional scattering by a single isolated spherical particle whose size is near or larger than the wavelength of incident radiation is typically attributed to G. Mie in 1908 and has historically been called

Mie scattering theory. (Stephens [1994] points out that identical but earlier work was done by Lorenz in 1890 with contributions from Clebsch in 1863, and that there is a current movement to rename Mie theory to Lorenz-Mie theory.) Several expanded recent works have provided the mathematical tools for routine Lorenz-Mie solutions [van de Hulst, 1957; Wiscombe, 1980; Bohren and Huffman, 1983]. A useful and well-tested computer code, called MIEV0, for Mie scattering by a single spherical particle was distributed by W. Wiscombe (at NASA/Goddard) and was the basis of the Mie calculations in this work.

The Mie solution to attenuation by a spherical particle yields a scattering and absorption efficiency, Q_S and Q_A, and a complex amplitude function, $S(\Theta)$, which contains the directional dependence after van de Hulst [1957]. These quantities have λ, r, and m dependencies. The λ and r dependencies are carried by the size parameter, $x = 2\pi r/\lambda$. For a given value of x and m, the scattering and absorption extinction cross section for a single particle is then given as $2\pi r^2 Q_S$ and $2\pi r^2 Q_A$, respectively, and the phase function is given by Eq. A.2. MIEV0 returns Q_S, Q_A, and $S(\Theta)$ and the Legendre coefficients (a_l)

$$P(\Theta) = 4\pi \frac{|S(\Theta)|^2}{\int_{4\pi} |S(\Theta)|^2 d\Omega} \qquad \textbf{A.2}$$

where: Ω = solid angle

$$P(\Theta) = \sum_{l=0}^{n} a_l P_l \qquad \textbf{A.3}$$

necessary to express the phase function as a Legendre expansion given by Eq. A.3, where P_l is the lth Legendre polynomial and $n+1$ is the number of terms to be used.

A.2.2 Mie calculations for a population of spheres

Scattering and absorption by a population of aerosol particles are frequently found by applying the assumption that the particles are sufficiently separated in space such that there is no interaction between them, and then integrating their individual contributions [Diermendjian, 1969; Hansen and Travis, 1974]. Total vertical column aerosol number concentrations following volcanic eruptions can be as high as several times 10^7 cm^{-2} at an aerosol radius of 0.3 μm. This translates to the aerosols' maximum optical cross sections filling 5% to 6% of a cm^{-2}. Although there is no fixed value at which the noninteraction assumption becomes invalid, these seem near the upper limit. The noninteraction and summation assumptions are used for all applications in this work.

Optical properties over a broad range of wavelengths for a population of spherical particles can be directly computed from Mie solutions if size distribution and refractive indices are known, using Eqs. A.4-A.6. When numerically integrating over the size population it is necessary to sum over individual cross sections and amplitude functions, and then compute resulting extinction and phase function using the total geometric cross-

$$\tau_{AS}(\lambda) = \int_r \pi r^2 Q_s(\lambda,r) n(r) dr \qquad \textbf{A.4}$$

$$\tau_{A}(\lambda) = \int_r \pi r^2 Q_e(\lambda,r) n(r) dr \qquad \textbf{A.5}$$

$$P(\Theta,\lambda) = \frac{1}{\tau_{AS}} \int_r 2\pi r^2 Q_s(\lambda,r) P'(\Theta,\lambda,r) n(r) dr \qquad \textbf{A.6}$$

section of all particles [Hansen and Travis, 1974]. All computed quantities in Eqs. A.4 - A.6 still have a spectral and aerosol refractive index dependence. A computer program, MIEV0X, was written, based on MIEV0, to compute the extinction efficiencies, Legendre weights, and integrate using Eqs. A.4-A.6 for all necessary wavelengths. Computed extinctions and phase functions for test size distributions are compared to those of Diermendjian [1969] in Table A.1.

Table A.1 Aerosol population optical properties computed by MIEV0X compared to Diermendjian (1969)

Aerosol		Diermendjian					MIEV0X				
Model	λ	τ	ω_o	P(0)	P(90)	P(180)	τ	ω_o	P(0)	P(90)	P(180)
Haze M	0.7	.105	1.000	5.17	.008	.0192	.106	1.000	5.18	.009	.0197
Haze M	1.19	.088	1.000	2.86	.009	.0109	.089	1.000	2.85	.007	.0108
Haze L	1.19	.022	1.000	1.52	.015	.0099	.023	1.000	1.52	.013	.0098
Haze L	1.94	.0089	.9804	.925	.029	.0139	.0090	.9804	.920	.018	.0133
Haze H	0.70	.0099	1.000	.954	.012	.0109	.0100	1.000	.952	.014	.0109
Haze H	1.94	.0007	.9443	.255	.096	.0467	.0007	.9443	.255	.049	.0467
Haze H	3.00	.0039	.0814	.174	.114	.0783	.0039	.0814	.174	.057	.0783

A.2.3 Size distributions from Mie inversion theory

Inverse Mie calculations can be preformed to derive estimated aerosol size distributions from $\tau_A(\lambda)$ observations and a reasonable value of *m* [e.g., King et al., 1984]. This was accomplished by the iterative solution of Eq. A.5 for *n(r)* as described by Yamamoto and Tanaka [1969] and King et al. [1978]. Application of inverse techniques requires consideration of observational error and the fact that the inversion process does not yield a unique solution. Inversion solutions using King's method are constrained according to a specified uncertainty in $\tau_A(\lambda)$. This uncertainty is difficult to quantify accurately. Sensitivity of RT models to varying Mie inversions for a single $\tau_A(\lambda)$ is

discussed in Appendix D. Following is a discussion of the Mie inversion process using computer code supplied by M. King (NASA, Goddard) and called RADINV.

A refractive index of 1.45 + 0.00i is appropriate for H_2SO_4 over a wide range of solar wavelengths and was used here in RADINV. The Q_S and Q_A for a large range of x were computed from forward Mie theory with the results saved for subsequent computations for a range of wavelengths. $\tau_A(\lambda)$ and an estimate of its accuracy were specified. A first guess size distribution was taken as the linear log-log distribution proposed by Junge [1963] which can easily be calculated from one parameter (slope) fit to the $\tau_A(\lambda)$ vs. λ data. Inversion outcomes are sensitive to the first guess solution. Inversions are also sensitive to the particle size range over which a solution is sought. Size range should be restricted to the approximate wavelength range in input $\tau_A(\lambda)$, since information beyond that range diminishes quickly. The exact size range cannot be uniquely specified and solutions are not always found, depending on the variability and uncertainty in $\tau_A(\lambda)$. When a solution is found, the size distribution will closely reproduce the $\tau_A(\lambda)$ observations in forward Mie calculations, subject to specified convergence limits and the uncertainty in the observation. For El Chichón, Pinatubo, and background cases, a solution was most always obtained for the Junge best fit initial guess and size range from 0.1 ±0.02 μm to 0.9 ±0.2 μm. This range closely bounds the $\tau_A(\lambda)$ observations used and is near the expected and observed range of most aerosol sizes.

Relationships between directly observed and inverted *n(r)* are investigated in Chapter 5, Sec. 5.1.1. Uncertainties are known to exist in both sources of *n(r)* information and ideal comparisons were not possible. Inverted size distribution will be used for most of the investigations of V because $\tau_A(\lambda)$ observations are more continuous and common.

Comparisons in Sec. 5.1.1 between V computed with inverted $n(r)$ and computed with directly observed $n(r)$ show only minor differences.

A.3 Summary

Given that a volcanic cloud is H_2SO_4 spheres in 75% solution, aerosol optical properties necessary for RT calculations can be found, if accurate $\tau_A(\lambda)$ observations are available. The approach of using $\tau_A(\lambda)$ inversions instead of directly observed size distributions was taken because continuous time series of $\tau_A(\lambda)$ are more abundant and because it insures that reasonable spectral extinction will be introduced into the RT models. The number of wavelengths, the frequency of observation, and the spatial distribution of available measurements will determine the resolution and completeness of V that can be computed for any given eruption. An important task becomes acquiring, assembling, and validating sufficient information on a global scale.

Appendix B. Observational Uncertainties

The observations used in this study are subject to potentially large and detrimental errors. Comparison between observed and calculated V will be no better than the combined errors of the two. It was, therefore, important to be aware of observational errors when introducing observations into models and when contrasting models with the observations for verification. Following is a summary of the possible errors believed to exist in the observational data used in this work.

B.1 Monochromatic Optical Depth

An analysis of possible errors in sunphotometer observations of $\tau_A(\lambda)$ was given by Russell and Shaw [1975], Dutton et al. [1984], Reddy et al. [1990], and Russell et al. [1993], among others. Errors arise from calibration, wavelength specification, Rayleigh and path determination, temperature sensitivities, temporal stability, and instrument sensitivity and resolution. Typically, a well calibrated and characterized narrow band sunphotometer will produce aerosol optical depths to within 0.015 optical depth units. Observations under ideal conditions where the assumptions implicit in the Langley calibration process are frequently valid can consistently yield τ to within ± 0.002 [Dutton et al., 1994].

Subtraction of the tropospheric background to obtain perturbed stratospheric optical depths introduces additional error for the applications here. Such errors are not easily quantified since the observed value is a vertically integrated sum of the two. The

standard deviation of the background tropospheric aerosol is a measure of uncertainty caused by the subtraction of that aerosol from that following a volcanic event. At MLO the normal background aerosol optical depth is 0.007 at 500 nm and is generally considered insignificant in the presence of a major volcanic eruption, except for the determination of return to background. At other sites where tropospheric aerosols are more abundant the problem is more serious [Kent et al., 1994].

Accurate stratospheric aerosol optical depths should be obtained from the SAM I and II and SAGE I and II satellites because they are self-calibrating relative to the actual extraterrestrial solar constant with each orbital scan. This was true until the sensors fail to detect the sun through aerosol saturated paths. The SAGE II data saturates near τ_A = 0.02 km^{-1} (vertical extinction) [Thomason, 1992] varying with wavelength depending mostly on the wavelength dependence of Rayleigh scattering. Until saturation begins, SAGE II optical depth should be accurate to better than 0.001, according to thresholds reported by Thomason [1992]. During the Pinatubo event these accuracies were maintained for the edges of the initial spreading cloud and for the upper layers of the cloud where less aerosol resided [Pitts and Thomason, 1993]. Attempts are underway to correct for the saturation [L. Thomason, NASA/Langley, personnel communication] using independent observations and reasonable downward extrapolations when saturation was encountered. Also, SAGE II takes approximately 45 days to complete a global survey, not including polar regions. Zonal averages, such as those used by Sato et al. [1993], formed from this data have unknown additional uncertainty due to these data gaps. While longitudinal variability in the Pinatubo aerosol was observed by SAGE II, AVHRR, and ERBE [Minnis et al., 1993], it was not specifically considered in the current work.

B.2 Wideband Optical Depth

The wideband aerosol optical depth derived from AVHRR channel one (0.55-0.71 μm) [Rao et al., 1989 and Stowe et al., 1992] have not been assigned an uncertainty by the authors. Other data sources now suggest that the AVHRR τ_A data are accurate to within ~0.05 (Fig. 2.7), although this accuracy may be per chance since the procedures used in the derivation of the AVHRR τ_A are applicable specifically to tropospheric aerosols.

Wideband aerosol optical depths reported by Dutton and Christy [1992] have a higher level of uncertainty than monochromatic observations because of the dependence on absolute calibration and more complex data reduction. An accuracy of no better than 0.03 was assigned to that data. Those τ_A(vis) have been quantitatively used in this work only to evaluate the general global distribution of aerosols, examine the relative impact at several sites between the two eruptions, and to scale local $\tau_A(\lambda)$ when no better information was available.

B.3 Size Distributions

Hofmann and Rossen [1984], Oberbeck et al. [1983], Knollenburg and Huffman [1983], Deshler et al. [1993], and Pueschel et al. [1994] discuss uncertainties in some types of direct aerosol size distribution measurements. Published error bars suggest <10% error in the size range of 0.1-0.6, and up to >100% at the larger sizes. Common error sources are due to inlet losses and calibrations. King et al. [1978] present an error analysis of their size inversion procedures, which obviously varies with the accuracy of input information. Inverted size distributions were compared to those directly observed in order to confirm inversion performance (Fig. 2.10 and Pueschel et al. [1994]).

B.4 Solar Irradiance

Accuracy and precision of solar irradiance observations using surface-based pyranometers is a well-studied subject [e.g., Dutton et al., 1985b; Meyers, 1988; Kozelmann et al., 1993]. Lack of pyranometer accuracy was blamed, in part, for failure to verify computed $_{Sd}V$ following Agung [Coakley, 1981] and following El Chichón [Mass and Portman, 1990]. The absolute accuracy of a typical pyranometer of U.S. manufacture can be held to better than ±0.5% under clear skies when nonlinear calibration functions are used [Nelson and Dutton, 1994]. Typically, only linear calibration scaling factors were applied in the pyranometer data reduction. For the linear scaling factors the percentage errors can become large, >5%, for zenith angles ≥75° due to typical cosine response errors in the instrument. For selected instruments with better than average cosine response error, the total error can be ≈ 5 W m^{-2} or 1%, whichever is larger, over the entire range of zenith angles [Dutton, 1990b]. Because of the sensitivity to zenith angle, measurements made at the same zenith angle with the same stable, or frequently calibrated, instrument should be used when looking for a small temporal change in irradiance.

Concerns over pyranometer cosine response errors are reduced if the total solar irradiance is measured with a combination of a pyrheliometer and a shaded, diffuse, pyranometer. In this configuration, the pyranometer is always measuring only the diffuse sky irradiance, which is subject to less cosine response error. The MLO total irradiance data were acquired in this manner and the pyrheliometer was routinely (monthly) intercompared with an active cavity radiometer, Eppley Kendall #12843. These MLO data are expected to have better than normal accuracy, < ±1% over long periods. At other sites used in this study the typical well-executed pyranometer accuracies of ±2% and short-term precision of ±1% apply for $\theta_0 < 70°$.

Temporal drift in the pyranometer sensitivity is a potential major source of error once an instrument is calibrated and sent to the field; therefore, the rate of sensor sensitivity change must be known. Although not all of the post Pinatubo calibrations have been completed, all the surface irradiance data acquired and used here were from instruments known to have less than ~0.5% per year drift. Errors of interest here are relative errors over 1- to 2-yr periods and are, therefore, < 1%. However, automated unattended operation of these instruments, and other surface-based instruments discussed previously, can invite gross errors such as those due to shading and other obstructions of the sensors. Such obvious errors have been removed from the data base during editing operations.

Appendix C. Radiative Transfer Equation and Atmospheric Models

The basic RTE has been developed using physical aspects of the transmission of electromagnetic radiation through a homogeneous, semitransparent, absorbing, scattering, and emitting medium. Its derivation and commonly used geometry and notation are given in several text books and references. The recent formulations given by Liou [1992] are used in the following development. Eq. C.1 is an expression of the RTE in its most general form.

$$dI_\lambda = (I_\lambda - J_\lambda)\,d\delta_\lambda \qquad \textbf{C.1}$$

where:

I_λ = incident radiation from one direction into a volume;

dI_λ = net gain or loss of radiation within the volume, along the original direction;

J_λ = any sources into the forward direction;

$d\delta_\lambda$ = slant path optical depth of the volume;

(Note: λ dropped in subsequent development except where necessary for clarity).

The source term in Eq. C.1 includes both the emission and scattering into the path. Emission into the path *(B)* is given by Planck's Law, Eq. C.3,

$$J = B + M_S \qquad \textbf{C.2}$$

$$B(\lambda,T) = \frac{2h\nu^3c^2}{e^{hc\nu/k'T}-1} \qquad \textbf{C.3}$$

where:

h = Plank's constant;

$\upsilon = 1/\lambda$;

k' = Boltzmann constant;

c = speed of light;

T = temperature (K).

The multiple (first term RHS) and single scatter (second term RHS) into the direction of the original beam can be formulated by Eq. C.4,

$$M_S = \frac{\omega_o}{4\pi}\int_0^{2\pi}\int_{-1}^{1} I(\tau,\mu)P(\mu,\mu')\,d\mu'd\phi + \frac{\omega_o}{4\pi}F_oP(\mu,\mu_o)e^{-\tau/\mu_o}, \qquad \textbf{C.4}$$

where:

μ = cos(θ), θ is the angle of interest relative to a reference plane;

P = Scattering phase function, describing the scatter from μ' into μ;

F_O = incident solar irradiance;

μ_O = cosine(θ_O), θ_O is the solar zenith angle.

As is common in many RTE solutions, P is replaced by its Legendre series representation, Eq. C.5.

$$P(\theta) = P(\mu,\mu') = \sum_l a_l P_l(\mu)P_l(\mu') \qquad \textbf{C.5}$$

Two separate equations were conveniently developed, one accounting for only solar radiation, $\lambda \leq 3.0$ μm, and the other for thermal IR, $\lambda \geq 4.0$ μm. The lower limit for the solar and upper limit for the IR are determined by the tails of the Planck function when the integrated area under the Planck curve is no longer significantly contributed to by shorter (solar) or longer (IR) wavelengths. These limits were chosen to be 0.18 μm and 100 μm, respectively, where less than 1.3% of the Planck energy (at representative temperatures) lies beyond either of those limits. The justification for the separation of solar and IR at ≈ 3.5 μm for earth climate related studies is fourfold, although the exact boundary is arbitrary within the approximate range of 3-5 μm. First, there is insignificant energy at longer wavelengths in the sun's emission spectrum (as measured at a distance of 1 A.U. from the sun) at longer wavelengths. Second and similarly, there is negligible energy at shorter wavelengths for Planck curves at terrestrial temperatures. Third, the scattering described by Eq. C.4 is small, $\omega_o < 0.05$ in the IR wavelengths (see Fig 2.8), such that multiple scatter can be neglected. Fourth, a variable-geometry direct-beam source need only be included for the solar source. Therefore, two simplified monochromatic RTEs can be developed, which when spectrally integrated over separate ranges, adequately account for the radiative energy in the atmosphere.

C.1 Solar Radiation Model

The RTE applicable to solar wavelengths was formed by dropping the emission terms from Eqs. C.2 and C.1 and addressing the complexity of the multiple scattering term. Multiple scattering becomes important at shorter solar wavelengths in Rayleigh scattering, over a large range of wavelengths in water/ice clouds, and with larger aerosol optical depths ≥0.3 [van de Hulst, 1957], such as encountered after volcanic eruptions. Maximum vertical aerosol optical depths encountered after El Chichón and Pinatubo were

0.4-0.6, but when slant paths are considered, these are increased accordingly, approximately as $1/\cos(\theta_o)$.

A goal was to be able to compute upward and downward solar irradiance at various levels in the atmosphere given seasonally variable incident solar intensity and geometry at the top of the atmosphere, optical properties of the atmosphere, and surface reflection. Optical properties include total optical depth (τ), the relative scattering and absorption, or attenuation, by aerosols and molecules ($1-\omega_o$ and ω_o), and P; all as a function of wavelength.

The coordinate system used with the RTE is shown in Fig. C.1, where the vertical coordinate is optical depth and the horizontal domain is taken as infinite and plane parallel. θ defines the direction of travel, relative to the vertical for a given radiant beam; $\theta = 0$ is directed downward. Individual streams of radiation are denoted by the directions μ_i. The plane-parallel assumption is most valid near the earth's surface and degenerates with height where downward beams do not necessarily intersect the earth's surface. (From an altitude of 30 km, the earth's limb subtends an angle of 169^o, such that downward directed energy between $\theta = 90^o$ and 84.5^o in the plane-parallel coordinate system will not intersect the earth's surface.) Solar energy lost from the surface in spherical compared to plane-parallel coordinates at these and lower altitudes is minimized because of the small range of affected angles, the forward and backward peaked Mie scatters, and the solar zenith angles at which most of the daily integral energy is received. The plane-parallel coordinates will be considered valid up to the altitudes of interest in this work, $\leq$ 30 km, although calculations to complete the vertical profile are carried out for higher altitudes. Azimuthal variations are not considered in the subsequent development.

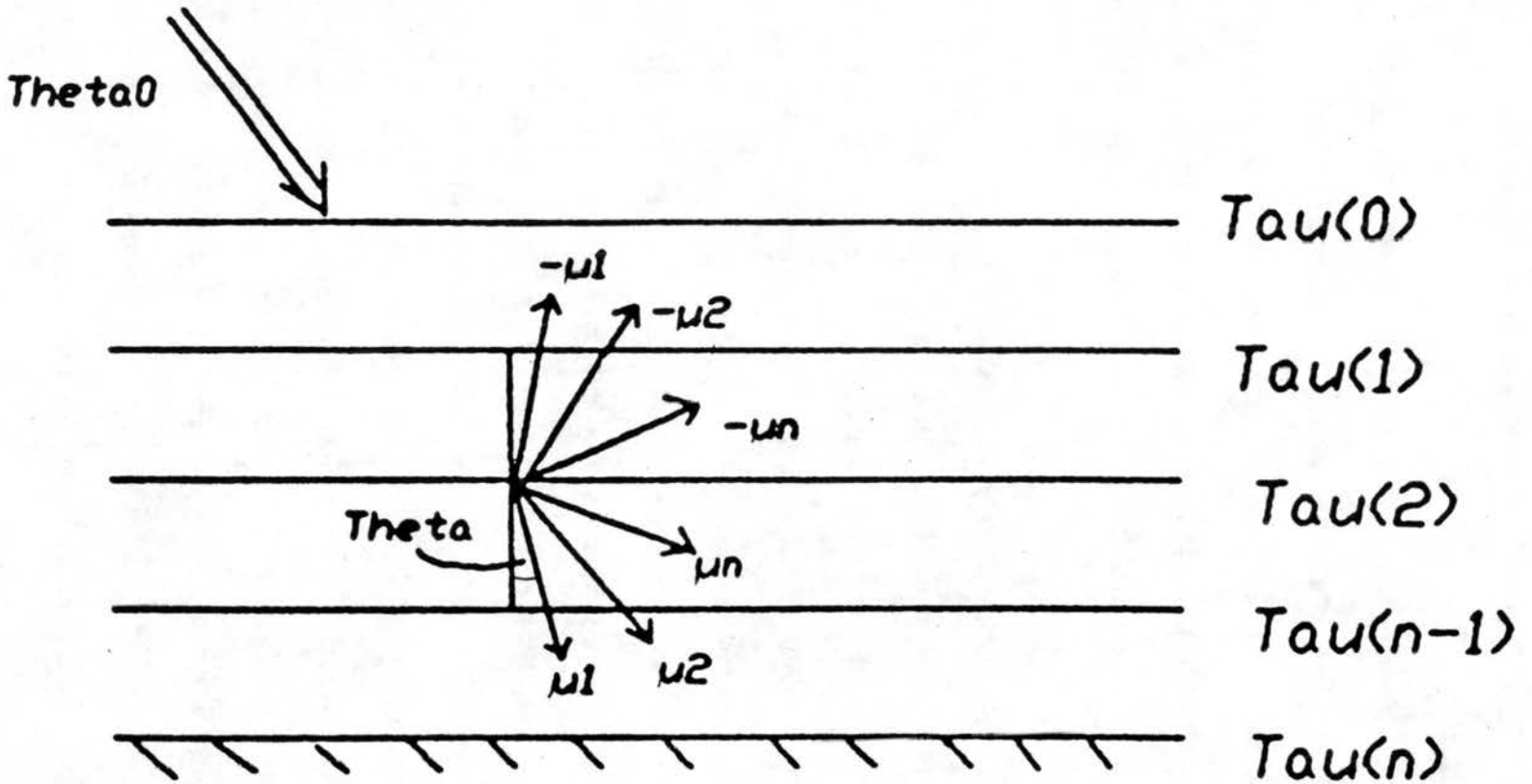

Fig. C.1 Schematic of vertical and angular structure of the DISORT (and DISORTX) RT models, with n = 33 and n' = 5. in DISORTX. "Theta0" is incident solar irradiance at TOA.

It is convenient to separate the solar RTE into two separate equations, one for the directly transmitted solar beam, and one that describes the diffusely transmitted or reflected (scattered) radiation, with the total resultant flux at any level being the sum of vertical components of the two. Directly transmitted radiation is given by the straight forward solution of Eq. C.6.

$$I = I_O e^{-\tau/\mu_O} \qquad \textbf{C.6}$$

The basic RTE for diffuse solar radiation (radiance) is obtained by substituting Eq. C.5 into Eq. C.4 and combining Eqs. C.1, C.3, and C.4. Then, ignoring thermal sources and assuming azimuthal independence gives Eq. C.7,

$$\mu\frac{dI}{d\tau} = I - \frac{\omega_o}{2}\sum_{l=0}^{N} a_l P_l(\mu)\int_{-1}^{1} P_l(\mu')I\,d\mu' - \frac{\omega_o}{4\pi}\sum_{l=0}^{N} a_l P_l(\mu)P_l(-\mu_O)F_o e^{-\tau/\mu_o} + \delta_{(\mu,\mu_o)}\mu_o F_o e^{-\tau/\mu_o} \qquad \textbf{C.7}$$

where: $\delta_{(\mu,\,\mu O)} = 1$ if $\mu = \mu_o$, or $= 0$ if $\mu \neq \mu_o$.

Because of the nonlinear term, $I(\mu)P_l(\mu')$, the direct analytical solution to the solar RTE is not possible. Various approximate solutions to Eq. C.7 have been advanced and are commonly used. Arbitrarily accurate solutions are possible, depending on the number of quadrature angles used, by discretizing the equation and solving a system or ordinary differential equations. Recent improvements in numerical techniques have provided a practical and stable method for accomplishing this solution for nonhomogeneous atmospheres [Liou, 1980; Stamnes et al., 1988; and references therein]. The DO technique is adapted here to obtain irradiance fields in a realistic atmosphere, influenced

by stratospheric volcanic aerosols. The DO solution is summarized below, after Liou [1992].

The integration over zenith angle is replaced with a summation over Gaussian quadrature angles, as in Eq. C.8.

$$\int_{-1}^{1} f(x) = \sum_{i} \chi_i f(x_i) \qquad \textbf{C.8}$$

In Eq. C.8, χ_is are appropriate quadrature weights [Liou, 1980]. Substituting Eq. C.8 into Eq. C.7 and dropping the second direct beam term gives:

$$\mu \frac{dI(\tau,\mu_i)}{d\tau} = I - \frac{\omega_o}{2} \sum_{l=0}^{N} a_l P_l(\mu_i) \sum_{j=-n}^{n} P_l(\mu_j) \chi_j I(\tau_i,\mu_j) - \frac{\omega_o}{4\pi} \sum_{l=0}^{N} a_l P_l(\mu) P_l(-\mu_o) F_o e^{-\tau/\mu_o} . \qquad \textbf{C.9}$$

Eq. C.9 can be simplified by choosing for $j = 1 \ldots n$ for μ_j, $j = -1 \ldots -n$ for $-\mu_j$, μ_O for the solar zenith angle, defining $\chi_O = 1$, and combining the following definitions:

$$c_{i,j} = \frac{\omega_O}{2} \chi_j \sum_{l=0}^{N} a_l P(\mu_i) P_l(\mu_j), \qquad \textbf{C.10}$$

$$b_{ij} = \frac{c_{ij}}{\mu_i} - \frac{\delta_{ij}}{\mu_i}, \qquad \textbf{C.11}$$

$$I(\tau,\mu_O) = e^{-\tau/\mu_O} \frac{F_O}{2\pi}. \qquad \textbf{C.12}$$

For Legendre Polynomials, $c_{i,-j} = c_{-i,j}$ and $c_{-i,-j} = c_{i,j}$ for $j \neq -0$, thus

$$\frac{dI(\tau,\mu_i)}{d\tau} = \sum_{j=-n}^{n} b_{i,j} I(\tau,\mu_j). \qquad \textbf{C.13}$$

Denoting vectors of upward and downward streams by $\boldsymbol{I}^+$ and $\boldsymbol{I}^-$, respectively:

$$\begin{aligned} \boldsymbol{I}^+ &= I(\tau,\mu_i)_{i=1\to n} \\ \boldsymbol{I}^- &= I(\tau,-\mu_i)_{i=1\to n} \end{aligned} \qquad \textbf{C.14}$$

and

$$\begin{aligned} \boldsymbol{b}^+ &= b_{i,j} = b_{-i,-j} \\ \boldsymbol{b}^- &= -b_{-i,j} = b_{i,-j}. \end{aligned} \qquad \textbf{C.15}$$

Combining the above gives:

$$\frac{d}{d\tau}\begin{bmatrix} \boldsymbol{I}^+ \\ \boldsymbol{I}^- \end{bmatrix} = \begin{bmatrix} \boldsymbol{b}^+ & \boldsymbol{b}^- \\ -\boldsymbol{b}^- & -\boldsymbol{b}^+ \end{bmatrix} \begin{bmatrix} \boldsymbol{I}^+ \\ \boldsymbol{I}^- \end{bmatrix}. \qquad \textbf{C.16}$$

Here, $\boldsymbol{b}^+$ and $\boldsymbol{b}^-$ represent the transmission and reflection from above the intervening layer represented by $d\tau$, and $-\boldsymbol{b}^+$ and $-\boldsymbol{b}^-$ represent transmission and reflection of a radiant beam from below the layer.

Equation C.16 constitutes a system of ordinary differential equation for which a solution is possible. One possibility is to assume a homogeneous solution of the form

$$I^{\pm} = \phi^{\pm} e^{-\kappa\tau} \qquad \text{C.17}$$

$$\begin{bmatrix} b^{+} & b^{-} \\ -b^{-} & -b^{+} \end{bmatrix} \begin{bmatrix} \phi^{+} \\ \phi^{-} \end{bmatrix} = -\kappa \begin{bmatrix} \phi^{+} \\ \phi^{-} \end{bmatrix} \qquad \text{C.18}$$

given by Eq. C.17. Substituting Eq. C.17 into Eq. C.16 gives Eq. C.18, which is a standard eigenvector/eigenvalue problem for which numerical solutions exist. Stamnes t al. [1988] show further simplification by recognizing the symmetry of the b matrix that

$$(b^{+}-b^{-})(b^{+}+b^{-})(\phi^{+}+\phi^{-}) = \kappa^{2}(\phi^{+}+\phi^{-}) \qquad \text{C.19}$$

allows Eq. C.18 to be reduced to C.19 by expanding Eq. C.18, adding and subtracting the two equations and solving for $(\phi^{+} + \phi^{-})$. Equation C.19 is also an eigenvalue problem and is solved for $(\phi^{+} + \phi^{-})$ which is substituted into equations from intermediate steps in deriving C.19 to solve for ϕ^{+} and ϕ^{-}, which, with κ, are substituted into Eq. C.17 to obtain radiances. A final complete solution is possible when appropriate boundary conditions at the top and bottom are specified. The numerical details of solving Eq. C.19 and application to a vertically inhomogeneous medium were given by Stamnes et al. [1988] and references therein.

Downward and upward diffuse irradiance is computed from:

$$F_{dif}\downarrow = 2\pi \int_{0}^{1} I(\tau,\mu)d\mu$$
$$F_{dif}\uparrow = 2\pi \int_{-1}^{0} I(\tau,\mu)d\mu. \qquad \text{C.20}$$

The vertical component of the direct solar beam, at any height τ is given by

$$F_{dir} = \mu_O F_O e^{-\tau/\mu_O} \qquad \textbf{C.21}$$

and spectral integration for the solar downward *(SD)*, upward *(SU)*, and net *(SN)* irradiance are given by :

$$SD = \int_{0.2}^{3.0} (F_{dir} + F_{dif}\downarrow) d\lambda ,$$

$$SU = \int_{0.2}^{3.0} F_{dif}\uparrow d\lambda , \qquad \textbf{C.22}$$

$$SN = SD - SU .$$

C.2 Thermal Infrared Radiation

IR is considered here solely originating from the earth's surface or atmosphere. Multiple scattering and reflection in the thermal infrared are generally negligible since for the aerosols ω_o is < 0.05 (Fig. 2.8) and ground and water surface emittance is near 1.0. The applicable radiative transfer equations are developed from Eq. C.1 and C.2 excluding solar sources and multiple scattering terms, as given by:

$$\mu \frac{dI}{d\tau} = I - B \qquad \textbf{C.23}$$

The solution to Eq. C.23 is obtained by multiplying by $e^{-\tau/\mu}$, rearranging terms, and integrating from one level to another. This yields:

$$I(\tau,\mu) = I(\tau^*,\mu)e^{-(\tau^*-\tau)/\mu} + \frac{1}{\mu}\int_{\tau}^{\tau^*} B(T)e^{-(t-\tau)/\mu}dt. \qquad \text{C.24}$$

In Eq C.24, τ and τ^* are taken at the top and bottom of the layer, respectively. (Note: single scattering out of a beam is accounted for by using total optical depth in the attenuation terms.) Irradiances were formed from computed radiances as before with Eq. C.20.

C.3 RTE Model Implementations

Useful implementation of the solutions to RTE for climate related problems in the atmosphere requires integration over wide spectral ranges and must account for the vertical, horizontal, and temporal inhomogeneities of the atmosphere. Widely used and tested numerical solutions to Eq. C.18 and Eq. C.24 applicable to the earth's atmosphere have been provided by Stamnes et al. [1988] and Kneizys et al. [1988], respectively. Application of each to the current problem is given next.

C.3.1 DISORT, solar wavelengths

The Stamnes et al. [1988] solution to Eq. C.18 through Eq. C.20 was distributed by the authors in Fortran code called DISORT. DISORT computes monochromatic radiances and irradiances for a layered medium where τ, ω_0, and P are specified for each layer and the upper and lower boundary conditions, incident irradiance at the top, and surface reflection at the bottom, are given. For irradiances, the number of quadrature angles, or streams, must be specified and P provided and resolved accordingly. P is input as the Legendre weights, a_l, which were computed by MIEV0X, if the size distribution and

refractive index are known. The vertical coordinate in DISORT is accumulated τ, starting with 0 at the top. Upward and downward irradiances and/or radiances can be returned at any value (level) between 0 and τ.

The complete atmospheric solar radiative transfer model developed here, based on DISORT, will be subsequently called DISORTX. Figure C.1 identifies the layer structure for the multilevel model developed to account for the inhomogeneous atmosphere. DISORTX has 33 layers, 16 for Rayleigh and 17 for gases and aerosols. Gaseous absorption of O_3, O_2, H_2O, and CO_2 are accounted for. For the shorter wavelengths (< 0.65 μm) the molecular absorption coefficients were used. At wavelengths longer than 0.65 μm the correlated *k*-distributions [Lacis and Oinas, 1991] for O_3, H_2O, and CO_2 were used to account for highly structured spectral gaseous attenuation.

Atmospheric constituent concentrations and their spectral optical properties were not provided with DISORT. The five seasonal and latitudinal variable model atmospheres of McClatchey et al. [1972] – mid-latitude winter and summer, subarctic winter and summer, and tropical – were used to incorporate vertical profiles of O_2, O_3, H_2O, CO_2, air density, and air temperature into the models. Air pressure and temperature were required to scale the absorber amounts and to specify Rayleigh scattering, as discussed in Sec. C.3.2 and Sec. C.3.1.2, respectively.

C.3.1.1 Correlated *k*-distributions

Spectral integration of the RTE is complicated by terms in Eq. C.18 that include $e^{-\tau}$ because τ is highly variable over narrow spectral ranges. Band models have been developed [e.g., Goody, 1952], which allow $e^{-\tau}$ in the RTE to be replaced by a statistical transmission function. Pressure and temperature dependencies of the band models were explicitly accounted for over a defined homogeneous absorber path. This approach becomes invalid in vertically nonhomogeneous atmospheres, particularly when multiple

scattering is included, because specifying temperature and pressure dependencies of absorption coefficients over the large variety of paths is impossible. The vertically correlated *k*-distribution method of Lacis and Oinas [1991] offers an approach by which spectral integration can be carried out over wide (5-70 nm) intervals under these conditions because the line-by-line temperature and pressure dependencies are retained. The vertical correlation of the *k*-distribution allows the same bands to be used over the entire vertical range of the model, assuming only that the relative positions of the strong and weak bands do not change. While this assumption is not strictly valid, the accuracy of the correlated *k*-distribution method is within 1% of the line-by-line models over a wide range of conditions [Goody et al., 1989; Lacis and Oinas, 1991].

The *k*-distribution technique was developed by recognizing that the order of integration over spectral lines in a finite band width, over which the incident radiation can be considered constant with wavelength, was not important. Liou [1992] gives a derivation of the *k*-distribution that allows one to express the transmission as:

$$T_{\Delta\lambda}(u) = \int_{\Delta\lambda} e^{-k_\lambda u} d\lambda = \int_0^\infty e^{-k_i u} f(k_i) dk_i \qquad \textbf{C.25}$$

where:

T = transmission;

u = absorber amount;

k = extinction coefficient;

$f(k)$ is the probability distribution function of k_λ over the wavelength interval under consideration and is defined such that:

$$\int_0^{\infty} f(k)\mathrm{d}k = 1.0 \quad \text{C.26}$$

Integrating $f(k)$ over k to define $g(k)$ as:

$$g(k) = \int_0^{k} f(k')\mathrm{d}k', \quad \text{C.27}$$

and then use Eq. C.27 to determine $k(g) = g^{-1}(k)$ so that:

$$T_{\Delta\lambda} = \int_0^{1} e^{-k(g)u}\mathrm{d}g \approx \sum_j e^{-\sum_i k_j(g)\mathrm{d}u_i} \Delta g_j, \quad \text{C.28}$$

where $\mathrm{d}u_i$ is an absorber amount over a homogeneous sublayer. This replaces a very high resolution integration over λ with lower resolution over g in intervals of Δg. The same arguments can be applied whenever $e^{-\tau_i}$ appears in Eq. C.18 by replacing it, for each layer, with

$$e^{-\tau_i} = e^{-(\tau_i' + k_j(g)\mathrm{d}u_i)}; \quad \text{C.29}$$

where τ' is from spectrally smooth varying constituents.

Then, designating the resulting radiances or irradiances from any level within the model as $F_{k(g)}$, the total over a narrow spectral interval, or band is:

$$F_{\Delta\lambda} = \sum_j F_{k_j(g)} \Delta g_j . \qquad \textbf{C.30}$$

When multiple absorbers are present in a wavelength interval, Eq. C.31 applies.

$$F_{\Delta\lambda} = \sum_j \sum_m F_{k_j(g),k_m(g)} \Delta g_j \Delta g_m . \qquad \textbf{C.31}$$

Values of Δg_j for specified k_is were determined from least-squares fits to Malkmus band model parameters using line-by-line data and were supplied here by M.D. Chou [NASA Goddard, through P. Stackhouse, personal communication) for water vapor, carbon dioxide, and oxygen in the 0.67-4.0 μm range in 20 cm^{-1} band widths with 37 subintervals within each band. Bands with overlap between gases, primarily H_2O and CO_2, therefore required up to 37^2 solutions of DISORT for each band; this is far fewer than what would have been required to achieve the same accuracy with line-by-line computations. Correlated-k is particularly advantageous in multiple scattering models because each calculation with a single value of $k(g)$ can be treated monochromatically through all vertical levels.

C.3.1.2 Rayleigh scatter

Rayleigh scatter enhances the irradiance incident at the bottom of a stratospheric aerosol layer and, to a lesser extent, decreases that incident on top. Since Rayleigh scattering has a separate and distinct phase function from aerosol scatter, every second model layer was designated as a Rayleigh scattering layer, between aerosol scattering and gaseous absorbing layers. Layer Rayleigh optical depth is given by:

$$\tau_{R_{1-2}} = \frac{(p_1 - p_2)}{1013.25} 0.00877 \lambda^{-4.05}, \qquad \text{C.32}$$

[Robinson, 1966; as adjusted to results of Young, 1981]. The Rayleigh phase function is:

$$P_R(\theta) = \frac{3}{4}(1 + \cos^2(\theta)), \qquad \text{C.33}$$

which can be expressed by three Legendre polynomial weights of 1, 0, and 0.5.

C.3.1.3 Aerosol layers

For the aerosol and absorption layers, τ_i and ω_o were determined by Eqs. C.34 and C.35. The scattering phase functions for these layers are represented by Legendre weights returned from MIEV0X for appropriate aerosol size distributions. It has been suggested by Kondratyev et al. [1981] and Liou [1992] that the phase functions for aerosols and Rayleigh scatterers could be weighted and combined in single layers but that approach was not used here. The entire vertical structure of the model was input into the DISORTX RTE program for a single execution for each spectral and sub Δg interval. Tropospheric aerosols were not explicitly included because very little was known about the global distribution of their optical properties, although the net effect of tropospheric aerosols on upwelling short wave radiation at the bottom of a stratospheric layer was included in the treatment of tropospheric albedo, Sec 2.8.

$$\tau_{i,j} = \tau_{aer_i} + \sum_{c=1}^{n} k(g)_{j,c}(g) u_i \qquad n = \text{no. of k-dist constituents}$$

or

$$\tau_i = \tau_{aer_i} + \sum_{c=1}^{m} \kappa_{c_\lambda} u_j, \qquad m = \text{no. of constituents } \lambda < 0.65\ \mu m \qquad \text{C.34}$$

$$\omega_{O_i} = \frac{\tau_{AS_i}}{\tau_i} \qquad \text{C.35}$$

Spectral integration was achieved here by specifying optical properties over 127 bands and summing individual DISORTX output over 0.18 to 3 μm. The extraterrestrial solar spectrum used here, taken from Bird and Riordan [1986], is shown in Fig. C.2. The spectral resolution is variable and was selected to represent the major spectral features of the convoluted extraterrestrial spectrum and atmospheric attenuation. Constituent optical properties were applied at the midpoint of each spectral band.

Surface reflectance was specified at the lower boundary in DISORTX. The albedo specified in DISORTX depends on the application. For comparison to local clear-sky irradiance observations, an appropriate local surface albedo was specified. When using DISORTX to simulate seasonal means for zonal regions the ERBE derived albedos were used.

C.3.2 IR, LOWTRAN7

Although the IR RTE (Eq. C.24) is inherently simpler than the solar expression because of the absence of multiple scattering and $\omega_o \approx 0.0$, additional complexity is encountered in the large number of absorbing gases with complex spectral features across almost the entire spectral range. DISORT includes the IR terms of the RTE, but comparisons between an IR version DISORTX and LOWTRAN7 code suggested

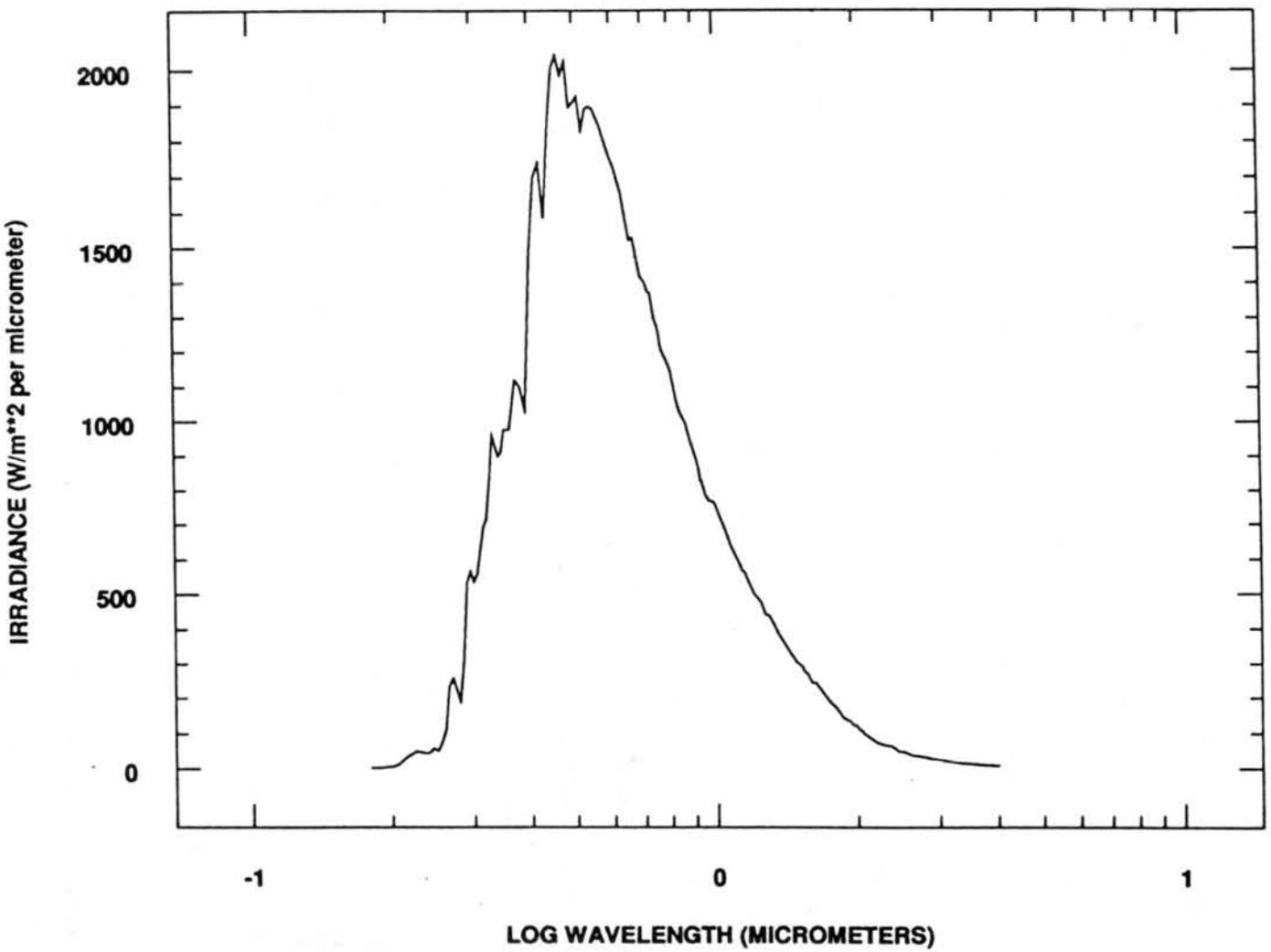

Fig. C.2 Extraterrestrial solar irradiance, normally incident at the top of the earth's atmosphere at a distance of 1 A.U., spectrally resolved into 146 bands plotted at the bands' midpoint.

deficiencies in the supplied *k*-distribution information in the IR region, or its implementation in DISORTX. (Comparisons to LOWTRAN7 in the solar regions indicated no problem with the *k*-distribution implementation.) Since LOWTRAN7 also includes spherical atmospheric geometry, several additional trace constituents, and water vapor continuum, LOWTRAN7 was chosen for the IR calculations in this study. The details of the development, implementation, and utilization of LOWTRAN7 were given in Kneizys et al. [1980, 1983, and 1988] and are summarized briefly in the following.

LOWTRAN7 uses a discrete form of Eq. C.24 to compute IR radiance in any direction at any level in the model, as given by:

$$I_l(\lambda,\mu) = \sum_{i=l}^{N} e^{-(\tau_{a_i}-\tau_{a_{i+1}})/\mu} B(\lambda,\bar{T}) e^{-\bar{\tau}_r/\mu} + B(\lambda,T_b) e^{-\sum_{l}^{N}(\tau_A+\tau_S)} . \qquad \textbf{C.36}$$

In Eq. 36, N is the total number of levels, T is temperature, l is the starting level, an overbar represents a mean of the layer, level l is the level at which the radiance is being computed, and subscript b indicates value at the boundary. Over small but finite spectral intervals, the exponential expressions in Eq. C.36 are replaced by transmission functions for gases based on empirical fits to transmission as a function of scaled absorber amounts using Eq. C.37. Inclusion of τ_s accounts for any scattering out of the incident direction, which is the only scattering considered. Small amounts of Mie scattering occur due to the larger aerosols in the shorter wavelengths of the IR band. The $B(T_b)$ term in Eq. C.36 only exists when the path through the atmosphere originates at the earth's surface, i.e., upward radiances. Transmissions are the products of the contributions from the different constituents. The gaseous transmission is defined by empirically determined functions with pressure and temperature scaling of the absorber amounts, u, as given by:

$$u^* = u\frac{T}{T_O}\sqrt[n]{\frac{p_O}{p}} \qquad \text{C.37}$$

where: p_O is the reference pressure, p is the actual pressure, and n varies from 0.5 to 0.9 depending on constituent being scaled.

A single transmission function was used for H_2O, and the major uniformly mixed gases, and a second function was used for O_3. Uniformly mixed gases included were: CO_2, CH_4, CO, N_2O, NH_3, and SO_2.

The water vapor continuum was included as a separate transmission expression and is a function of water vapor partial pressure, atmospheric total pressure, and temperature. Aerosol scattering and absorption transmission are given by $e^{-\tau_S}$ and $e^{-\tau_A}$, respectively, and the phase function was introduced as the asymmetry factor. For this study, user defined aerosol optical parameters were introduced into stratospheric layers of the LOWTRAN7 model in 30 spectral bands. This aerosol information was obtained from MIEV0X for the same aerosol size distributions used in DISORTX, but integrated over a size parameter range optimized for the IR bands.

Irradiance profiles were formed from separate LOWTRAN7 runs at each quadrature angle, upwards and downwards, and at each desired level. The full vertical resolution of the model was retained to permit examination of ${}_{Ln}V$ at many levels. Model runs have 20 cm^{-1} spectral resolution and were performed for the five model atmospheres with the surface temperature equal to the lowest level air temperature. The IR multi-stream atmospheric model developed for this work calculates vertical irradiance profiles from

multiple runs of LOWTRAN7 using the specified aerosol optical properties as determined in this study. This IR model is referred to here as LOWTRAN7X.

Appendix D. Sensitivity Tests

To examine the relative importance of the various model variables and to compare these results to previous models, sensitivity tests were preformed by either varying a single model variable over an appropriate range, or by changing a model assumption. Lacis et al. [1992] examined a one-dimensional multiple scatter RT model for sensitivity to several features of volcanic aerosols and concluded that midvisible aerosol optical depth and aerosol size effective radius are the two most important variables relative to potential climatic impact of volcanic aerosols, with optical depth being most important.

Several sensitivity tests with DISORTX and LOWTRAN7X were made to examine the influence of optical depth, size inversions, albedo, atmospheric model profile, source of aerosol size data, number of radiant streams, temporal averaging, and single scatter albedo. The effect of within grid spatial averaging of atmospheric constituents was not investigated because of lack of appropriate data.

D.1 Optical Depth

There is an obvious strong relationship between optical depth and V following from the elementary formulation of the equations of radiative transfer. This sensitivity is less obvious for realistic atmospheres with an integration over the complete spectrum and the effects of multiple scattering. This relationship is expected to be linear over a range of the smallest optical depths, becoming more nonlinear as multiple scattering increases. This linearity also depends on underlying albedo.

The sensitivity of V to τ_A was computed over the narrow wavelength range 0.53-0.57 μm. Figure D.1 shows the change in tropopause net solar irradiance for τ_A(500 nm) in the range 0.02-3.6 μm for otherwise fixed DISORTX parameters. The zenith angle for Fig. D.1 is 65° so the slant path optical depth is 2.4 times that for 0°, the abscissa parameter. The sensitivity (slope in Fig. D.1) varies at different wavelengths depending on other attenuators (primarily water vapor), $n(r)$, and multiple scattering. A small τ_A linear range is seen to exist from 0 to ~0.5. With the zonal and seasonal mean solar zenith angles to be used later in this study ranging from 85 to 50°, the need for including multiple scatter, when considering globally varying volcanic forcing, becomes apparent. A better test for the need to include multiple scattering is to examine the diffuse field integrated over the solar spectrum.

This importance of multiple scattering as a function of optical depth is shown in Fig. D.2. The difference in downward diffuse irradiance computed for single scattering and multiple scattering at different albedos and zenith angles is shown. It is clear that multiple scattering becomes important at the >10 W m^{-2} level for optical depths greater than ≈ 0.2 and has therefore been included in all solar calculations. With the scattering optical depths in the IR wavelengths not exceeding 0.02 for the volcanic cases considered, multiple scattering was not included in the IR computations.

Sensitivities of ${}_{An}V_{Tr}$ to aerosol optical depth for a fixed aerosol, H_2SO_4(75%) and specified $n(r)$, but for different θ_o and albedo are given in Fig. D.3. Figure D.3 shows that the ${}_{An}V_{Tr}$ response to increasing stratospheric aerosol optical depth be either negative or positive, depending on θ_o and albedo. Further evaluation of the θ_o and albedo dependencies is shown in Sec. D.3

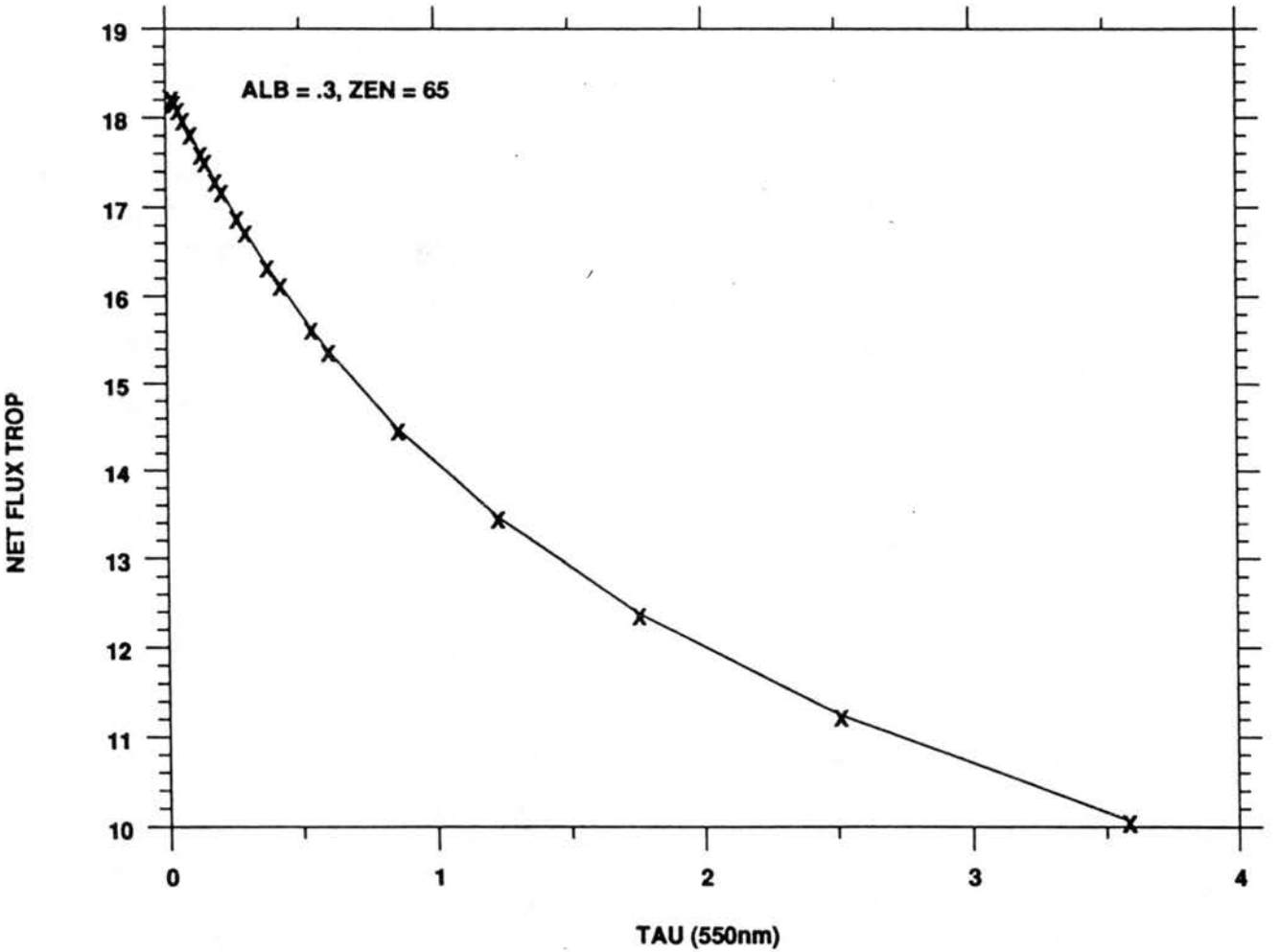

Fig. D.1 Net irradiance in W m^{-2} (0.53 to 0.57 μm) at the tropopause as a function of 550 nm aerosol optical depth in the stratosphere.

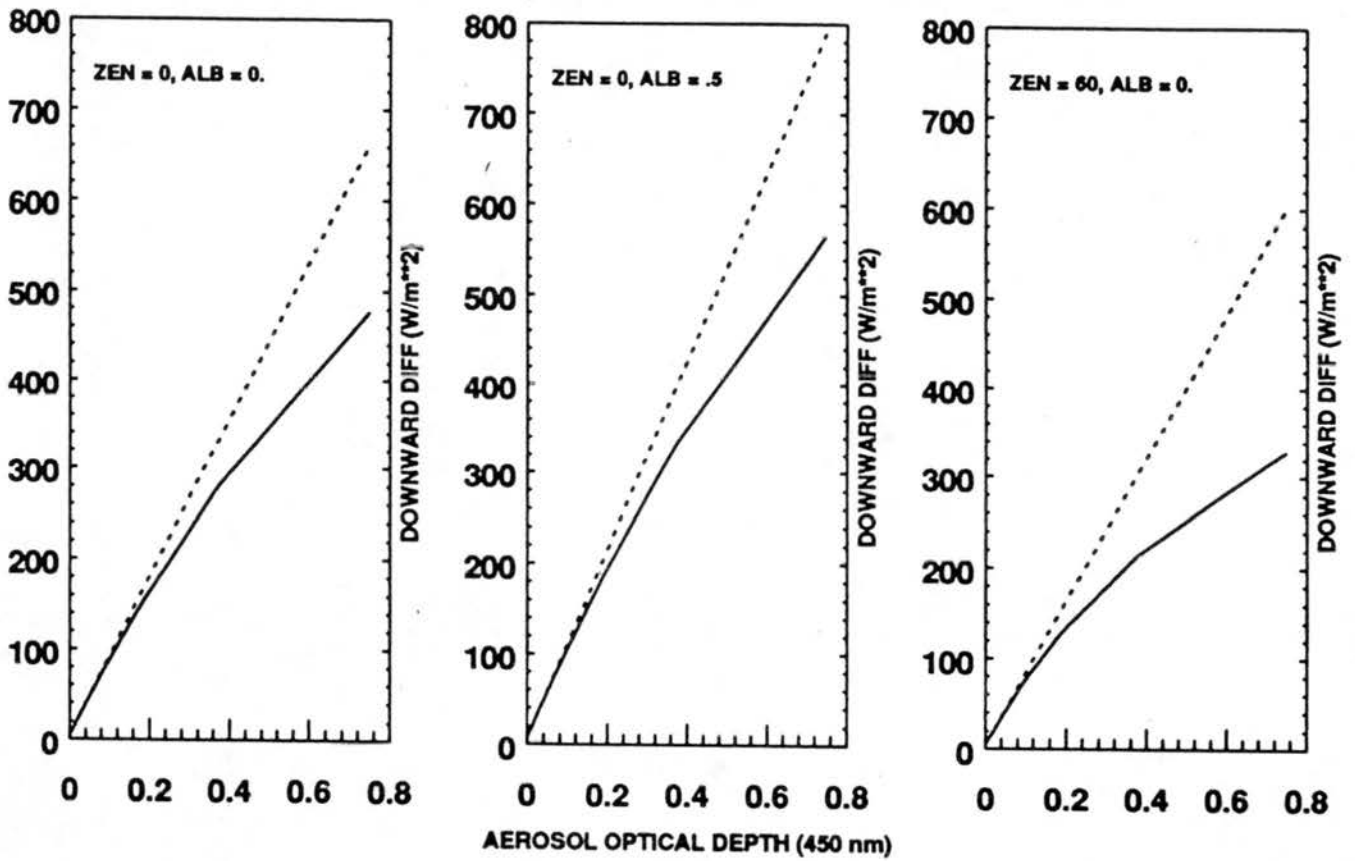

Fig. D.2 Modeled downward diffuse solar at 19 km ASL as a function of aerosol optical depth for single (dashed) and multiple (solid) scattering cases for different albedos and solar zenith angles as indicated.

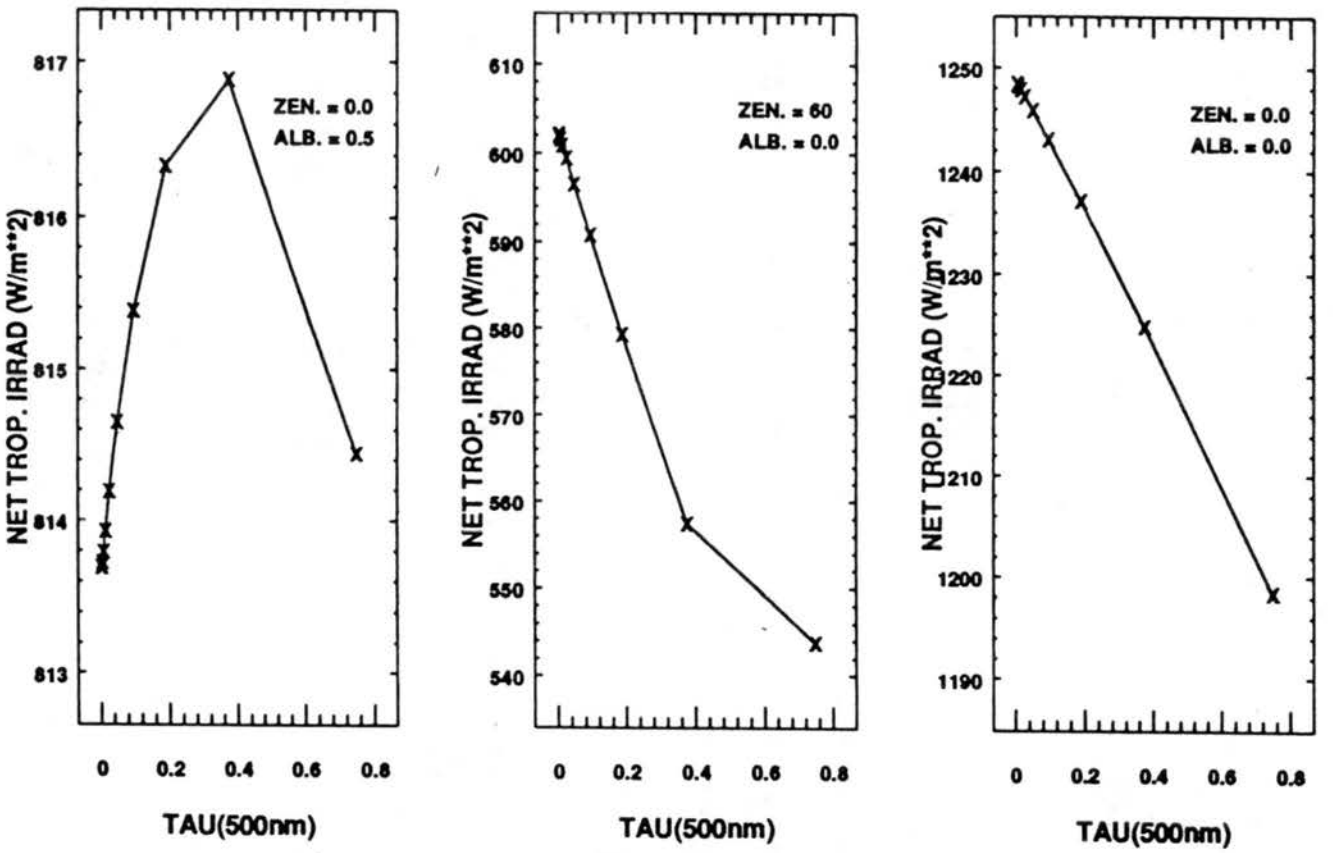

Fig. D.3 Net solar irradiance at tropopause as a function of varying stratospheric aerosol optical depth for different zenith angles and surface albedo cases.

D.2 Size Distribution

As pointed out previously (Secs. 2.4 and B.3), there is uncertainty in the aerosol size distributions available for this study. Model sensitivity to this size uncertainty was considered. Lacis et al. [1992] show the effects of varying the parameters of a Gamma size distribution, although the Gamma distribution may have been chosen more for computational convenience than consistency with observations. RT model sensitivity to uncertainty in $n(r)$ resulting from the size inversion process used here is considered next.

Sensitivity of V to uncertainties in inverted size distribution was explored by running DISORTX and LOWTRAN7X for a variety of size distributions obtained from a multiple Mie inversion of a single set of spectral optical depth observations, as shown in Fig. D.4. The different size distributions arise from different initial guesses and inversion radius ranges. Distributions shown in Fig. D.4 show a tight clustering in the size range corresponding to the wavelengths at which the optical depth observations were made but are varying by orders of magnitude in the larger and smaller sizes. Table D.1 shows the variations in ${}_{Sn}V_{Tr}$ and ${}_{Ln}V_{Tr}$ computed using each of the size distributions in Fig. D.4. The percentage range in radiative forcing is 9.7% in the IR and 5.6% in the solar, although the magnitude is 15 times greater in the solar. Comparisons between V computed with in situ measured sizes and those obtained from nearby spectral optical depth inversions were considered in Section 5.1.1.

Table D.1 Statistics related to ${}_{Sn}V_{Tr}$ and ${}_{Ln}V_{Tr}$ computed for the different size distributions shown in Fig. D.4.

	Mean	S.D.	Max.	Min.
	(W m^{-2})			
${}_{Ln}V_{Tr}$	1.059	0.032	1.13	1.02
${}_{Sn}V_{Tr}$	-29.7	0.508	-28.6	-30.2

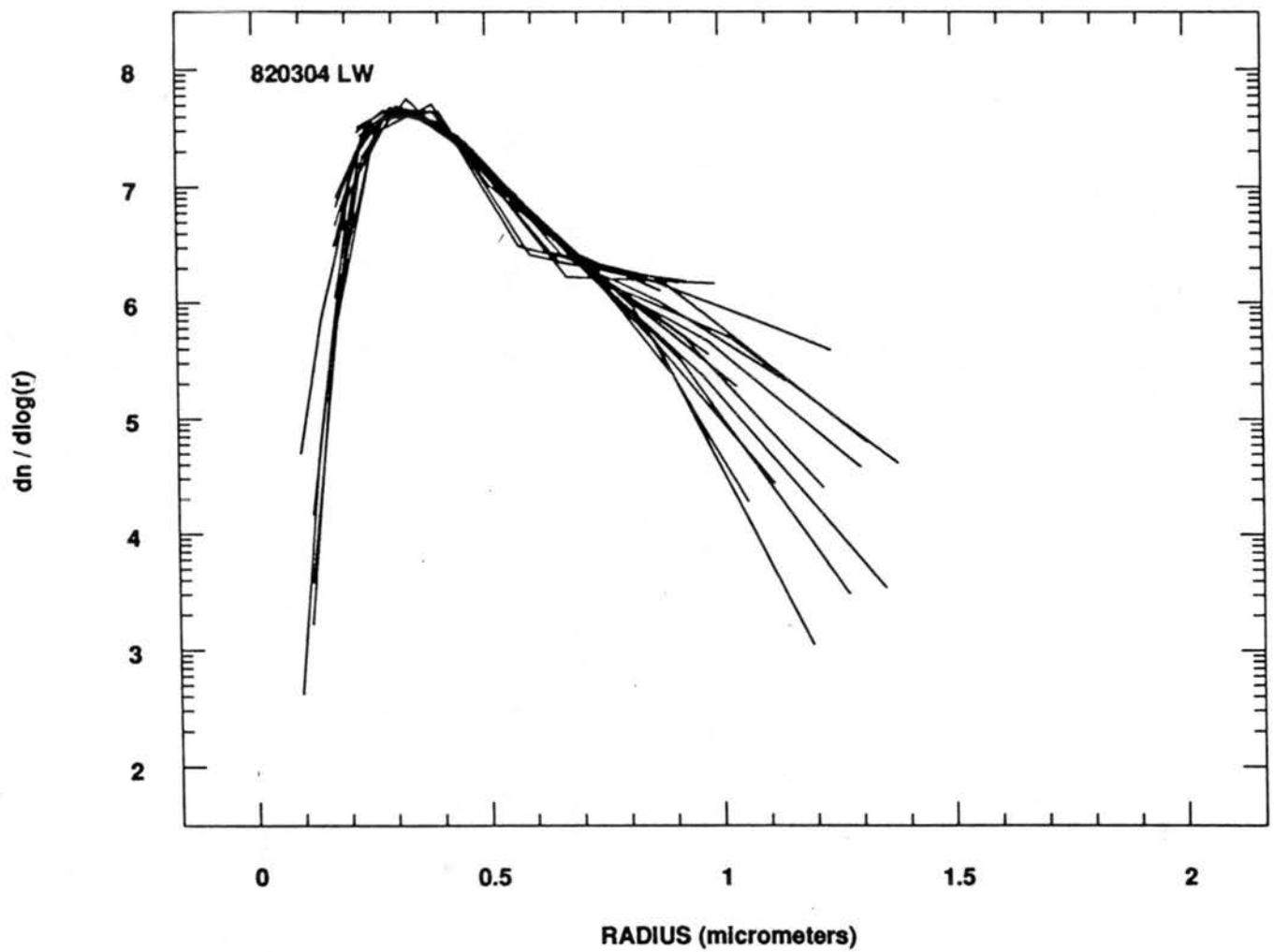

Fig. D.4 Various aerosol size distributions inverted from a single set of spectral aerosol optical depth observations, for grid-box 820304.

D.3 Albedo and Zenith Angle

The effects of varying surface and water/ice cloud induced reflectance on ${}_{Sn}V$ was reported by Harshvardhan [1979]. Surface and tropospheric cloud reflectivity varies with season, latitude, and longitude. Sensitivity to changes in underlying albedo increase with increasing incident solar zenith angle [Harshvardhan, 1979]. Several albedo sensitivity tests were performed.

To examine the albedo effect as a function of θ_0, a spectrally abbreviated (0.53-0.57 μm) DISORTX calculation was performed over a range of θ_0 and albedo for aerosol and no aerosol cases. The albedo and θ_0 effects are shown in Fig. D.5. As expected, the change in ${}_{550n}V_{Tr}$ becomes less as surface albedo increases for a fixed solar zenith angle. Also, for a fixed surface albedo ${}_{550n}V_{Tr}$ increases with increasing solar zenith angle, until $\approx 77^{\circ}$ when the total energy decreases rapidly. The radiative forcing is negative or positive depending on zenith angle and albedo. Over the global grid range of zenith angles (50° to 81°) and tropospheric albedo (0.2 to 0.6), ${}_{550n}V_{Tr}$ remains negative for this aerosol size distribution.

Figure D.6 shows the computed change in TOA albedo for the same conditions as in Fig. D.5 except the change in albedo has been normalized to unit optical depth, consistent with a similar result of Harshvardhan [1979, his Fig. 4]. Results similar to Harshvardhan's are seen considering he used a different phase function and multiple scattering scheme. Normalized planetary albedo increases with zenith angle (Fig. D.6). This is due to forward scatter being increasingly scattered into the upward direction and increasing direct beam path lengths in the aerosol layer. (Note that the plane parallel coordinate assumptions become less valid at large zenith angles.) Since the tropospheric albedo increases with latitude, for a given aerosol optical depth the impact of the aerosol

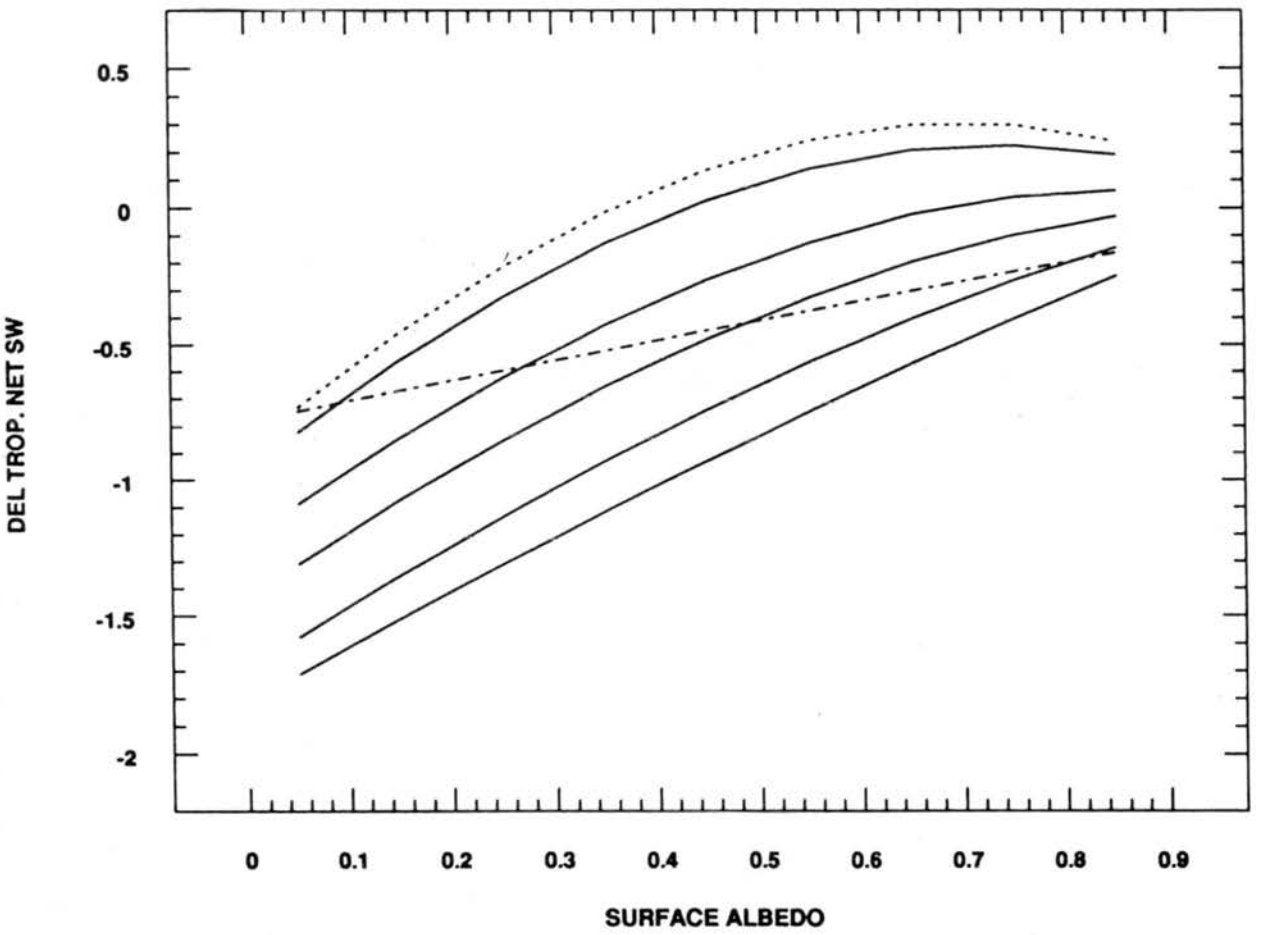

Fig. D.5 Sensitivity of ${}_{Sn}V_{Tr}$ (0.53 to 0.57 μm) to changes in surface albedo and solar zenith angle for grid-box 910404. The graphed lines are for different zenith angles, the top dashed line is for 5°, the next five lines, starting from the top are for 15°, 25°, 35°, 45°, 65°, and 75°, respectively. The dot/dash line is for 85° and represents an abrupt reversal that occurs between 75° and 85° with the line for 90° (not shown) being everywhere equal to zero.

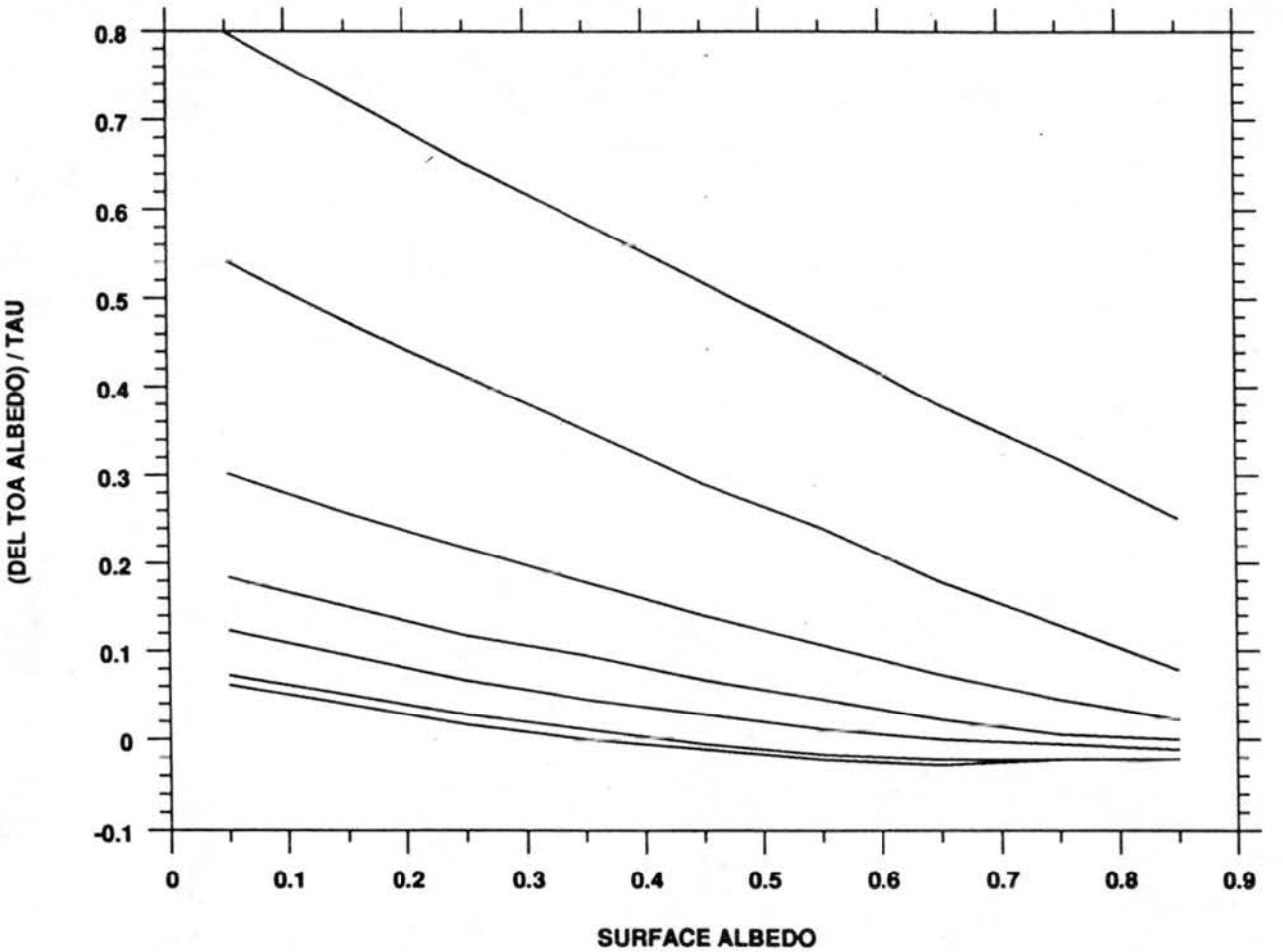

Fig. D.6 Sensitivity of the change in the TOA albedo, normalized to unit $\tau_A(500)$, as a function of surface albedo for various solar zenith angles. The solar zenith angles starting from the top of the graph are: 85^o, 75^o, 65^o, 45^o, 35^o, 25^o, 15^o, and 5^o. This figure was computed primarily for comparison to similar results presented by Harshvardhan [1979]

should decrease, but this effect is countered by the increasing mean solar zenith angles. These compensating effects will, of course, vary with season.

Throughout this study the lower boundary reflectance was treated as Lambertian rather than bidirectional. The impact of this practice is expected to be minimal since hemispheric irradiances were used and have been forced to equal observed TOA hemispheric irradiance albedos. (Although, bidirectional functions were applied to originally derive the ERBE results.) A brief investigation into the effect and applicability of non-Lambertian reflection follows. Minnis and Harrison [1984] give several surface bidirectional reflectance functions for differing surface types and incident solar zenith angles. The largest effect is over water surfaces and was of particular interest here because of the large oceanic areal extent. The functions of Minnis and Harrison were variable in zenith and azimuth and were based on November 1978 GOES-East observational data. These functions over ocean and within the vertical solar plane were used to simulate the effects of non-Lambertian surface reflection in the DISORTX model for a single test case. Reflectance variation in the solar plane only was used, and hence, the surface reflectance function was not truly bidirectional but rather varies only in the zenith angle coordinate of the model.

Non-Lambertian surface reflectance was introduced into DISORTX at the lower boundary by specifying the Legendre polynomial weights that represent the bidirectional reflectance function relative to the incident solar direction. The weights for the Minnis and Harrison [1984] functions were obtained by acquiring the digital reflectance data from P. Minnis and deriving the weights that describe the function for a given solar angle. Figure D.7 shows such a function, both as originally obtained from Minnis and from a Legendre expansion. Reflectances have been renormalized to the solar plane (originally normalized over a hemisphere) and have been multiplied by a mean Lambertian albedo

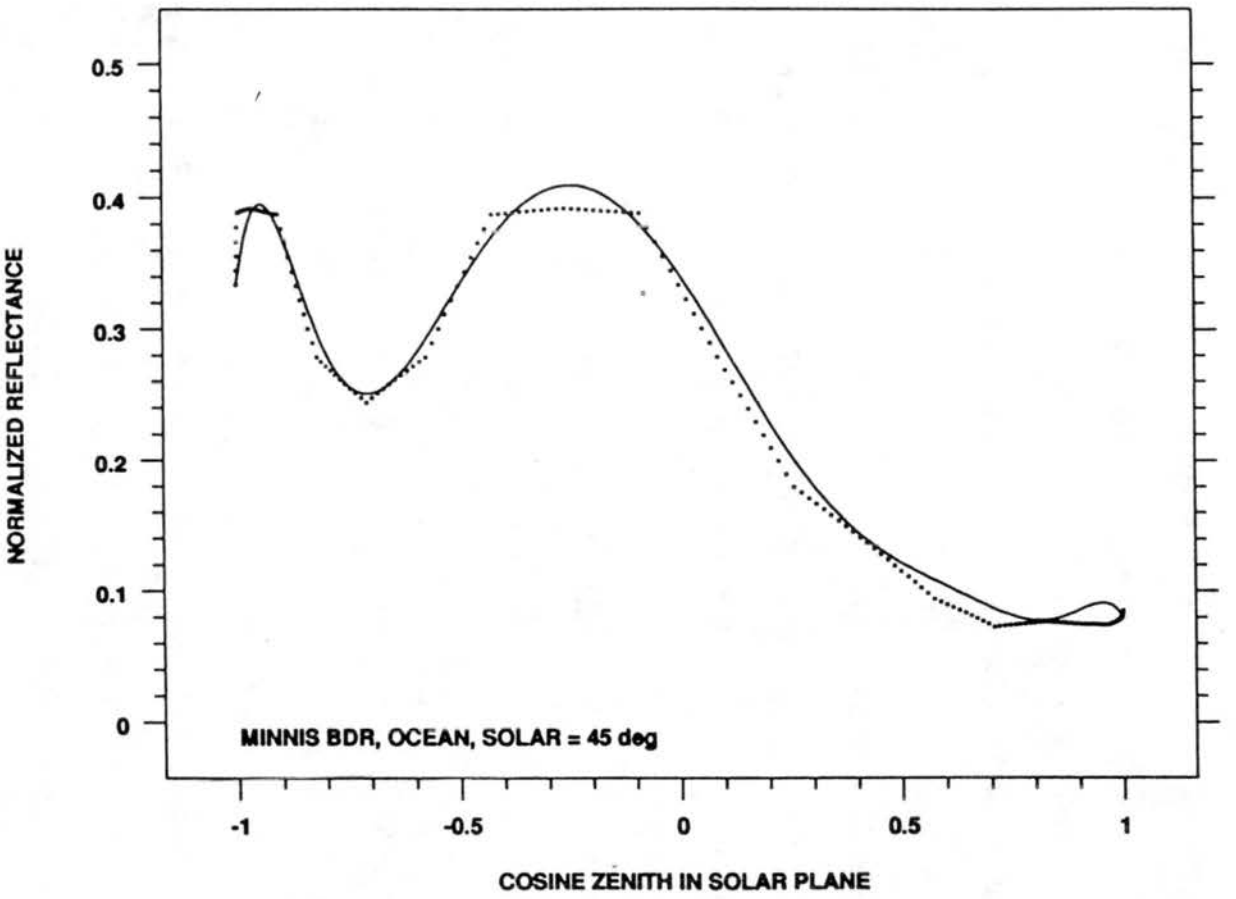

Fig. D.7 Oceanic bidirectional reflectance function in the solar plane for a solar zenith angle of 45°. Dotted curve represents data provided by P. Minnis and the solid curve is as reproduced by a 10th degree Legendre polynomial. The reflectance function was normalized to one over the solar plane and multiplied by a mean surface albedo of 0.24.

of 0.24. These reflectances are higher than what would be expected for the ocean alone, but were used since the mean albedo represents the tropospheric reflectance used in the global DISORTX models. This was a "worst-case-scenario" since the higher albedo value includes cloud reflection that is closer to Lambertian, according to Minnis and Harrison [1984].

As an example of the non-Lambertian reflection effect, ${}_{Sn}V_{Tr}$ was computed for a single case with and without the non-Lambertian surface reflectance. For the Lambertian case, ${}_{Sn}V_{Tr}$ was -21 W m^{-2} with an albedo of 0.22. Because the model assumes azimuthal symmetry, the non-Lambertian function (Fig. D.7) was introduced into the model in two halves, one for incoming solar quadrant, μ = 1.0 to 0.0, and one for the anti-solar quadrant, μ = -1.0 to 0.0. In the solar quadrant the surface reflectivity was decreased to 0.084 and ${}_{Sn}V_{Tr}$ increased accordingly to -25.9 W m^{-2}, consistent with the albedo sensitivity (Figs. D.5 and D.6). Similarly, the albedo was increased to 0.37 when the anti-solar reflection function was used and ${}_{Sn}V_{Tr}$ was decreased to -10.7 W m^{-2} for an average of 18.3 W m^{-2} compared with the 21 W m^{-2} for the Lambertian case. The upward reflected radiation at the tropopause, averaged over zonal bands and seasons is expected to be much less distorted than this example because of clouds, land surfaces, and haze.

D.4 Single Scatter Albedo and H_2SO_4 Solution Concentration

The ω_o values used here were found by using the imaginary refractive index of 75% sulfuric acid/H_2O solution and MIE calculations using a chosen size distribution. Departures from these ω_o values could arise from two principal sources: small amounts of contaminants from the original eruption plume [e.g., Sheridan et al., 1992; Pueschel et al., 1994] and/or variations in the H_2SO_4 solution concentration *(C)*. To examine these

possibilities, sample computations were carried out with larger and smaller values of C, and by decreasing ω_o in small steps to simulate solar energy absorbing impurities.

As a test, both DISORTX and LOWTRAN7X were run for grid-box 820304 with 65% and 85% H_2SO_4 solutions. The computed tropopause net irradiance ranged from 614.2 W m^{-2} to 612.7 W m^{-2} in the solar and -273.75 W m^{-2} to -273.79 W m^{-2} in the IR. These ranges correspond to a 6% and 4% change in of the computed ${}_{Sn}V_{Tr}$ and ${}_{Ln}V_{Tr}$, respectively. In both cases, the energy into the troposphere decreased as the concentration was increased. Since the percent solution has not been confirmed more accurately than in this approximate range [Grainger et al., 1993] the computed V will be only as accurate than indicated by these percentages. Accurate single scatter albedos, or imaginary refractive indices, for crustal material and other possible contaminants in the volcanic aerosol are not generally known. Incorporating material other than H_2SO_4 would have the greatest effect in the solar region where ω_o is taken to be near 1.000. To simulate the inclusion of impurities, DISORTX was run for grid-box 820304 at 0.55 μm with the imaginary part of the solar refractive index consecutively increased. Table D.2 shows relative increases in ${}_{Sn}V_{Tr}$ as ω_o decreases to 0.95. This increase removes additional energy from the troposphere but would result in further warming of the stratosphere, thereby affecting equilibrium ${}_{Ln}V$. The actual heating of the stratosphere has been constrained by observations [Christy and McNider, 1994] such that any enhanced IR effects due to increased solar heating were limited to those that can be calculated using the observed ΔT. In summary ${}_{Sn}V_{Tr}$ increases, ${}_{Ln}V_{Tr}$ decreases and ${}_{An}V_{Tr}$ remains nearly the same where ω_o is decreased.

Table D.2 Sensitivity of ${}_{Sn}V_{Tr}$ to variations in ω_o.

ω_o	λ (μm)	${}_{Sn}V_{tr}$ (%)
1.000	0.55	100.0
0.999	0.55	101.4
0.998	0.55	102.6
0.995	0.55	106.2
0.990	0.55	112.3
0.980	0.55	124.3
0.970	0.55	136.4
0.950	0.55	160.3

These results are consistent with those of Lacis et al. [1992] in that small possible fluctuations in ω_0 do not significantly change ${}_{An}V_{Tr}$. Much observational data cited in previous references support the fact that solar ω_0 for volcanic aerosols is not less than 0.98. Since the ω_0 is already small (< 1.0) in the IR, the addition of absorbing material has minimal effect and is not considered in these calculations.

D.5 Atmospheric State Profiles

Vertical profiles of atmospheric state variables in this study were seasonal and latitudinal mean models developed prior to either eruption [McClatchey et al., 1972], and are a source of additional uncertainty since they are not actual conditions. Because the model domain was seasonal, large variations from the seasonal model atmospheres are not to be expected. To evaluate the potential uncertainty arising from this assumption, the V differences among the five model atmospheres for otherwise fixed parameters were examined as shown in Table D.3. The range in ${}_{Sn}V_{Tr}$ is 2.7%; this is most likely due to variations in water vapor. The IR irradiance anomalies range over 125% due to both variations in water and temperature. A more representative range of the actual profile departures might be the difference between MLW and SAS, which is only 17% in the IR. Since the IR component is a factor of 10 less than the solar, the large percentage uncertainties in the IR have relatively little effect on ${}_{An}V$, which has a maximum range of 13% for the extremes in Table D.3.

Table D.3 Volcanic radiative forcing for fixed model inputs except for different model atmospheres as indicated.

Model atmos.	${}_{Ln}V_{Tr}$	${}_{Sn}V_{Tr}$
MLS	0.33	4.79
MLW	0.48	4.70
SAS	0.41	4.75
SAW	0.74	4.83
TRP	0.59	4.79

D.6 Number of Radiant Streams

Calculated irradiances become increasingly accurate as more radiance streams are used and integrated via Gaussian weighting (Eq. C.8). Computational limitations restrict the number of streams to a minimum that yields acceptable results. Table D.4 shows downward diffuse irradiance at the tropopause for different numbers of radiant streams. Ten streams, five up and five down, were chosen for normal DISORTX computations where asymmetric aerosol scattering is prevalent, whereas only four (two up and two down) were used in the IR where scattering is minor. Four streams are more accurate near the surface than higher because of the tendency for water vapor saturation near the surface to produce an isotropic radiance field at many wavelengths. According to Table D.4, additional streams at the higher altitudes would be desirable. More streams become a problem in LOWTRAN7X because of the earth curvature. With curvature some upward paths to not intercept, or originate at the earths surface giving erroneous results. The choice of the number of streams in the IR is less critical than in the solar when it comes to differencing aerosol and non-aerosol cases because IR radiance fields are less directionally dependent.

Table D.4 Irradiances calculated for different numbers of downward radiance streams at the tropopause for a volcanic aerosol case.

No. Dn.	Irrad. Dn. ($W\ m^{-2}$)	Model
2	112.38	DISORTX(15km)
3	111.31	"
4	111.26	"
5	111.37	"
6	111.43	"
7	111.46	"
8	111.46	"
1	383.3	LOWTRAN7X(surf)
2	391.3	"
3	393.4	"
4	393.9	"
1	14.3	LOWTRAN7X(15km)
2	15.9	"
3	16.6	"
4	17.0	"

D.7 Spatial and Temporal Averaging

To reduce computational demands in finding global, temporal, and spectrally complete evolution of volcanic radiative forcing, large-scale spatial and temporal averaging was invoked. Uncertainty introduced because of this grid and the implied averaging was next examined by using a higher spatial and temporal resolution over one grid-box and comparing to single calculation for mean grid-box conditions. It was assumed that sub-grid variations in cloudiness, surface albedo, and atmospheric constituents are random and the grid box average should be appropriate and not introduce any bias.

Solar zenith angle variations are not randomly distributed over earth's surface or within a seasonal mean. To investigate, a sub-grid within one latitude band was used. This sub-grid consisted of 10 equal area latitude bands (each 1/100 the area of the globe). Daily mean solar zenith angles and solar day lengths were computed for each sub-band. The mean of all the sub-grid ${}_{An}V_{Tr}$ is -2.40 W m^{-2} compared with -2.37 W m^{-2} for the single grid-box mean. Although these results could vary depending on which grid "box" was used, this was done for only one box, with the results not warranting further computation.

The effect of using seasonal average aerosol inputs rather than averaging the model results for daily varying inputs was investigated. DISORTX computations were performed using daily Mauna Loa aerosol optical depths and daily solar geometry with the results averaged for one season. The computed ${}_{An}V_{Tr}$ for that season varied by 2.3% from that using single mean quantities. This uncertainty will obviously vary with latitude and time and it was not possible to evaluate where actual $\tau_A(\lambda)$ observations did not exist on this time scale. Similarly, spatial variations within a zonal band cannot be evaluated with the available data.

References

Ackerman, S.A. and S.K. Cox, 1982. The Saudi Arabian Heat Low: Aerosol distributions and thermodynamic structure. *J. Geophys. Res., 87,* 8991-9002.

Ackerman, S.A. and K.I. Strabala, 1994. Satellite remote sensing of H_2SO_4 aerosol using the 8- to 12-μm window region: Application to Mount Pinatubo. *J. Geophys. Res., 99*, 18639-18649.

Amer. Geophys. Union, 1992. "Volcanism and Climate, American Geophysical Union Special Report." available from the American Geophysical Union, Washington D.C.

Angell, J.K., 1988. Impact of El Niño on the delineation of tropospheric cooling due to volcanic eruptions. *J. Geophys. Res., 93*, 3697-3704.

Angell, J.K. and J. Korshover, 1985. Surface temperature changes from major volcanic episodes between 1780 and 1980. *J. Appl. Meteorol., 24*, 937-951.

Ardanuy, P.E. and H.L. Kyle, 1986. Observed Perturbations of the earth's radiation budget: A response to the El Chichon stratospheric aerosol layer. *J. Clim. Appl. Meteorol., 25*, 505-516.

Asano, S., A. Uchiyama, and M. Shiobara, 1993. Spectral optical thickness and size distribution of the Pinatubo volcanic aerosols as estimated by ground-based sunphotometry. *J. Meteorol. Soc. Japan, 71*, 165-173.

Barth, C.A., R.W. Sanders, G.E. Thomas, G.J. Rottman, D.E. Rusch, R.J. Thomas, G.H. Mount, G.M. Lawrence, J.M. Zawodny, R.A. West, and J. London, 1982. Solar Mesosphere Explorer measurements of the El Chichón volcanic cloud. *Bull. Amer. Meteorol. Soc., 63*, 1314.

Bird, R.E. and C. Riordan, 1986. Simple solar spectral model for direct and diffuse irradiance on horizontal and tilted planes at the earth's surface for cloudless atmospheres. *J. Clim. Appl. Meteorol., 25*, 87-97.

Bluth, G.J.S., S.D. Doiron, C.C. Schnetzler, A.J. Krueger, and L.S. Walter, 1992. Global tracking of the SO_2 clouds from the June 1991 Mount Pinatubo eruptions. *Geophys. Res. Lett., 19*, 151-154.

Bodhaine, B.A. and R.M. Rosson (eds.), 1988. Geophysical Monitoring for Climatic Change, No. 16: Summary Report 1987. NOAA/ERL, Boulder, Colo., 110 pp.

Bohren, C. and D.R. Huffman, 1983. *Absorption and Scattering of Light by Small Spheres*. Wiley, New York, 530 pp.

Budyko, M.I., 1969. The effect of solar radiation variations on the climate of the Earth. *Tellus, 21*, 611-619.

Cadle, R.D., C.S. Kiang, and J.F. Louis, 1976. The global scale dispersion of the eruption clouds from major volcanic eruptions. *J. Geophys. Res., 81*, 3125-3132.

Campbell, G.G. and T.H. Vonder Haar, 1980. "Climatology of Radiation Budget Measurements from Satellites". Atmos. Sci. Paper No. 323, Dept. Atmos. Sci., Colorado State University, Fort Collins, Colo.

Cess, R.D., E.G. Dutton, J.J. DeLuisi, and J. Fiang, 1991. Determining surface solar absorption from broadband satellite measurements for clear skies: Comparison with surface measurements. *J. Clim., 4*, 236-247.

Chandrasekhar, S. 1960. *Radiative Transfer*. Dover, New York, 393 pp.

Christy, J.R. and R.T. McNider, 1994. Satellite greenhouse signal. *Nature, 367*, 325.

Chou, M.D., L. Peng, and A. Arking, 1984. Climatic studies with a multiplelayer energy balance model, Part3: Climatic impact of stratospheric aerosols. *J. Atmos. Sci., 41*, 579-767.

Clark, A.D. and R.J. Charlson, 1985. Radiative properties of the background aerosol: Absorptive component of extinction. *Science, 229*, 263-265.

Clark, A.D., R.J. Charlson, and J.A. Ogren, 1983. Stratospheric aerosol light absorption before and after El Chichón. *Geophys. Res. Lett., 10*, 1017-1020.

Coakley, J.E., 1981. Stratospheric aerosols and the tropospheric energy budget: Theory versus observations. *J. Geophys. Res., 86*, 9761-9766.

Coakley, J.E. and G.W. Grams, 1976. Relative influence of the visible and infrared optical properties of a stratospheric aerosol layer on the global climate. *J. Appl. Meteorol., 15*, 676-691.

Crow, E.L., F.A. Davis, and M.W. Maxfield, 1960. *Statistics Manual*. p. 183. Dover, New York, 288 pp.

DeFoor, T.E., E. Robinson, and S. Ryan, 1992. Early observations of the June 1991 Pinatubo volcanic plume over Mauna Loa Observatory, Hawaii, July 1991-November 1991. *Geophys. Res. Lett., 19*, 187-190.

DeLuisi, J.D. and B.M. Herman, 1977. Estimation of solar radiation absorption by volcanic stratospheric aerosols from Agung using surface based observations. *J. Geophys. Res., 82*, 3477-3480.

DeLuisi, J.D., E.G. Dutton, K.L. Coulson, T.E. DeFoor, and B.G. Mendonca, 1983. On some radiative features of the El Chichón volcanic stratospheric dust cloud and a cloud of unknown origin observed at Mauna Loa. *J. Geophys. Res., 88*, 6769-6772.

DeLuisi, J.D., T. DeFoor, K. Coulson, and F. Fernald, 1984. Lidar observations of the stratospheric aerosol over Mauna Loa Observatory. NOAA Data Rep. ERL-ARL-5, NOAA, Boulder, Colo., 78 pp.

Deirmendjian, D., 1969. *Electromagnetic Scattering on Spherical Polydispersions.* Elsevier, New York, 291 pp.

Deshler, T., B.J. Johnson, and W.R. Rozier, 1993. Balloonborne measurements of Pinatubo aerosol during 1991 and 1992 at 41° N: vertical profiles, size distributions, and volatility. *Geophys. Res. Lett., 20*, 1435-1438

Deshler, T., D.J. Hofmann, B.J. Johnson, and W.R. Rozier, 1992. Balloonborne measurements of Mt. Pinatubo aerosol size distribution and volatility at Laramie, Wyoming, during the summer of 1991. *Geophys. Res. Lett., 19*, 199-202.

Diaz, H.F. and G.N. Kiladis, 1993. Atmospheric teleconnections associated with extreme phases of the southern oscillation. in *El Niño: Historical and Paleoclimatic Aspects of the Southern Oscillation.* H.F. Diaz and V. Markgaf, Eds., Cambridge University Press, Cambridge Mass, 7-27.

Dutton, E.G., 1990a. Comments on "Major volcanic eruptions and climate: a critical review". *J. Clim., 3*, 557-588.

Dutton, E. G., 1990b. Annual forcing of the surface radiation balance diurnal cycle measured from a high tower near Boulder, Colorado. *J. Clim., 3*, 1400-1408.

Dutton, E.G. and J.R. Christy, 1992. Solar radiative forcing at selected locations and evidence for global lower tropospheric cooling following the eruptions of El Chichón and Pinatubo. *Geophys. Res. Lett., 19*, 2313-2316.

Dutton, E.G. and J.J. DeLuisi, 1983. Spectral extinction of direct solar radiation by the El Chichón cloud during December 1982. *Geophys. Res. Lett., 10*, 1013-1016.

Dutton, E.G., J.J. DeLuisi, and B.A. Bodhaine, 1984. Features of aerosol optical depth observed at Barrow, March 10-20, 1983. *Geophys. Res. Lett., 11*, 385-388.

Dutton, E. G., J. J. DeLuisi, and Daniel Endres, 1985a. Barrow solar radiation 1976-1983. NOAA Data Rep., DR-ERL-ARL-6, NOAA-ERL, Boulder, Colo., 112 pp.

Dutton, E.G., J.J. DeLuisi, and A.P. Austring, 1985b. Interpretation of Mauna Loa atmospheric transmission relative to aerosols, using photometric precipitable water amounts. *J. Atmos. Chem., 3*, 53-68.

Dutton, E. G., J. J. DeLuisi, and A. P., Austring, 1987. Measurement of solar radiation at Mauna Loa Observatory 1978-1985, with emphasis on the Effects of the eruption of El Chichon". NOAA Data Rep. ERL-ARL-13, NOAA-ERL, Boulder Colo., 35 pp.

Dutton, E.G., R.S. Stone, and J.J. DeLuisi, 1989. South Pole surface radiation balance measurements April 1986 to February 1988. NOAA Data Rep. ERL ARL-17, NOAA ERL, Boulder, Colo., 49 pp.

Dutton, E.G., R.S. Stone, D.W. Nelson, and B.G. Mendonca, 1991. Recent interannual variations in solar radiation, cloudiness, and surface temperature at the South Pole. *J. Clim., 4*, 848-858.

Dutton, E.G., P.J. Reddy, S. Ryan, and J.J. DeLuisi, 1994. Features and effects of aerosol optical depth observed at Mauna Loa, Hawaii: 1982-1992. *J. Geophys. Res., 99*, 8295-8306.

Dyer, A.J. and B.B. Hicks, 1965. Stratospheric transport of volcanic dust inferred from solar radiation measurements. *Nature, 208*, 131-133.

Ellingson, R.G., J. Ellis, and S. Fels, 1991. The intercomparison of radiation codes used in climate models: Longwave results. *J. Geophys. Res., 96*, 8929-8953.

Fouquart, Y. and B. Bonnel, 1991. Intercomparing shortwave radiation codes for climate studies. *J. Geophys. Res., 96*, 8955-8968.

Goodman, J., K.G. Snetsinger, R.F. Pueschel, G.V. Ferry, and S. Verma, 1994. Evolution of Pinatubo aerosol near 19 km altitude over western North America. *Geophys. Res. Lett., 21*, 1129-1132.

Goody, R.M., 1952. A statistical model for water vapor absorption. *Q. J. R. Meteorol. Soc., 78*, 165-169.

Goody, R.M., 1964. *Atmospheric Radiation I: Theoretical Basis*. Oxford Press, London, 436 pp.

Goody, R.M., R. West, L. Chen, and D. Crisp., 1989. The correlated-k method for radiation calculations in nonhomogeneous atmospheres. *J. Quant. Spectrosc. Radiat. Transfer, 42*, 539-550.

Graf, H-F., I. Kirchner, A. Robock, and I. Schult, 1993. Pinatubo eruption winter climatic effects: model versus observations. *Clim. Dynamics, 9*, 81-93.

Grainger, R.G., A. Lambert, J.J. Remedios, C.D. Rogers, M. Corney, B.J. Kerridge, and F.W. Taylor, 1993. Infrared absorption by volcanic stratospheric aerosols observed by ISAMS. *Geophys. Res. Lett., 20*, 1283-1286.

Halbert, M.S., C.F. Ropelewski, T.R. Carl, J.K. Angell, L.L. Stowe, R.R. Heim Jr., A.J. Miller and D.R. Rodenhuis, 1993. 1992 brings return to moderate global temperatures. *EOS Tans. Amer. Geophys. Union, 74*, 433.

Hansen J. E. and L.D. Travis, 1974. Light scattering in planetary atmospheres. *Space Sci. Rev. 16*, 527-610.

Hansen, J.E., W.C. Wong, and A.A. Lacis, 1978. Mount Agung provides a test of a global climate perturbation. *Science, 199*, 1065-1068.

Hansen, J., I. Fung, A. Lacis, D. Rind, S. Lebedeff, R. Ruedy, G. Russell, and P. Stone, 1988. Global climate changes as forecast by the GISS 3-D model. *J. Geophys. Res., 93*, 9341-9364.

Hansen, J., A. Lacis, R. Ruedy, and M. Sato, 1992. Potential climate impact of Mount Pinatubo eruption. *Geophys. Res. Lett., 19*, 215-218.

Hansen, J., A. Lacis, R. Ruedy, M. Sato, and H. Wilson, 1993. How sensitive is the world climate? *Nat. Geogr. Res. Explor., 9*, 142-158.

Harshvardhan, 1979. Perturbation of the zonal radiation balance by a stratospheric aerosol layer. *J. Atmos Sci., 36*, 1274-1285.

Harshvardhan and R.D. Cess, 1976. Stratospheric aerosols: Effect upon atmospheric temperature and global climate. *Tellus, 28*, 1-10.

Hay, J.E. and R. Darby, 1984. El Chichon - influence on aerosol optical depth and direct, diffuse and total irradiance at Vancouver, B.C. *Atmos.-Ocean, 22*, 354-368.

Hayasaka, T., N. Iwasaka, G. Hashida, I. Takizawa, and M. Tanaka, 1994. Changes in stratospheric aerosols and solar insolation due to Mt. Pinatubo eruption as observed over the western Pacific. *Geophys. Res. Lett., 21*, 1137-1140.

Herman, B.M., S.R. Browing, and R. Rabinoff, 1976. The change in Earth-atmosphere albedo and radiational equilibrium temperatures due to stratospheric pollution. *J. Appl. Meteorol., 15*, 1057-1067.

Hofmann, D.J., 1988. Aerosols from past and present volcanic emissions. In *Aerosols and Climate*. A. Deepak Publishing, Hampton, Virginia, 195-214.

Hofmann, D.J., 1993. 20 years of balloonborne tropospheric aerosol measurements at Laramie, Wyoming. *J. Geophys. Res., 98*, 12753-12766.

Hofmann, D.J. and J.M. Rosen, 1983. Sulfuric acid droplet formation and growth in the stratosphere after El Chichón. *Science, 222*, 325-327.

Hofmann, D.J. and J.M. Rosen, 1984. Measurements of the sulfuric acid weight percent in the stratospheric aerosol from El Chichón eruption. *Geofisica International, 23*, 309-320.

Hofmann, D.J., J.M. Rosen, T.J. Pepin, and R.G. Pinnick, 1975. Stratospheric aerosol measurements, I. Time variations at northern midlatitudes. *J. Atmos. Sci., 32*, 1446-1456.

IPCC, 1995. *Radiative Forcing of Climate, 1994*. Intergovernmental Panel on Climate Change (IPCC), World Meteorological Organization, Cambridge University Press, 339 pp.

Junge, C.E., 1963. *Air Chemistry and Radioactivity*. Academic Press, New York, 117 pp.

Junge, C.E., C.W. Chagnon, and J.E. Manson, 1961. Stratospheric Aerosols. *J. Meteorol.*, 18, 81-108.

Kasten, F., 1968. Falling speed of aerosol particles. *J. Appl Meteorol.*, 7, 944-947.

Kent, G.S., M.P. McCormick, and P.-H. Wang, 1994. Validation of stratospheric aerosol and gas Experiments I and II satellite aerosol optical depth measurements using surface radiometer data. *J. Geophys. Res., 99*, 10333-10339.

Kiehl, J.T. and B.P. Briegleb, 1993. The relative roles of sulfate aerosols and greenhouse gases in climate forcing. *Science, 260*, 311-314.

Kiehl, J.T. and S. Solomon, 1986. On the radiative balance of the stratosphere. *J. Atmos. Sci., 43*, 1525-1534.

King, M.D., D.M. Byrne, B.M. Herman, and J.A. Reagan, 1978. Aerosol size distributions obtained by inversion of spectral optical depth measurements. *J. Atmos. Sci., 35*, 2153-2167.

King, M.D., Harshvardhan, and A. Arking, 1984. A model of the radiative properties of the El Chichón stratospheric layer. *J. Clim. Appl. Meteorol., 23*, 1121-1137.

Kneizys, F.X., E.P. Shettle, W.O. Gallery, J.H. Chetwynd, Jr., L.W. Abreu, J.E.A. Selby, R.W. Fenn, R.A. McClatchey, 1980. Atmospheric Transmittance/Radiance Computer Code LOWTRAN 5. Air Force Geophysical Laboratory Tech. Rep., AFGL-TR-80-0067, Hanscom AFB, Mass. 233 pp.

Kneizys, F.X., E.P. Shettle, W.O. Gallery, J.H. Chetwynd, Jr., L.W. Abreu, J.E.A. Selby, S.A. Clough, and R.W. Fenn, 1983. Atmospheric Transmittance/Radiance Computer Code LOWTRAN 6. Air Force Geophysical Laboratory Tech. Rep., AFGL-TR-83-0187, Hanscom AFB, Mass., 200 pp.

Kneizys, F.X., E.P. Shettle, L.W. Abreu, J.H. Chetwynd, Jr., G.P. Anderson, W.O. Gallery, J.E.A. Selby, and S.A. Clough, 1988. Users guide to LOWTRAN 7. Air Force Geophysical Laboratory Tech. Rep., AFGL-TR-88-0177, Hanscom AFB, Mass. 137 pp.

Knollenberg, R.G. and D. Huffman, 1983. Measurements of the aerosol size distributions in the El Chichón cloud. *Geophys. Res. Lett. 10*, 1025-1028.

Kondratyev, K.Y., R.M. Welch, S.K. Cox, V.S. Grishechkin, V.A. Ivanov, M.A. Prokofyev, V.F. Zhvalev, and O.B. Vaselyev, 1981. Determination of vertical profiles of aerosol size spectra from aircraft radiative flux measurements: 1. Retrieval of spherical particle size distributions. *J. Geophys. Res., 86*, 9783-9793.

Kousky, V.E., ed., 1994. *Climate Diagnostic Bulletin.* No. 94/1-12, NOAA/National Weather Service/Climate Analysis Center, Washington, D.C.

Kozelmann, T., et al, 1994. Parameterization of global and longwave incoming radiation for the Greenland ice sheet. *Global and Planetary Change, 9*, 143-164.

Krueger, A.J., 1983. Sighting the El Chichón sulfur dioxide clouds with the Nimbus-7 total ozone mapping spectrometer. *Science, 220*, 1377-1379.

Labitzke, K. and M.P. McCormick, 1992. Stratospheric temperature increases due to the eruption of Mt. Pinatubo. *Geophys. Res. Lett., 19*, 207-210.

Lacis, A.A. and V. Oinas, 1991. A description of the correlated *k* distribution method for modeling nongray gaseous absorption, thermal emission, and multiple scattering in the vertically inhomogeneous atmospheres. *J. Geophys. Res., 96*, 9027-9063.

Lacis, A., J. Hansen, and M. Sato, 1992. Climate forcing by stratospheric aerosols. *Geophys. Res. Lett., 19*, 607-1610.

Lamb, H.H., 1970. Volcanic dust in the atmosphere; with a chronology and assessment of its meteorological significance. *Phil. Trans. Roy. Soc. London, A266*, 424-533.

Lambert, A., R.G. Grainger, J.J. Remedios, C.D. Rodgers, M. Corney, and F.W. Taylor, 1993. Measurements of the evolution of the Mt. Pinatubo cloud by ISAMS. *Geophys. Res. Lett., 20*, 1287-1290

Lary, D.J., M. Bulluch, and S. Bekki, 1994. Solar heating rates after a volcanic eruption: The importance of SO_2 absorption. *Q. J. R. Meteorol. Soc., 120*, 1683-1688.

Lenoble, J., D. Tanre, P.Y. Deschamps, and M. Herman, 1982. A simple method to compute the change in earth-atmosphere radiative balance due to stratospheric aerosol layer. *J. Atmos. Sci., 39*, 2565-2576.

Li, Y-H., T-H. Peng, W. Broecker, and H. G. Östlund, 1984. The average vertical mixing coefficient for the oceanic thermocline. *Tellus, 36b*, 212-217.

Liou, K.N., 1980. *Introduction to Atmospheric Radiation*. Academic Press, Orlando, Fla., 392 pp.

Liou, K.N., 1992. *Radiation and Cloud Processes in the Atmosphere*. Oxford, New York, 487 pp.

Lockwood, G.W. and D.T. Thompson, 1986. Atmospheric extinction: The ordinary and volcanically induced variations, 1972-1985. *Astro. J., 92*, 976-985.

Long, C.S. and L.L. Stowe, 1994. Using the NOAA/AVHRR to study stratospheric aerosol optical thickness following the Mt. Pinatubo eruption. *Geophys. Res. Lett., 21*, 2215-2218.

Mass, C.F. and D.A. Portman, 1989. Major volcanic eruptions and climate: A critical review. *J. Clim., 2*, 566-593.

Mass, C.F. and D.A. Portman, 1990. Reply to Comments on "Major volcanic eruptions and climate: a critical review." *J. Clim., 3*, 590-591.

Mass, C.F. and S.H. Schneider, 1977. Statistical evidence of the influence of sunspots and volcanic dust on long term temperature records. *J. Atmos. Sci., 34*, 1995-2008.

McClatchey, R.A., R.W. Fenn, J.E.A. Selby, F.E. Volz, and J.S. Garing, 1972. Optical properties of the atmosphere (Third edition). Rep. AFCRL-7-0497, Air Force Cambridge Res. Lab., Bedford Mass., 108 pp.

McCormick, M.P. and C.R. Trepte, 1987. Polar stratospheric clouds and aerosols, 1978-1985. *J. Geophys. Res., 92*, 4297-4306.

McCormick, M.P. and R.E. Veiga, 1992. SAGEII measurements of early Pinatubo aerosols. *Geophys. Res. Lett., 19*, 155-158.

McCormick, M.P., T.J. Swissler, W.P. Chu, and W.H. Fuller, Jr., 1978. Post volcanic stratospheric aerosol decay measured by Lidar. *J. Atmos. Sci.*, 35, 1296-1303.

McCormick, M.P., and T.J. Swissler, 1983. Stratospheric aerosol mass and latitudinal distribution of the El Chichón eruption cloud for October 1982. *Geophys. Res. Lett., 10*, 877-880.

McCormick, M.P., and T.J. Swissler, W.H. Fuller, W.H. Hunt, and M.T. Osborne, 1984. Airborne and ground based lidar measurements of the El Chichón stratospheric cloud from 90° N to 56° S. *Geofisica International, 23*, 187-221.

Mendonca, B.G., K.J. Hanson, and J.J. DeLuisi, 1978. Volcanically related secular trends in atmospheric transmission at Mauna Loa Observatory, Hawaii. *Science, 202*, 513-515.

Meyers, D., 1988. Uncertainty analysis for thermopile pyranometer and pyrheliometer calibrations performed by SERI. Solar Energy Research Institute Tech. Rep., SERI/TR-215-3294, Golden, Colo., 129 pp.

Michalsky, J.J., E.W. Pearson, and B.A. LeBaron, 1990. An assessment of the impact of volcanic eruptions on the Northern Hemisphere's aerosol burden during the last decade. *J. Geophys. Res., 95*, 5677-5688.

Minnis, P., E.F. Harrison, L.L. Stowe, G.G. Gibson, F.M. Denn, D.R. Doelling, and W.L. Smith, Jr., 1993. Radiative climate forcing by the Mount Pinatubo eruption. *Science, 259*, 1411-1415.

Minnis, P. and E.F. Harrison, 1984. Diurnal variability of regional cloud and clear-sky radiative parameters derived for GOES data. Part III: November 1978 radiative parameters. *J. Clim. Appl. Meteor., 23*, 1023-1051.

Mitchell, J.M., 1961. Recent secular changes of global temperature. *Annals. N.Y. Acad. Sci., 95*, 235-250.

Moorthy, K.K., P.R. Nair, B.V.K. Murthy, and S.K. Satheesh, 1994. Time evolution of the optical effects and aerosol characteristics of Mt. Pinatubo origin from ground based measurements. *J. Atmos. Terrest. Phys.*, in press.

Nelson, D.W. and E.G. Dutton, 1994. Improved characterization of "traditional" 2pi steradian broadband solar radiometers. Preprints, Eighth Conference on Atmospheric Radiation, 23-28 January 1994, Nashville Tenn., Amer. Meteorol. Soc., Boston Mass.

Newhall, C.G. and S. Self, 1982. The volcanic explosivity index (VEI) - an estimate of the explosive magnitude for historical volcanism. *J. Geophys. Res., 87*, 1231-1238.

Oberbeck, V.R., E.F. Danielsen, K.G. Snetsinger, G.V. Ferry, W. Fong, and D.M. Hays, 1983. Effect of the eruption of El Chichón on stratospheric aerosol size and composition. *Geophys. Res. Lett., 10*, 1021-1024.

Ogren, J.A., R.J. Charlson, L.F. Radke, and S.K. Damonkos, 1981. Absorption of visible radiation by aerosols in the volcanic plume of Mount St. Helens. *Science, 211*, 834-836.

Oliver, R.C., 1976. On the response of Hemispheric mean temperature to stratospheric dust. *J. Appl. Meteorol., 15*, 933-950.

Palmer, K.F. and D. Williams, 1975. Optical constants of sulfuric acid; application to the clouds of Venus? *Appl. Opt., 14*, 208-219.

Pinnick, R.G, J.M. Rosen, and D.J. Hofmann, 1976. Stratospheric aerosol measurements III: Optical model calculations. *J. Atmos. Sci., 33*, 304-320.

Pinto, J.P., R.P. Turco, and O.B. Toon, 1989. Self limiting physical and chemical effects in volcanic eruption clouds. *J. Geophys. Res., 94*, 11165-11174.

Pitts, M.C. and L.W. Thomason, 1993. The impact of the eruptions of Mount Pinatubo and Cerro Hudson on Antarctic aerosol levels during the 1991 austral spring. *Geophys. Res. Lett., 20*, 2451-2454.

Pollack, J.B. and T.P. Ackerman, 1983. The possible effects of the El Chichón volcanic cloud on the radiation budget of the northern tropics. *Geophys. Res. Lett. 10*, 1057-1060.

Pollack, J.B., O.B. Toon, C. Sagan, A. Summers, B Baldwin, and W. VanCamp, 1976. Volcanic eruptions and climatic change: A theoretical assessment. *J. Geophys. Res., 81*, 1071-1083.

Pollack, J.B., O.B. Toon, and D. Wiedman, 1981. Radiative properties of the background stratospheric aerosols and implications for perturbed conditions. *Geophys. Res. Lett., 8*, 26-28.

Pollack, J.B., O.B. Toon, E.F. Danielson, D.J. Hofmann, and J.M. Rosen, 1983. The El Chichón volcanic cloud: An introduction. *Geophys. Res. Lett., 10*, 989-992.

Pollack, J.B., F. C. Witteborn, K. O'Brien, and B. Flynn, 1991. A determination of the infrared optical depth of the El Chichón volcanic cloud. *J. Geophys. Res., 96*, 3115-3122.

Post, M.J., 1984. Aerosol backscatter profiles at CO2 wavelengths: The NOAA data base. *Appl. Opt., 23*, 2507.

Post, M.J., C.J. Grund, A.O. Langford, and M.H. Proffitt, 1992. Observations of Pinatubo ejecta over Boulder, Colorado by lidars of three different wavelengths. *Geophys. Res. Lett., 19*, 195-198.

Pueschel, R.F., P.B. Russell, D.A. Allen, G.V. Ferry, and K.G. Snetsinger, 1994. Physical and optical properties of the Pinatubo volcanic aerosol: Aircraft observations with impactors and a sun-tracking photometer. *J. Geophys. Res., 99*, 12915-12922.

Rampino, M.R. and S. Self, 1984. Sulphur rich volcanic eruptions and stratospheric aerosols. *Nature, 310*, 677-679.

Rao, C.R.N., L.L. Stowe, and E.P. McLClain, 1989. Remote sensing of aerosols over the oceans using AVHRR data: Theory, practice, and applications. *Int. J. Remote Sens., 10*, 743-749.

Rao, C.R., and W.A. Bradley, 1983. Effect of El Chichón dust cloud on insolation measurements at Corvalis Oregon, U.S.A. *Geophys. Res. Lett., 10*, 389-391.

Read, W.G., __Froidevzux, and J.W. Water, 1993. Microwave limbsounder measurements of SO_2 from Mt. Pinatubo volcano. *Geophys. Res. Lett., 20*, 1299-1302.

Reddy, P.J., F.W. Kreiner, J.J. DeLuisi, and Y. Kim, 1990. Aerosol optical depths over the Atlantic derived from shipboard sunphotometer observations during the 1988 global change expedition. *Global Biogeochem. Cycles, 4*, 225-240.

Robinson, N., 1966. *Solar Radiation*. Elsevier, Amsterdam, 347 pp.

Robock, A. and Y. Liu, 1994. The volcanic signal in Goddard Institute for Space Studies three-dimensional model simulations. *J. Clim., 7*, 44-55.

Robock, A. and J. Mao, 1992. Winter warming in surface temperature observations. *Geophys. Res. Lett., 19*, 2405-2408.

Robock, A., and M. Matson, 1983. Circumglobal transport of the El Chichón volcanic dust cloud. *Science, 221*, 195-197.

Rosen, H., A.D.A. Hansen, L. Gundel, and T. Novakov, 1978. Identification of the optically absorbing component of urban aerosols. *Atmos. Environ., 15*, 1371-1374.

Russell, P.B. and M.P. McCormick, 1989. SAGE II aerosol data validation and initial data use: An introduction and overview. *J. Geophys. Res., 94*, 8335-8338.

Russell, P.B. and G.E. Shaw, 1975. Comments on "The precision and accuracy of Volz sunphotometry." *J. Appl. Meteorol., 14*, 1206-1209.

Russell, P.B., W. Viezee, R.D. Hake, Jr., and R.T.H. Collis, 1976. Lidar observations of stratospheric aerosol: California, October 1972-March 1974. *Q. J. R. Meteorol. Soc., 102*, 619-639.

Russell, P.B., J.M. Livingston, E.G. Dutton, R.F. Pueschel, J.A. Reagan, T.E. DeFoor, M.A. Box, D. Allen, P. Pilewskie, B.M. Herman, S.A. Kinne, and D.J. Hofmann, 1993. Pinatubo and Pre-Pinatubo optical-depth spectra: Mauna Loa measurements, comparisons, inferred particle size distributions, radiative effects, and relationship to lidar data. *J. Geophys, Res., 98*, 22969-22985.

Sassen, K.D., D. O'C. Starr, G.G. Mace, M.R. Poellot, S.H. Melfi, W.L. Eberhard, J.D. Spinhirne, E.W. Eloranta, D.E. Hagen, and J. Hallett, 1995. The 5-6 December 1991 FIRE II jet stream cirrus case study: possible influences of volcanic aerosols. *J. Atmos. Sci., 52*, 97-132.

Sato, M., J.E. Hansen, M.P. McCormick, and J.B. Pollack, 1993. Stratospheric aerosol optical depths, 1850-1990. *J. Geophys. Res., 98*, 22987-22994.

Saunders, R., 1993. Radiative properties of Mount Pinatubo volcanic aerosols over the tropical Atlantic. *Geophys. Res. Lett., 20*, 137-140.

Self, S., J-X. Zhao, R.E. Holasek, R.C. Torres and A.J. King, 1995. The atmospheric impact of the 1991 Mount Pinatubo eruption. In *The 1991-1992 Eruptions of Mount Pinatubo, Philippines.* Punongbayan, R.S. and C.G. Newhall (eds.) U.S. Geological Survey Professional Paper., in press.

Shapiro, M.A., R.C. Schnell, F.P. Parungo, S.J. Oltmans, and B.A. Bodhaine, 1984. El Chichón volcanic debris in an Arctic tropopause fold. *Geophys. Res. Lett., 11*, 421-424.

Shaw, G.E., 1983. Sun photometry. *Bull. Am. Meteorol. Soc., 64*, 4-10.

Sheridan, P.J., R.C. Schnell, D.J. Hofmann, and T. Deshler, 1992. Electron microscope studies of Mt. Pinatubo aerosol layers over Laramie, Wyoming during summer 1991. *Geophys Res. Lett., 19*, 203-206.

Spencer, R.W. and J.R. Christy, 1990. Precise monitoring of global temperature trends from satellites. *Science, 247*, 1558-1562.

Spencer, R.W. and J.R. Christy, 1992. Precision and radiosonde validation of satellite grid point temperature anomalies. Part II: A tropospheric retrieval and trends during 1979-90. *J. Clim., 5*, 858-866.

Spinhirne, J.D., 1983. El Chichón eruption cloud: Latitudinal variation of the spectral optical thickness measurement for October 1982. *Geophys. Res. Lett., 10*, 881-884.

Stamnes, K., S-C. Tsay, W. Wiscombe, and K. Jayaweera, 1988. Numerically stable algorithm for discrete-ordinate-method radiative transfer in multiple scattering and emitting layered media. *Appl. Opt., 27*, 2502-2509.

Stephens, G.L., 1994. *Remote Sensing of the Lower Atmosphere, An Introduction.* Oxford University Press, New York, 251 pp.

Stone, R.S., J.R. Key, and E.G. Dutton, 1993. Properties and decay of stratospheric aerosols in the Arctic following the 1991 eruptions of Mount Pinatubo. *Geophys. Res. Lett., 20*, 2359-2362.

Stowe, L.L., R.M. Carey, and P.P. Pellegrino, 1992. Monitoring the Mt. Pinatubo aerosol layer with NOAA/11 AVHRR data. *Geophys. Res. Lett., 19*, 159-162.

Strong, A.E. and L.L. Stowe, 1993. Comparing stratospheric aerosols from El Chichón and Mount Pinatubo using AVHRR data. *Geophys. Res. Lett., 20*, 1183-1186.

Tanaka, M.T., M. Shiobara, T. Nakajima, M. Yamano, and K. Arao, 1989. Aerosol optical characteristics in the yellow sand events observed in May 1882 at Nadasaki–Part I Observations. *J Meteorol. Soc. of Japan, 67*, 267-278.

Thomason, L.W., 1992. Observations of a new SAGE II aerosol extinction mode following the eruption of Mt. Pinatubo. *Geophys. Res. Lett., 19*, 2179-2182.

Toon, O.B. and J.B. Pollack, 1973. Physical properties of the stratospheric aerosols. *J. Geophys. Res., 78*, 7051-7056.

Toon, O.B. and J.B. Pollack, 1980. Atmospheric aerosols and climate. *Am. Sci., 68*, 268-278.

Trepte, C.R., L.W. Thomason, and G.S. Kent, 1994. Banded structures in stratospheric aerosol distributions. *Geophys. Res. Lett., 21*, 2397-2400.

Turco, R.P., R.C. Whitten, and O.B. Toon, 1982. Stratospheric aerosols: Observations and theory. *Rev. Geophys. Space Phys., 20*, 233-279.

Valero, F.P.J. and P. Pilewskie, 1992. Latitudinal survey of spectral optical depths of the Pinatubo volcanic cloud-derived particle sizes, columnar mass loadings, and effects on planetary albedo. *Geophys. Res. Lett., 19*, 163-166.

van de Hulst, H.C., 1957. *Light Scattering by Small Particles*. Dover , New York, 470 pp.

Viebrock, H.J. and E.C. Flowers, 1968. Comments on the recent decrease in solar radiation at the South Pole. *Tellus, 20*, 400-411.

Wendler, G., 1984. Effects of the El Chichón volcanic cloud on solar radiation received at Fairbanks, Alaska. *Bull. Amer. Meteorol. Soc., 65*, 216-218.

Whitlock, C.H., T.P. Charlock, W.F. Staylor, R.T. Pinker, I. Laszio, R.C. DiPasquale, and N.A. Ritchy, 1993. WCRP surface radiation budget shortwave data product - version 1.1. NASA Tech. Memo. - 107747, Langley Research Center, Hampton, Virginia, 28 pp.

Winker, D.M. and M.T. Osborn, 1992. Preliminary analysis of observations of the Pinatubo volcanic plume. *Geophys. Res. Lett., 19*, 155-158.

Wiscombe, W., 1980. Improved Mie scattering algorithms. *Appl. Opt., 19*, 1505-1509

Witteborn, F.C., K.O. O'Brien, H.W. Crean, J.B. Pollack, and K.H. Bilski, 1983. Spectroscopic measurements of the 8- to 13-micrometer transmission of the upper atmosphere following the El Chichón eruptions. *Geophys. Res. Lett., 10*, 1009-1012.

Yamamoto, G. and M. Tanaka, 1969. Determination of aerosol size distribution from spectral attenuation measurements. *Appl. Opt., 8*, 447-453.

Young, A.T., 1981. On the Rayleigh-scattering optical depth of the atmosphere. *J. Appl. Meteorol., 20*, 328-330.

Young, R.E., H. Houben, and O.B. Toon, 1994. Radiatively forced dispersion of the Mt. Pinatubo volcanic cloud and induced temperature perturbations in the stratosphere during the first few months following the eruption. *Geophys. Res. Lett., 21*, 369-362.

Yue, G.K., M.P. McCormick, and E.W. Chiou, 1991. Stratospheric aerosol optical depth observed by Stratosphere Aerosol and Gas Experiment II: Decay of the El Chichón and Ruiz volcanic perturbations. *J. Geophys. Res., 96*, 5209-5219.